Electroanalysis of Solid Particles

A thesis submitted for the degree of Doctor of Philosophy
in Physical and Theoretical Chemistry

Qianqi Lin
St John's College

Hilary Term 2017

Abstract

This thesis reports theoretical and experimental work with the primary aim of developing new electrochemical methods to detect and characterise solid particles at the micron-scale, specifically alumina (aluminium oxide) particles and graphene nanoplatelets, as representative of insulating and conductive particles, respectively.

The fundamentals of thermodynamics, kinetics and mass transport in electrochemistry are introduced in Chapter 1, with the elaboration of electrodes, voltammetry and chronoamperometry used for electroanalysis. A comparison of non-electrochemical and electrochemical techniques used to analyse solid particles is also given. Chapter 2 provides information on both the experimental procedures and theoretical simulations used in the studies.

Chapter 3 first investigates the oxidation of catechol (1,2-hydroxybenzene) in the pH range from 1.0 to 14.0 voltammetrically using a clean glassy carbon electrode. Analysis of the voltammograms allows the inference of the reaction mechanism in full and kinetics using a "scheme of squares". When the electrode surface is covered with sparse coverages of alumina particles, strong *apparent* catalysis of the reaction is discovered. The cause of such an apparent catalysis is then examined in Chapter 4. Comparison of the voltammograms at alumina- and graphene nanoplatelets-modified electrodes reveals that a change in the thermodynamics of the intermediate species, rather than a change of electron transfer rate, results in the apparent electrocatalysis of the redox process.

With understanding of the oxidation of catechol electrocatalysed by alumina-modified electrodes, Chapter 5 reports to innovative "tagging" of catechol onto the surface of alumina. A new electrochemistry method based on particle impacts is used to quantify the

adsorption of catechol on single alumina particles. In these experiments, particles suspended in solution impact a microelectrode held at a suitable potential for the oxidation or reduction of the adsorbed species. The current "spikes" induced from the impacts can be simulated to derive information such as the size of the particles, the surface coverage of modifiers, and the diffusion coefficients of charge transfer over the surface of the particles. The method is further applied to various modifiers, including 9,10-anthraquinone, tetrachloro-1,4-benzoquinone, and poly(vinylferrocene) in Chapter 6.

The investigation of solid particles then proceeds from alumina to graphene nanoplatelets. In Chapter 7, graphene nanoplatelets are "tagged" with a ferrocene derivative prior to impact experiments. Two types of charge transfer are involved in the impacts: *Faradaic* due to redox of the modifier, and *capacitative* due to disruption of the electrical double layer at the electrode/solution interface. For the first time, both processes can be observed during the impacts of graphene nanoplatelets.

Chapter 8 exploits the impacts method to evaluate the electron transfer rate of the ferrocene/ferrocenium redox couple immobilised on graphene nanoplatelets in aqueous solution. Single graphene nanoplatelets modified with poly(vinylferrocene) are allowed to impact a microelectrode. By adopting the potential applied, each graphene nanoplatelet temporarily acts as a "chemically modified nanoelectrode" for the duration of the impact, facilitating the resolution of fast electron transfer for the redox couple.

Finally, Chapter 9 demonstrates the use of poly(vinylferrocene)-modified graphene nanoplatelets as a mediator for the oxidation of L-cysteine in aqueous solution. The theory of catalytic particle impacts is developed. The kinetics and mechanism of the catalysis is then assessed harnessing both experiment and theory.

Acknowledgements

First and foremost I would like to express my deep gratitude to Professor Richard Compton for his guidance and inspiration throughout my Part II and DPhil over the last four and half years. I would also like to thank him for being always supportive to me, for understanding and trusting me. Not only his expertise in electrochemistry, but also his hard work, kindness and sense of humour, will always encourage me.

The second thank you must go to Dr. Christopher Batchelor-McAuley, who helped to interpret complicated experimental results and taught me a tremendous amount. Mr. Haoyu Wu, Mr. Jeffrey Poon and Ms. Chuhong Lin should be acknowledged for their contribution in the production of part of this work.

Thank you also to Dr. Linhongjia Xiong for being my "sister" over the years from Somerville to St John's, and kindly helping me in both work and life. A big thank you to Dr. Qian Li for taking me into the world of electrochemistry, and for being patient and helpful to me. I would also like to thank Dr. Enno Kätelhön and Professor Kristina Tschulik for all the good-old-time drinks, memory that will always make me smile. Thanks also go to Dr. Patty Lee Alcantar and Dr. Her Shuang Toh for their very helpful advice, and for a wonderful reunion in California. Many thanks to Peilin, Xiaofei, Mendy, Xiuting, Chuhong, Crystal and Jake for being my lunch buddies over different periods of my degrees. To other members of the Compton Group - Ying, Rita, Eden, Tom, Shaltiel, Dia, Korbua, Lifu, Prof. Chen, Prof. Liu, Prof. Yang, and every other member, thank you for making my time working here so great.

To other extraordinary people I have met in Oxford - Ben Ban, Alex, Simson, Ricky, Arthur, thank you for being a member of "BASIRA", and I am looking forward to our next journey to see the stars. Sharon, Yapei, Jason, Flora, TT and Ben Lo, thank you for being my besties since our undergrad, so I know I will never be alone. Carly and Ed, thank you for being the best neighbours and my family here. Shaun, Lesley, Stan and Hayley, thank you for making me delicious Sunday roasts, and always taking care of me.

Last, a very special thanks to my parents, for their endless love and support, and for being proud of me. I am who I am because you give the best to me.

Glossary

Roman Symbols

Symbol	Meaning	Unit
(ads)	adsorption phase	
(aq)	aqueous phase	
a_i	activity	unitless
A	area	cm^2
C_i	concentration	mol cm^{-3}
$C_{i,bulk}$	bulk concentration	mol cm^{-3}
C_d	capacitance per area	μF cm^{-2}
D_i	diffusion coefficient	cm^2 s^{-1}
E	electrode potential	V
E^0	standard electrode potential	V
E_f^0	formal electrode potential	V
$E_{1/2}$	half-wave potential	V
E_{mid}	mid-point potential	V
E_p	peak potential	V
ΔE_p	peak-to-peak separation	V
F	Faraday constant (96 485)	C mol^{-1}
G	Gibbs energy	J mol^{-1}
i	species	
I	current	A
I_p	peak current	A
I_{ss}	steady-state current	A
J	flux	mol cm^{-2} s^{-1}
k^0	standard electrochemical rate constant	cm s^{-1}
k_c	catalytic rate constant	M^{-1} s^{-1}
k_{re}, k_{ox}	heterogeneous rate constants	cm s^{-1}
l	electrode length	cm
(m)	electrode metallic phase	

Symbol	Meaning	Unit
m_T	mass transport coefficient	cm s^{-1}
m	mass	g
M	molar mass	g mol^{-1}
n	number of electrons transferred	unitless
n'	number of electrons transferred before the rate-determining step	unitless
n''	number of experimental data points	unitless
Nu	dimensionless current	unitless
Q	charge	C
r_e	electrode radius	cm
r_s	sphere radius	cm
R	universal gas constant (8.314)	J K^{-1} mol^{-1}
$\boldsymbol{R}$	resistance	Ω
(sol)	solution phase	
S	surface area	cm^{-2}
t	time	s
T	absolute temperature	K
$v(x)$	solution velocity in the x direction	cm s^{-1}
Z_i	ionic charge	C

Greek Symbols

Symbol	Meaning	Unit
α	Butler-Volmer reductive transfer coefficient	unitless
β	Butler-Volmer oxidative transfer coefficient	unitless
Δ	difference in a quantity	
∇	vector operator in a three-dimensional Cartesian space	
η	overpotential	V
γ_i	activity coefficient	unitless
Γ_i	surface coverage	mol cm^{-2}
Λ	Matsuda-Ayabe parameter	unitless
μ_i^0	standard chemical potential	J mol^{-1}
ν	scan rate	V s^{-1}
ϕ_i	electrical potential	V
$\sum$	sum of	
τ	dimensionless time	unitless

Contents

Chapter 1

Fundamentals of Electrochemistry

This chapter introduces essential ideas underlying the results in this thesis.

1.1 Electrochemical Equilibrium: the Nernst Equation

At the interface between a metallic working electrode (m) and a solution phase (aq), a general one-electron reduction can be described as:

$$\mathrm{Ox_{(aq)}}^{q} + \mathrm{e^-_{(m)}} \underset{k_{ox}}{\overset{k_{re}}{\rightleftharpoons}} \mathrm{Re_{(aq)}}^{q-1} \tag{1.1}$$

where Ox and Re are the oxidised and reduced species in solution phase, k_{re} and k_{ox} are the electron transfer rate constants for the reduction and the oxidation, respectively. Since the process involves electron transfer between the two distinct phases, (m) and (aq), at the point of equilibrium, there is a charge separation between the electrode and the solution. This is the origin of the electrode potential established at the electrode/solution interface. An *electrochemical* equilibrium is, hence, established. While we are familiar that the position of a *chemical* equilibrium is controlled by the chemical potentials of reactants and products, that of an electrochemical equilibrium represents a balance between chemical and electrical potentials. This is due the fact that the two phases involved in electron

transfer, the electrode and the solution, have two different electrical potentials, ϕ_m and ϕ_s (V). For a basic one-electron redox couple, the relation of ϕ_m and ϕ_s can be quantitatively described by the *Nernst Equation*[1]:

$$\phi_m - \phi_s = \frac{\Delta\mu^0}{F} + \frac{RT}{F} \ln \frac{a_{\mathrm{Ox}}}{a_{\mathrm{Re}}} \tag{1.2}$$

$$\text{with} \quad a_i = \gamma_i C_i \tag{1.3}$$

where $\Delta\mu^0 = \mu^0_{Ox} + \mu_{\mathrm{e}^-} - \mu^0_{Re}$ and the three terms are the chemical potentials of Ox, e^- and Re, respectively. R is the gas constant (8.314 J K^{-1} mol^{-1}), T is the absolute temperature (K), and F is the Faraday constant (96 485 C mol^{-1}). a_i is the activity and γ_i is the activity coefficient (unitless) of species i, allowing the non-ideality of the solution. C_i is the concentration (mol cm^{-3}). Here $\phi_m - \phi_s$ is an absolute value. Such quantities cannot be measured. Rather a two-electrode system is needed. The potential applied between a *test* electrode and a *reference* electrode, E (V), is

$$E = (\phi_{test} - \phi_s) - (\phi_{reference} - \phi_s) \tag{1.4}$$

For this "two-electrode" system, the Nernst Equation becomes

$$E = E^0 + \frac{RT}{F} \ln \frac{a_{\mathrm{Ox}}}{a_{\mathrm{Re}}} \tag{1.5}$$

where E^0 is the standard electrode potential (V) when the reference electrode is a standard hydrogen electrode (SHE), and the rest of the terms have been previously defined. To avoid the inconvenient use of activities, the formal potential, E^0_f (V), is introduced:

$$E = E^0_f + \frac{RT}{F} \ln \frac{C_{\mathrm{Ox}}}{C_{\mathrm{Re}}} \tag{1.6}$$

$$\text{where} \quad E^0_f = E^0 + \ln \frac{\gamma_{\mathrm{Ox}}}{\gamma_{\mathrm{Re}}} \tag{1.7}$$

As Nernst Equation only applies to equilibrium conditions when fast electron transfer is observed, the following section describes the current-potential behaviour away from equilibrium.

When a potential is *applied* to the working electrode to disturb the equilibrium discussed in the previous section, two types of processes may occur at the working electrode, depending on whether electrons are transferred across the electrode/solution interface (Faradaic currents) or not (non-Faradaic currents).

1.2 Faradaic Processes

When *Faradaic* processes take place, electrons are transferred across the electrode / solution interface during the electrolysis of the electroactive species. This results in electrochemical reaction, and the charge transferred can be quantified by *Faraday's Law of Electrolysis*[1]:

$$m = \frac{QM}{Z_i F} \tag{1.8}$$

where m is the mass of the electroactive species (g), Q is the total electric charge passed (C), M is the molar mass of the species (g mol^{-1}), Z_i is the number of electrons passed per ion, and F is the Faraday constant (96 485 C mol^{-1}).

1.2.1 Electrode Kinetics: the Butler-Volmer Equation

To discuss the electrode kinetics, the following reaction is considered:

$$\mathrm{Ox_{(aq)}}^{q} + \mathrm{e^-_{(m)}} \underset{k_{ox}}{\overset{k_{re}}{\rightleftarrows}} \mathrm{Re_{(aq)}}^{q-1} \tag{1.9}$$

Note reaction 1.9 differs from reaction 1.1 by the use of arrows instead of harpoons, indicating absence of equilibrium. The electron transfers result in the passage of a Faradaic

current, I (A), through the electrode, which can be expressed by the equation

$$I = I_{re} + I_{ox} = FAJ \tag{1.10}$$

$$\text{with} \quad J = J_{re} + J_{ox} = k_{re}[\text{Ox}]_0 - k_{ox}[\text{Re}]_0 \tag{1.11}$$

where A is the electrode area (cm^2) and J is the heterogeneous reaction flux at the interface (mol m^{-2} s^{-1}). k_{re} and k_{ox} are the electron transfer rate constants for the reduction and the oxidation, respectively. They are dependent on the electrode potential. $[\text{Ox}]_0$ and $[\text{Re}]_0$ are the surface concentrations (mol cm^{-3}) of oxidised and reduced species, respectively. The surface concentrations are usually different to their bulk concentrations since electrolysis takes place and locally depletes or builds up material near the interface.

Using Transition State Theory[2, 3], electrode kinetics can be related to the potential difference at the electrode/solution interface *via* the Gibbs energy. The relationship can be further described by the *Butler-Volmer Equation*[1]:

$$J = k^0[\text{Ox}]_0 \text{exp}\left(\frac{-\alpha F}{RT}\eta\right) - k^0[\text{Re}]_0 \text{exp}\left(\frac{\beta F}{RT}\eta\right) \tag{1.12}$$

$$\text{with} \quad k_{re} = k^0 \text{exp}\left(\frac{-\alpha F}{RT}\eta\right) \tag{1.13}$$

$$\text{and} \quad k_{ox} = k^0 \text{exp}\left(\frac{\beta F}{RT}\eta\right) \tag{1.14}$$

where k^0 is the standard electrochemical rate constant (cm s^{-1}), η is the overpotential (V) applied to the working electrode with $\eta = E - E_f^0$. α is the reductive transfer coefficient ranging from 0 to 1 in the one-electron transfer case, and $\alpha + \beta = 1$, where β is the oxidative transfer coefficient. If α is close to 0, the transition state is reactant-like (Ox like); if α is close to 1, the transition state is product-like (Re like). A typical value of α is close to 0.5, indicating the transition state has intermediate behaviour. The combination

of Eqs. 1.10 and 1.12 gives the current-potential relationship:

$$I = FA\left[k^0[\mathrm{Ox}]_0 \exp\left(\frac{-\alpha F}{RT}\eta\right) - k^0[\mathrm{Re}]_0 \exp\left(\frac{\beta F}{RT}\eta\right)\right] \tag{1.15}$$

Based on the Butler-Volmer kinetics, the Tafel Law can be derived. When the reduction process in reaction 1.9 is sufficiently fast that the back reaction (oxidation) becomes negligible, the flux can be expressed as

$$J_{re} = k^0[\mathrm{Ox}]_0 \exp\left(\frac{-\alpha F}{RT}\eta\right) \tag{1.16}$$

Similarly, when the oxidation process is sufficiently fast relative to the reduction, the flux becomes

$$J_{ox} = k^0[\mathrm{Re}]_0 \exp\left(\frac{\beta F}{RT}\eta\right) \tag{1.17}$$

Assuming $[\mathrm{Ox}]_0$ and $[\mathrm{Re}]_0$ are not greatly changed from their constant bulk values, the above equations can be rearranged as

$$\ln|I_{re}| = -\frac{\alpha F E}{RT} + \text{constant} \tag{1.18}$$

$$\ln|I_{ox}| = \frac{\beta F E}{RT} + \text{constant} \tag{1.19}$$

where I_{re} and I_{ox} are the reduction and oxidation currents respectively. Plots of $\ln|I_{ox}|$ *vs.* E, or $\ln|I_{re}|$ *vs.* E, named *Tafel plots*, can be used to determine the value of transfer coefficients α and β:

$$\frac{\partial \ln|I_{re}|}{\partial E} = -\frac{\alpha F}{RT} \tag{1.20}$$

$$\frac{\partial \ln|I_{ox}|}{\partial E} = \frac{\beta F}{RT} \tag{1.21}$$

1.2.2 Electrochemical Cells

A typical dynamic electrochemical experiment is performed using three electrodes (Figure 1.1): a working electrode, a counter electrode and a reference electrode. The current flows between the *working* electrode and the *counter* electrode, and the potential is applied at the *working* electrode and measured against a *reference* electrode.

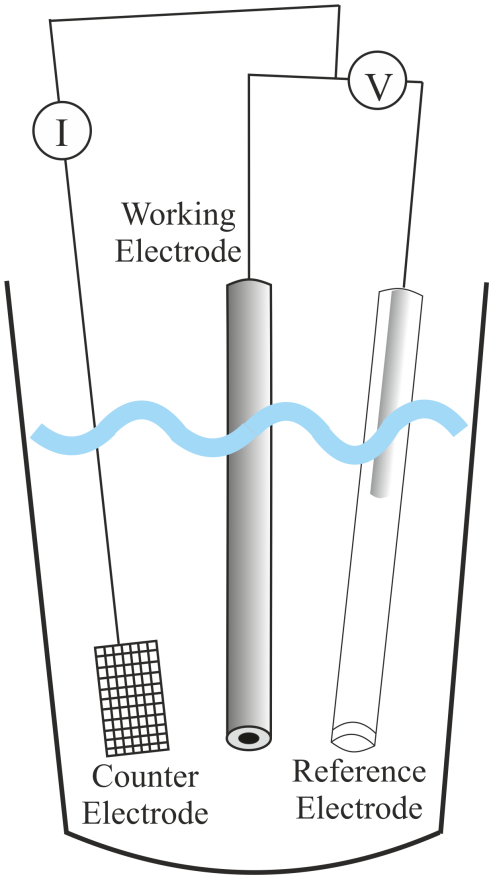

Figure 1.1: Diagram of a three-electrode cell.

The use of a *counter* electrode here is to minimise any potential drop between the working electrode and reference electrode, named 'ohmic drop'. The current passes through the *counter* electrode, rather than the *reference*. The introduction of the counter electrode thus ensures that no chemical changes occur within the reference electrode. Application of an external potential, E (V), would give

$$E = (\phi_{working} - \phi_s) - (\phi_{reference} - \phi_s) + I\boldsymbol{R} \tag{1.22}$$

where $\phi_{working}$, $\phi_{reference}$ and ϕ_s refer to the electrical potentials (V) of the working electrode, the reference electrode and the solution phase, respectively. The extra $\boldsymbol{IR}$ term compared to Eq. 1.4 is the ohmic drop, which reflects the unknown and undesirable electrical resistance of the bulk solution, between the working and reference electrode. Through the use of a counter electrode, the $\boldsymbol{IR}$ term is minimised since with this there is no need to pass a current through the reference electrode.

The use of microelectrodes (will be introduced in Section 1.5) can also minimise the $\boldsymbol{IR}$ term. Such electrodes have small dimensions and so pass very low current (*c.a.* 10^{-9} A), so the $\boldsymbol{IR}$ term becomes small enough to neglect even with a simple two-electrode (working and reference) system.

1.3 Non-Faradaic Processes

Non-Faradaic processes do not involve any electrochemical reactions or charge transfers, as they take place due to the charging and discharging of the double layer capacitance. Non-Faradaic processes can be minimised by addition of supporting electrolyte to the solution. The following sections will elaborate the three important concepts of the electrical double layer, of capacitative currents, and of the use of supporting electrolyte.

1.3.1 the Electrical Double Layer

When a potential is applied to an electrode, the electrode becomes charged. In order to maintain electrical neutrality, an equal but opposite charge migrates from solution and builds up adjacent to the electrode. The electrode/solution interface behaves like a capacitor, and the whole array of charged species existing at the interface is known as the *electrical double layer* (Figure 1.2) being overall electro-neutral.[4] The solution side of the double layer can be thought of comprising several "layers". The *compact layer*

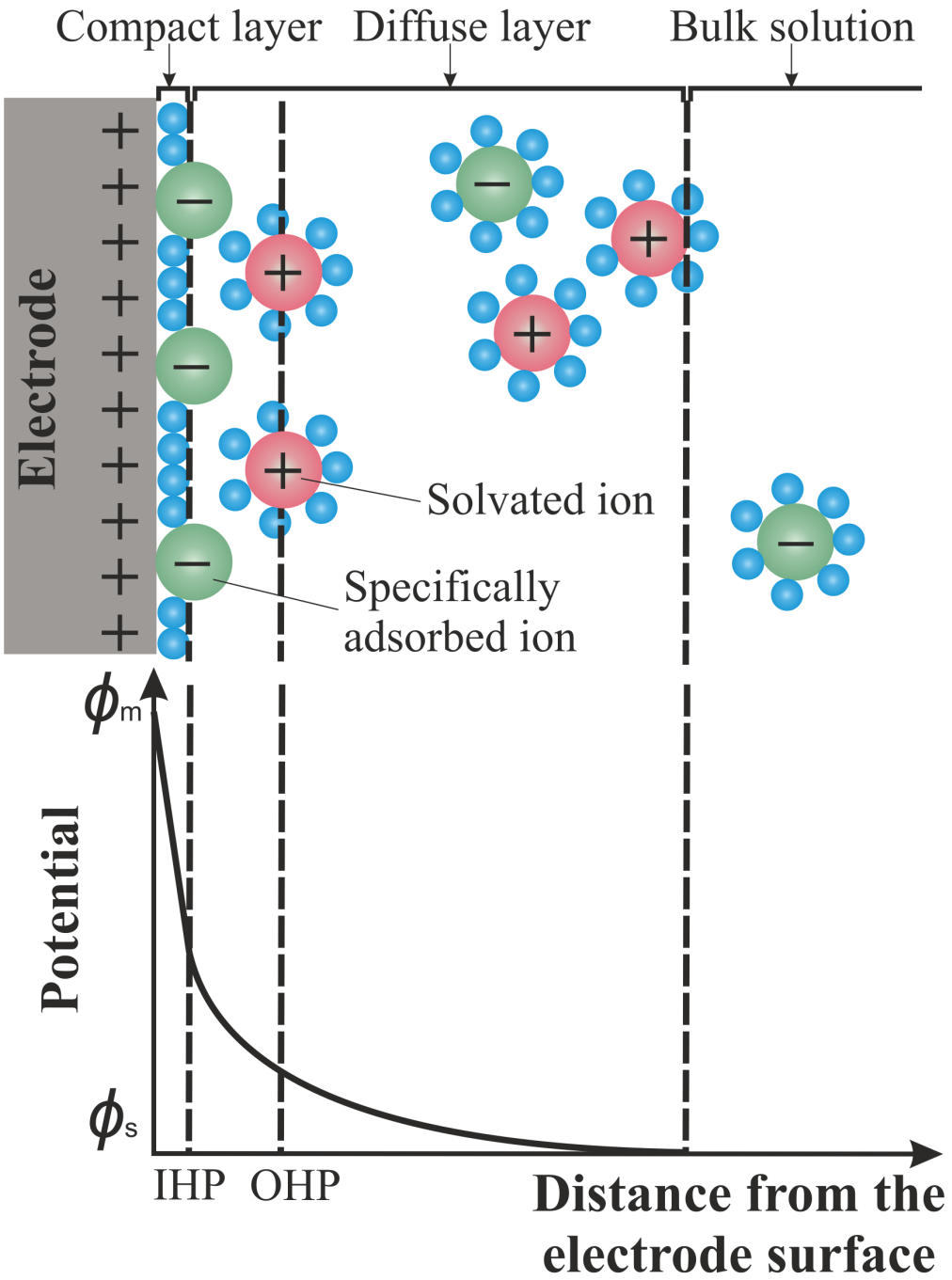

Figure 1.2: Top: model of the electrical double layer. Bottom: drop in potential across the double layer.

is located closest to the electrode, where ions lose their solvation shell and are directly in contact with the electrode. They are called *specifically adsorbed* ions. This ability is strongly dependent on the ions' chemical identity[5]. The position of the electrical centres of the specifically adsorbed ions is called the *Inner Helmholtz Plane* (IHP). In the *diffuse layer*, solvated ions undergo Brownian motion due to diffusion, and they can only approach the electrode to a certain distance. The interaction of the solvated ions with the charged electrode involves only long-range electrostatic forces, hence the interaction is independent of the chemical property of the ions. The position of the centres of these nearest solvated ions is called the *Outer Helmholts Plane* (OHP). Figure 1.2 also shows the potential variation across the double layer. Within the compact layer, the potential is thought to decrease linearly with the distance away from the electrode surface. In the diffuse layer, the potential decreases less rapidly and gradually to that of the bulk solution, which is electro-neutral.

1.3.2 Capacitative Current

When a potential is applied across the "capacitor", a flow of charges induces a *capacitative current*, or *non-Faradaic current*, which is expressed as,

$$I = \frac{dQ}{dt} = C_d A \frac{dE}{dt} = C_d A \nu \tag{1.23}$$

where C_d is the capacitance of the double layer per area (μF cm^{-2}), A is the double layer area (cm^2), and ν is the scan rate (V s^{-1}). At a given potential, C_d is typically in the range of $10 \sim 40$ μF cm^{-2}. However, unlike real capacitors, whose capacitances are independent of the voltage across them, C_d is often a function of potential[6].

Capacitative currents are often minimised, so that analysis of Faradaic currents only becomes easier in the study of an electrochemical reaction. For this reason, capacitative

current can be reduced by the use of a small electrode surface *e.g.* a microelectrode, or a slow scan rate.

1.3.3 Supporting Electrolyte

The thickness of the diffuse layer depends on the total ionic concentration in the solution. For example, when the ionic concentration is greater than 10^{-2} M, the thickness is less than *ca.* 100 Å. In order to compress the electrical double layer, an electrochemically inert background *electrolyte* salt can be added to the solution, usually with a high concentration exceeding 0.1 M. This can be advantageous in several ways. First, it compresses the double layer, so migration of charged species can be minimised, making modelling in terms of diffusion only mass transport easier (see later in Section 1.4.2). Second, the potential drop between the electrode and bulk solution is ensured to occur over a distance of 10 $\sim$ 20 Å, which is compatible with electron quantum tunnelling between the electrode species and solution phase; otherwise only part of the driving force, $\phi_m - \phi_s$, is available at the site of electron transfer. Third, addition of electrolyte enhances the conductivity of the solution and the ionic strength becomes nearly constant, which subsequently maintains the formal potential of the reactant as effectively constant. It also, fourth, reduces ohmic drop.

The choice of supporting electrolyte may depend on its interaction with the studied electroactive species. For example, 0.1 M KCl was used as supporting electrolyte in most of the work reported in the chapters below. However, 0.1 M $NaClO_4$ is used in Chapters 7 and 8 due to the strong ion-pairing between Cl^- anions and ferrocenium cations.

1.4 Mass Transport

For any electrochemical reaction, the overall kinetics may not only be controlled by the rate of electron transfer, but also by the rate of mass transport. *Mass transport* is the movement of a substance in solution, either diffusively due to random molecular motion or resulting from an applied external stimulus, such as a mechanical force, a concentration gradient or an electric field. Three main processes contribute to mass transport: diffusion, migration and convection, which can be quantified by the one-dimensional form of the *Nernst-Planck Equation*[4]:

$$J_i(x) = -D_i \frac{\partial C_i(x)}{\partial x} - \frac{Z_i F}{RT} D_i C_i \frac{\partial \phi(x)}{\partial x} + C_i \upsilon(x) \tag{1.24}$$

where $J_i(x)$ is the flux (mol cm^{-2} s^{-1}) and the rest of the terms will be defined in the following sections. In order to simplify the description of an electrochemical reaction, the terms of migration and convection are usually eliminated by the methods described in the following sections. Modelling in terms of diffusion only transport thus becomes much easier than using the full Eq. 1.24.

1.4.1 Diffusion

Diffusion is the spontaneous movement of a species down a concentration gradient, so as to maximise entropy. The rate of this process is modelled mathematically by *Fick's First Law* relating the diffusive flux in one dimension (x), $J_{d,i}(x)$ (mol cm^{-2} s^{-1}), to the concentration gradient by the equation[1]

$$J_{d,i}(x) = -D_i \frac{\partial C_i(x)}{\partial x} \tag{1.25}$$

where D_i is the diffusion coefficient ($cm^2\ s^{-1}$) and its typical magnitude lies in the range $10^{-6} \sim 10^{-5}\ cm^2\ s^{-1}$. $C_i(x)$ is the concentration (mol cm^{-3}) at point x over a time t (s). Note that the negative sign implies the flux is down the concentration gradient from a higher to a lower level. For the diffusive flux in three dimensions (x, y, z), $\mathbf{J}_{d,i}$ (mol $cm^{-2}\ s^{-1}$), Fick's First Law becomes[4]

$$\mathbf{J}_{d,i} = -D_i \nabla C_i \tag{1.26}$$

where ∇ is a vector operator in a three-dimensional Cartesian space,

$$\nabla = \mathbf{i}\frac{\partial}{\partial x} + \mathbf{j}\frac{\partial}{\partial y} + \mathbf{k}\frac{\partial}{\partial z} \tag{1.27}$$

$\mathbf{i}$, $\mathbf{j}$, and $\mathbf{k}$ is the unit vector along the x, y, and z axis, respectively.

Fick's Second Law relates the evolution of the species concentration to the time variation, in one dimension, by the equation[1]

$$\frac{\partial C_i(x)}{\partial t} = D_i \frac{\partial^2 C_i(x)}{\partial x^2} \tag{1.28}$$

In three dimensions, Fick's Second Law becomes[4]

$$\frac{\partial C_i}{\partial t} = D_i \nabla^2 C_i \tag{1.29}$$

$$\text{where} \quad \nabla^2 = \frac{\partial^2}{\partial x^2} + \frac{\partial^2}{\partial y^2} + \frac{\partial^2}{\partial z^2} \tag{1.30}$$

Eq. 1.29 will be used in Chapter 9 to derive the theoretical model for the mediated L-cysteine oxidation on individual graphene nanoplatelets.

Diffusion is the dominant term of mass transport, and it is very important here to establish an understanding of the *diffusion layer* (Fig. 1.3). When a planar electrode is

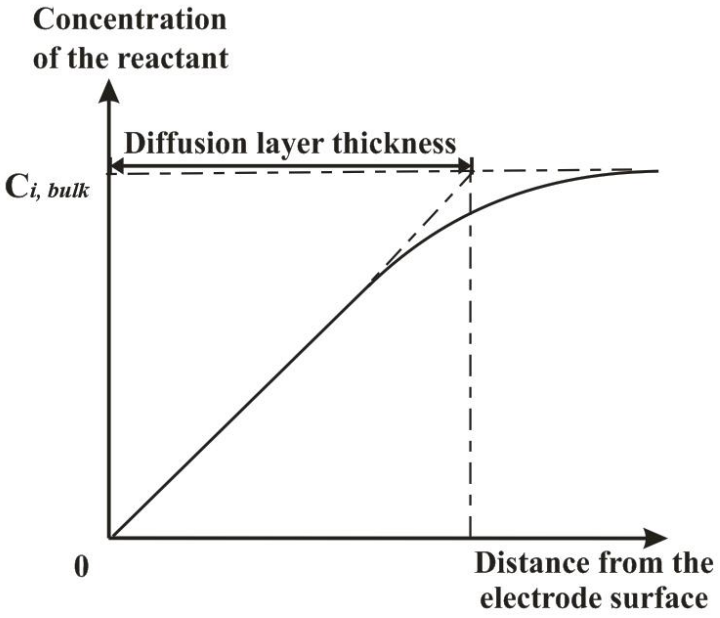

Figure 1.3: Nernst diffusion layer thickness.

placed in a container of a reactant, the bulk concentration of the reactant is constant. If the electrode is then connected so as to drive the electrolysis, reactant at the electrode *interface* is oxidised or reduced. Consequently, a concentration gradient is induced between the electrode and bulk solution, and a 'diffusion layer' is created close to the electrode, corresponding to the zone of depletion of the reactant.

The molecular basis of Fick's First Law in one dimension and three dimensions are shown in Figure 1.4. Consider the one-dimensional motion of a molecule, Figure 1.4a shows a 'box' of width $2\delta x$. Assumption is made that in each 'half box', a molecule has equal probabilities of moving to the right and to the left; and that a molecule moves δx in time δt. It follows that the number of particles travelling is $\left(\frac{1}{2}C_1 A\delta x\right)$ from left to right, and $\left(\frac{1}{2}C_2 A\delta x\right)$ from right to left. The net rate of transfer through a plane positioned at x is

$$\text{rate} = \frac{(C_1 - C_2)A\delta x}{2\delta t} \tag{1.31}$$

The flux is given by

$$J_{d,i}(x) = \frac{(C_1 - C_2)\delta x}{2\delta t} \tag{1.32}$$

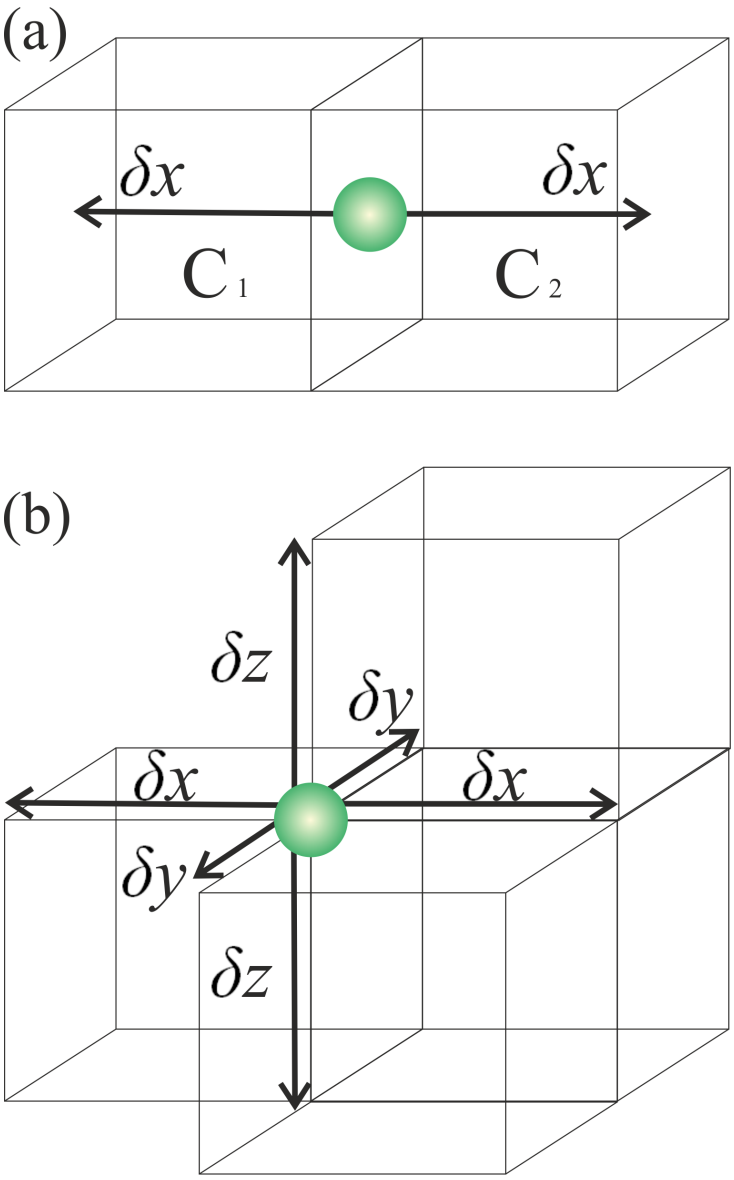

Figure 1.4: The molecular basis of Fick's First Law. (a) One dimension. (b) Three dimensions.

and the concentration gradient is

$$\frac{\partial C_i(x)}{\partial x} = \frac{-(C_1 - C_2)}{\delta x} \tag{1.33}$$

Combining Eqs. (1.32) and (1.33) gives

$$J_{d,i}(x) = -\frac{1}{2}\frac{(\delta x)^2}{\delta t}\frac{\partial C_i(x)}{\partial x} \tag{1.34}$$

which is equivalent to Fick's First Law (Eq. 1.25), if

$$D_i = \frac{(\delta x)^2}{2\delta t} \tag{1.35}$$

The diffusion coefficient, D_i, describes how far the molecule travels in a certain time. The diffusion layer thickness, δ (cm), thus can be expressed by the root mean square displacement in time, t, as

$$\delta = \sqrt{< x^2 >} = \sqrt{2D_i t} \tag{1.36}$$

which is the Einstein-von Smoluchowski equation.[7, 8] Similarly, the three-dimensional diffusion layer thickness is

$$\delta = \sqrt{6D_i t} \tag{1.37}$$

Diffusion will be discussed with respect to the electrode size in Section 1.5.

1.4.2 Migration

As explained in Section 1.3, the potential drop at electrode/solution interface produces an electric field. This field may interact with charged species within the solution and cause movement either to or from the electrode. This is known as *migration*. The migratory flux, $J_{m,i}$ at a point is proportional to the diffusion coefficient of the ion (D_i, cm^2 s^{-1}), the

concentration of the ion (C_i, mol cm^{-3}), the charge of the ion (Z_i, C), and the gradient of the electric potential (or "electric field", $\frac{\partial\phi(x)}{\partial x}$, V cm^{-1})

$$J_{m,i}(x) = -\frac{Z_i F}{RT} D_i C_i \frac{\partial\phi(x)}{\partial x} \tag{1.38}$$

Diffusive ($J_{d,i}$) and migratory ($J_{m,i}$) flux may be in the same or opposite directions, depending on the electric field and the charge of the electroactive species i. Figure 1.5 shows $J_{m,i}$ is in the same direction as $J_{d,i}$ when positively charged species are reduced at cathodes, while $J_{m,i}$ opposes $J_{d,i}$ when negatively charged species are reduced at cathodes. Migration can severely affect the current in electrochemical experiments, so it is often made negligible to simplify the mathematical treatment of experimental data. As discussed in Section 1.3, a supporting electrolyte at a concentration much larger than that of the electroactive species can be added, so that the $\frac{\partial\phi(x)}{\partial x}$ term is eliminated, and the double layer becomes very thin with respect to the diffusion layer. The migratory flux is hence reduced to negligible levels.

1.4.3 Convection

Convection is the movement of a species due to a mechanical force, and there are two forms of convection. *Natural* convection arises from the thermal gradients or density differences in the solution, which can unpredictably perturb electrochemical experiments. The poor reproducibility of natural convection makes quantitative analysis of the system very difficult and hence it is undesirable. *Forced* convection is caused by mechanical agitation of the solution *via* gas bubbling, stirring or pumping. It can be exploited deliberately to eliminate the effect of natural convection, thus allowing well-defined quantitative analysis *e.g.* a rotating disc electrode can be used to enhance forced convection, and the voltammetric signal thus increases significantly compared to that under quiescent (no stirring)

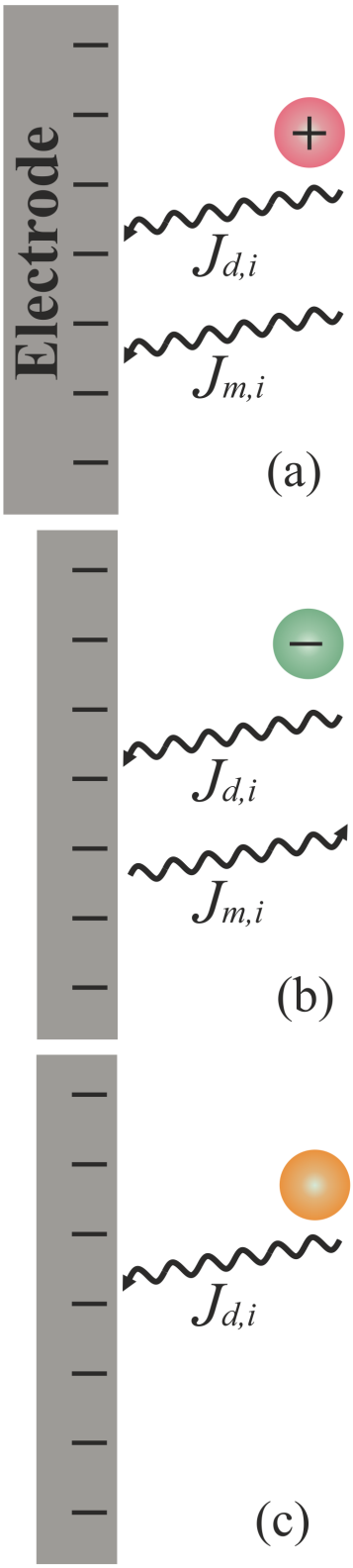

Figure 1.5: Reduction process with different directions of migratory flux. (a) Positively charged species. (b) Negatively charged species. (c) Uncharged species.

conditions. The flux due to convection is given by:

$$J_{c,i}(x) = C_i \upsilon(x) \tag{1.39}$$

where υ(x) is the solution velocity in the x direction (cm s^{-1}) and C_i is the concentration (mol cm^{-3}).

1.5 Macroelectrodes *vs.* Microelectrodes

The difference in behaviour between macro- and microelectrodes originates from their distinctive dimensions; while macroelectrodes have their size of the order of millimetres or more, microelectrodes have at least one dimension of the order of microns in size.

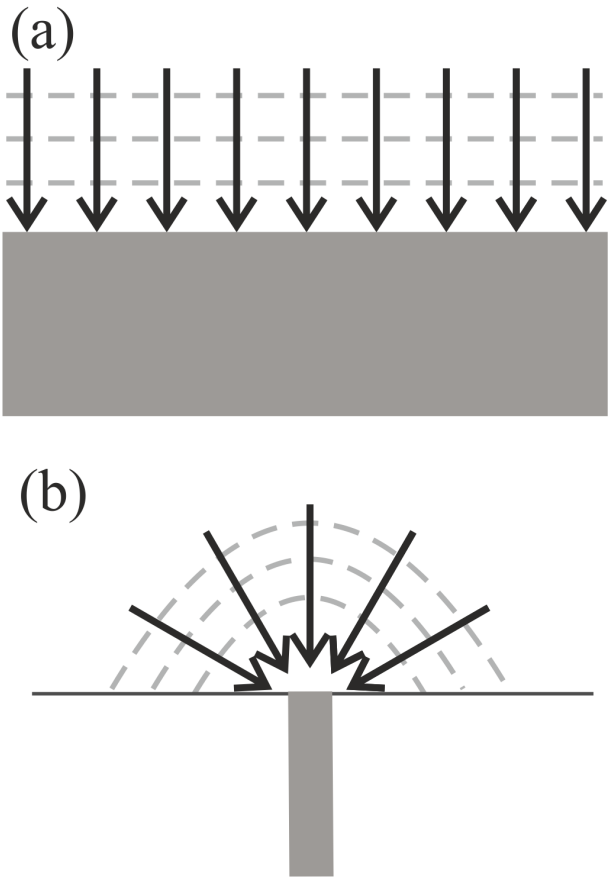

Figure 1.6: (a)Linear diffusion at a macroelectrode. (b)Convergent diffusion at a microdisc electrode. Arrows: diffusion of electroactive species. Dashed line: the diffusion layers.

Macroelectrodes have a much larger radius than the thickness of the diffusion layer *i.e.* $r_e \gg \delta$, where r_e (cm) is the radius of the electrode. Within the experimental time scale, the diffusion layer is normal to the electrode surface and *linear* diffusion (Figure 1.6a) prevails. When electrolysis proceeds, the thickness of the diffusion layer becomes progressively larger. As the diffusive flux is in one dimension, the diffusion layer thickness can be found by using Eq. 1.36. This will be used in Chapter 4 to derive the diffusion layer thickness of catechol (1,2-hydroxybenzene) at glassy carbon electrodes.

Conversely, microdisc electrodes have such small dimensions that the thickness of the diffusion layer formed during electrolysis is larger than their radius, $r_e \ll \delta$. Within the experimental time scale, a hemispherical diffusion layer is developed, and electroactive species are drawn towards the electrode from all directions (Figure 1.6b). This *convergent* diffusion is more efficient than *linear* diffusion. In other words, the rate of transport to microdisc electrodes is much greater than for macroelectrodes. As the diffusive flux is in three dimensions, diffusion layer thickness can be found by using Eq. 1.37.

Microdisc electrodes have three major advantages over macroelectrodes: reduced ohmic drop (Section 1.2.2), reduced capacitative currents (Section 1.3.2), and enhanced Faradaic current density. Thanks to the high rate of mass transport, measurement of faster electron transfer process becomes achievable using microdisc electrodes.

Microwire electrodes, made from a cylindrical carbon fibre typically with a length of millimetres and a diameter of microns (fabrication details will be provided in Section 2.3.2), are also used in this thesis. Compared to a macrodisc, microwire electrodes have a significantly higher rate of mass transport due to their micron-scale size but compared to microdiscs, microwire electrodes have a larger surface area. These properties are vital to allow electrochemical characterisation of large solid particles, such as graphene nanoplatelets as introduced in Section 2. Due to the cylindrical curvature of the electrode surface, as well as the relative size of the diffusion layer to the electrode dimension, both

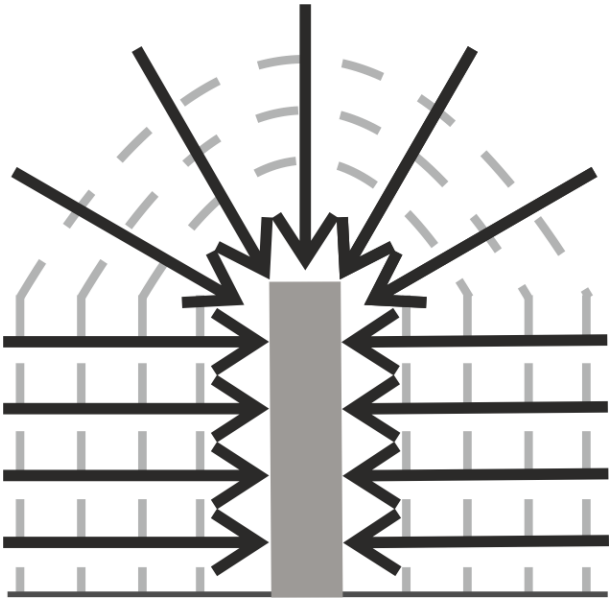

Figure 1.7: Diffusion at a microwire electrode. Arrows: diffusion of electroactive species. Dashed line: the diffusion layers.

linear and convergent diffusion take place to the microwire electrodes (Fig. 1.7).[9]

Quantitative analysis of electrochemical reactions using different electrodes can be achieved by two common methods: *voltammetry*, in which the current is measured as a function of the applied voltage, and *amperometry*, where the current is measured as a function of time at a set potential. The two electrochemical techniques are introduced in the subsequent section.

1.6 Cyclic Voltammetry

In cyclic voltammetry (CV), the current is measured as the potential is scanned linearly at a constant scan rate, ν (V s^{-1}), from a starting potential E_1 to a second potential E_2, and then reversed, as shown in Fig. 1.8. The scan rate is defined by:

$$\nu = \frac{\partial E}{\partial t} \tag{1.40}$$

Variation of the scan rate significantly affects the wave-shape of the voltammetry: a faster ν allows a shorter time for the diffusion layer to relax into the solution, and hence by Fick's First Law a larger flux of electroactive species is produced towards the electrode surface.

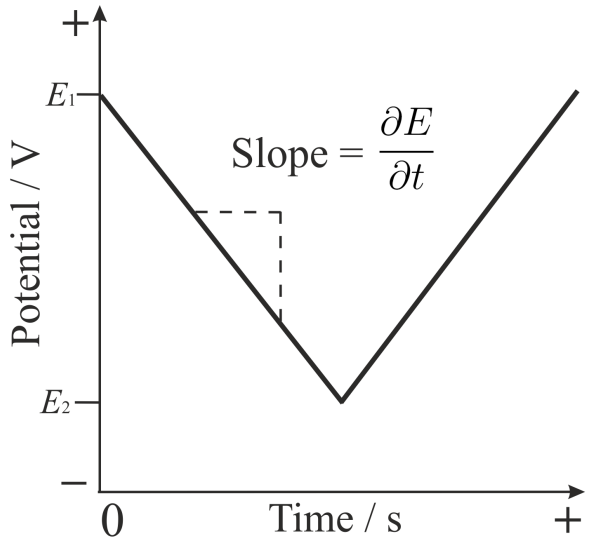

Figure 1.8: The potential-time profile of a cyclic voltammogram for a reduction. E_2 is more negative than E_1.

In this section, voltammetry of electrochemically reversible and irreversible process is first introduced. As explained in Section 1.5, the electroactive species exhibit different diffusional behaviour towards different size of electrodes, which has a profound influence on the shape of voltammograms. Therefore, the voltammetry of macro- and microelectrodes is also compared. Last, the voltammetry of multiple electron transfer process is studied.

1.6.1 Reversible *vs.* Irreversible System

Figures 1.9 and 1.10 illustrate the voltammetry of the reduction of Ox (see reactions 1.1 and 1.9) at macroelectrodes and microdisc electrodes, respectively. In both voltammograms, the potential is scanned from positive to negative, then reversed ($E_1 \rightarrow E_2 \rightarrow E_1$). The formal potential, E_f^0 (V), for the redox couple Ox/Re is shown in both diagrams, and it will be discussed later. The curves I $\sim$ III in both figures show the transition from fast

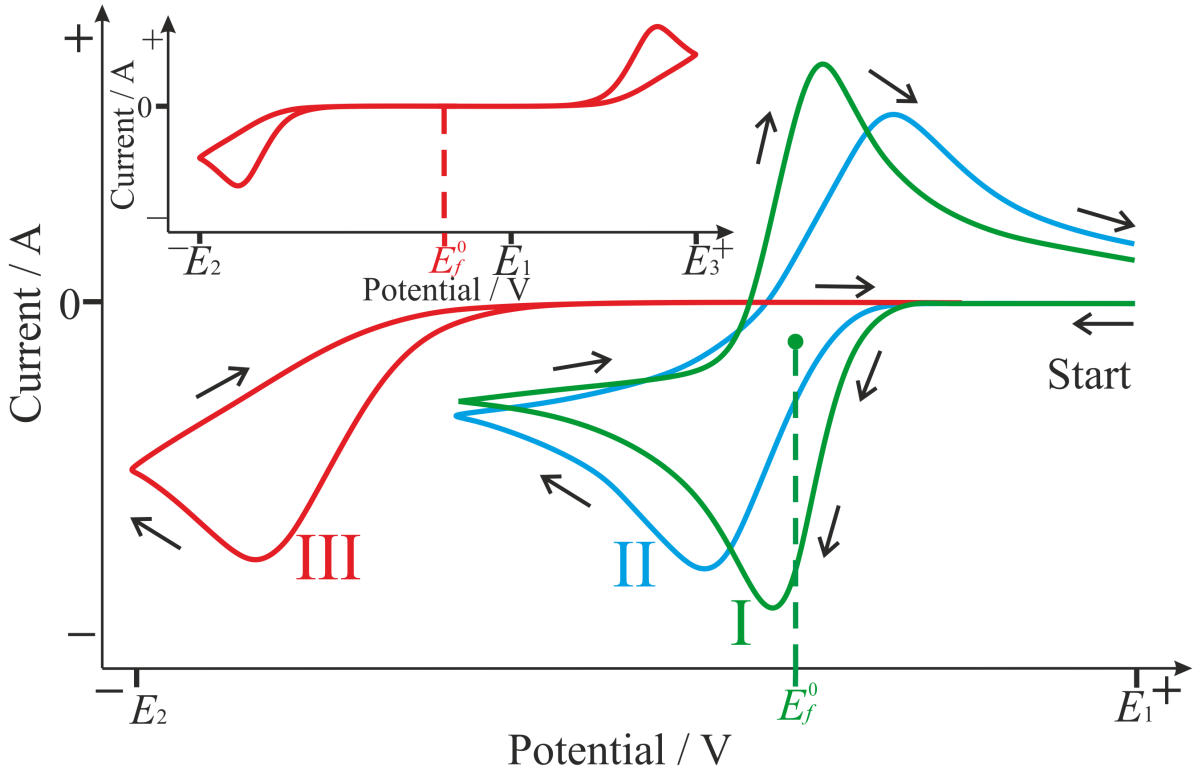

Figure 1.9: Reductive voltammetry of diffusive species at macroelectrodes: peaked shaped responses. (I) Reversible, (II) quasi-reversible, and (III) irreversible systems. Inlay: a fuller potential window for III. Arrows show the starting point and scan direction.

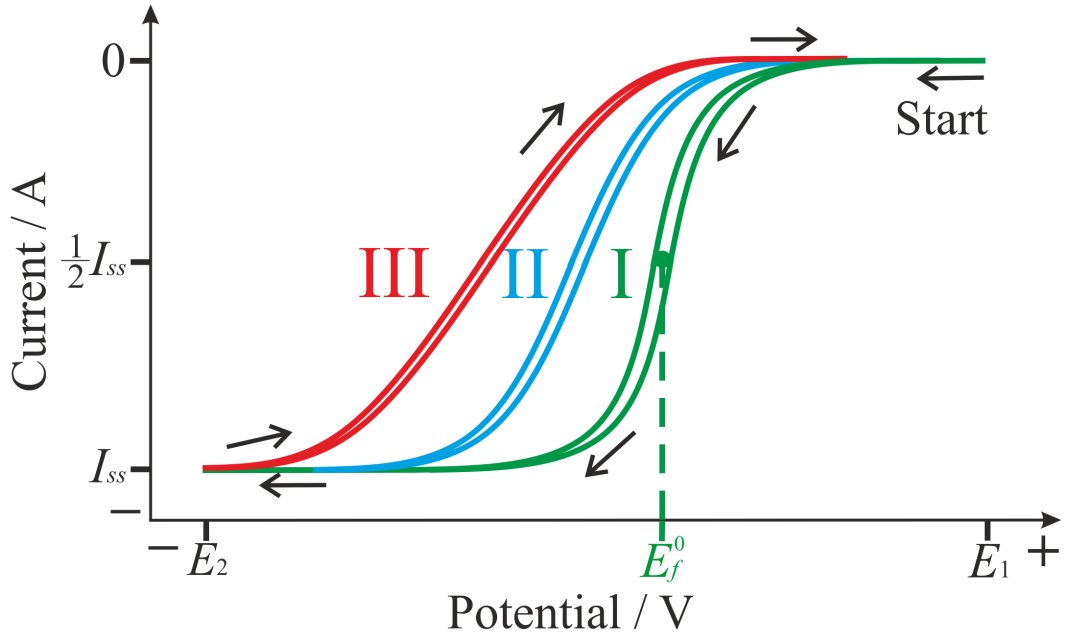

Figure 1.10: Reductive voltammetry of diffusive species at microdisc electrodes: sigmoidal response. (I) Reversible, (II) quasi-reversible, and (III) irreversible systems. Arrows show the starting point and scan direction.

(I) to slow (III) electron transfer.

In Figure 1.9, the peak-to-peak separation of the forward and back peak, ΔE_p (V), is

$$\Delta E_p = |E_{p,re} - E_{p,ox}| \tag{1.41}$$

where $E_{p,re}$ is the potential (V) of the forward reductive peak, and $E_{p,ox}$ is the potential (V) of the back oxidative peak. From the curves I to III, the forward peak shifts to more negative potential, and ΔE_p increases with a small decrease in the peak current, I_p (A). The curve III shows an extreme case when the back peak occurs at an extremely positive potential, so it is lost from the potential window studied, unless it is unusually wide (see Figure 1.9, inlay).

In Figure 1.10, a broadening from the curves I to III is seen, with a displacement of the half-wave potential moving towards a more positive value. Half-wave potential, $E_{1/2}$ (V), is the potential where the current is

$$I = \frac{1}{2} I_{ss} \tag{1.42}$$

and I_{ss} is the steady-state current (A). The electrochemical processes can be referred as "reversible" (I), "quasi-reversible" (II) and "irreversible" (III), respectively.

The reversibility of a process can be understood by comparison of electron transfer, measured by the standard electrochemical rate constant, k^0, with the mass transport, given by the mass transport coefficient, m_T (cm s^{-1}), where

$$m_T = \frac{D_i}{\delta} \tag{1.43}$$

where D_i is the diffusion coefficient (cm^2 s^{-1}) and δ is the diffusion layer thickness (cm). According to Eq. 1.36, $\delta = \sqrt{2Dt}$. The experimental time, t, can be related to the scan

rate, ν, *via*

$$t \sim \frac{RT}{F\nu} \tag{1.44}$$

m_T can hence be expressed by the following relation,

$$m_T \sim \sqrt{\frac{FD_i\nu}{RT}} \tag{1.45}$$

When $k^0 \gg m_T$, the process is *reversible*; while $k^0 \ll m_T$, the process is *irreversible*. The process in between these two limits is referred to as being *quasi-reversible*.

The three classifications can be more precisely interpreted by a parameter, Λ, introduced by Matsuda and Ayabe[10]:

$$\Lambda = \frac{k^0}{\sqrt{\frac{FD_i\nu}{RT}}} \tag{1.46}$$

where the terms have been defined previously. The reversibility of an electrochemical process under linear diffusion (at macroelectrodes) can be classified by

I. Reversible:

$$\Lambda \geq 15 \qquad k^0 \geq 0.3\upsilon^{0.5} \tag{1.47}$$

II. Quasi-reversible:

$$15 > \Lambda > 10^{-3} \qquad 0.3\upsilon^{0.5} > k^0 > 2 \times 10^{-5}\upsilon^{0.5} \tag{1.48}$$

III. Irreversible:

$$\Lambda \leq 10^{-3} \qquad k^0 \leq 2 \times 10^{-5}\upsilon^{0.5} \tag{1.49}$$

where the numerical values relate to 298 K and α is assumed to be 0.5.

With respect to the macroelectrode voltammograms, the value of peak-to-peak sepa-

ration, ΔE_p (V), can be used to classify the reversibility of the electrochemical process. When ΔE_p is at *ca.* 59 mV (for a one-electron process) at 298 K, the process is electrochemically reversible (Figure 1.9, curve I). When ΔE_p is bigger than 59 mV, the process becomes electrochemically quasi-reversible (Figure 1.9, curve II). When ΔE_p cannot be quantified due to a missing back peak (Figure 1.9, curve III), the process may be electrochemically irreversible. The word "may" is used here because *chemically irreversible* reactions can also result in diminished back peak (Chapter 3):

$$\mathrm{A} + \mathrm{e}^- \rightarrow \mathrm{B} \tag{1.50}$$

$$\mathrm{B} + \mathrm{C} \rightarrow \mathrm{D} \tag{1.51}$$

After A is reduced to B, B undergoes further chemical reaction with C. Therefore, depletion of B prohibits its oxidation back to A. In contrast, all the other reactions discussed so far are *chemically reversible*:

$$\mathrm{A} + \mathrm{e}^- \rightleftharpoons \mathrm{B} \tag{1.52}$$

where B can be oxidised back to A.

1.6.2 Macroelectrodes *vs.* Microelectrodes

Voltammetry at Macroelectrodes

First, the voltammetry at a *macroelectrode* (Figure 1.9) is discussed. The formal potential, E_f^0 (V), for the redox couple Ox/Re can be related to the mid-point potential of the forward and back peak, E_{mid} (V), *via*[1]

$$E_{mid} = \begin{cases} E_f^0 + \dfrac{RT}{2F} \ln \dfrac{D_{\mathrm{Re}}}{D_{\mathrm{Ox}}}, & \text{Reversible} \\ E_f^0 + \dfrac{RT}{2\alpha F} \ln \dfrac{D_{\mathrm{Re}}}{D_{\mathrm{Ox}}}, & \text{Irreversible} \end{cases} \tag{1.53}$$

$$\text{with} \quad E_{mid} = \frac{E_{p,re} + E_{p,ox}}{2} \tag{1.54}$$

It is often a reasonable approximation to assume that diffusion coefficients of Ox and Re are equal. When $D_{\mathrm{Re}} = D_{\mathrm{Ox}}$, Eq. 1.53 becomes $E_{mid} = E_f^0$. The formal potential of the couple hence can be found from the mid-point potential, as shown in Figure 1.9.

Figure 1.9 shows at E_1, the applied potential is not negative enough to reduce Ox, so no current passes. When the voltammetry is scanned towards E_f^0, the applied potential becomes sufficiently negative to drive the reduction of Ox. The electron transfer is induced, and the current rises from baseline. For electrochemically reversible system (curve I), at this stage the product is formed at the electrode surface, as predicted by the Nernst Equation (Eq. 1.6). For irreversible system (curve III), this indicates the electrochemical reaction is controlled by electrode kinetics, and hence the current follows the Butler-Volmer Equation (Eq. 1.15). During the electrolysis, Ox is consumed near the electrode surface, and a concentration gradient is built between the electrode surface and bulk solution. A diffusion layer (Figure 1.3) is hence created, Ox from the bulk solution has to travel to reach the electrode surface. As explained in Section 1.5, at macroelectrodes the linear diffusion is less efficient. The diffusion of Ox thus cannot compensate the depletion in the surface concentration of Ox. Therefore, after the current reaches a maximum, it decreases as the diffusion layer thickness increases. A *peaked shaped* voltammogram is observed, with the absence of a steady-state.

The peak current, I_p (A), for the one-electron process at a macroelectrode can be predicted by the *Randles-Ševčík* Equations[1]:

$$I_p = \begin{cases} (2.69 \times 10^5) A D_i^{0.5} C_i \nu^{0.5}, & \text{Reversible, } k^0 \to \infty \\ (2.99 \times 10^5) \alpha^{0.5} A D_i^{0.5} C_i \nu^{0.5}, & \text{Irreversible, } k^0 \to 0 \end{cases} \tag{1.55}$$

where the terms have been defined previously.

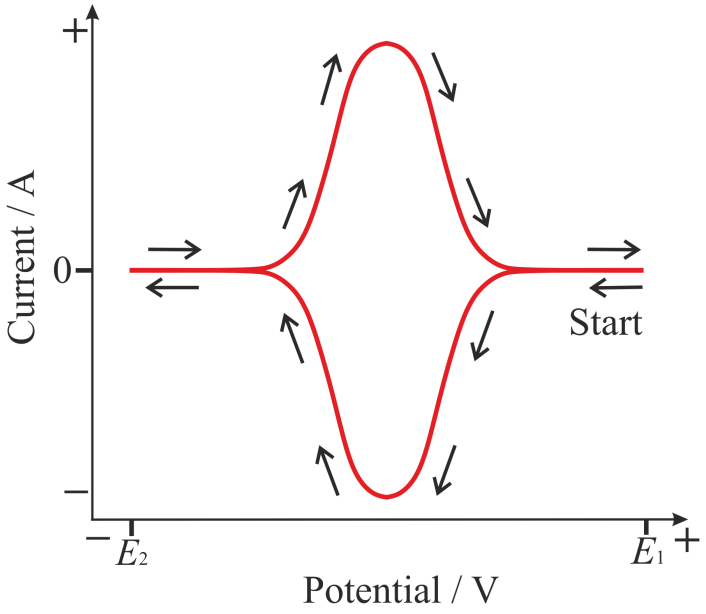

Figure 1.11: Reversible voltammetry of a surface-bound species at macroelectrodes: symmetrical wave-shape. Arrows show the starting point and scan direction.

Apart from the solution phase, the electroactive species might be adsorbed on the electrode surface. The *surface-bound* species produces a distinctive voltammetry compared to that of the diffusive species. As shown in Figure 1.11, for an ideal behaviour of a surface-bound species, symmetric forward and back peaks prevail when the process is electrochemically reversible. The current also drops to zero after the peak. These characters are a consequence of the finite quantity of electroactive species adsorbed on the electrode surface, and hence the wave-shape is controlled only by the electron transfer, but no diffusion is involved. Ideally, the voltammetric peak current, I_p (A), for a reversible process can be related to the surface coverage, Γ_i (mol cm^{-2}) by the equation[11]:

$$I_p = (9.39 \times 10^5) n^2 A \Gamma_i \nu \tag{1.56}$$

where the terms have been defined previously. However, the voltammetry is often distorted as a result of slow electron transfer, and/or associated capacitive effects.

Voltammetry at Microdisc Electrodes

Voltammetry at a *microdisc electrode* (Figure 1.10) is next introduced. The formal potential, E_f^0 (V), for the redox couple Ox/Re can be related to the half-wave potential, $E_{1/2}$ (V), *via*[4]

$$E_{1/2} = \begin{cases} E_f^0 + \dfrac{RT}{2F} \ln \dfrac{D_{\mathrm{Re}}}{D_{\mathrm{Ox}}}, & \text{Reversible} \\ E_f^0 + \dfrac{RT}{\alpha F} \ln \dfrac{r_e k^0}{D_{Ox}}, & \text{Irreversible} \end{cases} \tag{1.57}$$

$E_{1/2}$ is the potential where the current is half of the steady-state current. When $D_{\mathrm{Re}} = D_{\mathrm{Ox}}$, Eq. 1.57 becomes $E_{1/2} = E_f^0$ at reversible limit. The formal potential of the couple can be shown as the half-wave potential in the voltammetry, as shown in Figure 1.10. The formal potential of the couple at irreversible limit is dependent on the electrochemical rate constant, hence it is not shown.

Figure 1.10 illustrates when the applied potential is scanned from E_1 to E_f^0, the current response is similar to Figure 1.9. However, when the potential is scanned further negative to E_2, a steady-state is reached. This limiting rather than peak current results from the more efficient convergent diffusion at microdisc electrodes (Section 1.5). The diffusion of Ox is able to compensate the depletion in the surface concentration of Ox, thus the reduction is fully driven. A typical *sigmoidal* response with a steady-state is generated, except for very fast scan rates when the experimental time scale is so short that diffusion becomes less efficient. As the scan rate increases, a transition from convergent to linear diffusion of Ox takes place at the electrode surface, leading to a change in voltammetry from a sigmoidal response to a peaked shaped response.

The *steady-state current* at a microdisc electrode, I_{ss} (A), can be expressed by the equation[12]:

$$I_{ss} = 4nFD_iC_ir_e \tag{1.58}$$

where r_e is the radius of the electrode (cm), and the rest of the terms have been defined

previously.

Voltammetry at Microwire Electrodes

Last, voltammetry at a *microwire electrode* is discussed. Figure 1.12 demonstrates the reduction of Ox at a microwire electrode. At a lower scan rate (Figure 1.12, curve I), a sigmoidal response with a quasi-steady-state is observed. A true steady-state is not reached due to the macroscopic length dimensions. At higher scan rates (Figure 1.12, curves II $\sim$ IV), the voltammetry changes to a peaked shaped response. The former observation is a result of the small dimension of the microwire electrodes where convergent diffusion prevails. The latter is attributed to the high scan rates, at which the experimental time scale becomes so short that diffusion becomes less efficient.

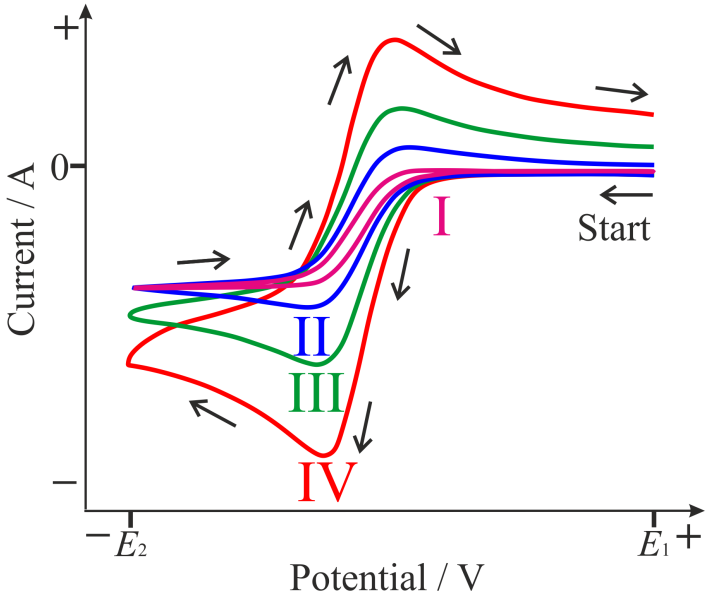

Figure 1.12: Voltammetry of diffusive species at microwire electrodes: quasi-steady-state response. Arrows show the starting point and scan direction.

The peak current, I_p (A), can be predicted based on the work of Aoki *et al.* by the

equation[13, 14]:

$$I_p = 2\pi nFC_iD_il\left(0.446h + 0.335h^{0.15}\right) \quad (1.59)$$

$$\text{with} \quad h = \left(\frac{nFr_e^2\nu}{RTD_i}\right)^{0.5} \quad (1.60)$$

where l is length of the electrode (cm) and the rest of the terms have been defined previously. The first term here corresponds to the linear diffusion, while the second term relates to the convergent diffusion towards the electrode.

1.6.3 Multiple Electron Transfer

In Chapters $3 \sim 5$, the electron transfer and mass transport of two-electron processes are extensively studied *via* the use of cyclic voltammetry. Voltammograms of two-electron reduction processes are introduced as below. The discussion first covers electrochemically reversible systems, then proceeds to irreversible systems. The Tafel Law and the Randles-Ševčík Equation for general n-electron processes are also discussed.

Electrochemically Reversible System

Consider the *electrochemically reversible* two-electron reductions,

$$\mathrm{A} + \mathrm{e}^- \rightleftharpoons \mathrm{B}, \quad E^0_{f1} \quad (1.61)$$

$$\mathrm{B} + \mathrm{e}^- \rightleftharpoons \mathrm{C}, \quad E^0_{f2} \quad (1.62)$$

As the reversible limit operates, the electron transfer of both couples is fast compared to mass transport. The voltammetry hence depends on the relative magnitude of the formal potentials of both couples, E^0_{f1} and E^0_{f2}. Figure 1.13 is generated by varying E^0_{f2}, at a fixed value of E^0_{f1}. k^0_1 and k^0_2 are set at 10 cm s^{-1} as the fully reversible limit.

When $E^0_{f2} \ll E^0_{f1}$, two voltammetric waves are observed (Figure 1.13, curve I). The

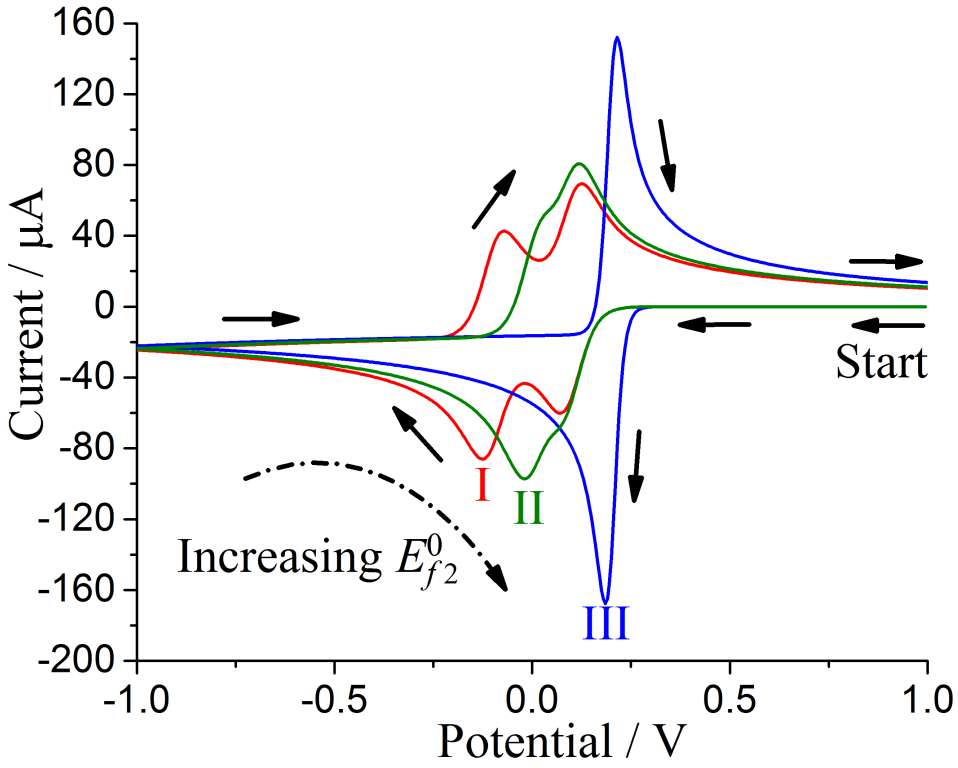

Figure 1.13: Voltammetry for an electrochemically reversible two-electron reduction. The value of E^0_{f2} is (I) −0.1, (II) 0, (III) 0.3 V. E^0_{f1} = 0.1 V. $k^0_1 = k^0_2$ = 10 cm s^{-1}. $\alpha_1 = \alpha_2$ = 0.5. $D_{\mathrm{A}} = D_{\mathrm{B}} = D_{\mathrm{C}} = 10^{-5}$ cm s^{-2}. $C_{\mathrm{A,bulk}} = 10^{-3}$ M. A = 0.0707 cm^2. Scan rate = 1 V s^{-1}.[1]

first wave at the more positive potential corresponds to the reduction of A to B. The second wave occurs when the potential is scanned sufficiently negative to drive the reduction of B to C.

When $E^0_{f2} \gg E^0_{f1}$, only one voltammetric wave is seen (Figure 1.13, curve III). This is because reduction of B takes place thermodynamically more easily than the reduction of A. After A is reduced, B formed at the surface of the electrode experiences a potential more negative than that required to reduce B to C. Therefore, a net conversion of A to C takes place, resulting in a single peak.

When $E^0_{f2} \simeq E^0_{f1}$, two merged broad waves are observed (Figure 1.13, curve II), as a half-way case between the above two limits.

This explains why in Chapters 3 and 4, a single wave will be observed for the reversible two-electron process.

Electrochemically Irreversible System

The discussion now proceeds to *electrochemically irreversible* two-electron reductions. There are two effects accounting for the shape of a voltammetry: thermodynamics and kinetics.

$$\mathrm{A} + \mathrm{e}^- \underset{k_{1,ox}}{\overset{k_{1,re}}{\rightleftarrows}} \mathrm{B}, \quad E^0_{f1} \tag{1.63}$$

$$\mathrm{B} + \mathrm{e}^- \underset{k_{2,ox}}{\overset{k_{2,re}}{\rightleftarrows}} \mathrm{C}, \quad E^0_{f2} \tag{1.64}$$

where E^0_{f1} and E^0_{f2} are the formal potentials of the first and second electron transfer, respectively. $k_{1,re}$ and $k_{2,re}$ are the electron transfer rate constants for the first and second reductive processes; $k_{1,ox}$ and $k_{2,ox}$ are the electron transfer rate constants for the first and second oxidative processes. The transfer coefficients for the two reductive processes are α_1 and α_2.

First, the thermodynamic effect is demonstrated. Figure 1.14 is generated by varying E^0_{f2}, at a fixed value of E^0_{f1}. k^0_1 and k^0_2 are set at 10^{-4} cm s^{-1} as the irreversible limit. Curve I shows two separate waves when $E^0_{f2} \ll E^0_{f1}$. As E^0_{f2} is made more and more positive, the second peak moves to more positive potential (II), until the two waves merge into one broad peak (III). The peak then becomes sharp (IV) when $E^0_{f2} \geqslant E^0_{f1}$.

Second, the kinetic effect is considered. The electrochemical rate constants in reactions 1.63 and 1.64 are given by the Butler-Volmer Equations (Eq.1.12),

$$k_{1,re} = k^0_1 \mathrm{exp}\left\{-\frac{\alpha_1 F}{RT}(E - E^0_{f1})\right\} \tag{1.65}$$

$$k_{1,ox} = k^0_1 \mathrm{exp}\left\{\frac{\beta_1 F}{RT}(E - E^0_{f1})\right\} \tag{1.66}$$

$$k_{2,re} = k^0_2 \mathrm{exp}\left\{-\frac{\alpha_2 F}{RT}(E - E^0_{f2})\right\} \tag{1.67}$$

$$k_{2,ox} = k^0_2 \mathrm{exp}\left\{\frac{\beta_2 F}{RT}(E - E^0_{f2})\right\} \tag{1.68}$$

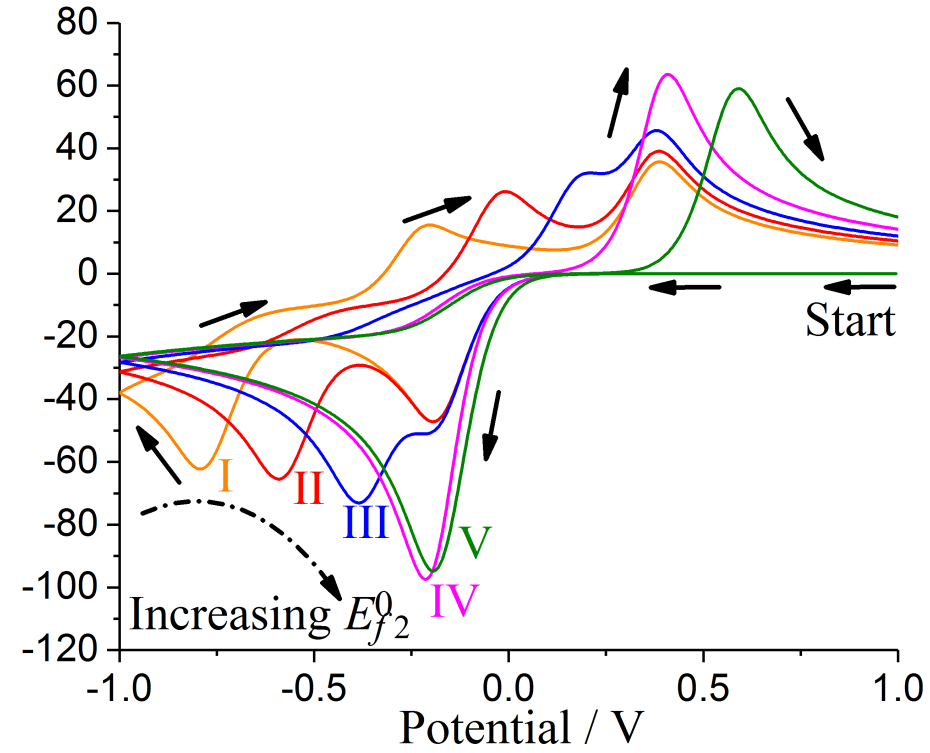

Figure 1.14: Voltammetry for an electrochemically irreversible two-electron reduction: thermodynamic effect. The value of E^0_{f2} is (I) −0.5, (II) −0.3, (III) −0.1, (IV) 0.1, (V) 0.3 V. $E^0_{f1} = 0.1$ V. $k^0_1 = k^0_2 = 10^{-4}$ cm s^{-1}. $\alpha_1 = \alpha_2 = 0.5$. $D_\mathrm{A} = D_\mathrm{B} = D_\mathrm{C} = 10^{-5}$ cm s^{-2}. $C_\mathrm{A,bulk} = 10^{-3}$ M. $A = 0.0707$ cm^2. Scan rate = 1 V s^{-1}.[1]

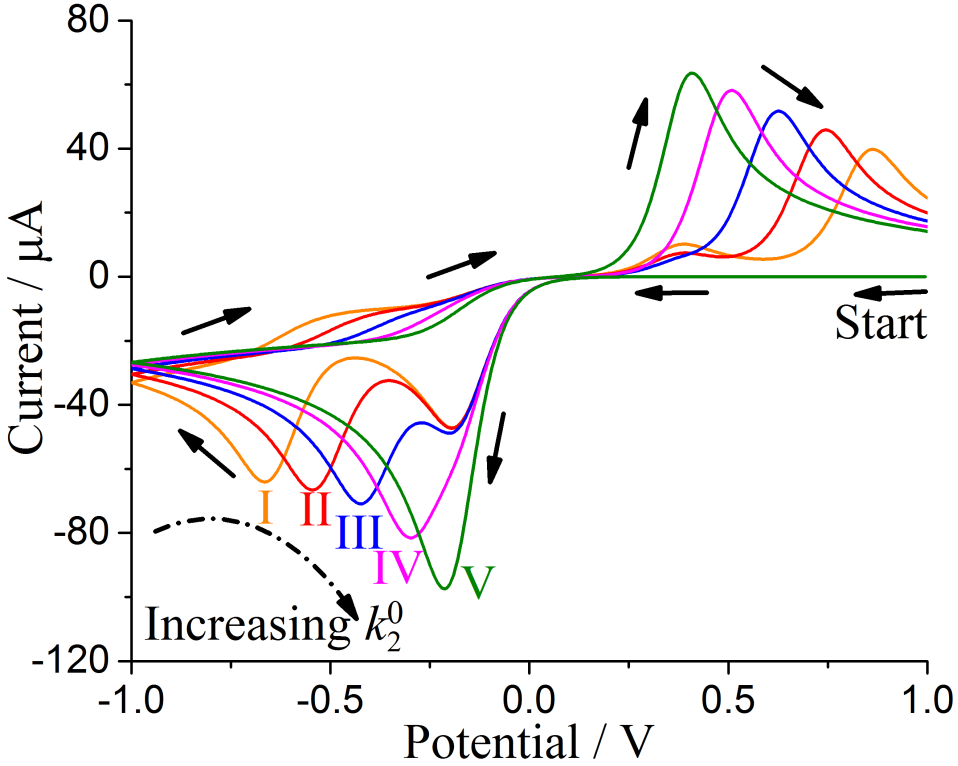

Figure 1.15: Voltammetry for an electrochemically irreversible two-electron reduction: kinetic effect. The value of k^0_2 is (I) 10^{-8}, (II) 10^{-7}, (III) 10^{-6}, (IV) 10^{-5}, (V) 10^{-4} cm s^{-1}. $k^0_1 = 10^{-4}$ cm s^{-1}. $E^0_{f1} = E^0_{f2} = 0.1$ V. $\alpha_1 = \alpha_2 = 0.5$. $D_\mathrm{A} = D_\mathrm{B} = D_\mathrm{C} = 10^{-5}$ cm s^{-2}. $C_\mathrm{A,bulk} = 10^{-3}$ M. $A = 0.0707$ cm^2. Scan rate = 1 V s^{-1}.[1]

where E is the applied potential (V), α_1 and α_2 are the transfer coefficients for the first and second reductive processes; β_1 and β_2 are the transfer coefficients for the first and second oxidative processes. Figure 1.15 is generated by varying k_2^0, at fixed values of k_1^0, E_{f1}^0 and E_{f2}^0. When $k_{1,re}$>$k_{2,re}$, two separate waves are seen. Upon making $k_{2,re}$ bigger and bigger, the second peak moves to more positive potential, and it gradually merges with the first peak. When $k_{2,re}$>$k_{1,re}$, only a single wave is seen.

General Multiple Electron Processes: the Tafel Law and the Randles-Ševčík Equation

To conclude this section, for the n-electron process in which the rate-determining step (RDS) is the reaction of N' to O',

$$\begin{aligned}
&\mathrm{A} + \mathrm{e}^- \rightleftarrows \mathrm{B} \\
&\mathrm{B} + \mathrm{e}^- \rightleftarrows \mathrm{C} \\
&\vdots \\
&\vdots \\
&\vdots \\
&\mathrm{L'} + \mathrm{e}^- \rightleftarrows \mathrm{M'} \\
&\mathrm{M'} + \mathrm{e}^- \rightleftarrows \mathrm{N'} \qquad n'^{\mathrm{th}} \text{ electron transfer} \\
&\mathrm{N'} + \mathrm{e}^- \overset{slow}{\rightarrow} \mathrm{O'} \qquad (n'+1)^{\mathrm{th}} \text{ electron transfer, RDS} \\
&\vdots \\
&\vdots \\
&\vdots \\
&\mathrm{X} + \mathrm{e}^- \rightarrow \mathrm{N} \qquad n^{\mathrm{th}} \text{ electron transfer}
\end{aligned}$$

The Tafel Law is given as[1]

$$\frac{\partial \ln |I_{re}|}{\partial E} = -\frac{(n' + \alpha_{n'+1})F}{RT} \tag{1.69}$$

where n' is the number of electrons transferred before the RDS, $\alpha_{n'+1}$ is the transfer coefficient of the RDS, N' + e^- $\rightarrow$ O'.

The peak current, I_p (A), for the n-electron process can be predicted by the Randles-Ševčík Equations[1]:

$$I_p = \begin{cases} (2.69 \times 10^5) n^{1.5} A D_i^{0.5} C_i \nu^{0.5}, & \text{Reversible, } k^0 \rightarrow \infty \\ (2.99 \times 10^5) n (n' + \alpha_{n'+1})^{0.5} A D_i^{0.5} C_i \nu^{0.5}, & \text{Irreversible, } k^0 \rightarrow 0 \end{cases} \tag{1.70}$$

where n is the number of electrons transferred, and the rest of the terms have been defined previously.

1.7 Chronoamperometry

In chronoamperometry, the potential (Figure 1.16a) is stepped instantaneously from a starting potential E_1, to a second potential E_2, corresponding respectively to no electrolysis, and to electrolysis at the electrode surface. Therefore, immediately after the step, a large current (Figure 1.16b) is observed, which then falls steadily with time as depletion occurs.

The current response at a *macroelectrode* as a function of time is described by the *Cottrell Equation*:

$$I = \frac{nFAD_i^{0.5} C_i}{\pi^{0.5} t^{0.5}} \tag{1.71}$$

assuming the potential E_2 is large enough so that $C_i = 0$ at electrode surface. n is the number of electrons transferred, A is the electrode area (cm^2), D_i and C_i are the diffusion

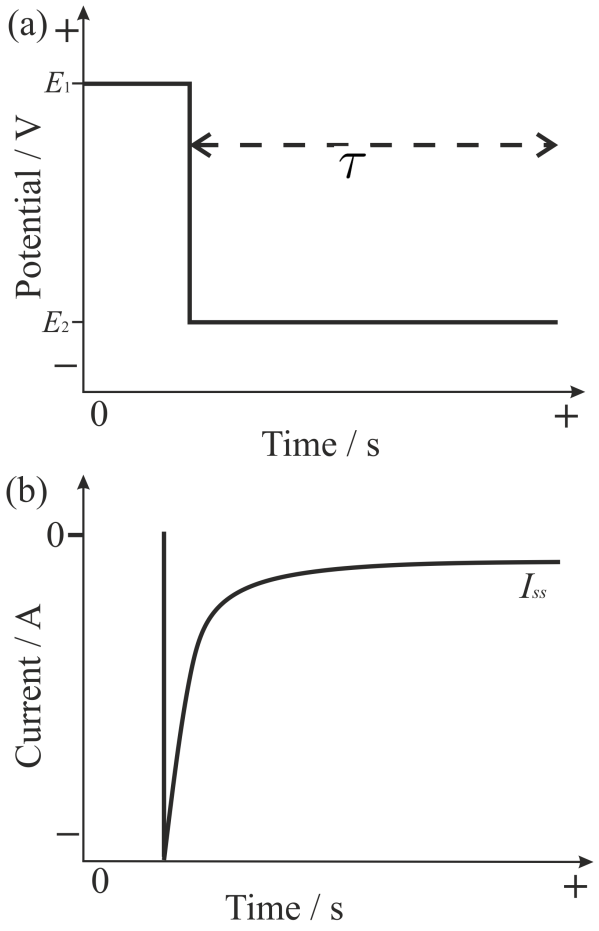

Figure 1.16: (a) The potential-time profile for a single step chronoamperometry experiment. b) The resulting chronoamperometric response at microelectrodes.

coefficient (cm^2 s^{-1}) and the concentration (mol cm^{-3}), respectively. t is the time (s) during which the response is recorded, and $I \to 0$ as $t \to \infty$.

In contrast, the current transient at a *microdisc electrode* leads to a steady-state when $t \to \infty$ and E_2 is sufficient that $C_i = 0$ at the electrode surface. The transient can be described by *Shoup and Szabo Equation*[15]:

$$I = -4nFD_iC_ir_ef(\tau) \tag{1.72}$$

$$\text{with} \quad f(\tau) = 0.7854 + 0.8863\tau^{-0.5} + 0.2146\exp(-0.7823\tau^{-0.5}) \tag{1.73}$$

where the dimensionless time parameter, τ, is given by:

$$\tau = \frac{4D_i t}{r_e^2} \tag{1.74}$$

r_e is the radius of the electrode (cm) and the rest of the terms have been defined previously.

The current transient at a *microwire electrode* is given by Szabo *et al.*[16]:

$$I = 2\pi n F D_i C_i l f(\tau) \tag{1.75}$$

$$\text{with} \quad f(\tau) = \frac{2e^{-\sqrt{\pi\tau}/20}}{\sqrt{\pi\tau}} + \frac{1}{\ln\left[(e^{-\kappa}\tau)^{0.5} + e^{5/3}\right]} \tag{1.76}$$

$$\text{and} \quad \tau = \frac{4D_i t}{r_e^2} \tag{1.77}$$

where l is the length of the electrode (cm), κ is a constant derived from the limits of the Bessel functions in the full formula for $f(\tau)$ with a value of 0.5772156... At short times, Eq. 1.75 reduces to Cottrell Equation. At long times, τ becomes large and its ln term dominates, Eq. 1.75 reduces to

$$I_{qss} = \frac{4\pi n F D_i C_i l}{\ln(\tau)} \tag{1.78}$$

This equation shows a mix of linear and convergent diffusion. A true steady-state is not reached, because of the macroscopic length dimensions.

1.8 Analysis of Solid Particles

The introduction now focuses on solid particles. A review of their properties, applications and detections will be given, facilitating comprehension of the results present later in this thesis.

Microparticles are a class of particle with dimension between 0.1 and 100 μm according

to IUPAC[17]. Due to their small size, microparticles have a much higher surface area to volume ratio in comparison with their macro-scale materials. Hence, their behaviour may deviate significantly from that of the bulk material with respect to aggregation, catalytic activity and surface chemistry. There are two types of microparticles: solid and hollow, varying in density. While hollow particles are commonly used as additives to lower the density of a material[18], solid particles are made from robust and stable materials, such as polymers, glass, and ceramics. Solid particles have extensive applications depending on their size[19–22], shape[23, 24], and surface functionalisation[25]. In particular, solid particles incorporated with dyes are actively used as tracers in the medical industry. For example, polystyrene microspheres (diameter 15 μm)[26] were used to measure organ blood flow[27]. Amino-modified polystyrene microspheres (diameter 3 μm)[28] were used to quantify the binding between specific antibodies and target molecules[29].

In this thesis, the electrochemical properties of solid particles are analysed. The two candidates selected for investigation are alumina (aluminium oxide) particles and graphene nanoplatelets, as representatives for insulating and conducting particles, respectively.

Micron and submicron alumina particles have high electrical insulation, good heat resistance and high hardness[30]. They have important applications including use as abrasive media, filler materials, adsorbents and catalysts. Spherical alumina particles, in comparison to irregular ones, have been found to possess improved performance in ceramics[31, 32], mechanical polishing[33, 34], magnetic data storage[35], and enhanced packing density of the filler[30].

The interest in graphene and related carbon materials has boomed in the last decade, ever since the discovery of graphene by Novoselov and Geim in 2004 [36], which was awarded the 2010 Nobel Prize in Physics.[37, 38] The enhanced electrical and thermal conductivity, large surface area, high mechanical strength of graphene materials allow their widespread applications in predominantly sensing and energy storage technologies.[39–

42] A wide range of possible applications of graphene also span from manufacturing of supercapacitors[43–49], dye-sensitised solar cells[50, 51], biological molecule sensors[52, 53], and catalyst supports[54], to the field of nano-medicine using pristine graphene or graphene materials[55, 56]. However, the manufacture of pristine graphene is expensive *via* graphite exfoliation or graphite oxide reduction[57]. The produced graphene also possesses poor stability leading to ripples at sizes of 1 nm width[58, 59]. Therefore, graphene nanoplatelets (GNPs) have become a more suitable alternative with advantageous properties of highly ordered graphitic materials, but circumventing the poor stability of graphene.

In order to detect and characterise solid particles, a number of methods have been suggested by the International Life Science Institute Research Foundation/Risk Science Institute.[60, 61] Scanning electron microscopy (SEM)[62, 63] and transmission electron microscopy (TEM)[63–66] are the two main microscopy methods in use. Laser techniques such as dynamic light scattering (DLS)[65] are also widely used. Surface analysis such as X-ray diffraction (XRD)[66] and X-ray photon spectroscopy (XPS)[63] are also employed. Ultra-violet visible (UV-vis) spectroscopy[67] measuring light transmittance can also be used.

In this thesis, scanning electron microscopy and electrochemical particle impacts are combined to detect and characterise alumina particles and graphene nanoplatelets. The chosen techniques will be discussed in the following sections.

1.8.1 Scanning Electron Microscopy

Scanning electron microscope (SEM) is widely used in the characterisation of the size and shape of solid particles. While the optical microscope uses the transmission of light through a sample to resolve an image, SEM uses the transmission of electrons to generate the image. In an optical microscope, the glass lenses bend or reflect the light beams passing through them to achieve magnification. Since electrons are charged particles and

they can be bent in a magnetic field, lenses for electrons in SEM are constructed with a series of coil-shaped electromagnets (Figure 1.17).

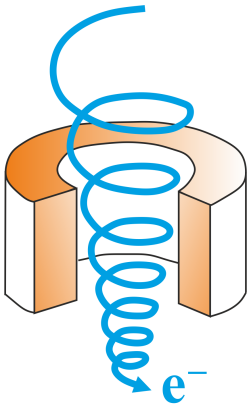

Figure 1.17: Schematic of the coil-shaped magnetic lense used in SEM.

Figure 1.18 shows the major components of a SEM. The chambers of SEM must be pumped down to vacuum so that the filament does not oxidise or burn out. Interference from the air onto the electron beam can also be prevented under vacuum. The components as follows:

- Electron gun: a high energy electron beam is produced at an electron gun. A voltage is applied to the tungsten filament, which acts like a cathode. When the filament heats up, electrons are emitted. The filament is often made to have a very sharp tip, so that the electron beam can be very narrow.

- Anode: the electron beam is accelerated at the anode. A strong electric field is present between the cathodic electron gun and the anode, so the electric force drives the electrons to pass through the anode.

- Condenser lens: the cone of the electron beam is converged to a spot at the first condenser lens, before the beam flares out again it is converged back again by the second condenser lens.

- Objective lens: the electron beam is focused onto the sample *via* the objective lens.

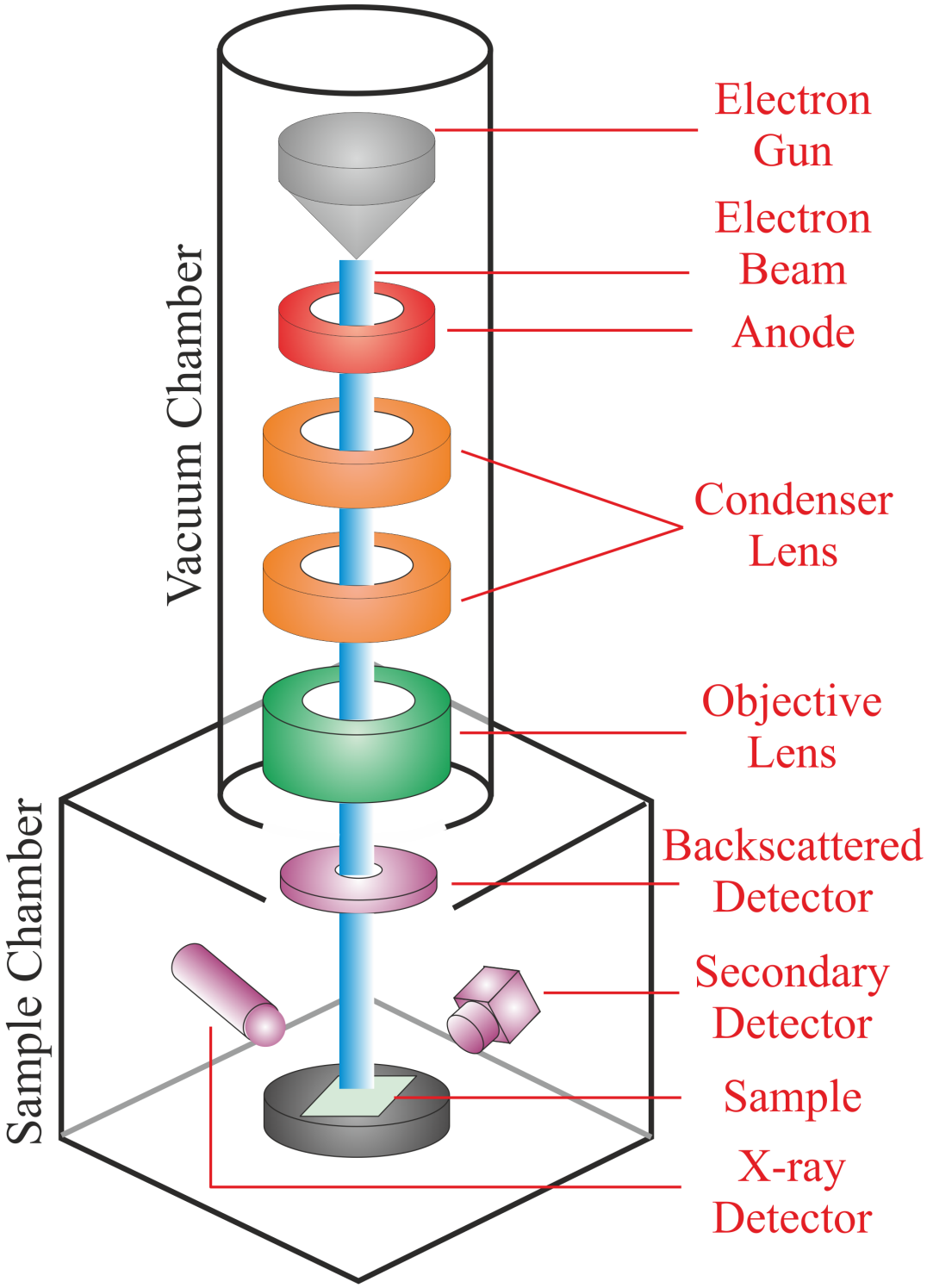

Figure 1.18: Schematic of the major components of a scanning electron microscope.

- Sample: the sample is mounted on a stage in the sample chamber. The electrons are scattered from the sample to the detectors. The number of scattered electrons depends on the properties of the sample. A variety of detectors can be used to characterise different properties of the sample.

- Backscattered detector: it detects the backscattered high-energy primary electrons. The atoms composed in the sample can be identified by using this detector. Because the higher the atomic number, the more primary electrons are scattered out of the sample, a brighter image will be generated.

- Secondary detector: for routine SEM images, it detects the low-energy secondary electrons. The main information generated is the shape of the sample, as the edges look brighter than the rest of the image due to the higher amount of electrons scattered.

- X-ray detector: it detects the x-ray released upon the collisions between the incident electrons and the atoms in the sample. Characteristic X-rays are produced for each element, so information of what elements exist in the sample can be generated.

One of the advantages of SEM is that it enables solid particles to be 'seen', making it the only technique allowing the shape, size and surface of the particles to be visualised. However, the sample has to be conductive to be detected by SEM. An extremely thin layer ($\sim$ 10 nm) of heavy metals, such as gold or platinum, is often required as coating for insulating particles.[68] Another limitation of SEM is that the sample must be dry, so it cannot be used to study the particles in solution phase.[69] Most importantly, chemical properties of the particles, such as surface coverage, reaction mechanism, electron transfer rate, and catalytic performance, are not assessable by SEM. Therefore, electrochemical particle impacts will be introduced as an alternative technique.

1.8.2 Electrochemical Particle Impacts

As a powerful electroanalytical method, the particle impacts has been developed rapidly in the recent decades. The technique provides a simple but efficient and reliable way to characterise solid particles. Recent developments on the particle impacts were covered in the literature reviews [70–73]. Impact events can be measured by immersing a micro-electrode into a solution containing a suspension of particles. By virtue of its Brownian motion, a single particle may diffusively collide with the electrode. If a certain potential is applied to the electrode, a redox reaction of the particle can be triggered. As the charge is transferred between the particle and the potentiostatted electrode, a current "spike" can be observed in chronoamperometry (Figure 1.19). Impact spikes can be used to identify the composition of the particles, to measure the size and concentration, and to study the aggregation and catalytic properties of the particles, as discussed in details below.

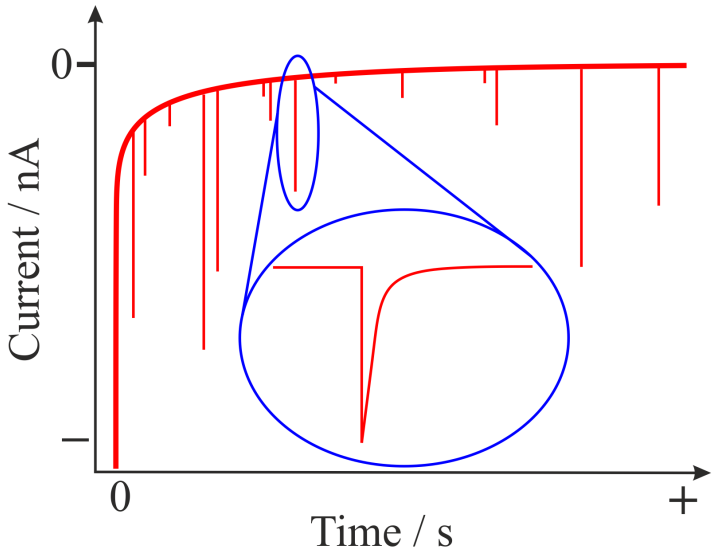

Figure 1.19: A typical particle reductive impact spike in chronoamperometry.

Early work in this area was carried out by Heyrovský *et al.* on metal oxide semi-conducting particles, such as SnO_2, TiO_2 and Fe_2O_3.[74–77] Voltammetric signals were generated during the mediated proton reduction to hydrogen upon collisions between the particles and mercury drop electrodes. The work was extended to metal powders, such

as Cu, Fe, Ni, Mo and W, again with mercury drop electrodes.[78] A set of spikes were observed in the voltammograms, attributed to the reduction of surface oxides of particles upon collisions. Although Heyrovský did not study the amperometric impact of individual particles, he reported two routes *via* studies on ensembles that are used in impacts nowadays for single nanoparticle studies: direct and indirect detection of particles. While *direct* detection corresponds to the oxidation/reduction of the particles themselves (Figure 1.20a), *indirect* detection involves the redox reaction of a solution phase species mediated by the particles (Figure 1.20b). In the former case, particles are consumed after impacting the potentiostatted electrode, while in the latter the particles persist as the electrochemical reaction only takes place on the surface of the particles.

Direct detection *via* impacts can be used to identify the particles. By examining the onset potential at which the impact event is triggered, the type of particles involved can be inferred, as their oxidation/reduction occurs at a defined potential. Stuart *et al.* reported the identification of nickel and silver particles by impact experiments.[79] While the onset potential of silver oxidation is at *ca.* +0.45 V (*vs.* silver/silver chloride reference electrode), nickel oxidation happens only when the potential is +1.55 V or higher. Both onset potentials are consistent with the oxidation potentials observed in voltammetry, so the identity of the two types of particles can be confirmed.

By measuring the charge transferred per individual spike (from the area of the spike), the amount of ions/molecules can be quantified *via* Faraday's Law of Electrolysis (Eq. 1.8). The size of the single particles can thus be determined. Oxidative impacts has been extensively applied in electrochemical sizing of metal particles, such as Ag[80], Au[81], Ni[79], and Cu[82]. The size of metal oxide particles, such as Fe_3O_4[83], were determined by both oxidative and reductive impacts. More recently, electrochemical sizing has been developed for organic particles, such as indigo dye[84], oil blue dye[85], and liposomes containing vitamin C[86]. It has been shown that the sizes of various particles derived

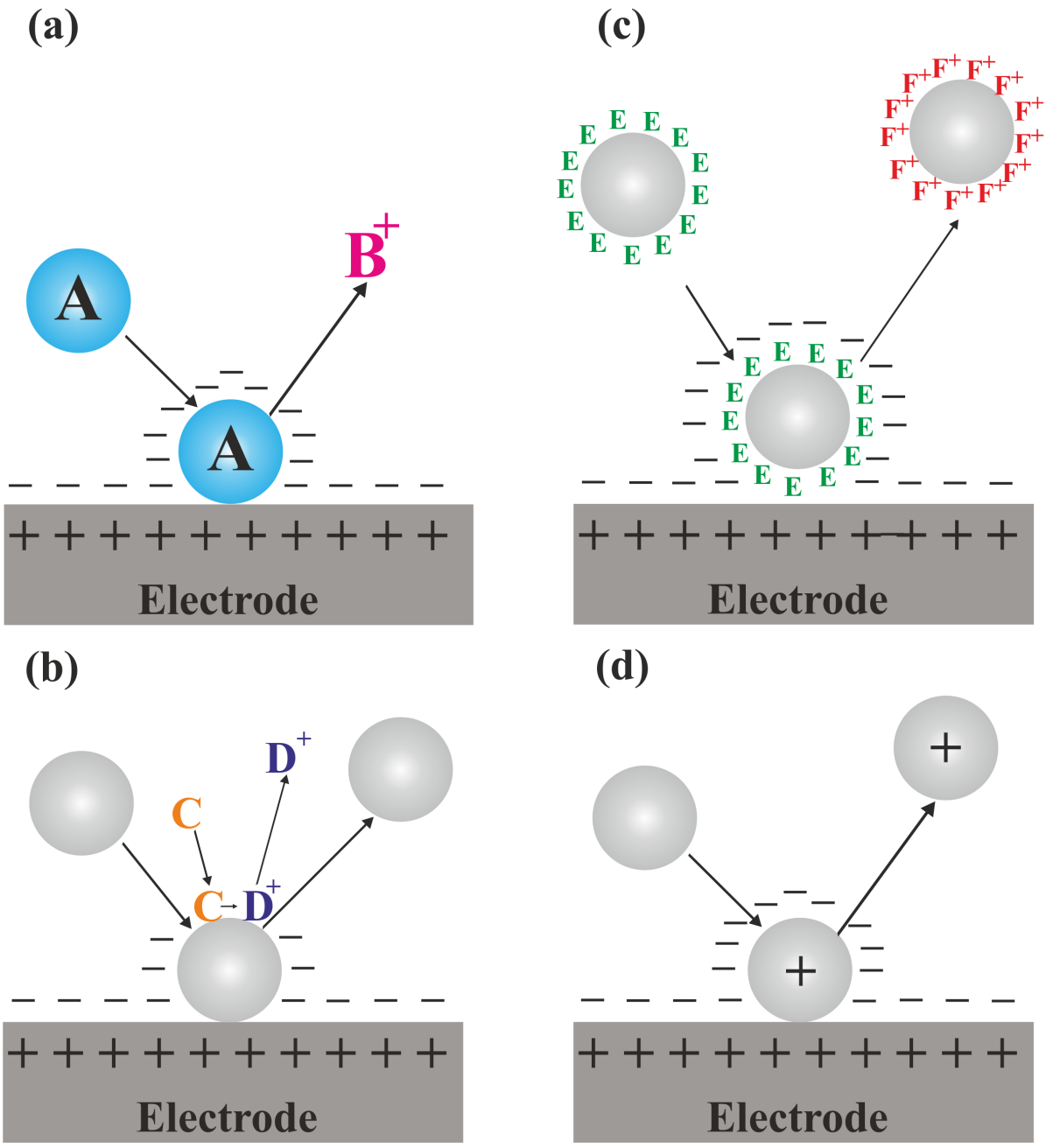

Figure 1.20: Cases of particle impacts. (a) Faradaic impact, direct detection of particles. $A \rightleftarrows B^+ + e^-$. (b) Faradaic impact, indirect detection of particles. $C \rightleftarrows D^+ + e^-$. (c) Faradaic impact, detection of tagged particles. $E \rightleftarrows F^+ + e^-$. (d) Capacitative impact. Anions are provided from the supporting electrolyte.

from impacts are consistent with the measurements from SEM images.

In addition to sizing, the aggregation of the particles can be inferred if the size is plotted against time.[87] Ellison *et al.* determined the proportion of monomer, dimer, trimer, tetramer, pentamer and hexamer of Ag particles by using impact experiments.[14] Lees *et al.* found that it is achievable to slow down the rate of Ag particles agglomeration/aggregation by the use of a high concentration of tri-sodium citrate as the capping agent, thanks to its particle stabilising property.[88] Furthermore, impacts also allows the concentration of the particles to be derived, as the frequency of the spikes scales with the particle concentration in the solution.[79]

Indirect detection of impacting particles involves three components: an electroactive species supported with electrolyte in the solution phase, an electrode, and the particles. While the potentiostatted electrode is inert to the redox reaction of the species, the particles are catalytic. When the single particle collides with the electrode, it mediates the redox process of the species in the solution phase, giving rise to a signal. The frequency of the impacts is related to the concentration of the particles, and the amplitude of the catalytic signals indicates the concentration of the species. The first experiment was conducted by Xiao and Bard using a carbon electrode to indirectly detect impacting Pt particles *via* reduction of proton to hydrogen.[89] The technique was further developed in water oxidation catalysed by IrO_x particles[90], hydrogen peroxide reduction catalysed by Ag particles[91] and CeO_2 particles[92], and proton reduction catalysed by Ni/NiO particles[93].

An alternative non-destructive detection of impacting particles named "tagged redox coulometry" (Figure 1.20c) has been proposed.[94, 95] In this method, the surface of the particles are tagged by a redox active molecules. Upon impacts, the particles themselves remain unchanged while the tag molecules undergo redox reaction. In the case of monolayer coverage, the charge passed per individual spike infers the number of molecules on

the surface of the single particle. With the known molecular area, the surface area of the single particle can be derived. The size of the particle can thus be determined, assuming the particle is spherical. In the work of Zhou *et al.*, Ag particles were tagged with 1,4-nitrothiophenol.[94, 95] The size determined from impact experiments was shown in excellent agreement with those obtained from the naked Ag particles. Plowman *et al.* further used 1,4-nitrothiophenol to tag Au nanorods to derive the volume and surface area of the nanorods, which were also shown to be consistent with electron microscopic measurements.[96]. More lately, there is an increasing interest in applying the method to biological detection. Sepunaru *et al.* used Ag particles to tag *Escherichia coli* bacteria[97] and influenza viruses[98]. The frequency of impacts was found to scale with the concentration of the bacteria or virus under examination.

The particle impacts discussed so far are all Faradaic process. Capacitative (non-Faradaic) impacts may also occur (Figure 1.20d), when the applied potential deviates from the potential of zero charge (PZC) of the electrode/solution interface. Upon impact, the single particle disrupts the double layer and gets charged. When the particle leaves, the double layer reforms. In order to maintain electro-neutrality, electron flow in or out of the electrode to discharge or charge the double layer capacitance. Either an oxidative spike (when the applied potential is positive of PZC), a reductive spike (when the applied potential is negative of PZC), or no spike (when the applied potential equals PZC) will be observed. Scholz *et al.* actively used capacitative impacts to study the collisions of liposomes[99, 100], and montmorillonite particles[101], with mercury drop electrodes. Similar experiments were carried out by Banks *et al.* using suspensions of heptane droplets[102] and various solid particles[103] to generate capacitative impact spikes induced by sonication. The charge passed per spike was found to scale with the size and conductivity of the particle, as well as the applied potential.

In this thesis, alumina particles and graphene nanoplatelets are not electroactive.

Hence they can be tagged with redox active molecules. Such a modification significantly opens the particle impacts technique to insulating and conductive particles. Faradaic impacts will be used predominantly to measure the size of the particles (Chapter 5), the surface coverage of molecules on the particles (Chapters 5 $\sim$ 8), the diffusion coefficient of charge transferred between the molecules on the particle (Chapters 5 and 6), the electron transfer rate between the molecule and the particle (Chapter 8), and the catalytic rate of the tagged particles (Chapter 9). Capacitative impacts will also be demonstrated (Chapter 7).

References

[1] Compton, R. G.; Banks, C. E. *Understanding Voltammetry, 2nd edition*; Imperial College Press, 2011.

[2] Truhlar, D. G.; Hase, J. T., W. L. & Hynes *Journal of Physical Chemistry* **1983**, *87*, 5523.

[3] Truhlar, D. G.; Garrett, B. C.; Klippenstein, S. J. *Journal of Materials Chemistry* **1996**, *100*, 12771–12800.

[4] Bard, A. J.; Faulkner, L. R. *Electrochemical methods: fundamentals and applications*; Wiley New York, 2001.

[5] Fisher, A. C. *Electrode dynamics*; Oxford University Press Oxford, 1996.

[6] Hoijtink, G. J.; van Schooten, J.; de Boer, E.; Aalbersberg, W. I. *Recueil des Travaux Chimiques des Pays-Bas* **1954**, *73*, 355–375.

[7] Einstein, A. *Annalen der Physik* **1905**, *17*, 549–560.

[8] von Smoluchowski, M. *Annaden der Physik* **1906**, *21*, 756–780.

[9] Ellison, J.; Batchelor-McAuley, C.; Tschulik, K.; Compton, R. G. *Sensors and Actuators B: Chemical* **2014**, *200*, 47–52.

[10] Matsuda, H.; Ayabe, Y. *Berichte der Bunsengesellschaft für physikalische Chemie* **1955**, *59*, 494–503.

[11] Compton, R. G.; Batchelor-McAuley, C.; Dickinson, E. J. F. *Understanding Voltammetry - Problems and Solutions*; Imperial College Press, 2012.

[12] Saito, Y. *Review of Polarography 15*, 178–187.

[13] Aoki, K.; Honda, K.; Tokuda, K.; Matsuda, H. *Journal of Electroanalytical Chemistry and Interfacial Electrochemistry* **1985**, *182*, 267 – 279.

[14] Ellison, J.; Tschulik, K.; Stuart, E. J. E.; Jurkschat, K.; Omanović, D.; Uhlemann, M.; Crossley, A.; Compton, R. G. *ChemistryOpen* **2013**, *2*, 69–75.

[15] Shoup, D.; Szabo, A. *Journal of Electroanalytical Chemistry and Interfacial Electrochemistry* **1982**, *140*, 237–245.

[16] Szabo, A.; Cope, D. K.; Tallman, D. E.; Kovach, P. M.; Wightman, R. M. *Journal of Electroanalytical Chemistry and Interfacial Electrochemistry* **1987**, *217*, 417–423.

[17] Vert, M.; Doi, Y.; Hellwich, K.-H.; Hess, M.; Hodge, P.; Kubisa, P.; Rinaudo, M.; Schu, F. *Pure and Applied Chemistry* **2012**, *84*, 377–410.

[18] Wood, K. *Composites Technology* **2008**, *14*.

[19] Zauner, W.; Farrow, N.; Haines, A. *Journal of Controlled Release* **2001**, *71*, 39–51.

[20] Rejman, J.; Oberle, V.; Zuhorn, I.; Hoekstra, D. *Biochemical Journal* **2004**, *377*, 159–169.

[21] Pacheco, P.; White, D.; Sulchek, T. *PLoS ONE* **2013**, *8*, cited By 29.

[22] Shang, L.; Nienhaus, K.; Nienhaus, G. *Journal of Nanobiotechnology* **2014**, *12*.

[23] Barua, S.; Yoo, J.-W.; Kolhar, P.; Wakankar, A.; Gokarn, Y.; Mitragotri, S. *Proceedings of the National Academy of Sciences of the United States of America* **2013**, *110*, 3270–3275.

[24] Gratton, S.; Ropp, P.; Pohlhaus, P.; Luft, J.; Madden, V.; Napier, M.; DeSimone, J. *Proceedings of the National Academy of Sciences of the United States of America* **2008**, *105*, 11613–11618.

[25] Saha, K.; Kim, S.; Yan, B.; Miranda, O.; Alfonso, F.; Shlosman, D.; Rotello, V. *Small* **2013**, *9*, 300–305.

[26] Triton Technology Inc., Users Manual for Dye-Trak & Dye-Trak VII+. 2010.

[27] Hakkinen, J. P.; Miller, M. W.; Smith, A. H.; Knight, D. R. *Cardiovascular Research* **1995**, *29*, 74–79.

[28] Thermo Fisher Scientific Inc.., Fluorescent Microspheres. https://www.thermofisher.com/uk/en/home/life-science/cell-analysis/qdots-microspheres-nanospheres/fluorescent-microspheres.html.

[29] Hnninen, P.; Soini, A.; Meltola, N.; Soini, J.; Soukka, J.; Soini, E. *Nature Biotechnology* **2000**, *18*, 548–550, cited By 67.

[30] Nippon Steel & Sumikin Materials Co., Ltd, Silica and Alumina Spherical Fine Particles. http://www.nssmc.com/en/tech/report/nsc/pdf/n9315.pdf.

[31] ZielińAski, P.; Schulz, R.; Kaliaguine, S.; Neste, A. V. *Journal of Materials Research* **1993**, *8*, 2985–2992.

[32] Hench, L. *Journal of the American Ceramic Society* **1991**, *74*, 1487–1510.

[33] Basim, G.; Adler, J.; Mahajan, U.; Singh, R.; Moudgil, B. *Journal of the Electrochemical Society* **2000**, *147*, 3523–3528.

[34] Basim, G.; Adler, J.; Mahajan, U.; Singh, R.; Moudgil, B. *Proceedings - Electrochemical Society* **2000**, *26*, 45.

[35] Trippel, G.; Steiner, W.; Joppien, G.; Hofmann, U. Process for the preparation of spherical alpha-aluminium oxide particles, aluminium oxide particles and their use. 1988; http://www.google.com.na/patents/EP0250616A1?cl=en, EP Patent App. EP19,860,108,654.

[36] Novoselov, K. S.; Geim, A. K.; Morozov, S.; Jiang, D.; Zhang, Y.; Dubonos, S.; ; Grigorieva, I.; Firsov, A. *Science* **2004**, *306*, 666–669.

[37] Jouikov, V.; Simonet, J. *Electrochemistry Communications* **2014**, *45*, 32–36.

[38] Jouikov, V.; Simonet, J. *Electrochemistry Communications* **2014**, *46*, 132–136.

[39] Pumera, M. *Electrochemistry Communications* **2013**, *36*, 14–18.

[40] Neto, A. C.; Guinea, F.; Peres, N.; Novoselov, K. S.; Geim, A. K. *Reviews of Modern Physics* **2009**, *81*, 109.

[41] Ambrosi, A.; Chua, C. K.; Bonanni, A.; Pumera, M. *Chemical Reviews* **2014**, *114*, 7150–7188.

[42] Zhai, Y.; Dou, Y.; Zhao, D.; Fulvio, P. F.; Mayes, R. T.; Dai, S. *Advanced Materials* **2011**, *23*, 4828–4850.

[43] Miller, J. R.; Outlaw, R.; Holloway, B. *Electrochimica Acta* **2011**, *56*, 10443–10449.

[44] Zhao, X.; Tian, H.; Zhu, M.; Tian, K.; Wang, J.; Kang, F.; Outlaw, R. *Journal of Power Sources* **2009**, *194*, 1208–1212.

[45] Vivekchand, S.; Rout, C. S.; Subrahmanyam, K.; Govindaraj, A.; Rao, C. *Journal of Chemical Sciences* **2008**, *120*, 9–13.

[46] Zhang, L. L.; Zhou, R.; Zhao, X. *Journal of Materials Chemistry* **2010**, *20*, 5983–5992.

[47] Wang, Y.; Shi, Z.; Huang, Y.; Ma, Y.; Wang, C.; Chen, M.; Chen, Y. *Journal of Physical Chemistry C* **2009**, *113*, 13103–13107.

[48] Stoller, M.; Park, S.; Yanwu, Z.; An, J.; Ruoff, R. *Nano Letters* **2008**, *8*, 3498–3502.

[49] Chen, J.; Li, C.; Shi, G. *Journal of Physical Chemistry Letters* **2013**, *4*, 1244–1253.

[50] Dao, V.-D.; Larina, L. L.; Suh, H.; Hong, K.; Lee, J.-K.; Choi, H.-S. *Carbon* **2014**, *77*, 980–992.

[51] Miao, X.; Tongay, S.; Petterson, M. K.; Berke, K.; Rinzler, A. G.; Appleton, B. R.; Hebard, A. F. *Nano Letters* **2012**, *12*, 2745–2750.

[52] Loo, A. H.; Bonanni, A.; Pumera, M. *Nanoscale* **2013**, *5*, 7844–7848.

[53] Bonanni, A.; Chua, C. K.; Zhao, G.; Sofer, Z. k.; Pumera, M. *ACS Nano* **2012**, *6*, 8546–8551.

[54] Shao, Y.; Zhang, S.; Wang, C.; Nie, Z.; Liu, J.; Wang, Y.; Lin, Y. *Journal of Power Sources* **2010**, *195*, 4600–4605.

[55] Servant, A.; Bianco, A.; Prato, M.; Kostarelos, K. *Bioorganic & Medicinal Chemistry Letters* **2014**, *24*, 1638–1649.

[56] Servant, A.; Leon, V.; Jasim, D.; Methven, L.; Limousin, P.; Fernandez-Pacheco, E. V.; Prato, M.; Kostarelos, K. *Advanced Healthcare Materials* **2014**, *3*, 1334–1343.

[57] Choi, W.; Lahiri, I.; Seelaboyina, R.; Kang, Y. S. *Critical Reviews in Solid State and Materials Sciences* **2010**, *35*, 52–71.

[58] Meyer, J. C.; Geim, A. K.; Katsnelson, M.; Novoselov, K.; Booth, T.; Roth, S. *Nature* **2007**, *446*, 60–63.

[59] Liu, L.; Ryu, S.; Tomasik, M. R.; Stolyarova, E.; Jung, N.; Hybertsen, M. S.; Steigerwald, M. L.; Brus, L. E.; Flynn, G. W. *Nano Letters* **2008**, *8*, 1965–1970.

[60] Oberdörster, G.; Maynard, A.; Donaldson, K.; Castranova, V.; Fitzpatrick, J.; Ausman, K.; Carter, J.; Karn, B.; Kreyling, W.; Lai, D.; Olin, S.; Monteiro-Riviere, N.; Warheit, D.; Yang, H. *Particle and Fibre Toxicology* **2005**, *2*, 8.

[61] Arrigan, D. W. M., Ed. *Electrochemical Strategies in Detection Science*; RSC Detection Science; The Royal Society of Chemistry, 2016; pp P001–400.

[62] Poon, J.; Batchelor-McAuley, C.; Tschulik, K.; Compton, R. G. *Chemical Science* **2015**, *6*, 2869–2876.

[63] Lilloja, J.; Kibena-Pldsepp, E.; Merisalu, M.; Rauwel, P.; Matisen, L.; Niilisk, A.; Cardoso, E.; Maia, G.; Sammelselg, V.; Tammeveski, K. *Catalysts* **2016**, *6*.

[64] Strem Chemicals Inc., Graphene Nanoplatelets. https://secure.strem.com/uploads/resources/documents/graphene_nanoplatelets_copy1.pdf.

[65] Lammel, T.; Boisseaux, P.; Fernández-Cruz, M.-L.; Navas, J. M. *Particle and Fibre Toxicology* **2013**, *10*, 27.

[66] Van Bui, H.; Grillo, F.; Helmer, R.; Goulas, A.; van Ommen, J. R. *The Journal of Physical Chemistry C* **2016**, *120*, 8832–8840.

[67] Wei, J.; Atif, R.; Vo, T.; Inam, F. *Journal of Nanomaterials* **2015**, *2015*.

[68] Collins, A. M. *Nanotechnology Cookbook*; Elsevier, 2012.

[69] Atkins, P.; de Paula, J. *Atkin's Physical Chemistry*; Oxford University Press, 2010.

[70] Bard, A. J.; Zhou, H.; Kwon, S. J. *Israel Journal of Chemistry* **2010**, *50*, 267–276.

[71] Cheng, W.; Compton, R. G. *TrAC Trends in Analytical Chemistry* **2014**, *58*, 79–89.

[72] Pumera, M. *ACS Nano* **2014**, *8*, 7555–7558.

[73] Rees, N. V. *Electrochemistry Communications* **2014**, *43*, 83–86.

[74] Heyrovský, M.; Jirkovský, J. *Langmuir* **1995**, *11*, 4288–4292.

[75] Heyrovský, M.; Jirkovský, J.; Mueller, B. R. *Langmuir* **1995**, *11*, 4293–4299.

[76] Heyrovský, M.; Jirkovský, J.; Struplova-Bartackova, M. *Langmuir* **1995**, *11*, 4300–4308.

[77] Heyrovský, M.; Jirkovský, J.; Struplova-Bartackova, M. *Langmuir* **1995**, *11*, 4309–4312.

[78] Korshunov, A. V.; Heyrovskỳ, M. *Electroanalysis* **2006**, *18*, 423–426.

[79] Stuart, E. J.; Zhou, Y.-G.; Rees, N. V.; Compton, R. G. *RSC Advances* **2012**, *2*, 6879–6884.

[80] Zhou, Y.-G.; Rees, N. V.; Compton, R. G. *Angewandte Chemie International Edition* **2011**, *50*, 4219–4221.

[81] Zhou, Y.-G.; Rees, N. V.; Pillay, J.; Tshikhudo, R.; Vilakazi, S.; Compton, R. G. *Chemical Communications* **2012**, *48*, 224–226.

[82] Haddou, B.; Rees, N. V.; Compton, R. G. *Physical Chemistry Chemical Physics* **2012**, *14*, 13612–13617.

[83] Tschulik, K.; Haddou, B.; Omanović, D.; Rees, N. V.; Compton, R. G. *Nano Research* **2013**, *6*, 836–841.

[84] Cheng, W.; Zhou, X.-F.; Compton, R. G. *Angewandte Chemie* **2013**, *125*, 13218–13220.

[85] Zhou, X.-F.; Cheng, W.; Compton, R. G. *Nanoscale* **2014**, *6*, 6873–6878.

[86] Cheng, W.; Compton, R. G. *Angewandte Chemie International Edition* **2014**, *53*, 13928–13930.

[87] Rees, N. V.; Zhou, Y.-G.; Compton, R. G. *ChemPhysChem* **2011**, *12*, 1645–1647.

[88] Lees, J. C.; Ellison, J.; Batchelor-McAuley, C.; Tschulik, K.; Damm, C.; Omanović, D.; Compton, R. G. *ChemPhysChem* **2013**, *14*, 3895–3897.

[89] Xiao, X.; Bard, A. J. *Journal of the American Chemical Society* **2007**, *129*, 9610–9612.

[90] Kwon, S. J.; Fan, F.-R. F.; Bard, A. J. *Journal of the American Chemical Society* **2010**, *132*, 13165–13167.

[91] Stuart, E. J.; Rees, N. V.; Compton, R. G. *Chemical Physics Letters* **2012**, *531*, 94 – 97.

[92] Sardesai, N. P.; Andreescu, D.; Andreescu, S. *Journal of the American Chemical Society* **2013**, *135*, 16770–16773.

[93] Zhou, Y.-G.; Rees, N. V.; Compton, R. G. *Phys. Chem. Chem. Phys.* **2013**, *15*, 761–763.

[94] Zhou, Y.-G.; Rees, N. V.; Compton, R. G. *Chemical Communications* **2012**, *48*, 2510–2512.

[95] Rees, N. V.; Zhou, Y.-G.; Compton, R. G. *Chemical Physics Letters* **2012**, *525526*, 69–71.

[96] Plowman, B. J.; Young, N. P.; Batchelor-McAuley, C.; Compton, R. G. *Angewandte Chemie International Edition* **2016**, *55*, 7002–7005.

[97] Sepunaru, L.; Tschulik, K.; Batchelor-McAuley, C.; Gavish, R.; Compton, R. G. *Biomater. Sci.* **2015**, *3*, 816–820.

[98] Sepunaru, L.; Plowman, B. J.; Sokolov, S. V.; Young, N. P.; Compton, R. G. *Chem. Sci.* **2016**, *7*, 3892–3899.

[99] Hellberg, D.; Scholz, F.; Schauer, F.; Weitschies, W. *Electrochemistry Communications* **2002**, *4*, 305–309.

[100] Hellberg, D.; Scholz, F.; Schubert, F.; Lovrić, M.; Omanović, D.; Hernández, V. A.; Thede, R. *The Journal of Physical Chemistry B* **2005**, *109*, 14715–14726.

[101] Scholz, F.; Hellberg, D.; Harnisch, F.; Hummel, A.; Hasse, U. *Electrochemistry Communications* **2004**, *6*, 929–933.

[102] Banks, C. E.; Rees, N. V.; Compton, R. G. *Journal of Physical Chemistry B* **2002**, *106*, 5810–5813.

[103] Rees, N. V.; Banks, C. E.; Compton, R. G. *Journal of Physical Chemistry B* **2004**, *108*, 18391–18394.

Chapter 2

Experimental

This chapter outlines the general experimental approaches applied in this thesis, including chemical reagents and solutions, preparation of solid particles, electrochemical apparatus, scanning electron microscopy and simulations. Details specific to particular projects can be found in the individual experimental sections of Chapters 3 to 9.

2.1 Chemical Reagents and Solutions

The alumina particles (Al_2O_3, sold as '1 μm') were purchased from Buehler (Lake Bluff, IL, U.S.A.). The actual size of the alumina was determined by scanning electron microscope (SEM, Section 2.4) as 0.58 $\pm$ 0.40 μm in diameter (Figure 2.2). The graphene nanoplatelets (GNPs, bulk density of 1×10^5 g m^{-3}[1]) were purchased from Strem Chemicals (Newburyport, MA, U.S.A.). The GNPs were 16.5 $\pm$ 5 μm in width and 7.1 $\pm$ 2 nm in thickness (Figure 2.3), as confirmed by SEM[2]. The molecular weight of the GNPs was 2.07×10^{12} g mol^{-1}, assuming its density to be the same as that of graphite, 2.26×10^6 g m^{-3}[3]. Note that the bulk density corresponds to the GNPs loose powder but not the actual particles. Poly(vinylferrocene) (PVFc, molecular weight of *ca.* 50 000 g mol^{-1}, structure as shown in Figure 2.1) was purchased from Polyscience Inc. (Warrington, PA,

U.S.A.). 1-(Biphen-4-yl)ferrocene (structure as shown in Figure 2.1) was synthesised in collaboration with Dr. Luís M. Gonçalves and Dr. Carlos F. R. A. C. Lima (University of Porto, Porto, Portugal). The method will be elaborated in Section 7.2. All other chemicals were purchased from Sigma-Aldrich (St Louis, MO, U.S.A.). All reagents were used without further purification.

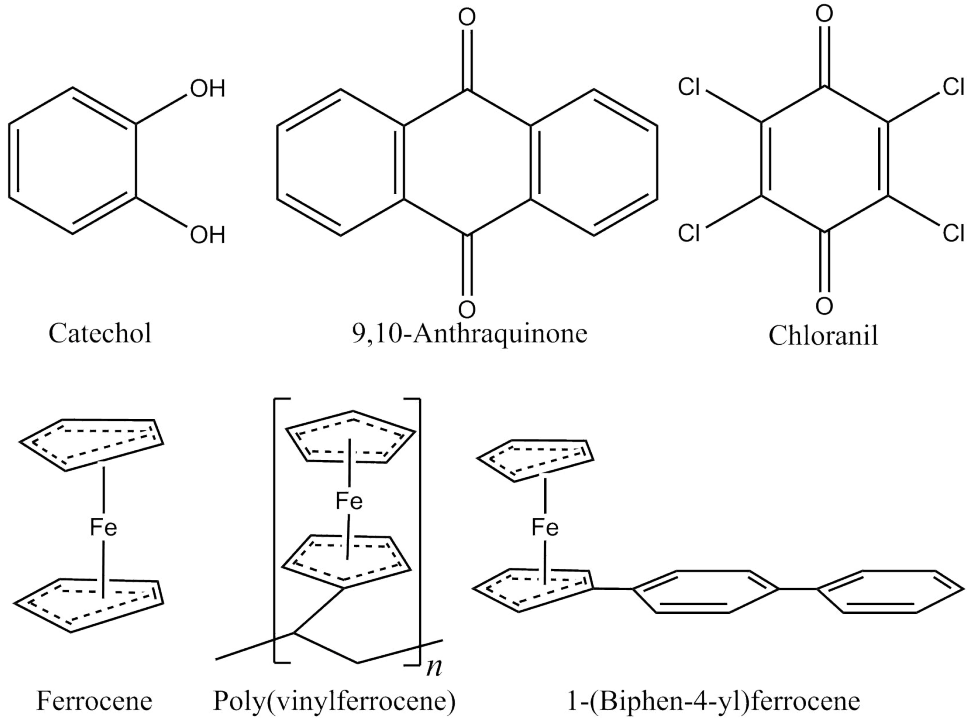

Figure 2.1: Structures of molecules.

Aqueous buffer solutions for different pH ranges were prepared using the following recipes: 0.1 M hydrochloric acid for pH 1.0 $\sim$ 2.5, 0.1 M citric acid/sodium citrate for pH 2.5 $\sim$ 5.5, 0.1 M monosodium phosphate/disodium phosphate for pH 5.5 $\sim$ 8.5, 0.1 M sodium carbonate/bicarbonate for pH 8.5 $\sim$ 11.5, and either NaOH or KOH for pH 12.0 $\sim$ 14.0. pH buffers were freshly made, measured by using a calibrated Hanna pH213 pH meter, and degassed with nitrogen. Either 0.1 M KCl or 0.1 M $NaClO_4$ was used as the supporting electrolyte. All aqueous solutions were prepared using deionised water with resistivity not less than 18.2 MΩ cm at 298 K (Merck Millipore, Billerica, MA, U.S.A.) and degassed with pure nitrogen. In the following sections, the 'blank' solution refers to

nitrogen degassed aqueous electrolytic solution.

2.2 Preparation of Solid Particles

2.2.1 Modified Alumina Particles

Catechol (1,2-hydroxybenzene), 9,10-anthraquinone, chloranil (tetrachloro-1,4-benzoquinone) and poly(vinylferrocene) modified alumina particles were prepared. Structures of the molecules are shown in Figure 2.1. The modified particles were abbreviated as H_2C-Al_2O_3, AQ-Al_2O_3, TCBQ-Al_2O_3 and PVFc-Al_2O_3, respectively. 0.159 g of '1μm' alumina particles were first mixed with 50 mL of solutions containing modifiers (concentrations and solvents are listed in Table 2.1). pH 3.0 buffer was used to dissolve catechol, as catechol was more stable against air oxidation in acidic conditions. Organic solvents were used to dissolve the other three modifiers, due to their low solubility in aqueous solution. The mixture was then sonicated (FB15050, 50/60 Hz, 80 W, Fisher Scientific, Schwerte, Germany) for 15 min to allow the full adsorption of modifiers onto alumina particles. For H_2C-Al, the mixture was centrifuged for 15 min and the excess catechol was washed using pH 3.0 aqueous buffer. The settled particles were transferred for further experiments. For the rest, the mixture was divided into several 5.0 mL portions, with each added to a sample vial and left in a desiccator under vacuum to evaporate the solvent. The excess modifiers were washed using the corresponding solvents, and the residual modified alumina particles were transferred for further reactions. The difference in preparation was due to the fact that water evaporates very slowly under vacuum.

2.2.2 Modified Graphene Nanoplatelets

To prepare modified graphene nanoplatelets, two stock solutions were made fresh daily: ferrocene derivatives (structures of the molecules are shown in Figure 2.1) was dissolved

Modifiers	Concentration / mM	Solvent
Catechol	20	pH 3.0 buffer
Anthraquinone	5	Acetonitrile
Chloranil	20	Acetonitrile
Ferrocene moiety of poly(vinylferrocene)	2	Dichloromethane

Table 2.1: Concentrations and solvents used in preparation of modified alumina particles.

in 5.0 mL of solvent (concentrations and solvents are listed in Table 2.2), and 7.0 mg of GNPs was added to another 25 mL of solvent. The latter was sonicated for 15 min to obtain a well suspended mixture. 1.0 mL of each stock solution was taken out and mixed in a sample vial. The mixture was dried in a desiccator for 30 min $\sim$ 1 h to evaporate the solvent. The excess ferrocene in the vial walls was washed with solvent, and the residual modified GNPs were transferred for further reactions.

Modifiers	Concentration / mM	Solvent
Ferrocene	2	Acetonitrile
1-(Biphen-4-yl)ferrocene	2	Acetonitrile
Ferrocene moiety of poly(vinylferrocene)	2	Dichloromethane

Table 2.2: Concentrations and solvents used in preparation of modified graphene nanoplatelets.

2.3 Electrochemical Apparatus

A standard three-electrode cell was employed to conduct all the electrochemical experiments. Either a glassy carbon electrode (GCE, diameter 3.0 mm, ALS distributed by BASi, Tokyo, Japan) or an edge-plane pyrolytic graphite (EPPG, diameter 4.0 mm, home made) electrode was used as the working electrode for voltammetric measurements. Either a carbon fibre microdisc electrode (μ-CE, diameter 10 or 33 μm, ALS distributed by BASi, Tokyo, Japan) or a carbon fibre microwire electrode (diameter 7.0 μm and length 1 mm, home made) was used as the working electrode for impact chronoamperometry.

Either a platinum mesh (99.99%, GoodFellow, Cambridge, U.K.) or a graphite rod was used as the counter electrode. A saturated calomel electrode (SCE, ALS distributed by BASi, Tokyo, Japan) was used as the reference electrode. Voltammetry was recorded using either a μAutolab II, or a μAutolab III, or an Autolab PGSTAT101 potentiostat (Autolab, Utrecht, Netherlands). Impact chronoamperometry was conducted using either a μAutolab II or an in-house-built low-noise potentiostat. The latter was built by Dr. Christopher Batchelor-McAuley with a low current-amplifier LCA-4K-1G (FEMTO, Messtechnik GmbH, Germany), with its output bandwidth limited using a 250 Hz 4-pole Bessel filter (Linear Technology DC338A-B, Farnell, Leeds, UK). The generated analogue signal was oversampled and digitised using LabJack U6 (LabJack Corporation, Lakewood, CO, U.S.A.) at a stream rate of 4 kHz. A highly stabilised (1 kHz bandwidth) classic adder potentiostat was used for potentiostat control.[4] All the experiments were performed in a Faraday cage thermostated at 25 $\pm$ 1 °C.

2.3.1 Fabrication of Edge-Plane Pyrolytic Graphite Electrodes

The EPPG electrodes were made in-house from highly ordered pyrolytic graphite (HOPG) (Le Carbone, Sussex, U.K.) of SP13 (ZYH) grade. The edge plane was exposed by orientating the disc surface perpendicular to the graphite crystal surface.

2.3.2 Fabrication of Carbon Fibre Microwire Electrodes

Carbon fibre microwire electrodes were fabricated in-house following the method provided by Ellison *et al.*[5]. First, a metal wire was connected to a carbon fibre (diameter of 7.0 μm, Goodfellow, Cambridge, U.K.) using silver epoxy (RS Components, Corby, U.K.) conductive adhesive. It was then placed in an oven at approximately 60 °C for 20 min to set the adhesive. After the wire cooled down, it was threaded through a plastic micro pipette tip, leaving only the carbon fibre out of the tip end. The gap between the wire and

the tip was sealed with cyanoacrylate adhesive. It was left for at least 12 h, to ensure the setting of adhesive. Finally, the exposed carbon fibre was cut to a length of approximately 1 mm from the tip end.

The length (l) of the carbon fibre microwire electrode was calibrated by analysing the voltammetric peak current (I_p) for the one electron reduction of 1 mM hexaammineruthenium(III) chloride in aqueous solution. A diffusion coefficient of 8.43 $\times$ 10^{-6} cm^2 s^{-1} at 298 K[6] was used to determine l by the following equation:[5]

$$\frac{I_p}{2\pi nFC_iD_il} = 0.446h + 0.335h^{0.15} \quad \text{with} \quad h = \left(\frac{nFr_e^2\nu}{RTD_i}\right)^{0.5} \tag{2.1}$$

where $n = 1$ is the number of electrons transferred, F is the Faraday constant (96 485 C mol^{-1}), C_i is the bulk concentration of hexaammineruthenium(III) chloride (mol cm^{-3}), D_i is the diffusion coefficient (cm^2 s^{-1}), r_e is the radius of the microwire electrode (cm), ν is the scan rate (V s^{-1}), R is the universal gas constant (8.314 J k^{-1} mol^{-1}) and T is temperature (K).

2.3.3 Working Electrodes Preparation

The GCE and EPPG electrode were polished by using either diamond sprays of decreasing particle sizes (3.0 $\sim$ 0.1 μm, Kemet, Kent, U.K.) or alumina of decreasing particle sizes (1.0 $\sim$ 0.05 μm, Buehler, Lake Bluff, IL, U.S.A.). The electrodes were sonicated and nitrogen blown dried, prior to voltammetric measurements. The μ-CE was cleaned by polishing in an alumina slurry of decreasing particle sizes, rinsing with water and drying with nitrogen, before it was used for impact chronoamperometry.

The radius (r_e) of the μ-CE was calibrated by analysing the steady-state limiting current (I_{ss}) for the reduction of 1 mM hexaammineruthenium(III) chloride in aqueous

solution. A value of r_e was determined by using the following equation:[7]

$$I_{ss} = 4nFD_iC_ir_e \tag{2.2}$$

where r_e is the radius of the microdisc electrode (cm) and other symbols have been defined in the preceding section. This equation was also used to determine the diffusion coefficient of catechol, as described later in Section 3.3.2.

The following sections describe the modification procedure performed on the GCE and EPPG electrode. While the immobilisation of solid particles was achieved by abrasive modification, the immobilisation of molecules on electrode surfaces was realised by adsorption transfer or drop-casting modification.

Abrasive Modification

Solid particles were abrasively modified onto the GCE or EPPG electrode surface by at least 100 "figure of 8" cycles of mechanical adhesion / polishing. The electrode preparation was finished by rinsing with water and drying with nitrogen.

Unmodified '1 μm' alumina particles or unmodified GNPs could be immobilised onto the electrodes. To study the apparent catalysis of catechol redox (Chapters 3 and 4), the modified electrode was transferred to 0.5 mM catechol pH buffered aqueous electrolytic solution. To obtain the background voltammetry (Chapters 5, 6, 7 and 9), it was transferred to a 'blank' solution.

Modified alumina particles (Section 2.2.1) or modified GNPs (Section 2.2.2) could also be immobilised onto the electrodes. To examine if modifiers could be adsorbed onto the solid particles, the modified electrode was transferred to a 'blank' solution to run the voltammetry (Chapters 5 $\sim$ 8). To investigate the modified GNPs mediated L-cysteine oxidation (Chapter 9), it was transferred to 10 mM L-cysteine pH buffered aqueous electrolytic solution.

Adsorption Transfer Modification

In Chapter 7, the immobilisation of ferrocene or 1-(biphen-4-yl)ferrocene onto EPPG electrode was achieved *via* adsorption transfer. The EPPG electrode was immersed into 2 mM ferrocene derivatives in acetonitrile for 30 s. In order to remove the excess of ferrocene derivative, the electrode was immersed into water for 5 s and dried with nitrogen. The modified EPPG electrode was transferred to a 'blank' solution for voltammetric study.

Drop-casting Modification

In Chapter 8, the immobilisation of poly(vinylferrocene) onto EPPG electrode was done *via* drop-casting. 5 μL of 0.5 mM poly(vinylferrocene) in dichloromethane was drop-casted on the surface of EPPG electrode. The electrode was left still to evaporate the organic solvent at room temperature. A layer of ferrocene derivative remains at the surface of the electrode. A total of 2.5 nmol poly(vinylferrocene) was hence modified onto the electrode, before it was transferred to a 'blank' solution for voltammetric study.

2.4 Scanning Electron Microscopy

The scanning electron microscope (SEM) imaging of the unmodified, alumina-modified and GNP-modified GCE surfaces was performed by Mr. Chris Salter and Dr. Colin Johnston (Department of Materials, University of Oxford). For the unmodified and alumina-modified GCE surfaces, a JEOL JSM-6500F Scanning Electron Microscope (JEOL GmbH, Eching b. München, Germany) was used for the imaging using an acceleration voltage of 10.0 kV and a detector in in-lens geometry. The GNP-modified GCE surface was imaged with a Zeiss Merlin-Analytical Scanning Electron Microscope (Zeiss, Oberkochen, Germany) using an acceleration voltage of 1.0 kV and a detector in in-lens geometry. The measured diameter of alumina was 0.58 $\pm$ 0.40 μm (Figure 2.2). The measured width

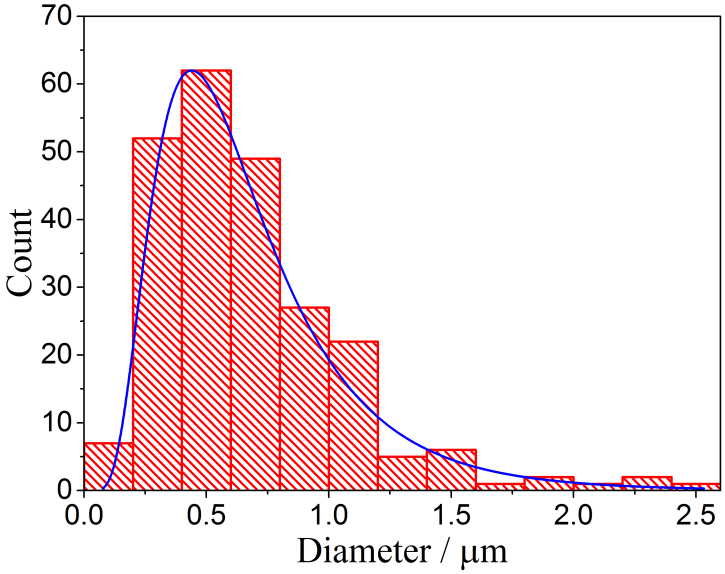

Figure 2.2: Diameter histogram of alumina particles measured from scanning electron microscope. The log-normal distribution is fitted in the blue line.[8]

and thickness of GNPs was 16.5 ± 5 μm and 7.1 ± 2 nm, respectively (Figure 2.3).

2.5 Simulations

The voltammetric simulations of catechol redox reactions in Chapters 3 and 4 were carried out using the commercial software package DIGISIM (version 3.03b, BASi Technicol, West Lafayette, IN, U.S.A.). DIGISIM is based on Butler-Volmer kinetics and the fully implicit finite difference (IFD) method proposed by Rudolph.[9, 10] All simulations were set as two consecutive one electron transfers. Pre-equilibration was enabled. The concentration of catechol (H_2C) was fixed at 0.50 mM, while the initial concentrations of the intermediate and product were set as 0 mM. The diffusion coefficients of all species involved were set to be 1.1 × 10^{-5} cm^2 s^{-1} as determined in Chapter 3. The diffusion mode was set as semi-infinite for a geometrically planar electrode with an area of 0.0707 cm^2 corresponding to the GCE surface.

In Chapters 5 and 6, the spike transients of particle impact chronoamperometry were simulated based on the theory for Fickian charge diffusion over the surface of the particle,

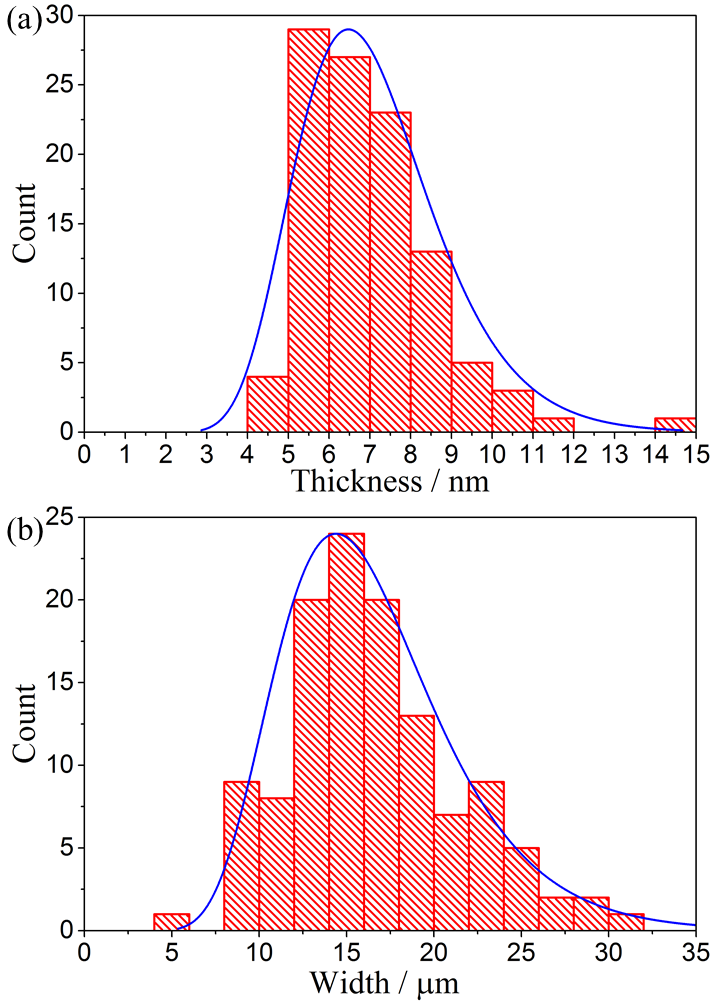

Figure 2.3: (a) Thickness, and (b) width histograms of graphene nanoplatelets measured from scanning electron microscope. The log-normal distribution is fitted in the blue line.[2]

as proposed by Thompson *et al.*[11]. The simulations of particle impact spike charges carried out by Ms. Chuhong Lin in Chapter 9 were achieved through the Newton-Raphson method and the alternative direction implicit (ADI) method.[12]

References

[1] Strem Chemicals Inc., Graphene Nanoplatelets. https://secure.strem.com/uploads/resources/documents/graphene_nanoplatelets_copy1.pdf.

[2] Poon, J.; Batchelor-McAuley, C.; Tschulik, K.; Compton, R. G. *Chemical Science* **2015**, *6*, 2869–2876.

[3] Entigris Inc., Properties and Characteristics of Graphite. Entegris Inc., Billerica, MA,, 2013.

[4] Batchelor-McAuley, C.; Ellison, J.; Tschulik, K.; Hurst, P. L.; Boldt, R.; Compton, R. G. *Analyst* **2015**, *140*, 5048–5054.

[5] Ellison, J.; Batchelor-McAuley, C.; Tschulik, K.; Compton, R. G. *Sensors and Actuators B: Chemical* **2014**, *200*, 47–52.

[6] Wang, Y.; Limon-Petersen, J. G.; Compton, R. G. *Journal of Electroanalytical Chemistry* **2011**, *652*, 13–17.

[7] Saito, Y. *Review of Polarography 15*, 178–187.

[8] Lin, Q.; Compton, R. G. *Journal of Physical Chemistry C* **2015**, *119*, 23463–23469.

[9] Rudolph, M. *Journal of Electroanalytical Chemistry and Interfacial Electrochemistry* **1991**, *314*, 13–22.

[10] Rudolph, M. *Journal of Electroanalytical Chemistry* **1992**, *338*, 85–98.

[11] Thompson, M.; Wildgoose, G. G.; Compton, R. G. *ChemPhysChem* **2006**, *7*, 1328–1336.

[12] Compton, R. G.; Laborda, E.; Ward, K. R. *Understanding Voltammetry: Simulation of Electrode Processes*; Imperial College Press, 2014.

Chapter 3

The Two Electron, Two Proton Oxidation of Catechol: Kinetics and Apparent Catalysis

The study of proton-coupled electron transfer reactions is of great current interest. In this chapter, the catechol redox process was studied voltammetrically in the pH range from 1.0 to 14.0 using a glassy carbon electrode. Analysis of the peak potentials and currents together with Tafel analysis allowed the inference of the likely transition states and electrode reaction mechanism. Modification of the glassy carbon electrode surface with sparse coverages of alumina particles was shown to lead to strong *apparent* catalysis of the catechol redox process at low pH. The work herein presented has been published in *The Journal of Physical Chemistry C*[1] and was carried out in collaboration with Dr. Qian Li and Dr. Christopher Batchelor-McAuley who helped with the interpretation of the experimental results.

3.1 Introduction

Catechol (1,2-hydroxybenzene) and catecholamine redox systems have been extensively investigated due to their importance in neurochemistry.[2] To probe brain chemistry, diverse analytical methods have been developed to monitor neurotransmitters including spectrophotometry[3], high-performance liquid chromatography[4, 5] and gas chromatography-

mass spectrometry[6]. Catechol can be detected *in vivo* by electrochemical methods such as cyclic voltammetry based on the oxidation of catechol to 1,2-benzoquinone at the electrode.[7–9] The advantage of *in vivo* voltammetry is that it can trace many of the dynamic chemical changes associated with neurotransmitter release. Specifically, it probes the time scale of a few milliseconds to seconds, giving information not accessible by any other technique.[9]

In fully buffered media the quinone/hydroquinone redox process involves changes in the protonation state of the molecule, resulting in the observation that potentiometric or amperometric equilibrium potentials vary with pH in a Nernstian manner.[10] This behaviour can be demonstrated in potential-pH diagrams and used as a basis of an electrochemical pH sensor.[11] This calibration-free pH sensor can effectively overcome the limitations of conventional glass electrodes relating to their fragility, alkali error and potential drift caused by dehydration of glass membrane.[11–14] The pH dependence of catechol redox process can be ascribed to a two proton-two electron ($2H^+2e^-$) transfer, commonly known as a proton-coupled electron transfer (PCET) reaction. Quinone/hydroquinone-based PCET agents play an important role in the metabolic oxidative phosphorylation of ADP to ATP.[15]

The PCET process can be understood using the "scheme of squares" as originally introduced by Jacq[23]. Specifically the $2H^+2e^-$ nine-member "scheme of squares" shown in Figure 3.1 can be applied to interpret the electrochemical properties of the quinone/hydroquinone redox systems. This model is usually based on the assumptions that electron transfer is the rate-determining step and that all protonations are at equilibrium. The reaction pathway depends heavily on the pK_a values of the species within the scheme as well as the pH of the local environment. The "scheme of squares" was later further developed by Laviron[24], assuming dimerisation and disproportionation could be neglected, so that the system behaves as a simple reaction with two successive one-

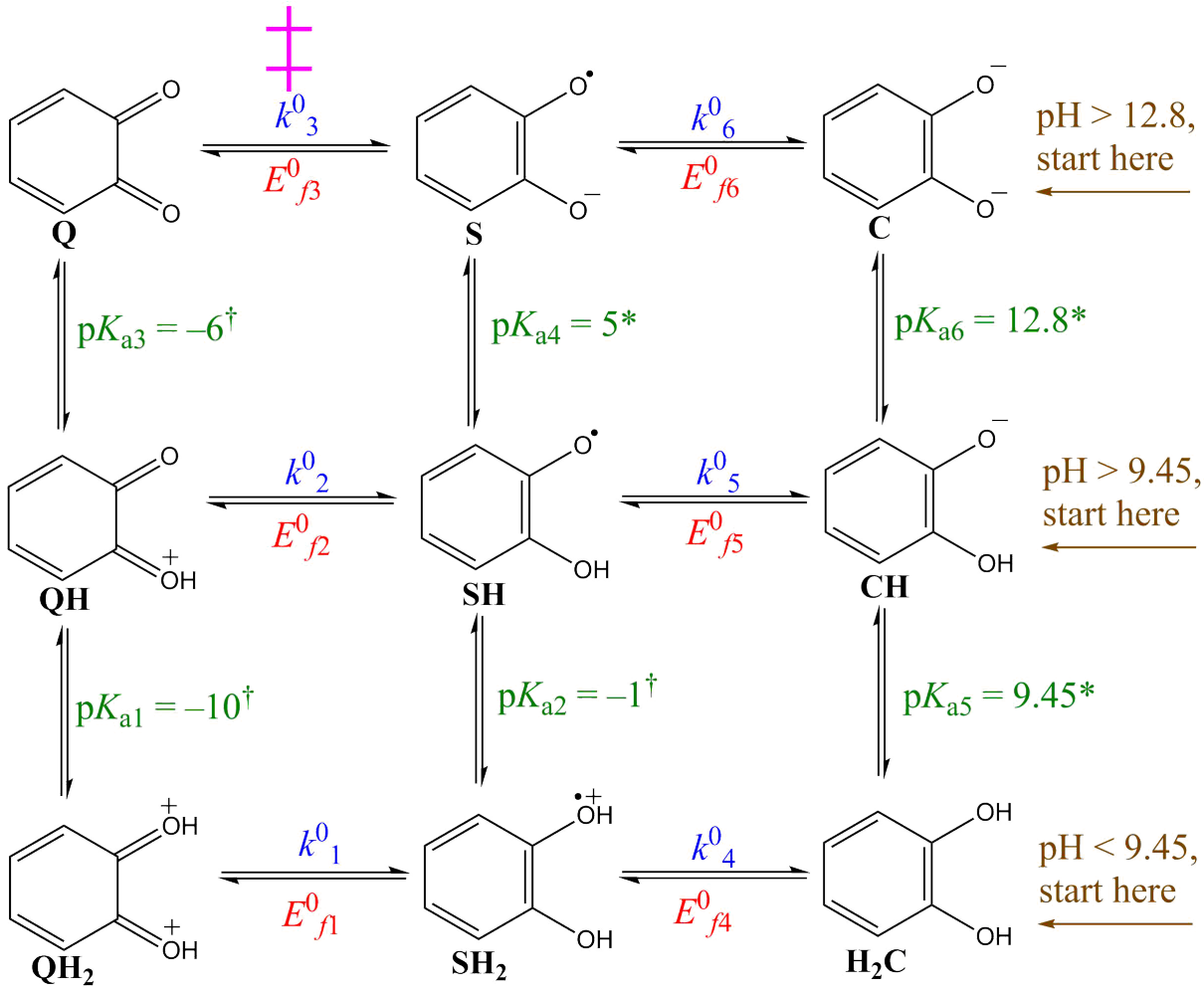

Figure 3.1: "Scheme of squares" for catechol oxidation. Each molecule is assigned an abbreviation, Q, QH, QH_2, S, SH, SH_2, C, CH and H_2C. ‡Location of transition state for the pH range 7.0 < pH < 9.0 and 9.0 < pH < 12.8. The potentials relate to the heterogeneous electron transfers. The pK_a values are associated with the proton transfers. ∗The literature values of p$K_{a4\sim6}$ for catechol were measured using pulse radiolysis: pK_{a4} = 5[15, 16], pK_{a5} = 9.45 and pK_{a6} = 12.8[17]. †pK_{a2} is not known for catechol, but it is −1.1 for duroquinone[18]. pK_{a3} cannot be determined due to the instability of benzoquinone in concentrated acid [19]. However, the behaviour of benzoquinone was reportedly examined by UV spectrophotometry, and pK_{a3} was estimated to be −6 or smaller[20]. pK_{a1} is not known but is likely significantly more negative than pK_{a3}. In this work, pK_{a1} = −10, pK_{a2} = −1 and pK_{a3} = −6 were used as assumptions in line with previous literature[20–22].

electron transfers, with apparent electrochemical rate constants (k^0) and redox potentials (E^0). This approach was applied to the voltammetric analysis of *p*-benzoquinone reduction on a platinum electrode[20] and the oxidation of substituted catechols on a carbon paste electrode[21, 22]. Recently, a simulation software DIGISIM (see Chapter 2, Section 2.5) has been utilised to facilitate the "scheme of squares" analysis on the reduction of flavin adenine dinucleotide[25, 26] and the reduction of anthraquinone-2,6-disulfonate and anthraquinone-2-sulfonate[27].

The electrochemical detection of catechol has been previously examined on both metal[20, 28–30] and carbon[21, 22, 31–33] electrodes. Of particular relevance to the work reported below are studies of catechol redox processes on native and modified glassy carbon surfaces, with investigation of the heterogeneous electron transfer between solid electrodes and catechol.[34–39] This chapter explores for the first time the system of catechol oxidation on a glassy carbon electrode over the pH range from 1.0 to 14.0. The present work additionally studies *apparent* catalysis using alumina modification of the electrode surface showing the role of adsorbed catechol on the latter, which assists the PCET between catechol and glassy carbon electrode. A possible application of this work would be to increase the sensitivity of detection of catechol and catecholamines in microfluidic devices.[40]

3.2 Experimental

Details about the chemical reagents and buffer solutions here utilised can be found in Chapter 2, Section 2.1. The structure of catechol (H_2C) is shown in Figure 3.1, along with the oxidation products, 1,2-benzoquinone (Q) and the semiquinone species (S, SH and SH_2). 0.1 M KCl was used as the supporting electrolyte. The electrochemical measurements were carried out using a μAutolab III potentiostat. A glassy carbon electrode (GCE, diameter 3.0 mm) and a carbon fibre microdisc electrode (μ-CE, diameter 10 μm),

were used as working electrodes with surface preparation as described in Chapter 2, Section 2.3.3. A platinum mesh and a saturated calomel electrode (SCE) were used as the counter and reference electrode respectively. Voltammetric simulations were achieved by using DIGISIM (see Chapter 2, Section 2.5).

3.3 Results and Discussion

This work first investigates the electrochemical response of catechol in pH range from 1.0 to 14.0 with analysis of the peak potentials and midpoint potentials. It then proceeds to analyse the cyclic voltammetry using peak potentials, currents and Tafel analysis to find the likely reaction pathways and transition states for catechol oxidation at a glassy carbon electrode. Finally, and most importantly, the *apparent* electrocatalysis of the catechol oxidation using alumina-modified glassy carbon electrodes is reported and discussed.

3.3.1 Cyclic Voltammetry: Variation with pH

The electrochemical response of 0.5 mM catechol was examined over the pH range from 1.0 to 14.0, as shown in Figure 3.2a and b. Cyclic voltammetry was run on a glassy carbon electrode (GCE) in an oxidative direction from -0.4 to 1.0 V (*vs.* SCE) and reversed to -0.4 V using variable scan rates (ν) from 16 to 400 mV s^{-1}. As can be seen from Figure 3.2a and b, the voltammogram shifts to more negative potentials as the pH increases. The voltammetry is pH dependent since the removal of electrons from catechol induces the loss of protons. Such a deprotonation process is more facile at higher pH, resulting in a thermodynamically more feasible electron transfer occurring at more negative potential. This pH dependency will be analysed more quantitatively in the following discussion, leading to an inference of the likely reaction pathways and transition state for catechol oxidation at a glassy carbon electrode particularly in light of Figure

3.1. Figure 3.2a and b also shows that the reductive (back) peak is gradually diminished as the pH increases. The diminished reductive peak potentially indicates a mechanistic transition from a chemically reversible redox process to a chemically irreversible oxidation only. This likely occurs since after catechol is oxidised to 1,2-benzoquinone, it is thought to undergo a nucleophilic attack by the hydroxyl ions through a 1,4-Michael addition reaction to give 1,2,4-trihydroxybenzene in relatively alkaline solutions.[41–43] This hydroxylation consumes 1,2-benzoquinone, and hence the overall reaction becomes chemically irreversible.

A plot of the oxidative peak potential ($E_{p,ox}$,▲), reductive peak potential ($E_{p,red}$, ▼), and midpoint potential (E_{mid}, ■) against pH for the voltammograms at a scan rate of 16 mV s^{-1} is depicted in Figure 3.3. Such a scan rate is chosen to minimise any ohmic distortion. At pH values above 9.0, only $E_{p,ox}$ is reported. The absence of E_{mid} and $E_{p,red}$ arises from the chemically irreversible behaviour mentioned above, leading to the absence of a back peak. The lines of best fit of E_{mid} and $E_{p,ox}$ are illustrated in Figure 3.3, with gradient changes near pH 9.25 and pH 13.0. These breaks agree well with the previously reported first and second acid dissociation constants for catechol being 9.45 and 12.8 at 25 °C.[17] Furthermore, the resulting gradients, within the three regions separated by the two acid dissociation constants, change from *ca.* 59 mV (E_{mid}), to *ca.* 40 mV ($E_{p,ox}$), to *ca.* 0 mV ($E_{p,ox}$) as shown explicitly in the figure.

For a simple electrochemically reversible voltammograms the midpoint potential obeys the following equation:[44]

$$\frac{\partial E_{mid}}{\partial \mathrm{pH}} \simeq -2.303 \frac{mRT}{nF} \tag{3.1}$$

where R is the gas constant (8.314 J K^{-1} mol^{-1}), T is the temperature (K) , F is the Faraday constant (96 485 C mol^{-1}), m and n are the number of protons and electrons involved in the oxidation, respectively. From Eq. 3.1, it can be seen that E_{mid} varies by the amount $0.059(m/n)$ V per pH unit. At pH values in the range $1.0 \sim 9.0$, the experimental

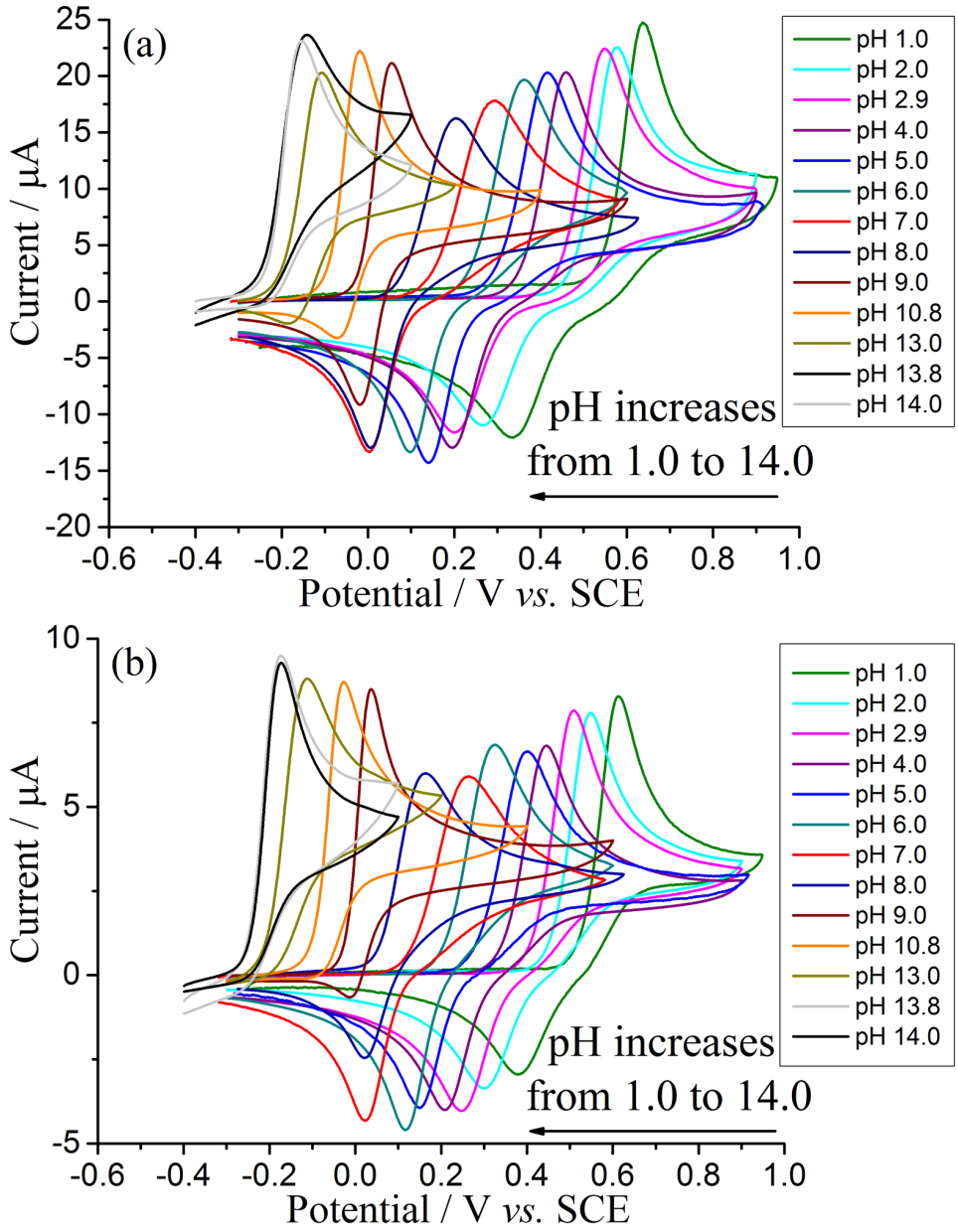

Figure 3.2: Voltammograms of 0.5 mM catechol in pH 1.0 $\sim$ 14.0 buffers recorded on an unmodified glassy carbon electrode at a scan rate of (a) 144 mV s^{-1} and (b) 16 mV s^{-1}, with voltammogram at each pH labelled.

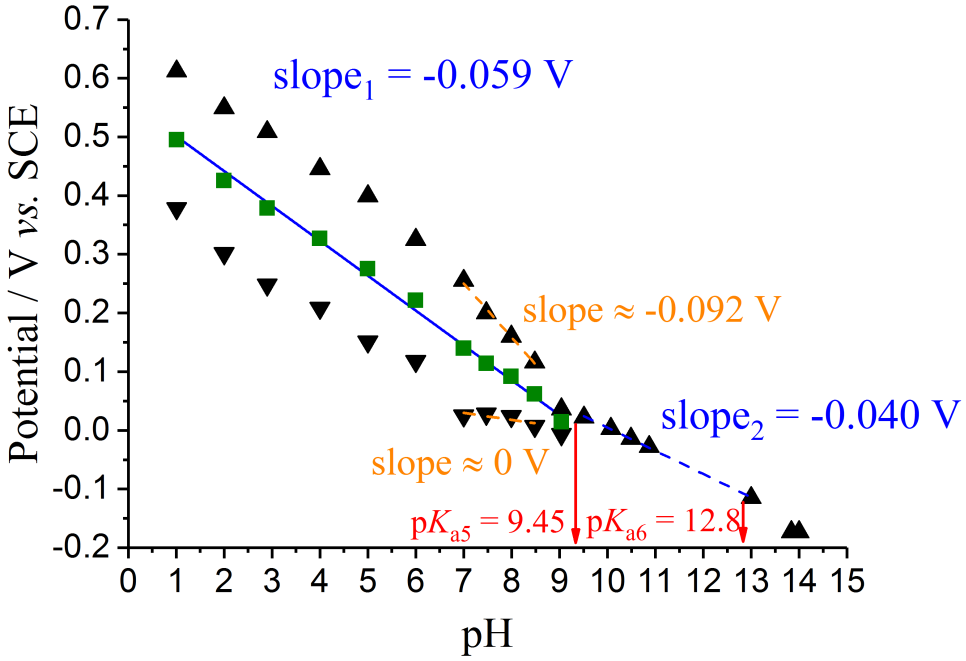

Figure 3.3: Plots of oxidative peak potential (▲), reductive peak potential (▼) and mid-point potential (■, green symbols) against different pH values, of voltammograms on an unmodified glassy carbon electrode. The gradient of the best-fit line is −0.059 V at pH 1.0 ∼ 9.45 (slope$_1$), which decreases to *ca.* −0.040 V at pH 9.45 ∼ 12.8 (slope$_2$). Scan rate = 16 mV s^{-1}.

measurement resulted in a 59 mV/pH shift, consistent with a $2H^+2e^-$ transfer in the electrochemical oxidation of catechol. As shown in Figure 3.1, the oxidation starts with H_2C when the pH range is below 9.45 and finishes with Q corresponding to the observed slope of *ca.* 59 mV/pH.

When the pH is above 9.0, the oxidative peaks, $E_{p,ox}$, demonstrate possibly conflated chemical and electrochemical irreversible behaviour. For an electrochemically irreversible process,[44]

$$\frac{\partial E_{p,ox}}{\partial \mathrm{pH}} \simeq -2.303 \frac{mRT}{(n' + \beta_{n'+1})F} \tag{3.2}$$

so that theoretically $E_{p,ox}$ shifts by an amount of $0.059[m/(n' + \beta_{n'+1})]$ V per pH unit, where n' is the number of electrons transferred before the rate-determining step and $\beta_{n'+1}$ is the transfer coefficient of the rate-determining step.

In the pH region 9.0 < pH < 12.8, the experimental $E_{p,ox}$ shift is 40 mV/pH, consistent

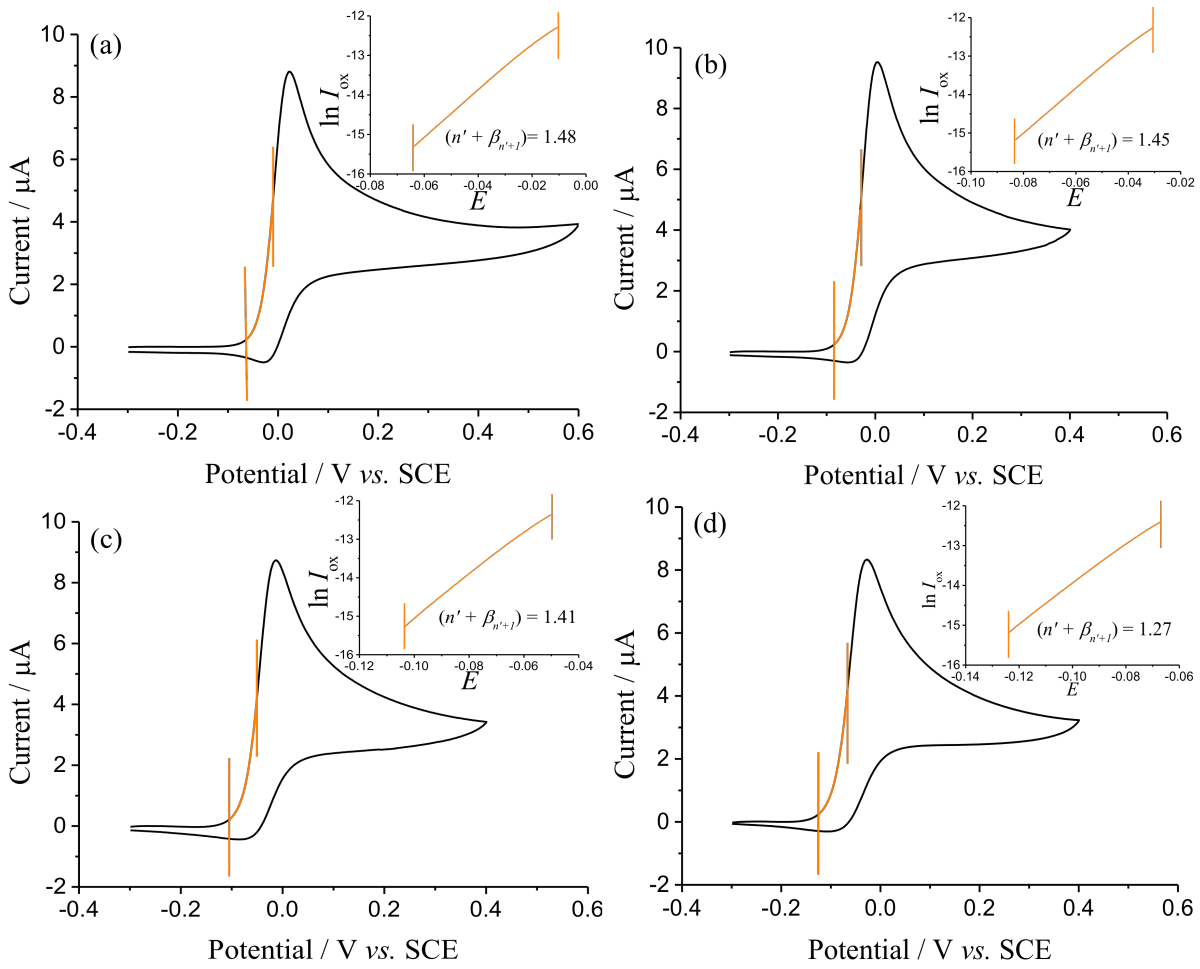

Figure 3.4: Cyclic voltammograms of 0.5 mM catechol in buffer solutions supported with 0.1 M KCl recorded on an unmodified glassy carbon electrode. (a) pH 9.5, (b) pH 10.0, (c) pH 10.5 and (d) pH 10.8. Scan rate = 16 mV s^{-1}. The forward scan region highlighted in orange was selected as the Tafel analysis region. Inlays are the corresponding Tafel plots, giving the values of transfer coefficient, $(n' + \beta_{n'+1}) = 1.40 \pm 0.09$.

with m and $(n' + \beta_{n'+1})$ being 1 and 1.49 ± 0.03, respectively. The value for $(n' + \beta_{n'+1})$ is close to those extracted from the Tafel plots (see Figure 3.4) with an average value of 1.40 ± 0.09. The values for m and $(n' + \beta_{n'+1})$ imply a $1H^+2e^-$ transfer, a monodeprotonation process accompanied by the loss of two electrons where the second electron transfer is the rate-determining step. Accordingly, the oxidation starts with CH as indicated in Figure 3.1.

The voltammetric data, both Tafel and peak potential against pH plot, are all consistent with a transition state (‡) located as shown in the "scheme of squares" (Figure

3.1) for the pH range between 9.0 and 12.8. The threshold pH values reflect the two pK_a values (pK_{a5} and pK_{a6}) as shown in Figure 3.1 and again in Figure 3.3.

The work next considers the pH range between 7.0 and 9.0. Considering the peak potential against pH plot in Figure 3.3, it can be seen that the oxidative peak, $E_{p,ox}$, varies with pH according to $\partial E_{p,ox}/\partial \mathrm{pH} \approx -0.092$ V while for the reductive peak, $\partial E_{p,red}/\partial \mathrm{pH} \approx 0$ V. The oxidative Tafel slope in this region was consistent with a value of $(n' + \beta_{n'+1})$ as 1.28. These data are again consistent with the transition state for the reaction being located as shown in Figure 3.1, corresponding to the second electron transfer.

Last we consider the pH range between 1.0 and 7.0 where there is a large separation (over 200 mV) between the oxidative and reductive peak potentials with both of these peak potentials apparently showing a Nernstian regime of 59 mV per decade. Tafel analysis showed an *apparent* transfer coefficient of $(n' + \beta_{n'+1}) \approx 1$ suggesting electrochemically reversible behaviour. It is clear that a change of mechanism has occurred relating to the behaviour at higher pH, and consideration of the pK_a values given in the "scheme of squares" (Figure 3.1) suggests that this is triggered by the protonated form, SH, of the semiquinone radical becoming stabilised relative to S (p$K_{a4} = 5$). The voltammetry hints at a behaviour where the H_2C/SH potential occurs at more positive values than the SH/Q potential - a phenomena commonly referred to as potential inversion[45–47]. Thus both the oxidative and reductive voltammetric peaks behave in an apparently electrochemically reversible fashion but with a wider potential separation than expected for a simple two electron transfer. Given these observations, the oxidative mechanism (for pH below 5.0) is likely to be:

$$\mathrm{H_2C} - \mathrm{e^-} - \mathrm{H^+} \rightleftarrows \mathrm{SH} \tag{3.3}$$

followed by disproportionation

$$2\mathrm{SH} \rightarrow \mathrm{H_2C} + \mathrm{Q} \tag{3.4}$$

Conversely for reduction we have

$$Q + e^- + H^+ \rightleftarrows SH \tag{3.5}$$

$$2SH \rightarrow H_2C + Q \tag{3.4}$$

These quantitative inferences were supported by DIGISIM modelling as reported in the following section.

3.3.2 Simulation for Apparent Parameters, k^0_{app} and $E^0_{f,app}$

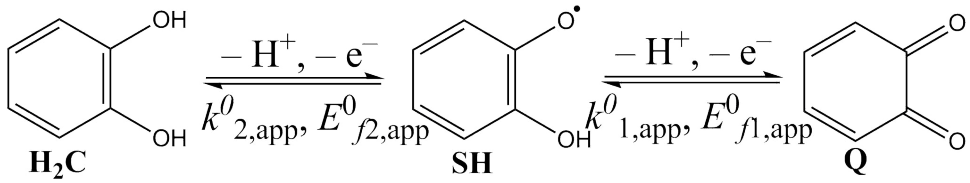

Figure 3.5: Two one-electron transfers of catechol (H_2C) along with the oxidation products, 1,2-benzoquinone (Q) and the semiquinone species (SH).

In order to focus on the $2H^+2e^-$ process in catechol oxidation, only the chemically reversible cyclic voltammograms at low pH range 1.0 $\sim$ 5.0 were studied quantitatively. Apparent parameters are introduced to the approximate, simplified mechanism proposed in Figure 3.5, where the apparent electrochemical rate constants (k^0_{app}) were set at 10 cm s^{-1} corresponding to the electrochemically fully reversible limit. Apparent formal potentials ($E^0_{f,app}$) can be derived *via* simulation using DIGISIM, as described in Chapter 2, Section 2.5. The equilibrium constant for disproportionation (K_{eq}) is generated by DIGISIM for the two $E^0_{f,app}$ values. The disproportionation rate constant (k_f) of SH was set at the diffusion controlled limit ($\sim 10^{10}$ dm^3 mol^{-1} s^{-1}). Transfer coefficients (α) of 0.5 and equality of all diffusion coefficients are assumed within our model.

To estimate the diffusion coefficient of catechol, cyclic voltammetry was run in 5 mM catechol in pH 2.9 buffered solution on a carbon fibre microdisc electrode (μ-CE, Figure

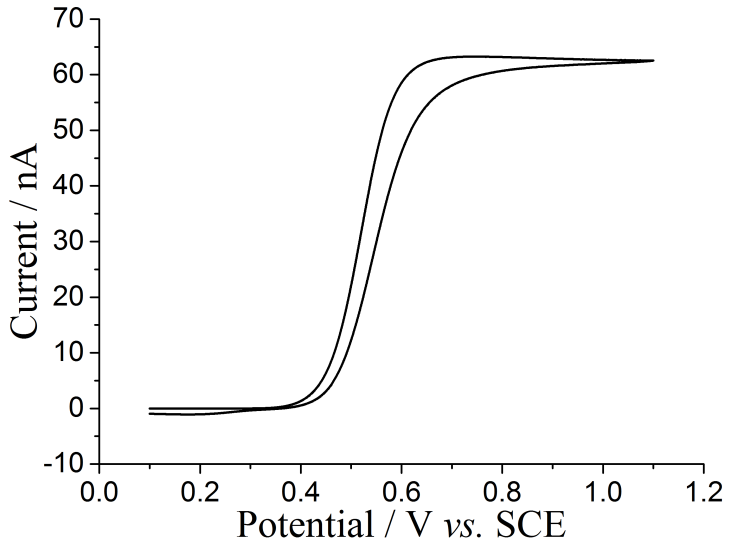

Figure 3.6: Cyclic voltammogram of 5 mM catechol in pH 2.9 buffered solutions supported with 0.1 M KCl recorded on a carbon microelectrode. Scan rate = 20 mV s^{-1}.

3.6). The potential was swept from 0 to 0.9 V (*vs.* SCE) and reversed to 0 V. The steady-state limiting current (I_{ss}) observed at 0.9 V was analysed by using Eq. 2.2 (see Chapter 2, Section 2.3.3) where the value of n is 2 for catechol oxidation. The resulting diffusion coefficient is $(1.1 \pm 0.1) \times 10^{-5}$ cm^2 s^{-1}. The high concentration of catechol examined here minimises capacitative current. The use of microelectrode limiting currents circumvents the effect from the associated electron transfer kinetics or separation between two redox potentials, which may occur in measurement *via* the use of a glassy carbon electrode (GCE).[27, 47] The value of diffusion coefficient is consistent with the previous literature reported values which range widely from 4.8×10^{-6} to 1.3×10^{-5} cm^2 s^{-1}[48–51].

The aim within simulations was to identify the dependence of peak potentials upon the separation between $E^0_{f1,app}$ and $E^0_{f2,app}$. Utilising the mechanism above, the experimental voltammetric response at variable scan rates (16 to 400 mV s^{-1}) from pH 1.0 to pH 5.0 could be simulated. $k^0_{1,app}$ and $k^0_{2,app}$ were set at the arbitrarily high value of 10 cm s^{-1} to ensure reversible electron transfer. A set of fitted data at the medium scan rate (144 mV s^{-1}) is shown in Figure 3.7. The error between the simulated (red circle) and the experimental (black line) voltammetries is less than 2% in peak potential and 9% in peak

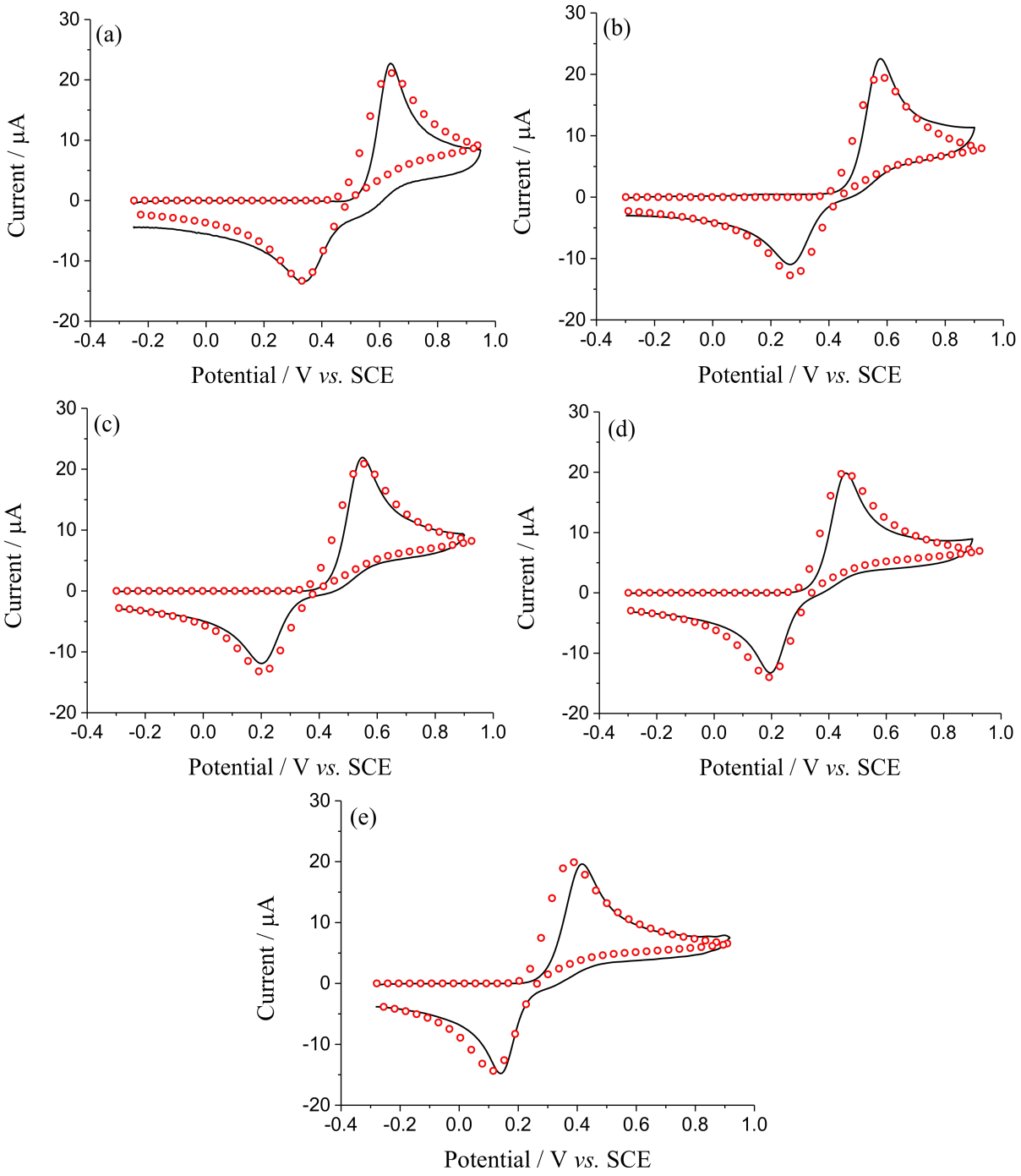

Figure 3.7: Comparison of the experimental (line) and simulated (circle) cyclic voltammograms of 0.5 mM catechol in pH buffered solutions. Simulations were optimised by adjusting apparent formal potentials, $E^0_{f1,app}$ and $E^0_{f2,app}$. Apparent electrochemical rate constants, $k^0_{1,app}$ and $k^0_{2,app}$ were set at the high reversible limit of 10 cm s^{-1}. (a) pH 1.0, (b) pH 2.0, (c) pH 2.9, (d) pH 4.0 and (e) pH 5.0. Scan rate = 144 mV s^{-1}.

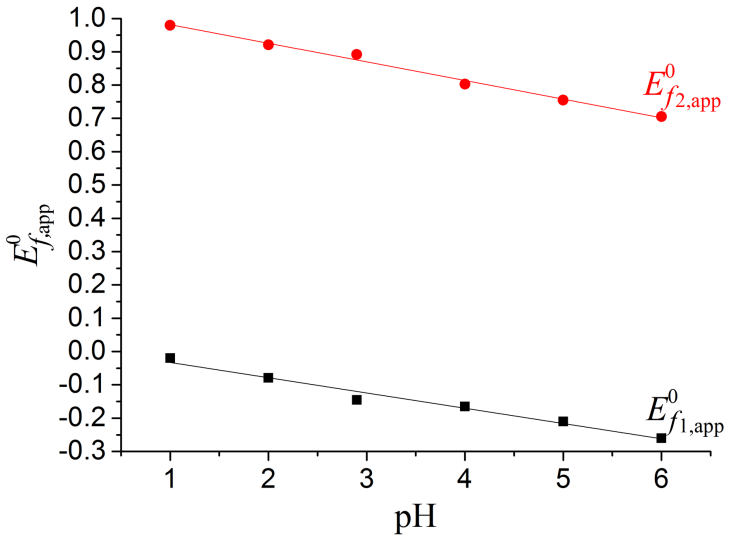

Figure 3.8: A plot of apparent formal potentials, $E^0_{f1,app}$ (■) and $E^0_{f2,app}$ (●), against pH. The lines of best fit yield the gradient for $E^0_{f1,app}$ and $E^0_{f2,app}$ being near -50 ± 10 mV/pH.

current. The simulated values of $E^0_{f,app}$ are listed in Table 3.1. It can be seen from Figure 3.8 that $E^0_{f1,app}$ is *ca.* 1.0 V more negative than $E^0_{f2,app}$.

pH	$E^0_{f1,app}$ **/ V *vs.* SCE**	$k^0_{1,app}$ **/ cm s^{-1}**	$E^0_{f2,app}$ **/ V *vs.* SCE**	$k^0_{2,app}$ **/ cm s^{-1}**
1.0	−0.020	10	0.980	10
2.0	−0.079	10	0.921	10
2.9	−0.145	10	0.892	10
4.0	−0.165	10	0.803	10
5.0	−0.21	10	0.755	10

Table 3.1: Simulated parameters for catechol redox in different pH solutions: apparent formal potentials ($E^0_{f1,app}$ and $E^0_{f2,app}$) and apparent electrochemical rate constants ($k^0_{1,app}$ and $k^0_{2,app}$).

The most important conclusion is that such a large potential inversion at low pH was found from similar work, such as *ca.* 0.7 V potential inversion on *p*-benzoquinone[20, 52–54] and *ca.* 0.31 V potential inversion on anthraquinone derivatives[27]. The lines of best fit of both $E^0_{f1,app}$ and $E^0_{f2,app}$ for catechol yield gradients of near -50 ± 10 mV/pH. In light of Eq. 3.1, these simulated results corroborate the proposed $1H^+1e^-$ within each net step over pH ranging from 1.0 to 5.0, recognising the approximation of the "scheme of squares" by Figure 3.5.

3.3.3 Apparent Electrocatalysis Using Alumina-Modified Glassy Carbon Electrodes

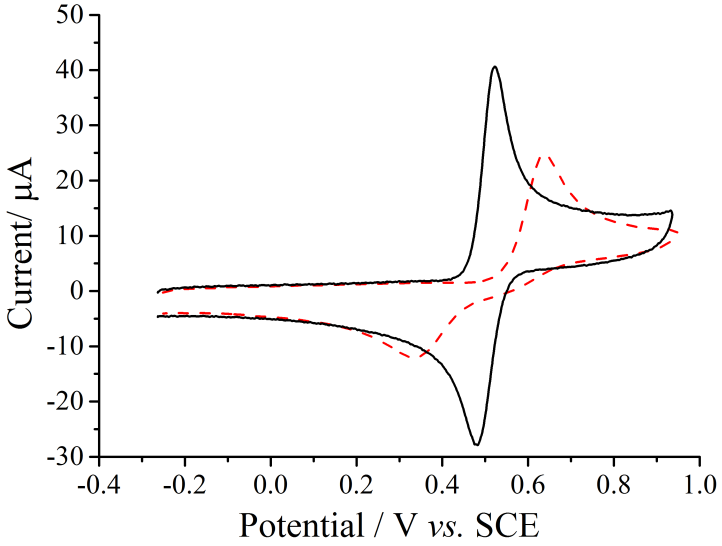

Figure 3.9: Comparison of cyclic voltammograms measured on an unmodified (dashed line) and alumina-modified (solid line) glassy carbon electrode, of 0.5 mM catechol in pH 1.0. Scan rate = 144 mV s^{-1}.

Next the effect of surface modification of the glassy carbon electrode (GCE) with alumina was studied in light of literature observations[38, 55]. To obtain an alumina-modified suface, the GCE was polished by using alumina slurry of decreasing particle sizes (1.0 $\sim$ 0.05 μm). After cleaning by sonication, the electrode was abrasively modified by using 1.0 μm alumina, rinsed with water and dried under nitrogen before each measurement. Figure 3.9 shows the cyclic voltammetry of 0.5 mM catechol in pH 1.0 solution measured on an unmodified GCE (dashed line) in comparison with that on a modified GCE (solid line) at a scan rate of 144 mV s^{-1}. It can be seen that ΔE_p is reduced from *ca.* 300 mV to *ca.* 40 mV, whereas the E_{mid} stays at *ca.* 0.50 V *vs.* SCE. Thus, the overall thermodynamics of the CH_2 to Q process are unchanged, but the reaction mechanism has clearly been altered significantly, possibly usefully in the context of pH sensing.

Similar observations of the reduced ΔE_p were found at higher pH, as depicted in Figure 3.10 and 3.11. The electrochemical response of catechol over the pH range from

1.0 to 14.0 was recorded by using an alumina-modified GCE, as shown in Figure 3.10a and b. The corresponding $E_{p,ox}$ (▲), $E_{p,red}$ (▼) and E_{mid} (■) are plotted against pH in Figure 3.11. The small ΔE_p seen at pH values below pH 9.0 is all suggestive of an altered mechanism on the modified GCE (Figure 3.11). As noted earlier, above pH 9.0 the system will be insensitive to further redox processes after the chemically irreversible step, and hence the reductive back peak is missing from the voltammogram. The inlay of Figure 3.11 depicts E_{mid} below pH 9.0 and $E_{p,ox}$ above pH 9.0 measured on the modified GCE (red symbols) overlaid with the corresponding measurements on the unmodified GCE (green symbols). This comparison further supports the finding that catechol oxidation is unchanged thermodynamically when studied at an alumina-modified GCE.

A "transfer experiment" was conducted to further examine the adsorption of catechol to the alumina on the electrode surface. 2g of '1.0 μm' alumina was stirred in 50 mL of 2 mM catechol in pH 3.0 buffered solution for 3 h, allowing catechol to be fully adsorbed by the alumina. The milky mixture was then left still for 3 min, which allows the alumina to settle under gravity. This catechol-alumina slurry was transferred to a polishing pad for GCE abrasive modification (as described in Chapter 2, Section 2.3.3). After rinsing with water and drying with nitrogen, the electrode was immerged into a pH 3.0 buffer. Cyclic voltammetry was run from -0.3 V to 0.9 V and reversed to -0.3 V for two consecutive scans at a scan rate of 144 mV s^{-1}, as shown in Figure 3.12 (black solid line: first, red solid line: second scan). For comparison, a 'blank' voltammogram was recorded in the same solution on a clean-alumina-modified GCE (Figure 3.12, black dashed line: first scan, red dashed line: second scan). It is apparent that the oxidation at *ca.* 0.42 V and the reduction at *ca.* 0.35 V are the results of catechol redox process, which demonstrates the strong adsorption of catechol to the alumina. Moreover, $E_{p,ox}$ and $E_{p,red}$ in both scans remain unshifted, implying that catechol is substantially retained on the electrode surface even after electrolysis. The slightly reduced $I_{p,ox}$ and $I_{p,red}$ in the second scan is due to

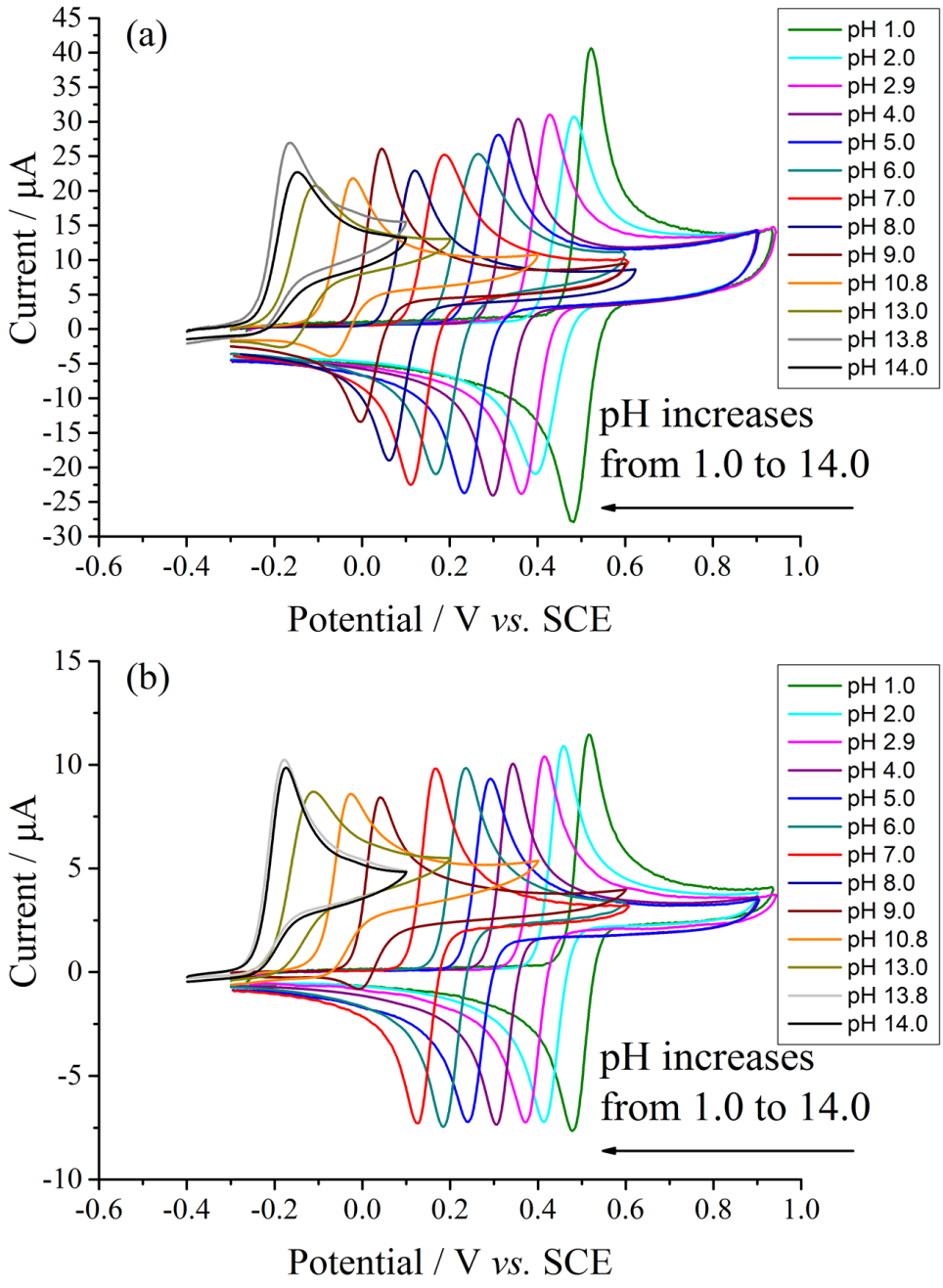

Figure 3.10: Voltammograms of 0.5 mM catechol in pH 1.0 $\sim$ 14.0 buffers recorded on an alumina-modified glassy carbon electrode at a scan rate of (a) 144 mV s^{-1} and (b) 16 mV s^{-1}, with voltammogram at each pH labelled.

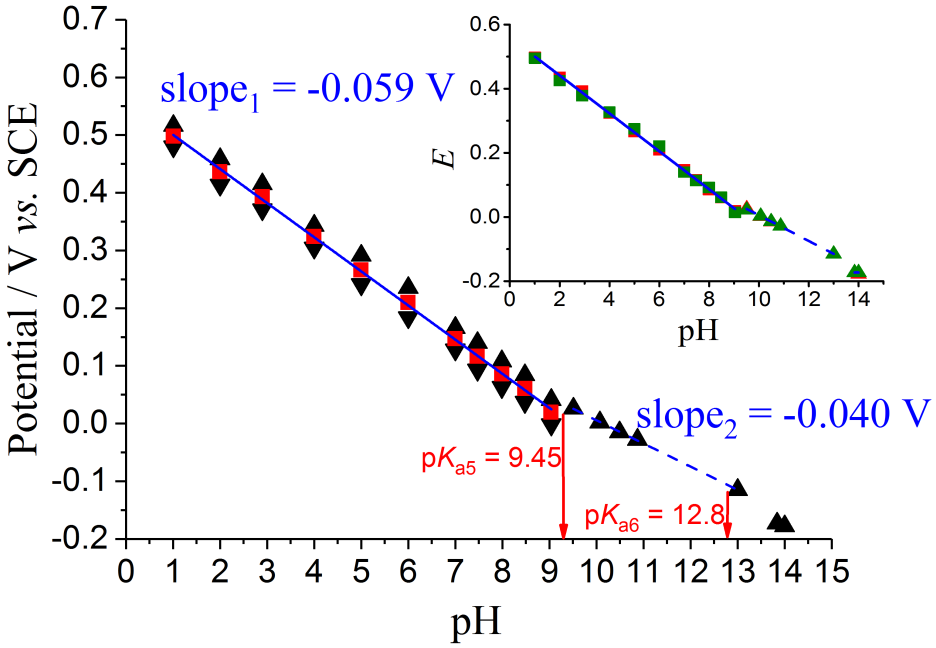

Figure 3.11: Plots of oxidative peak potential (▲), reductive peak potential (▼) and midpoint potential (■, red symbols) against different pH values, of voltammograms on an alumina-modified glassy carbon electrode. Inlay depicts the comparison with the data measured on an unmodified glassy carbon electrode (green symbols). Scan rate = 16 mV s^{-1}.

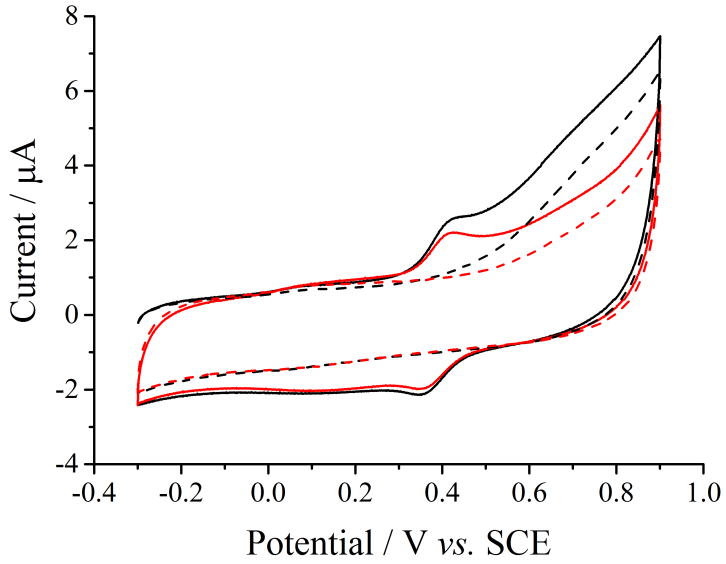

Figure 3.12: Comparison of cyclic voltammograms measured on a catechol-alumina-modified glassy carbon electrode (solid line) and on a clean-alumina-modified glassy carbon electrode (dashed line) of pH 3.0 buffer. Black solid and dashed lines correspond to the first scan, while red ones corresponds to the second scan. Scan rate = 144 mV s^{-1}.

the background current drop (see dashed lines).

3.4 Conclusions

In this chapter, the $2e^-$ $2H^+$ oxidation of catechol has been investigated from two aspects. Fisrt, the electrochemical redox of catechol was studied voltammetrically in the pH range from 1.0 to 14.0 using a glassy carbon electrode. Through the study of potentials and currents together with Tafel analysis, the likely transition state and redox mechanism have been established in the "scheme of squares" model. Second, modification of the glassy carbon electrode surface with sparse coverages of alumina particles was reported. Strong apparent catalysis of catechol redox process has been demonstrated at low pH. The cause of this apparent catalysis by adsorbed alumina will be elaborated in the next chapter.

References

[1] Lin, Q.; Li, Q.; Batchelor-McAuley, C.; Compton, R. G. *Journal of Physical Chemistry C* **2015**, *119*, 1489–1495.

[2] Anden, N. E.; Leander, S. *Journal of Neural Transmission* **1979**, *44*, 1–12.

[3] Figueiredo, E. C.; Tarley, C. R. T.; Kubota, L. T.; Rath, S.; Arruda, M. A. Z. *Microchemical Journal* **2007**, *85*, 290–296.

[4] Lee, B. L.; Ong, H. Y.; Shi, C. Y.; Ong, C. N. *Journal of Chromatography B: Biomedical Sciences and Applications* **1993**, *619*, 259–266.

[5] Cui, H.; He, C.; Zhao, G. *Journal of Chromatography A* **1999**, *855*, 171–179.

[6] Lourenço, E. L. B.; Ferreira, A.; Pinto, E.; Yonamine, M.; Farsky, S. H. P. *Chromatographia* **2006**, *63*, 175–179, Chroma.

[7] Boulton, A. A.; Baker, G. B.; Adams, R. N. *Voltammetric Methods on Brain Systems*; Humana Press: Totowa NJ, 1995.

[8] Ewing, A. G.; Strein, T. G.; Lau, Y. Y. *Accounts of Chemical Research* **1992**, *25*, 440–447.

[9] Adams, R. N.; Adams, R. N. *Progress in Neurobiology* **1990**, *35*, 297–311.

[10] Kolthoff, I. M.; Lingane, J. J. *Polarography*, 2nd ed.; Interscience: New York, 1952; Vol. I, Chapters XIV and XV; II, Chapter XL.

[11] Lu, M.; Compton, R. G. *Analyst* **2014**, *139*, 2397–2403.

[12] Kristensen, H. B.; Salomon, A.; Kokholm, G. *Analytical Chemistry* **1991**, *63*, 885A–891A.

[13] Skoog, D. A.; West, D. M.; Holler, F. J.; Crouch, S. R. *Fundamentals of Electroanalytical Chemistry*, 8th ed.; 2004.

[14] Xiong, L.; Batchelor-McAuley, C.; Compton, R. G. *Sensors and Actuators B: Chemical* **2011**, *159*, 251–255.

[15] Trumpower, B. L. *Function of Quinones in Energy Conserving Systems*; Academic Press: New York, 1982.

[16] Steenken, S.; O'Neill, P. *The Journal of Physical Chemistry* **1977**, *81*, 505–508.

[17] Steenken, S.; Neta, P. *The Journal of Physical Chemistry* **1979**, *83*, 1134–1137.

[18] Land, E. J.; Porter, G. *Proceedings of the Chemical Society* **1960**, 84–85.

[19] Handa, T. *Bulletin of the Chemical Society of Japan* **1955**, *28*, 483–489.

[20] Laviron, E. *Journal of Electroanalytical Chemistry and Interfacial Electrochemistry* **1984**, *164*, 213–227.

[21] Deakin, M. R.; Wightman, R. M. *Journal of Electroanalytical Chemistry and Interfacial Electrochemistry* **1986**, *206*, 167–177.

[22] Deakin, M. R.; Kovach, P. M.; Stutts, K. J.; Wightman, R. M. *Analytical Chemistry* **1986**, *58*, 1474–1480.

[23] Jacq, J. *Journal of Electroanalytical Chemistry and Interfacial Electrochemistry* **1971**, *29*, 149–180.

[24] Laviron, E. *Journal of Electroanalytical Chemistry and Interfacial Electrochemistry* **1983**, *146*, 15–36.

[25] Smith, E. T.; Davis, C. A.; Barber, M. J. *Analytical Biochemistry* **2003**, *323*, 114–121.

[26] Cable, M.; Smith, E. T. *Analytica Chimica Acta* **2005**, *537*, 299–306.

[27] Batchelor-McAuley, C.; Li, Q.; Dapin, S. M.; Compton, R. G. *The Journal of Physical Chemistry B* **2010**, *114*, 4094–4100.

[28] Mu, S. *Biosensors and Bioelectronics* **2006**, *21*, 1237–1243.

[29] Ghanem, M. A. *Electrochemistry Communications* **2007**, *9*, 2501–2506.

[30] Su, L.; Mao, L. *Talanta* **2006**, *70*, 68–74.

[31] Nasr, B.; Abdellatif, G.; Cañizares, P.; Sáez, C.; Lobato, J.; Rodrigo, M. A. *Environmental Science & Technology* **2005**, *39*, 7234–7239.

[32] Wang, S. G.; Li, Y. Q.; Zhao, X. J.; Wang, J. H.; Han, J. J.; Wang, T. *Diamond and Related Materials* **2007**, *16*, 248–252.

[33] Mersal, G. A. *International Journal of Electrochemical Science* **2009**, *4*, 1167–1177.

[34] Cabaniss, G. E.; Diamantis, A. A.; Murphy, W. R.; Linton, R. W.; Meyer, T. J. *Journal of the American Chemical Society* **1985**, *107*, 1845–1853.

[35] Poon, M.; McCreery, R. L. *Analytical Chemistry* **1986**, *58*, 2745–2750.

[36] DuVall, S. H.; McCreery, R. L. *Analytical Chemistry* **1999**, *71*, 4594–4602.

[37] Allred, C. D.; McCreery, R. L. *Analytical Chemistry* **1992**, *64*, 444–448.

[38] Zak, J.; Kuwana, T. *Journal of the American Chemical Society* **1982**, *104*, 5514–5515.

[39] DuVall, S. H.; McCreery, R. L. *Journal of the American Chemical Society* **2000**, *122*, 6759–6764.

[40] Wang, J.; Pumera, M.; Chatrathi, M. P.; Escarpa, A.; Konrad, R.; Griebel, A.; Dörner, W.; Löwe, H. *Electrophoresis* **2002**, *23*, 596–601.

[41] Papouchado, L.; Petrie, G.; Adams, R. N. *Journal of Electroanalytical Chemistry and Interfacial Electrochemistry* **1972**, *38*, 389–395.

[42] Kiani, A.; Raoof, J.-B.; Nematollahi, D.; Ojani, R. *Electroanalysis* **2005**, *17*, 1755–1760.

[43] Ojani, R.; Raoof, J. B.; Hosseinzadeh, R.; Alinezhad, A. *Asian Journal of Chemistry* **2008**, *20*, 5863–5872.

[44] Compton, R. G.; Banks, C. E. *Understanding Voltammetry, 2nd edition*; Imperial College Press, 2011.

[45] Evans, D. H.; Hu, K. *Journal of the Chemical Society, Faraday Transactions* **1996**, *92*, 3983–3990.

[46] Evans, D. H. *Acta Chemica Scandinavica* **1998**, *52*, 194–197.

[47] Batchelor-McAuley, C.; Compton, R. G. *Journal of Electroanalytical Chemistry* **2012**, *669*, 73–81.

[48] Lawrence, N. S.; Davis, J.; Compton, R. G. *Talanta* **2001**, *53*, 1089–1094.

[49] de Cássia Silva Luz, R.; Damos, F. S.; de Oliveira, A. B.; Beck, J.; Kubota, L. T. *Sensors and Actuators B: Chemical* **2006**, *117*, 274–281.

[50] Raoof, J. B.; Ojani, R.; Nematollahi, D.; Kiani, A. *International Journal of Electrochemical Science* **2009**, *4*, 810–819.

[51] Di Fusco, M.; Favero, G.; Mazzei, F. *The Journal of Physical Chemistry B* **2011**, *115*, 972–979.

[52] Ilan, Y. A.; Czapski, G.; Meisel, D. *Biochimica et Biophysica Acta (BBA) - Bioenergetics* **1976**, *430*, 209–224.

[53] Bailey, S. I.; Ritchie, I. M.; Hewgill, F. R. *Journal of the Chemical Society, Perkin Transactions 2* **1983**, 645–652.

[54] Laviron, E. *Journal of Electroanalytical Chemistry and Interfacial Electrochemistry* **1984**, *169*, 29–46.

[55] Zak, J.; Kuwana, T. *Journal of Electroanalytical Chemistry and Interfacial Electrochemistry* **1983**, *150*, 645–664.

Chapter 4

Altered Electrochemistry at Graphene- or Alumina-Modified Electrodes: Catalysis *vs.* Electrocatalysis in Multistep Electrode Processes

The two-electron, two-proton oxidation of catechol has been observed in the previous chapter to undergo apparent catalysis by adsorbed alumina on the glassy carbon electrodes. In this chapter, the cause of such an apparent catalysis is examined by using glassy carbon electrodes modified with submonolayer quantities of alumina or graphene. While the voltammetric behaviour superficially hints at a change of electron transfer rate, an alternative explanation in terms of the changed thermodynamics of the intermediate species is advanced and rationalised.

This work has been published in *The Journal of Physical Chemistry C*[1] and was performed in collaboration with Mr. Jeffrey Poon, Dr. Christopher Batchelor-McAuley, Mr. Chris Salter and Dr. Colin Johnston (Department of Materials, University of Oxford). Mr. Jeffrey Poon provided experimental results and simulations with respect to graphene. Dr. Christopher Batchelor-McAuley helped with the interpretation of data. Mr. Chris Salter and Dr. Colin Johnston obtained the scanning electron microscope images.

4.1 Introduction

A vast effort is currently being undertaken with respect to seeking modified electrodes, so as to "improve" the electrochemical response of less than optimal surfaces. In many cases this involves the modification of relatively low cost electrodes, such as those made of carbon. Small quantities of a diverse range of materials, often nanomaterials, are used to bring about apparent "electrocatalysis". Both carbon nanotubes (single-walled[2], multiwalled[3], doped[4], etc.) and graphene[5, 6] are highly popular nanomaterials, and have been championed as especially effective for this purpose.[7]

Although the ultimate use of the modified electrodes would often be in energy transformation technologies, such as batteries and fuel cells, the method adopted for the evaluation of potential electrocatalysts is almost exclusively voltammetry. In this case, the electrode process of interest:

$$\mathrm{A} \pm \mathrm{e}^- \rightleftarrows \mathrm{B} \tag{4.1}$$

is examined in an electrochemical cell through the variation of current with applied potential, the latter usually applied in the form of "cyclic voltammetry" with a triangular potential waveform. The voltammetry generates a peak in the forward scan corresponding to the conversion of A to B local to the electrode and then a reverse scan used to bring about the reverse transformation, namely of B to A. Typically the separation of the two peaks in terms of voltage, ΔE_p, is used as a measure of the electron transfer rate. Assuming A and B are both solution-phase species free to diffuse, then the limit of ΔE_p corresponding to fast electron transfer kinetics (relative to prevailing mass transport rates) gives the so-called "reversible" limit and a peak-to-peak separation of[8, 9]

$$\Delta E_p = 2.218\frac{RT}{F} = 57 \text{ mV (298 K)} \tag{4.2}$$

For slower electron transfer kinetic, in the "irreversible" limit

$$\Delta E_p = \frac{RT}{\alpha F} \ln(\nu) + \text{constant} = \frac{25.7}{\alpha} \ln(\nu) + \text{constant (in mV, 298 K)} \quad (4.3)$$

where α (or β, $\beta = 1-\alpha$) is the transfer coefficient for the process occurring on the forward going reaction, R is the ideal gas constant (8.314 J K^{-1} mol^{-1}), T is the temperature (K), F is the Faraday constant (96 485 C mol^{-1}), ν is the scan rate; and α corresponds to a reduction and β to an oxidation in the Butler-Volmer parameterisation.[10] It is important to note that it is the peak-to-peak separation which indicates fast or slow electron transfer rather than the size of the current peak; the change in the latter for a simple one-electron transfer is merely *ca.* 30% between the fully reversible and irreversible limits.[11]

Experimental analysis is however not usually as straightforward in practice as the above implies. Underpinning this is the key notion that "fast" and "slow" electron transfer refers to that relative to the local, prevailing rates of mass transport at the relevant electrode surface as quantified by the mass transport coefficient, m_T (cm s^{-1}).[8] It follows that "reversibility" is not only an intrinsic property of the A/B redox couple of interest, but also of the electrode used to probe the voltammetry and indeed the selected voltage scan rate; put simply the rates of mass transport increase from macro- to microelectrodes (and to nanoelectrodes) and also as the voltage scan rate increases. Hence the degree of reversibility decreases, and electron transfer kinetics are "apparently" slower. Furthermore, the change between the reversible and the irreversible limits also reflects the electrode surface morphology. Eq. 4.2 and 4.3 assume semi-infinite diffusion to a planar electrode. Any change in these mass transport conditions can indirectly give the *illusion* of altered electrode kinetics.

It has been pointed out that there can be extreme situations of altered mass transport profoundly affecting the apparent electron transfer kinetics when electrodes are modified with relatively thick porous layers of conductive material.[12–15] Examples might include

graphene or carbon nanotubes, and "relatively" thick indicates the key distance scale is that of the diffusion layer to the unmodified electrode.[14, 16] Under these conditions the voltammetric responses reflect first a "thin-layer" contribution for the electrolysis of material occluded within the porous, conductive layer, and second a contribution from diffusion from bulk solution to the surface of the layer. The facilitated mass transport occurring *via* the first mode is such that the voltage required for electrolysis (and the generation of a voltammetric peak) is often less than that required under conditions of semi-infinite diffusion to a planar electrode; voltammetry under thin-layer conditions is more "reversible". Indeed under extreme conditions it is even possible to see the two peaks for an A/B couple in voltammograms, one from each mode of transport.[17] Considerations of electrode modification with graphene[18, 19] and with various types of carbon nanotubes[12, 13, 15, 20, 21], has suggested that the altered mass transport resulting from porous conducting layers used to modify the electrodes has played a significant role in possibly overestimating the electrocatalytic effect of the modifying layers. Indeed Punckt credibly asserts that this is *the* dominant effect seen in graphene modified electrode, and the major role of the modification lies in altered mass transport rather than in enhanced electron transfer kinetics.[18]

Three related points are important. First, the modification can be beneficial even if the mass transport is the dominant effect; specifically since in the thin-layer reversible limit the voltammetric peaks shift to occur at potentials reflecting the formal potential of the various A/B couples, the modification can then usefully improve analytical selectivity[17, 18] and different voltammetric peaks which are superimposed under purely diffusional conditions can become resolved. Second, even if the "modifying" layer is not thick in size but merely "roughens" the electrode surface, then measurable effects can be seen.[22] Equations have been developed for the effective electrode rate constants for both porous layers and rough surfaces.[22, 23] Third, the use of hydrodynamic electrodes does not in

itself overcome the porous/nonporous issue but may give the impression of minimising the effects[24, 25]; this is particularly noteworthy in the case of the search for oxygen reduction catalysts[26], where rotating disc electrodes are often employed, usually in a double-electrode (ring-disc) configuration to probe the intermediacy of hydrogen peroxide or not, and have established two- or four-electron processes.[14, 26]

Most studies of electron transfer processes at nanocarbon-modified electrodes have focused on simple one-electron processes such as the $[Ru(NH_3)_6]^{2+/3+}$, $[Fe(CN)_6]^{2+/3+}$ redox couples. Notwithstanding the potential complexity of even the relatively simple systems as discussed above, it is of considerable interest to extend the discussion to a consideration of multistep electron process, not least since systems such as O_2/MeOH, O_2/H_2O, N_2H_4/N_2, etc. are often the ultimate targets for the design of improved electron transfer catalysts. Moreover a multistep process offers an additional scope for mechanistic complexity and the probability of say graphene or carbon nanotube modifications acting in hitherto unexpected roles.

The two-electron, two-proton oxidation of catechol (1,2-hydroxybenzene, H_2C) has been selected here as a model multistep process. The process focuses on 1,2-benzoquinone (Q) as a product (Figure 4.1). The main reason for this choice is because the mechanism

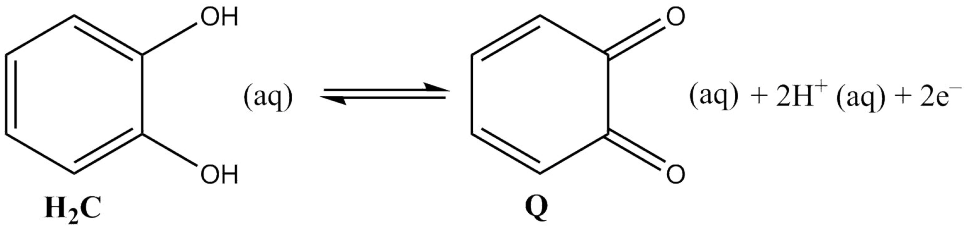

Figure 4.1: Two-proton, two-electron oxidation of catechol.

of this process at *unmodified* glassy carbon electrodes has been studied in depth *via* a (partial) "scheme of squares" type analysis (Chaper 3). Specifically the process proceeds *via* a semiquinone radical/radical ion intermediate (SH), and the voltmmetry suggests a behaviour where the H_2C/SH potential occurs at more positive values than the SH/Q

potential. This phenomenon is often referred to as a "potential inversion" and has been seen in some other quinone systems but not in all.[27] In the case of catechol both the oxidation and reduction peaks behave voltammetrically in a seemingly electrochemically reversible manner but with a significantly wider peak-to-peak separation than expected for a single Nernstian two-electron transfer. In particular for pH 5.0, the following oxidation process was suggested, supported by DIGISIM (see Chapter 2, Section 2.5) modelling:

$$H_2C - e^- - H^+ \rightleftarrows SH \tag{4.4}$$

$$2SH \rightarrow H_2C + Q \tag{4.5}$$

For the reverse, reductive process:

$$Q + e^- + H^+ \rightleftarrows SH \tag{4.6}$$

$$2SH \rightarrow H_2C + Q \tag{4.5}$$

Previously, Chapter 3 reported the apparent modification of the above mechanism by alumina particles used to modify the glassy carbon electrode surface. This chapter builds on these preliminary results and also makes comparison with graphene modified electrodes. Qualitatively, but not quantitatively, similar behaviour is seen with the two systems which is interesting since the alumina is, unlike graphene, not electronically conducting and moreover extremely small coverages of alumina are found to be effective. The systems individually and comparatively provide a new insight into a possible route for electrode modifier effects in changing the apparent electrode kinetics of a multistep redox system.

4.2 Experimental

Details about the chemical reagents and buffer solutions here utilised can be found in Chapter 2, Section 2.1. The structures of catechol (H_2C) and its oxidation product, 1,2-benzoquinone (Q) are shown in Figure 4.1. 0.1 M KCl was used as the supporting electrolyte. The electrochemical measurements were carried out using an Autolab PG-STAT101 potentiostat. Representative voltammograms are all baseline corrected for ease of comparison. Two glassy carbon electrodes (GCEs) were used one at a time as working electrodes. One electrode (electrode 1) was used exclusively for alumina electrode modification and the other (electrode 2) was used exclusively for graphene electrode modification. This was to avoid cross contamination of the modified electrode by another modification agent. The surface of working electrodes was prepared as described in Chapter 2, Section 2.3.3. A saturated calomel electrode was used as the reference electrode, and a platinum mesh as the counter electrode. Cyclic voltammetric responses were simulated by Mr. Jeffrey Poon using DIGISIM (see Chapter 2, Section 2.5). Scanning electron microscope images were obtained by Mr. Chris Salter and Dr. Colin Johnston (SEM, see Chapter 2, Section 2.4).

4.3 Results and Discussion

This work first reports the voltammetry of catechol with unmodified and with alumina-modified glassy carbon electrodes (GCEs). Second, the corresponding voltammetry at a graphene modified GCE is discussed, and similar effects are observed as for alumina. Third, the graphene voltammetry is analysed, which shows the causes, other than changed electrode kinetic, mass transport may operate in this multistep process.

4.3.1 Catechol Oxidation at Alumina-Modified Electrodes

As described in Chapter 2, Section 2.3.3, to obtain an unmodified surface, the GCE was polished using diamond spray of decreasing particle sizes. For a modified surface of electrode 1, the GCE was first polished on an alumina slurry of decreasing particle sizes. Afterwards the electrode was cleaned by sonication. The electrode was then abrasively modified by using 1.0 μm alumina. The surface was then rinsed with water and blow-dried with nitrogen.

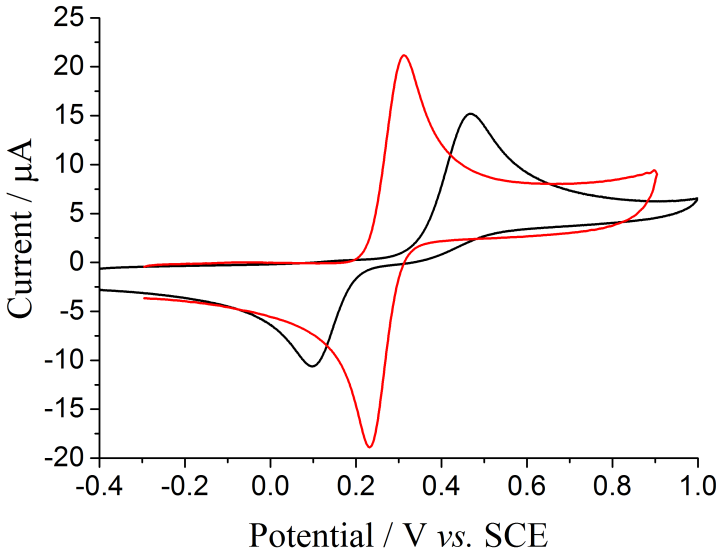

Figure 4.2: Representative voltammogram taken in 0.50 mM catechol in pH 5.0 buffer. Red: alumina-modified glassy carbon electrode. Black: unmodified glassy carbon electrode. Scan rate = 100 mV s^{-1}.

Figure 4.2 shows a voltammogram of 0.50 mM catechol in pH 5.0 buffer measured at a scan rate of 100 mV s^{-1} using an unmodified GCE (black line). Chapter 3 has shown that the scan rates, concentration and pH behaviour of this system are consistent with a potential inversion in which $E_{H_2C/SH} - E_{SH/Q} = 965$ mV. The following other parameters were found to model the system when simulated using DIGISIM: $k^0 = 10$ cm s^{-1}, $\alpha = 0.50$, diffusion coefficients of H_2C as $(1.1 \pm 0.1) \times 10^5$ cm^2 s^{-1}, and disproportionation rate constant (k_f) of SH as at the diffusion controlled limit ($\sim 10^{10}$ dm^3 mol^{-1} s^{-1}). Figure 4.2 (red line) shows the corresponding voltammogram measured with a GCE surface modified

with a sparse coverage of alumina.

Comparison of voltammograms across the full pH range was also obtained (from 1.0 to 13.0, see Figure 4.3). Figure 4.4 shows voltammograms recorded using an alumina-modified GCE at different scan rates. Figure 4.5 demonstrates that the corresponding oxidative peak current is proportional to the square root of the scan rate. It indicates that oxidation of catechol follows diffusional behaviour, which will be further discussed later.

Figure 4.6 shows comparison of the peak potentials and midpoint potentials. It can be seen that the voltammogram (Figure 4.2) of the unmodified electrode with its widely separated peaks ($\sim 385 \pm 7$ mV) is replaced by one in which the peak-to-peak separation (ΔE_p) is much reduced ($\sim 80 \pm 4$ mV) at the alumina-modified electrode surface. ΔE_p can also be seen reduced in the pH range from 1.0 to pH 9.0 (Figure 4.6). Figure 4.7 shows the SEM image of the unmodified and alumina-modified surface; it can be seen that only *ca.* 2% of the surface is covered with particles of *ca.* 1 μm diameter which are, on average, 11 ± 4 μm apart. It is evident that the tiny amount of alumina has a major influence on the observed voltammogram, while the extent of coverage and the surface roughness resulting from the modification can have only minimal influence on the mass transport prevailing to the electrode surface. Moreover the alumina is nonconducting so it cannot directly interfere the voltammetry. It is likely[28] that the role of the alumina is to provide adsorption sites which modify the reaction pathway. Note however the midpoint potential of the voltammograms in Figures 4.2 (black and red) are the same ($E_{mid} = 0.278 \pm 0.006$ V) to within the experimental error suggesting that the process

$$H_2C - 2e^- - 2H^+ \rightleftarrows Q \tag{4.7}$$

remains overall essentially unchanged thermodynamically. It is likely therefore that the adsorption involves the intermediate semiquinone species.

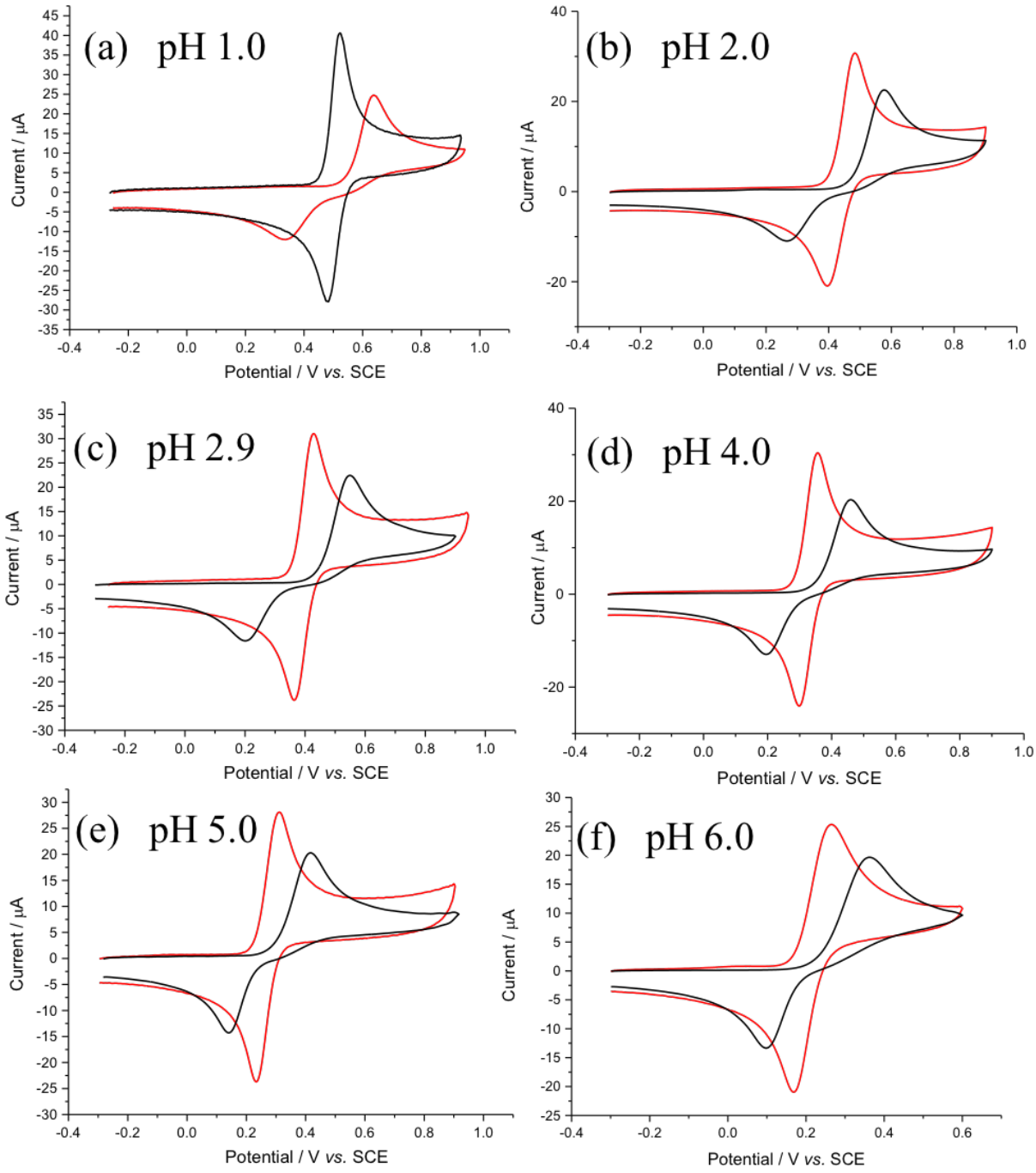

Figure 4.3: Voltammograms of 0.5 mM catechol in pH 1.0 $\sim$ 6.0 buffers. Red: alumina-modified glassy carbon electrode. Black: unmodified glassy carbon electrode. Scan rate = 144 mV s^{-1}.

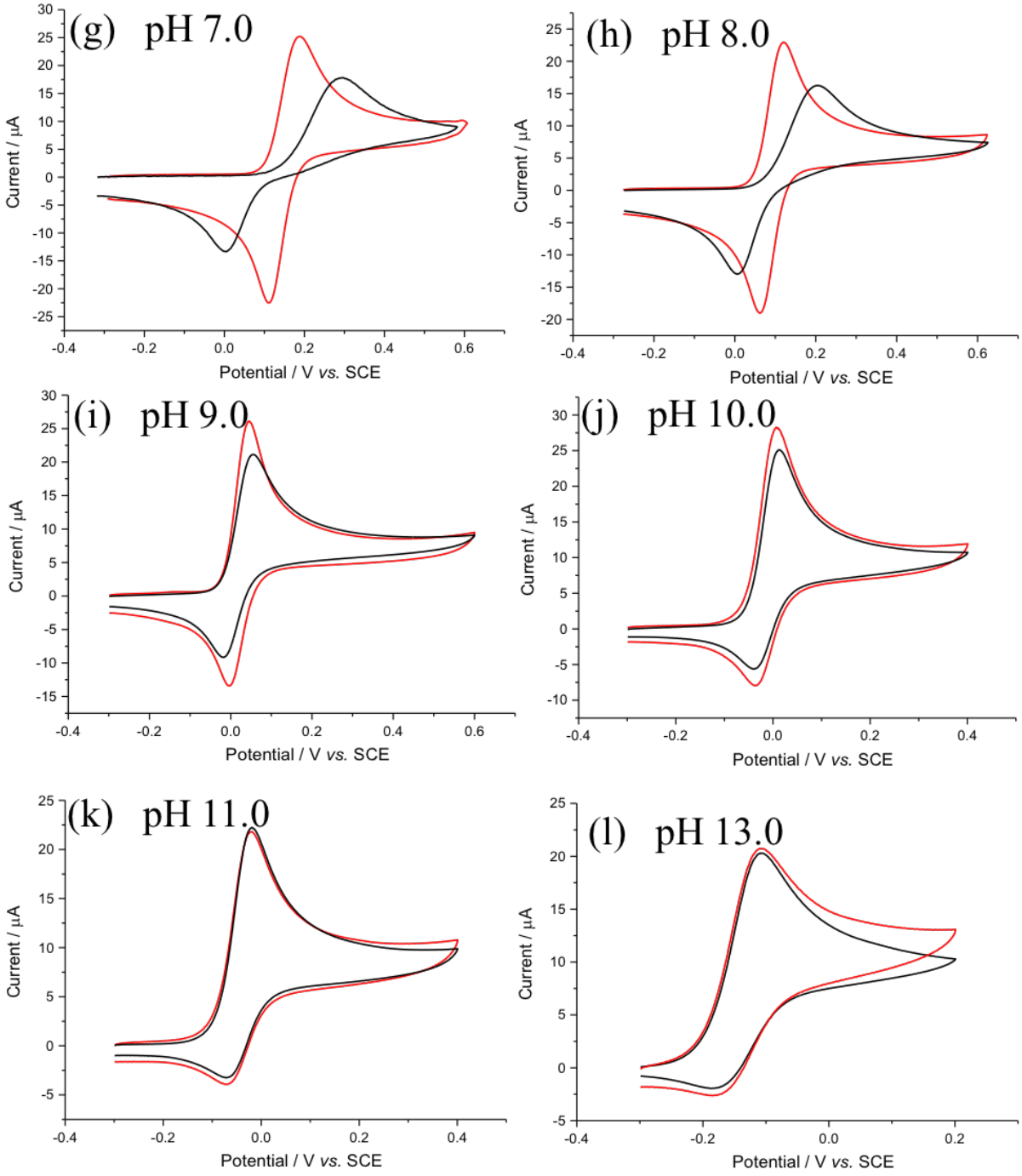

Figure 4.3: Voltammograms of 0.5 mM catechol in pH 7.0 $\sim$ 13.0 buffers. Red: alumina-modified glassy carbon electrode. Black: unmodified glassy carbon electrode. Scan rate = 144 mV s^{-1}.

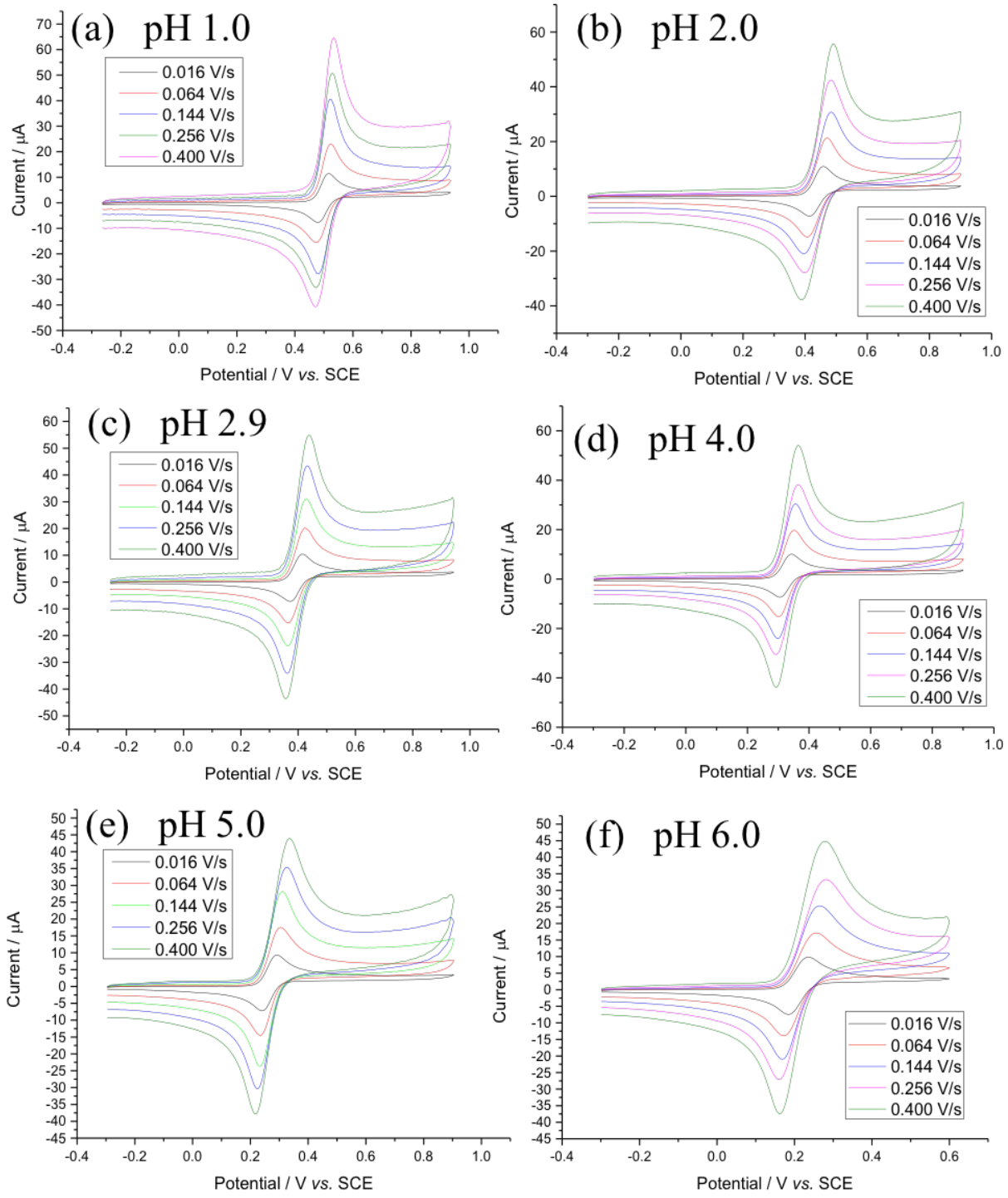

Figure 4.4: Voltammograms of 0.5 mM catechol in pH 1.0 $\sim$ 6.0 buffers at an alumina-modified glassy carbon electrode. Scan rates = 16, 64, 144, 256, 400 mV s^{-1}.

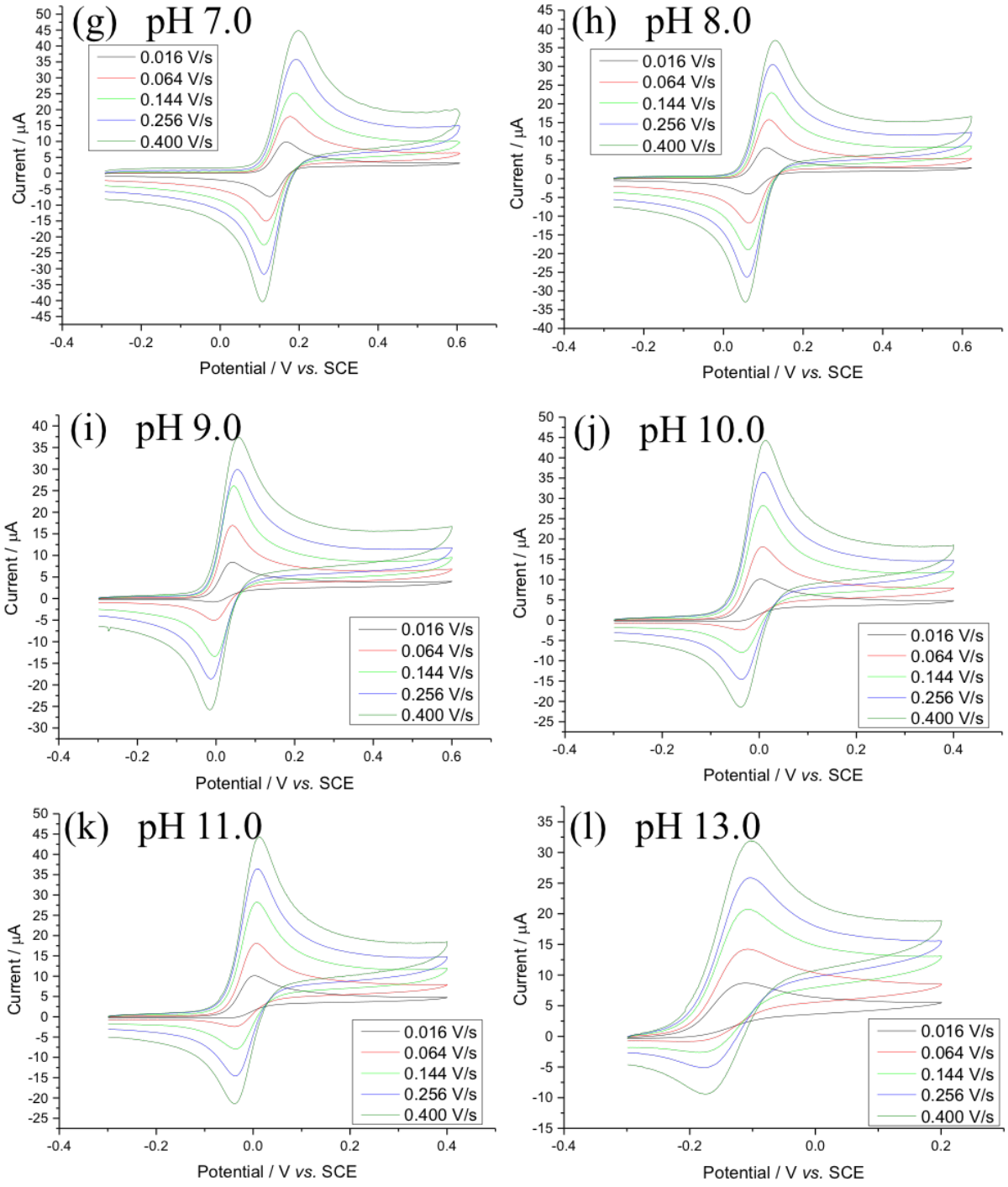

Figure 4.4: Voltammograms of 0.5 mM catechol in pH 7.0 $\sim$ 13.0 buffers at an alumina-modified glassy carbon electrode. Scan rates = 16, 64, 144, 256, 400 mV s^{-1}.

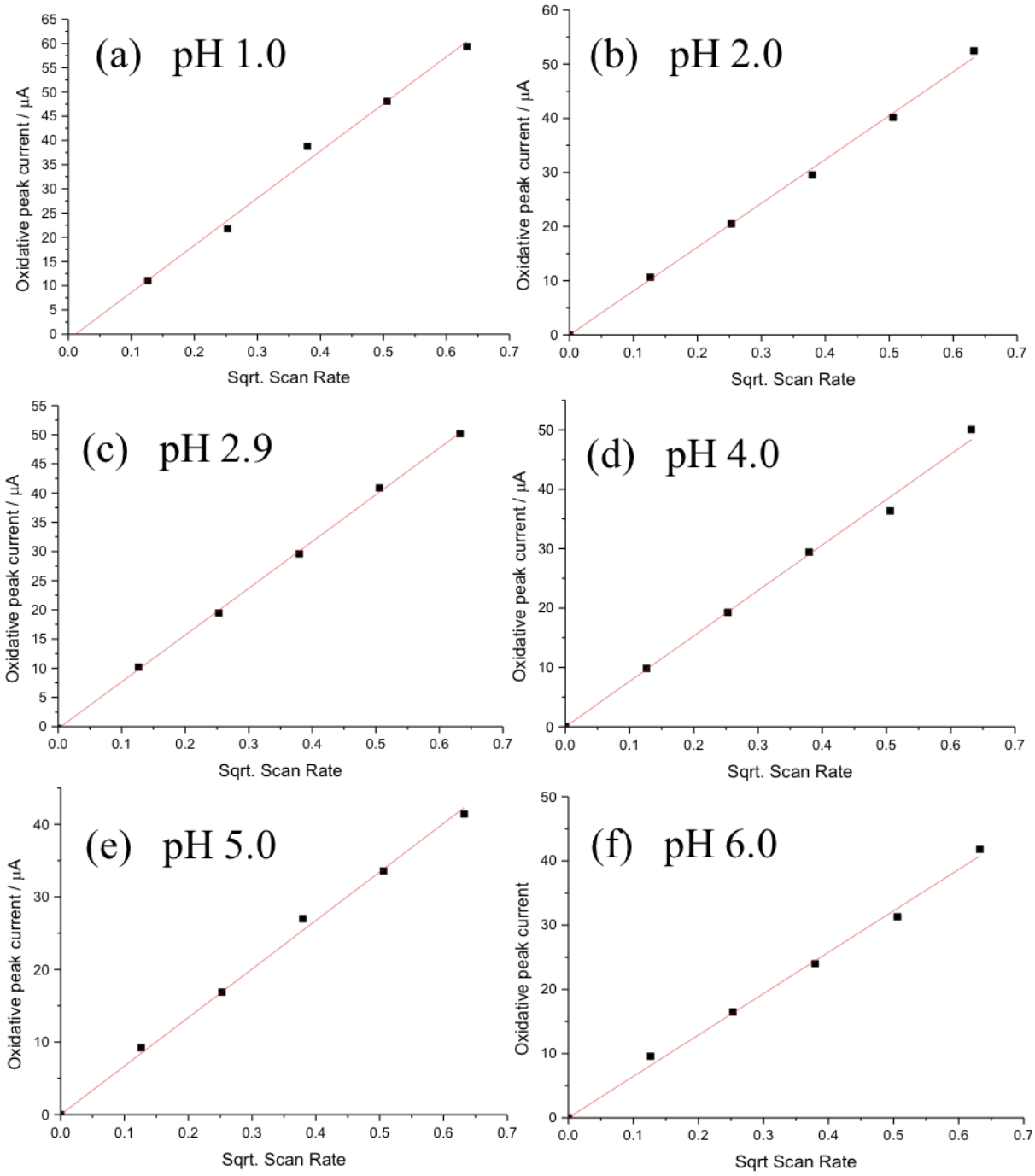

Figure 4.5: Plots of the oxidative peak currents against the square root of the scan rate for different pH values.

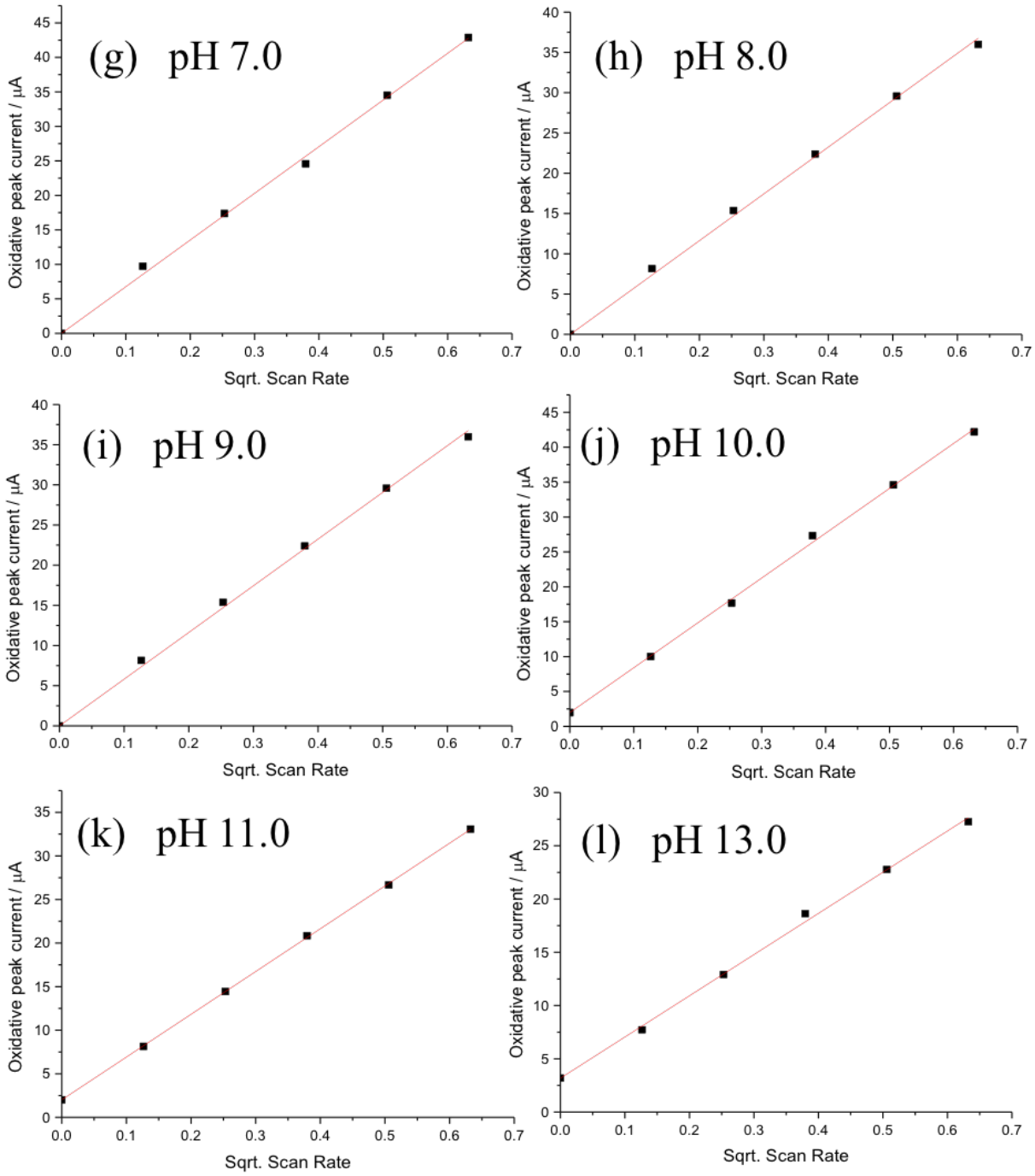

Figure 4.5: Plots of the oxidative peak currents against the square root of the scan rate for different pH values.

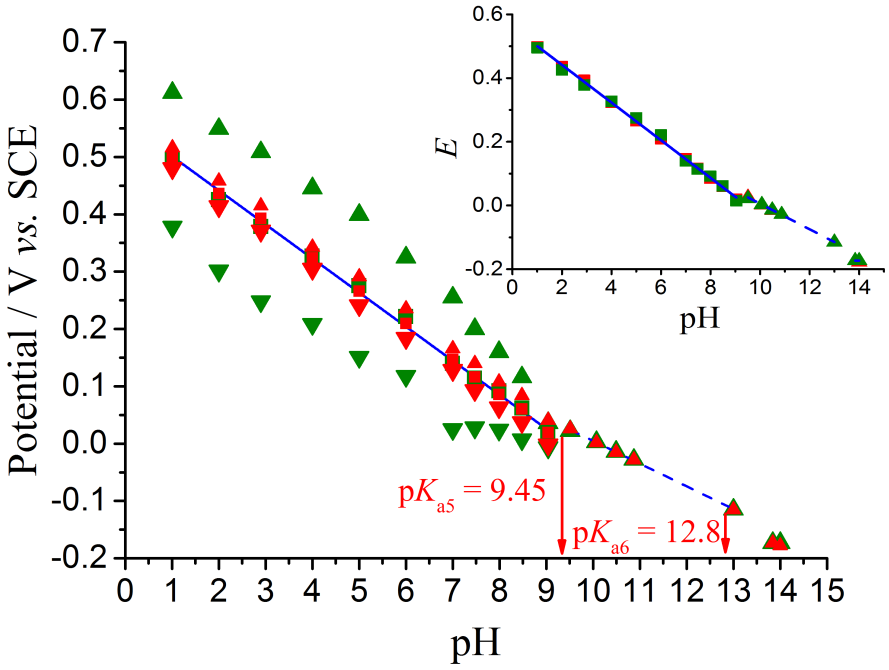

Figure 4.6: Plot of oxidative peak potential (▲), reductive peak potential (▼) and midpoint potential (■) against pH. Green symbols were measured on an unmodified glassy carbon electrode, while red symbols were measured on an alumina-modified glassy carbon electrode. Inlay shows the midpoint potential comparison of the two electrodes. Scan rate = 16 mV s^{-1}.

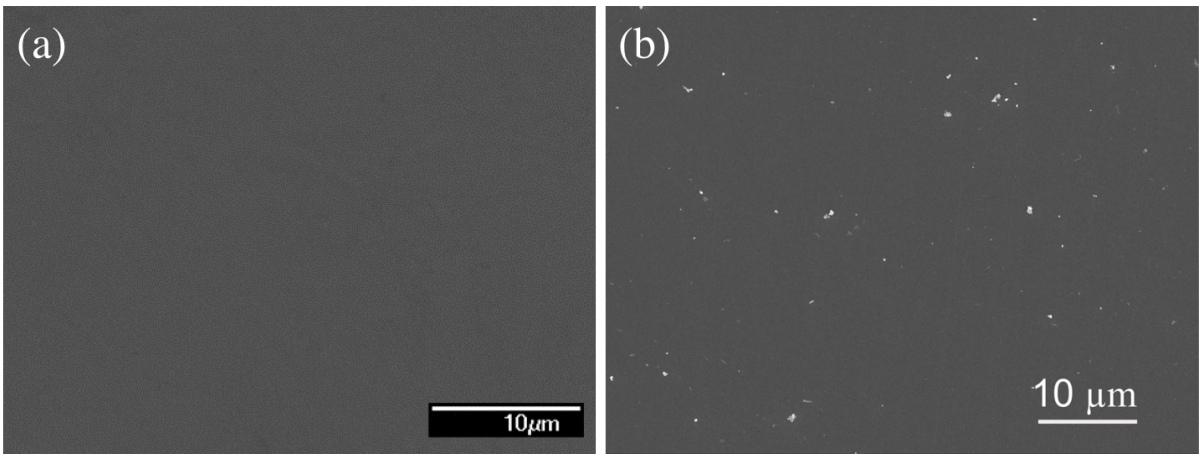

Figure 4.7: Scanning electron microscope image of (a) unmodified and (b) alumina-modified glassy carbon surface.

Consider the surface of the electrode partially blocked by insulating particles; individual diffusion (depletion) layers will build up. The resulting voltammetry is dependent of the size of the diffusion layer (δ), the absolute (but not relative) distance between adjacent blocking particles (p), and the radius of the single blocking particles (r_b, which is also the absolute distance between adjacent electrodes). There are four limiting cases (Figure 4.8) illustrated as the following.[8, 29, 30]

Case 1

In this limit, the blocking particles and the active electrode surface are both of 'macro' size. As a consequence, the active electrode surface experiences linear diffusion, while the concentration of the electroactive species in the zone of the blocking electrode surface remains effectively the same as that of the bulk solution.

Case 2

Here, the active electrode surface is of 'micro' dimension but the blocking particles are of 'macro' size. Therefore, the electrode behaves as a collection of isolated microelectrodes, each of which experiences convergent diffusion.

Case 3

In this limit, the active electrode surface is of 'micro' dimension and the blocking particles are sufficiently small, so that the diffusion fields of adjacent electrodes begin to overlap.

Case 4

This is the extreme limit of Case 3, where the distance between adjacent electrodes is so small that the diffusion fields are heavily overlapped. Consequently, the modified surface behaves almost like an unblocked electrode, and the entire electrode experiences linear diffusion to the electrode as a whole.

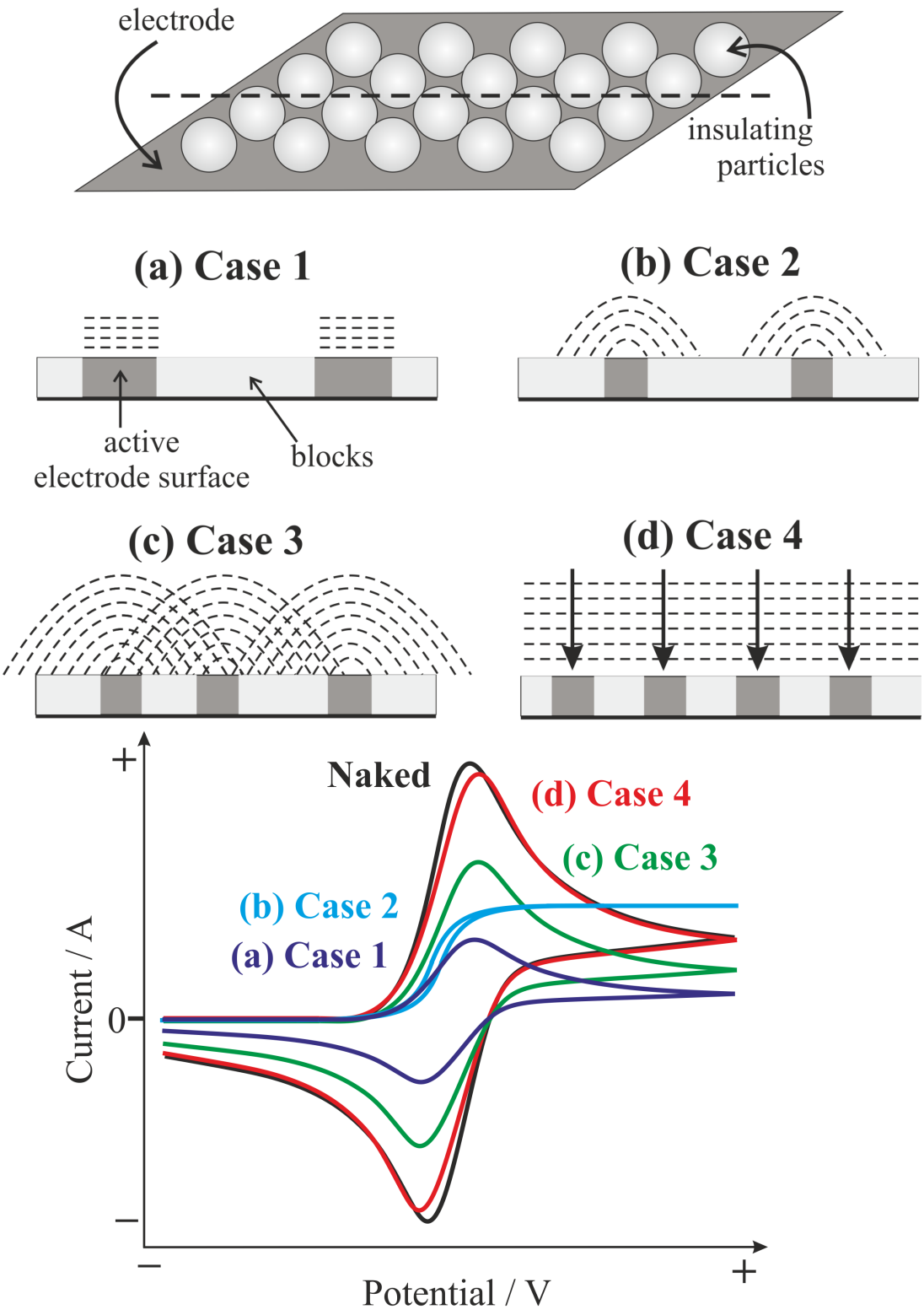

Figure 4.8: Cases of diffusion profile. (a) Case 1. Large electrodes, widely spaced individual diffusion layers: linear diffusion. (b) Case 2. Small electrodes, widely spaced individual diffusion layers: convergent diffusion. (c) Case 3. Small electrodes, closely spaced overlapping diffusion layers. (d) Case 4. Small electrodes, very closely spaced heavily overlapping diffusion layers: linear diffusion. The corresponding voltammetric responses are also shown.

Building on the general introduction to the four cases of diffusion profile at the electrode surface partially blocked by insulating particles, the analysis now classifies the diffusion at the alumina-modified GCE surface. The distance between the alumina particles (p) is less than the diffusion layer, $\delta = \sqrt{2Dt}$, where t is the voltammetric time scale of the experiments. Furthermore, the diameter of alumina particle is *ca.* 1 μm, indicating a very small distance between adjacent active electrodes. Therefore, Case 4 diffusion operates, and peak shaped voltammograms are seen reflecting linear diffusion of catechol to the full geometric area of the electrode.

4.3.2 Catechol Oxidation at Graphene-Modified Electrodes

Graphene nanoplatelets (GNPs) were first characterised using SEM imaging. The nanoplatelets were determined to have an average width of 16.5 $\pm$ 5 μm and an average thickness of 7.1 $\pm$ 2 nm.[31] This is consistent with the specification sheet provided by the supplier (Strem)[32]. As described in Chapter 2, Section 2.3.3, the GCE (electrode 2) was polished using diamond sprays of decreasing particle sizes. The electrode was then abrasively modified with GNPs by polishing the electrode in a GNP slurry.

Next voltammograms were recorded in 0.50 mM catechol in pH 5.0 buffer, for both unmodified and GNP-modified GCEs. Typical voltammograms are shown in Figure 4.9. At a scan rate of 100 mV s^{-1}, the peak potentials are altered, and the wide peak-to-peak separation of the unmodified GCE ($\sim$ 385 $\pm$ 7 mV) is replaced by a narrower separation of the GNP-modified GCE ($\sim$ 123 $\pm$ 3 mV).

Figure 4.10 presents data obtained across the full pH range (from 1.0 to 13.0). It is evident that modification using graphene has an influence on the voltammetry, albeit not to the same extent as seen for the case of alumina modifying the GCE surface. For example, at pH 5.0 and a scan rate of 100 mV s^{-1}, the alumina modification causes a change of peak-to-peak separation (ΔE_p) from 385 $\pm$ 7 mV for unmodified electrode

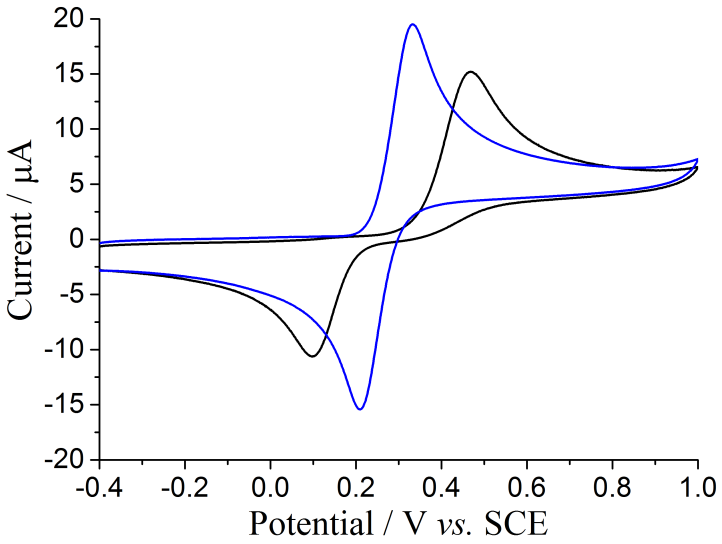

Figure 4.9: Representative voltammogram taken in 0.50 mM catechol in pH 5.0 buffer. Blue: graphene nanoplatelets-modified glassy carbon electrode. Black: unmodified glassy carbon electrode. Scan rate = 100 mV s^{-1}.

to 80 ± 4 mV for the alumina-modified GCE electrode 1, a 305 ± 8 mV decrease. In contrast the graphene nanoplatelets modification causes a change from 385 ± 7 mV for the unmodified electrode to 123 ± 3 mV for the GNP-modified electrode 2, a 262 ± 8 mV decrease.

It is worth noting the peak potential varies significantly with respect to changes in pH. For a fully electrochemically reversible electrode process, the midpoint potential (E_{mid}) obeys the following equation:

$$E_{mid} \simeq \text{constant} - 2.303\frac{mRT}{nF}\text{pH} \tag{4.8}$$

where m and n are, respectively, the number of protons and electrons involved in the electrochemical reaction, and other symbols have been defined in the preceding section. From Eq. 4.8, it can be seen that E_{mid} varies by $59(m/n)$ mV per pH unit. At pH values ranging from pH 1.0 to 9.0, the experimental measurements shown in Figure 4.10b demonstrates a 59 mV/pH shift from the slope of observed midpoint potential. This is consistent with a two-electron, two-proton transfer in the electrochemical oxidation of

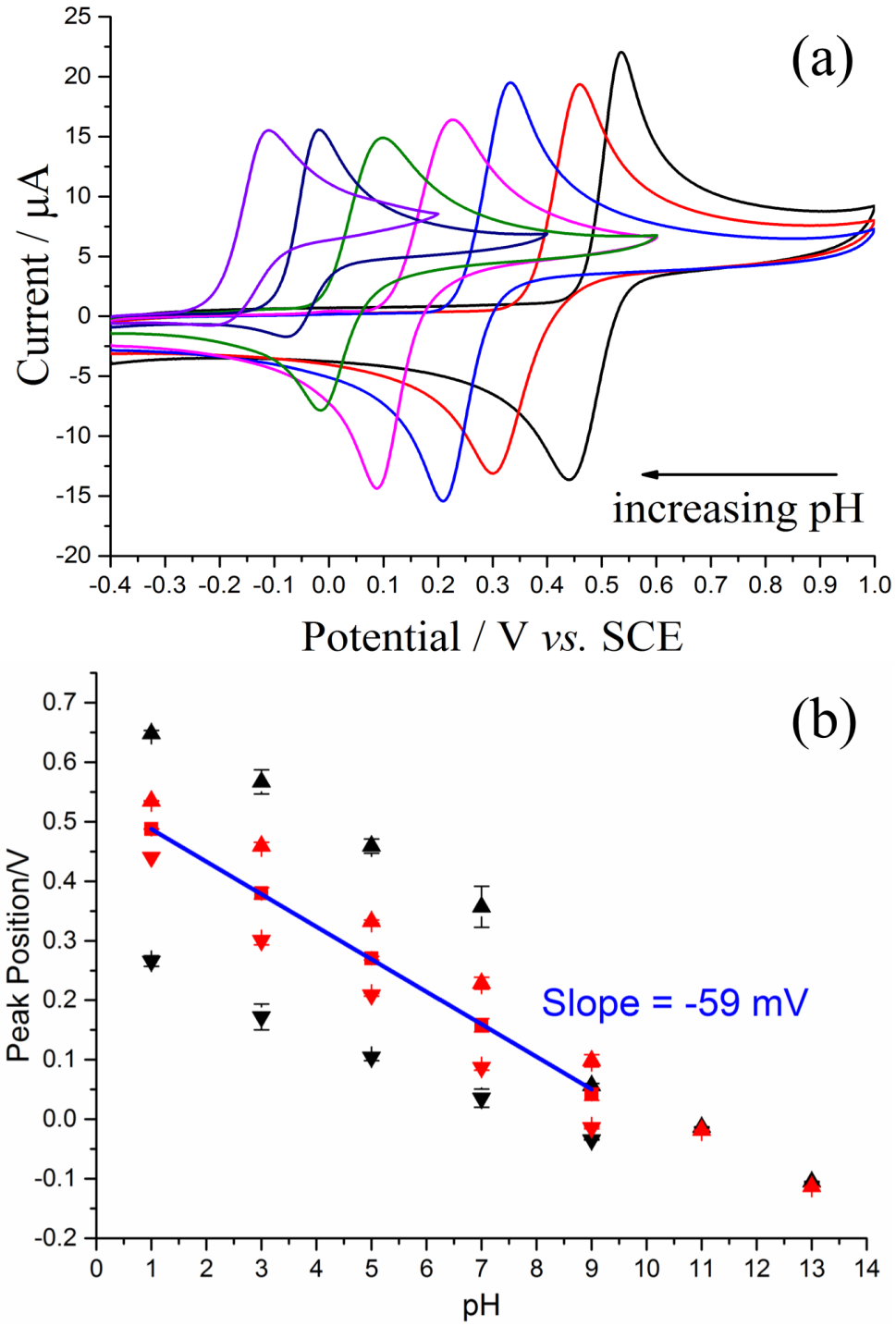

Figure 4.10: (a) Representative voltammograms of 0.50 mM catechol in various pH buffers at a graphene nanoplatelets-modified glassy carbon electrode. Black: pH 1.0. Red: pH 3.0. Blue: pH 5.0. Pink: pH 7.0. Green: pH 9.0. Dark Blue: pH 11.0. Purple: pH 13.0. b) Average forward (▲), backward (▼) peak potentials, and midpoint potential (■) with standard deviation error bars fitted. Black: unmodified glassy carbon electrode. Red: graphene nanoplatelets-modified glassy carbon electtode. Blue line: gradient of the midpoint potential. Scan rate = 100 mV s^{-1}.

catechol.

The observed voltammetry was then modelled using DIGISIM (see Chapter 2, Section 2.5). Due to the multiparameter nature of the redox process the measured diffusion coefficient of H_2C was applied to the species SH and Q. The electrochemical rate constant (k^0) and transfer coefficient ($\alpha = 0.50$) were approximated to be the same for both redox couples H_2C/SH and SH/Q. The key parameters in controlling the observed ΔE_p and are k^0 and the two formal potentials of the H_2C/SH and SH/Q redox couples. The difference of the formal potentials, ΔE_f^0, is defined as

$$\Delta E_f^0 = E_{f2,app}^0 - E_{f1,app}^0 \tag{4.9}$$

where $E_{f2,app}^0$ is the formal potential of the H_2C/SH redox couple and $E_{f1,app}^0$ is the formal potential of the SH/Q redox couple.

Figure 4.11 shows how the two parameters influence the peak current which, within the equal diffusion coefficient approximation, can give a partial resolution of the true parameters in terms of their control over the overall process. Specifically for very fast electrode kinetics the voltammetric peak behaves as a fully reversible, Nernstian peak such that the peak current (I_p) is proportional to $n^{3/2}$ where n (=2) is the number of electrons transferred; For less fast rate constants the peak current scales with n which reflects twice the current seen from a single one-electron process, according to Randles-Ševčík Equations (Chapter 1, Eq. 1.70). This changeover is evident in the inlay of Figure 4.11. At a constant k^0 value, after surpassing a particular ΔE_f^0 limit, the increase of ΔE_f^0 value decreases I_p and increases ΔE_p. For example, with $k^0 = 1$ cm s^{-1}, the ΔE_p starts to increase from $\Delta E_f^0 \approx 0.2$ V onward. In contrast, with $k^0 = 10$ cm s^{-1}, the ΔE_p starts to increase from $\Delta E_f^0 \approx 0.4$ V onward.

Figure 4.12 shows the approximate modelling of the peak-to-peak separation (ΔE_p) and peak current (I_p) using the difference in formal potential, ΔE_f^0, and the average rate

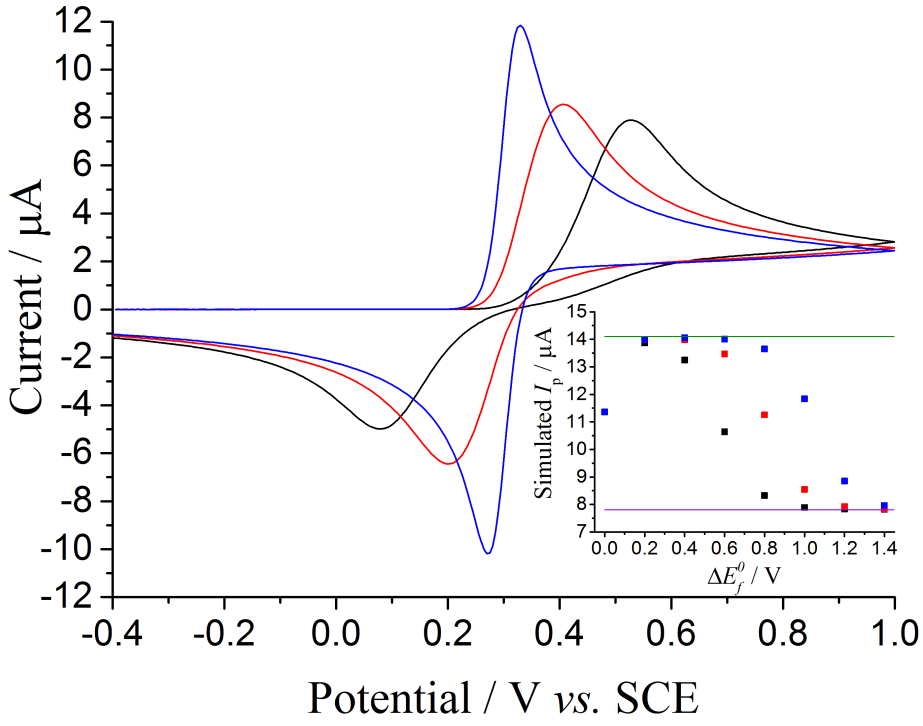

Figure 4.11: Simulated voltammograms with $\Delta E_f^0 = 1.0$ V with varying k^0. Black: $k^0 = 1$ cm s^{-1}. Red: $k^0 = 10$ cm s^{-1}. Blue: $k^0 = 100$ cm s^{-1}. Inlay: simulation demonstration of the effect of the parameters k^0 and ΔE_f^0 on the voltammetric peak currents. Black squares: $k^0 = 1$ cm s^{-1}. Red Squares: $k^0 = 10$ cm s^{-1}. Blue squares: $k^0 = 100$ cm s^{-1}. Green line: Reversible current limit. Purple line: Irreversible current limit.

constant, k^0, as simulation fitting parameters. In the fitting, parameters k^0 and ΔE_f^0 are varied. The simulated ΔE_p and I_p value for each k^0 and ΔE_f^0 setting generates its own percentage error with respect to the experimental values. In order to facilitate a more convenient simulation fit assessment, ΔE_p percentage error is combined linearly to I_p percentage error. The reason behind using the linear error addition is because the errors are not standard deviations. Therefore, the total error is calculated by:

$$\text{Total \% Error} = \text{\% Error } (E_p) + \text{\% Error } (I_p) \tag{4.10}$$

The combined error allows the contour plots of Figure 4.12 to reflect the goodness of fit for both properties concerned, ΔE_p and I_p.

In the contour plot, the colour scheme follows a rainbow palette where the violet

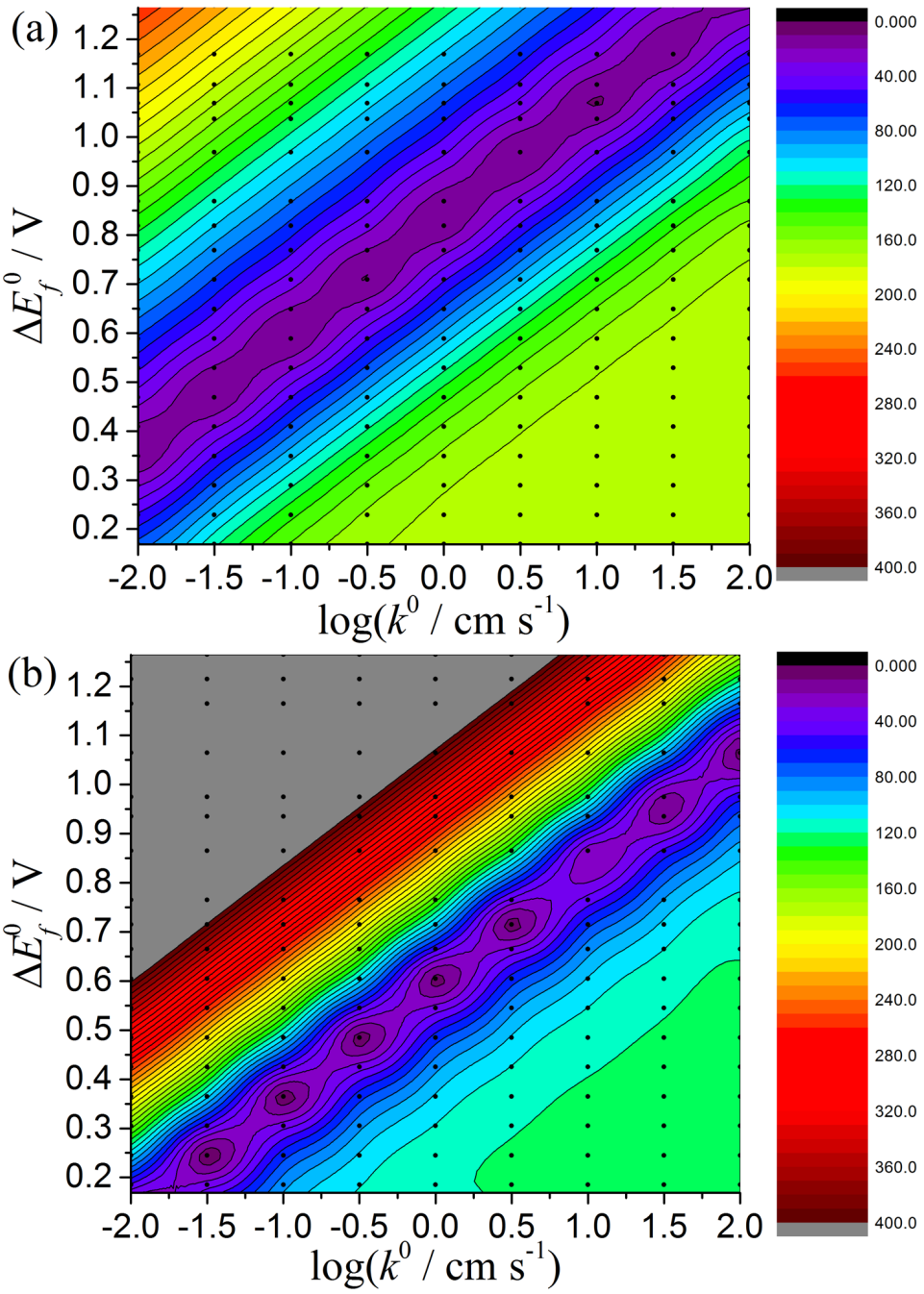

Figure 4.12: Contour plots of combined percentage errors of simulation fitting for (a) unmodified, and b) graphene nanoplatelets-modified glassy carbon electrodes. Any error above 400% is coloured grey. Black dots: data points of simulation. Experimental scan rate = 100 mV s^{-1}.

end denotes the lowest percentage error and the red end of the spectrum denotes the highest percentage error. A clear "trench" of low error fitting can be seen in both Figure 4.12a and b. Any "pits" of lower error in the "trench" is due to the distribution of the simulation data points. For each plot the "trench" of good fit is of identical gradient, where $d\Delta E_f^0/d\log(k^0) = 0.24$ V. Therefore a good fit is attained for a variety of ($\log(k^0)$, ΔE_f^0) points.

Drop-cast modifications were also done for comparison with abrasive modifications. 15 mg of GNPs was suspended in 10 ml chloroform, the suspension was shaken vigorously before use in order to ensure a homogenous suspension. 7.5 μg of GNPs were then drop-casted onto the GCE. This forms a much thicker layer of GNPs onto the electrode surface. From the voltammogram comparison as shown in Figure 4.13, ΔE_p of GNP-modified electrode decreases significantly in comparison to the unmodified electrode. This demonstrates the thin-layer behaviour expected for electrodes modified with thick porous layer as discussed in the introduction to this paper. The drop-cast ΔE_p value reductions are much lower, as shown in Figure 4.13 and 4.14, than those of the abrasive modification method. At pH 5.0, the unmodified electrode ΔE_p is 385 $\pm$ 7 mV, and for the GNP drop-cast modified electrode 2 the ΔE_p is 244 $\pm$ 25 mV, a 141 $\pm$ 26 mV decrease in ΔE_p. This is a much smaller decrease compared to the GNP abrasive modification, ΔE_p reduction of 262 $\pm$ 8 mV. This could be indicative of a passivation of the adsorptive ability of the GNPs due to the use of chloroform as the drop-cast suspension medium. It may thus be concluded that the shift in relative potential of the oxidative and reductive catechol peaks reflects either changes in k^0, ΔE_p, or a combination of both.

Figure 4.15 shows the SEM image of the GNP-modified GCE surface; it can be seen that the glassy carbon surface is sparsely populated with GNPs, where the distribution is on average 48 $\pm$ 32 μm apart. This is in stark contrast to the pristine surface seen on the unmodified GCE surface (Figure 4.7a). It is evident that the tiny amount of GNPs has a

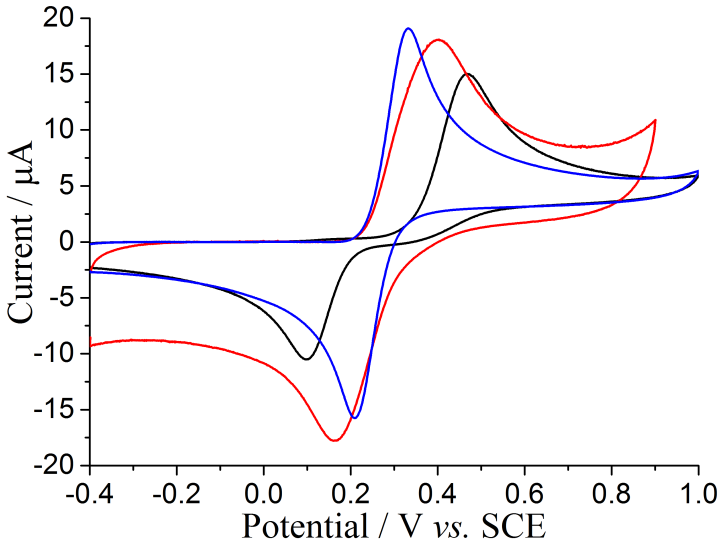

Figure 4.13: Representative voltammogram taken in 0.50 mM catechol in pH 5.0. Blue: graphene nanoplatelets-modified (*via* abrasive modification) glassy carbon electrode. Red: graphene nanoplatelets-modified (*via* drop-cast modification) glassy carbon electrode. Black: Unmodified glassy carbon electrode. Scan rate = 100 mV s^{-1}.

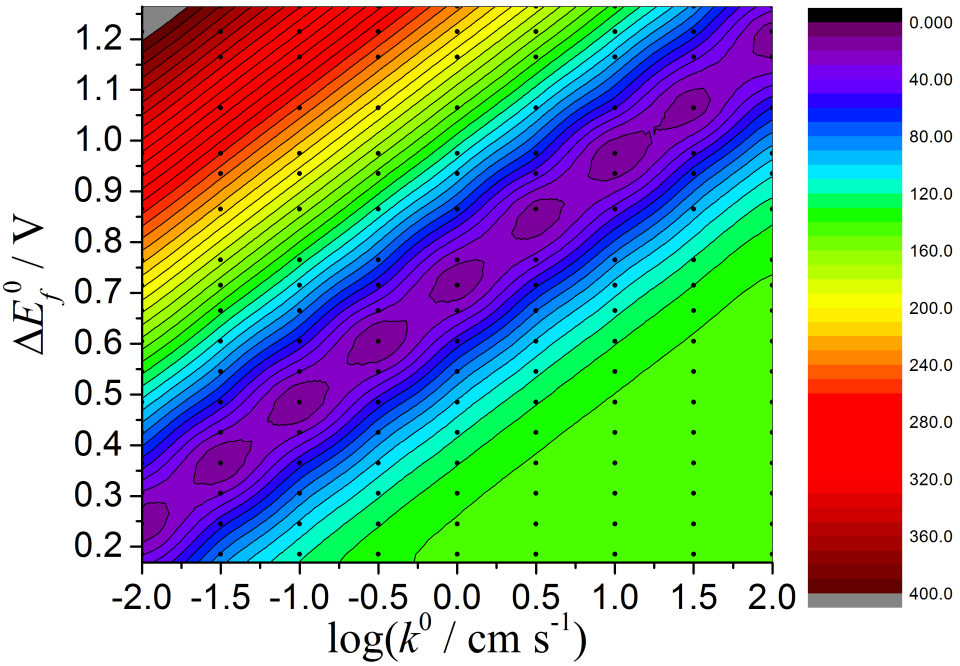

Figure 4.14: Contour plots of combined percentage errors of simulation fitting for graphene nanoplatelets drop-cast modified glassy carbon electrode. Any error above 400% is coloured grey. Black dots: data points of simulation. Scan rate = 100 mV s^{-1}.

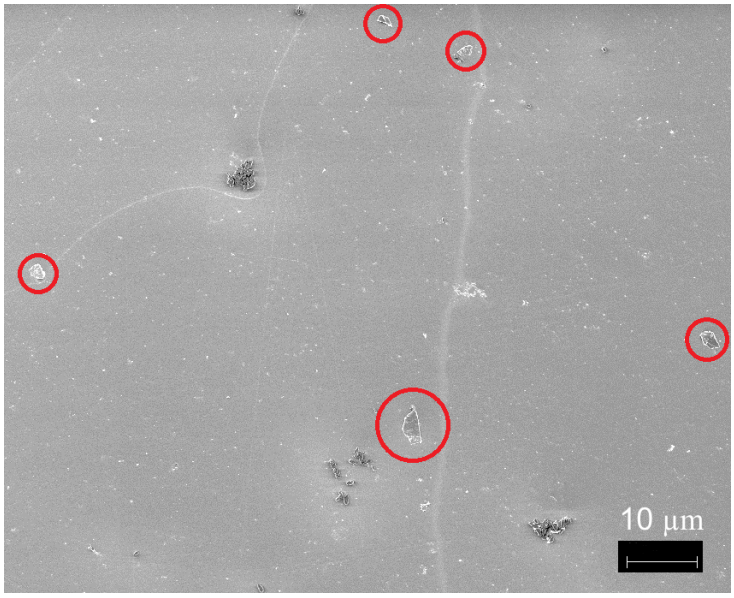

Figure 4.15: Scanning electron microscope image of graphene nanoplatelets-modified glassy carbon surface. Within the red circles are the observed nanoplatelets.

significant impact on the observed voltammogram. The sparse coverage implies minimal impact on the surface roughness and mass transport to the electrode surface. However, the effect of GNPs on the catechol oxidation voltammetric response is comparable to the alumina-modified GCE images seen in Figure 4.7b. This in turn supports the hypothesis that the changed voltammetry seen in alumina- and GNP-modified GCE surfaces is due to the provision of adsorption sites by the alumina and GNPs.

4.3.3 Discussion

The results reported in the two previous subsections show a profound influence by either adsorbed alumina or adsorped graphene on the surface of GCEs with respect to the two-electron, two-proton oxidation of catechol. In the case of the alumina modification the modifier is not conductive, and it seems likely that the role of the alumina is to adsorb the semiquinone intermediate:

$$H_2C\ (aq) \rightleftharpoons H_2C\ (ads) \overset{-e^-,-H^+}{\longrightarrow} SH\ (ads) \tag{4.11}$$

$$2\text{SH (ads)} \rightleftharpoons \text{H}_2\text{C (ads)} + \text{Q (ads)} \tag{4.12}$$

$$\text{Q (ads)} \rightleftharpoons \text{Q (aq)} \tag{4.13}$$

where the *weak* adsorption of H_2C and Q is suggested by the voltammetry of the catechol immobilised on the alumina and graphene nanoplatelets. The coverage of alumina in these experiments is tiny, but SEM shows the interparticle separation to be consistent with Case 4 diffusion[8, 29, 30]. Here the observed peak shaped voltammetry reflects catechol transport to the full geometric area of the GCE.

In the case of graphene, the observed behaviour, although not as catalytically apparent as with alumina, can be rationalised in terms of relatively altered formal potentials of the H_2C/SH and SH/Q redox couples and/or altered electrode kinetics.

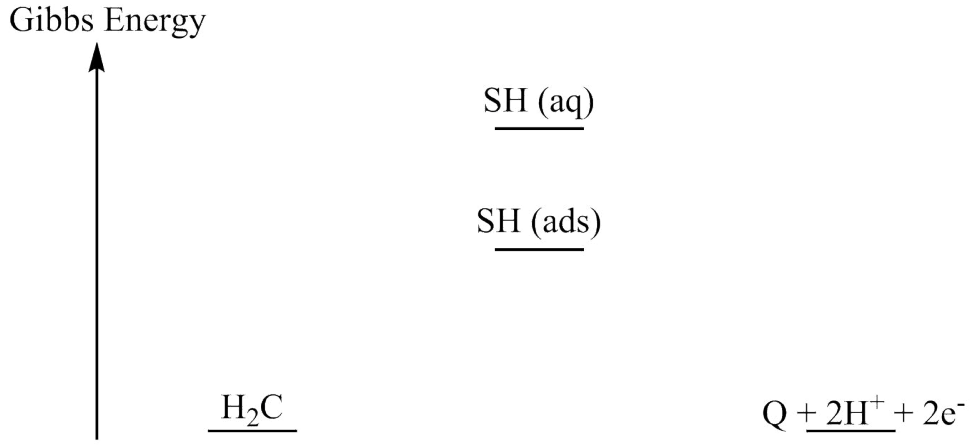

Figure 4.16: Scheme of the energetics of different reaction species where the electrode potential is held at a value corresponding to E_f^0 for the Q/H_2C couple.

A "unified" view of the observed catalysis can be proposed. In particular one mechanism in which a multistep electron transfer process can be catalysed can be understood in terms of the catechol to quinone reaction, *via* a semiquinone intermediate as discussed above. Specifically if the semiquinone radical is stabilised by the presence of an electrode modifier, for example *via* surface adsorption onto the modifier, then one would expect both of the types of catalysis seen for the systems reported. Thus, adsorption of semiquinone

is almost essential to understand the alumina catalysis, whereas for the graphene an enhanced process such as adsorption could explain the relative shifts of the $E^0_{f2,app}$ and $E^0_{f1,app}$ values inferred as one probable cause of the observed changed voltammetry. In both cases the energetics of the overall transformation could be altered as proposed in Figure 4.16, which shows the energetics for an applied electrode potential corresponding to the formal potential of the H_2C/Q couple.

4.4 Conclusions

The two-electron, two-proton oxidation of catechol at glassy carbon electrodes has been shown to be catalysed by the presence of either alumina or graphene on the electrode surface. While the precise mechanistic detail of the reaction is necessarily speculative at least in part, the observations are consistent with a stabilisation, probably *via* adsorption, of the semiquinone radicals on the surface of the modifying materials. Such a phenomena could represent a catalysis of the overall transformation but not an "electrocatalytic" process since the rate of the electron transfer step would only be influenced indirectly.

References

[1] Poon, J.; Lin, Q.; Batchelor-McAuley, C.; Salter, C.; Johnston, C.; Compton, R. G. *Journal of Physical Chemistry C* **2015**, *119*, 13777–13784.

[2] Xian, H.; Wang, P.; Zhou, Y.; Lu, Q.; Wu, S.; Li, Y.; Wang, L. *Microchimica Acta* **2010**, *171*, 63–69.

[3] Isogai, S.; Ohnishi, R.; Katayama, M.; Kubota, J.; Kim, D. Y.; Noda, S.; Cha, D.; Takanabe, K.; Domen, K. *Chemistry - An Asian Journal* **2012**, *7*, 286–289.

[4] Tang, Y.; Burkert, S. C.; Zhao, Y.; Saidi, W. A.; Star, A. *The Journal of Physical Chemistry C* **2013**, *117*, 25213–25221.

[5] Bonanni, A.; Loo, A. H.; Pumera, M. *TrAC Trends in Analytical Chemistry* **2012**, *37*, 12–21.

[6] Qu, L.; Liu, Y.; Baek, J.-B.; Dai, L. *ACS Nano* **2010**, *4*, 1321–1326.

[7] Pumera, M. *Electrochemistry Communications* **2013**, *36*, 14–18.

[8] Compton, R. G.; Banks, C. E. *Understanding Voltammetry, 2nd edition*; Imperial College Press, 2011.

[9] Guidelli, R.; Compton, R. G.; Feliu, J. M.; Gileadi, E.; Lipkowski, J.; Schmickler, W.; Trasatti, S. *Pure and Applied Chemistry* **2014**, *86*, 259–262.

[10] Guidelli, R.; Compton, R. G.; Feliu, J. M.; Gileadi, E.; Lipkowski, J.; Schmickler, W.; Trasatti, S. *Pure and Applied Chemistry* **2014**, *86*, 245–258.

[11] Kozub, B. R.; Rees, N. V.; Compton, R. G. *Sensors and Actuators B: Chemical* **2010**, *143*, 539–546.

[12] Henstridge, M. C.; Dickinson, E. J. F.; Aslanoglu, M.; Batchelor-McAuley, C.; Compton, R. G. *Sensors and Actuators B: Chemical* **2010**, *145*, 417–427.

[13] Sims, M. J.; Rees, N. V.; Dickinson, E. J. F.; Compton, R. G. *Sensors and Actuators B: Chemical* **2010**, *144*, 153–158.

[14] Batchelor-McAuley, C.; Compton, R. G. *The Journal of Physical Chemistry C* **2014**, *118*, 30034–30038.

[15] Streeter, I.; Wildgoose, G. G.; Shao, L.; Compton, R. G. *Sensors and Actuators B: Chemical* **2008**, *133*, 462–466.

[16] Eloul, S.; Batchelor-McAuley, C.; Compton, R. G. *Journal of Solid State Electrochemistry* **2014**, *18*, 3239–3243.

[17] Henstridge, M. C.; Dickinson, E. J. F.; Compton, R. G. *Russian Journal of Electrochemistry* **2012**, *48*, 629–635.

[18] Punckt, C.; Pope, M. A.; Aksay, I. A. *The Journal of Physical Chemistry C* **2014**, *118*, 22635–22642.

[19] Pumera, M. *The Chemical Record* **2009**, *9*, 211–223.

[20] Streeter, I.; Xiao, L.; Wildgoose, G. G.; Compton, R. G. *The Journal of Physical Chemistry C* **2008**, *112*, 1933–1937.

[21] Keeley, G. P.; Lyons, M. E. G. *International Journal of Electrochemical Science* **2009**, *4*, 794–809.

[22] Ward, K. R.; Gara, M.; Lawrence, N. S.; Hartshorne, R. S.; Compton, R. G. *Journal of Electroanalytical Chemistry* **2013**, *695*, 1–9.

[23] Ward, K. R.; Compton, R. G. *Journal of Electroanalytical Chemistry* **2014**, *724*, 43–47.

[24] Masa, J.; Batchelor-McAuley, C.; Schuhmann, W.; Compton, R. *Nano Research* **2014**, *7*, 71–78.

[25] Guo, S.-X.; Zhao, S.-F.; Bond, A. M.; Zhang, J. *Langmuir* **2012**, *28*, 5275–5285.

[26] Gara, M.; Ward, K. R.; Compton, R. G. *Nanoscale* **2013**, *5*, 7304–7311.

[27] Batchelor-McAuley, C.; Li, Q.; Dapin, S. M.; Compton, R. G. *The Journal of Physical Chemistry B* **2010**, *114*, 4094–4100.

[28] Lin, Q.; Li, Q.; Batchelor-McAuley, C.; Compton, R. G. *Journal of Physical Chemistry C* **2015**, *119*, 1489–1495.

[29] Davies, T. J.; Banks, C. E.; Compton, R. G. *Journal of Solid State Electrochemistry* **2005**, *9*, 797–808.

[30] Davies, T. J.; Ward-Jones, S.; Banks, C. E.; del Campo, J.; Mas, R.; Muoz, F. X.; Compton, R. G. *Journal of Electroanalytical Chemistry* **2005**, *585*, 51–62.

[31] Poon, J.; Batchelor-McAuley, C.; Tschulik, K.; Compton, R. G. *Chemical Science* **2015**, *6*, 2869–2876.

[32] Strem Chemicals Inc., Graphene Nanoplatelets. https://secure.strem.com/uploads/resources/documents/graphene_nanoplatelets_copy1.pdf.

Chapter 5

Quantifying Adsorption on Single Alumina Particles *via* Impact Voltammetry and Current Transient Analysis

Building on the understanding of the oxidation of catechol catalysed by alumina-modified electrode surfaces, in this chapter a new electrochemistry method based on particle impacts is introduced to quantify adsorption of redox active species on the surface of individual insulating particles. Using theory for charge diffusion over the surface of a sphere, the individual impact spikes arising from the electro-oxidation of adsorbed catechol can be modelled to derive the diffusion coefficient of charge transfer over the surface of alumina, as well as the coverage of catechol on the surface of alumina. The work herein presented has been published in *The Journal of Physical Chemistry C*[1].

5.1 Introduction

The oxidation of catechol to 1,2-benzoquinone (Chapter 4, Figure 4.1) at carbon electrodes is catalysed by the presence of alumina particles immobilised on the electrode surface (Chapters 3 and 4). In this chapter, a new electrochemistry method based on particle impacts (Chapter 1, Section 1.8.2) is developed in light of previous experiments with conductive nanoparticles[2, 3] to quantify adsorption of redox active species on the surface

of individual insulating particles. The particles, of *ca.* micron size, with surface adsorbed redox active molecules, are suspended in aqueous solution and undergo impacts with a potentiostatted microelectrode. Upon particle-electrode collisions, chronoamperometric current/time impact spikes will arise if the electrode is held at a potential at which the molecules are reduced or oxidised. The particle cores remain unchanged.

In this new method, the shape and size of individual impact spikes are modelled using theory for diffusion of charge over the surface of the particles as electrons hop from one molecule to another (Figure 5.1)[4, 5] Thompson *et al.*[4] reported the simulation of the chronoamperometry of electrolysis of species adsorbed on a perfectly spherical particle assuming charge transfer to a substrate electrode at a point contact of negligible resistance. In the present work, the transients from individual impacts, especially the curve shapes, are fitted in light of this theoretical model. Two parameters, the diffusion coefficient (D_i) of charge transfer between catechol molecules on the surface of alumina and the coverage (Γ_i) of catechol on the surface of alumina, are extracted.

Here, the theory for Fickian charge diffusion over the surface of a sphere is reviewed. The perfect sphere model[4] assumes that a full sphere (of radius of r_s, Figure 5.2), with redox active species attached on the surface, is in contact with an electrode surface at an angle (θ) of 0^0. This is the only contact point where charge transfer occurs and the electrode acts solely to transfer electrons in or out of the particle surface. The changing coverage ($\Gamma(\theta)$/mol cm^{-2}) of redox active species on the sphere surface during electrolysis can be normalised with respect to the initial coverage (Γ_i/mol cm^{-2}). The resulting dimensionless coverage is denoted as $\Gamma(\theta)/\Gamma_i$. The boundary condition for chronoamperometry is that when t < 0, $\Gamma(\theta)/\Gamma_i = 1$ everywhere on the sphere; when t > 0, $\Gamma(\theta)/\Gamma_i = 0$ at $\theta = 0$.

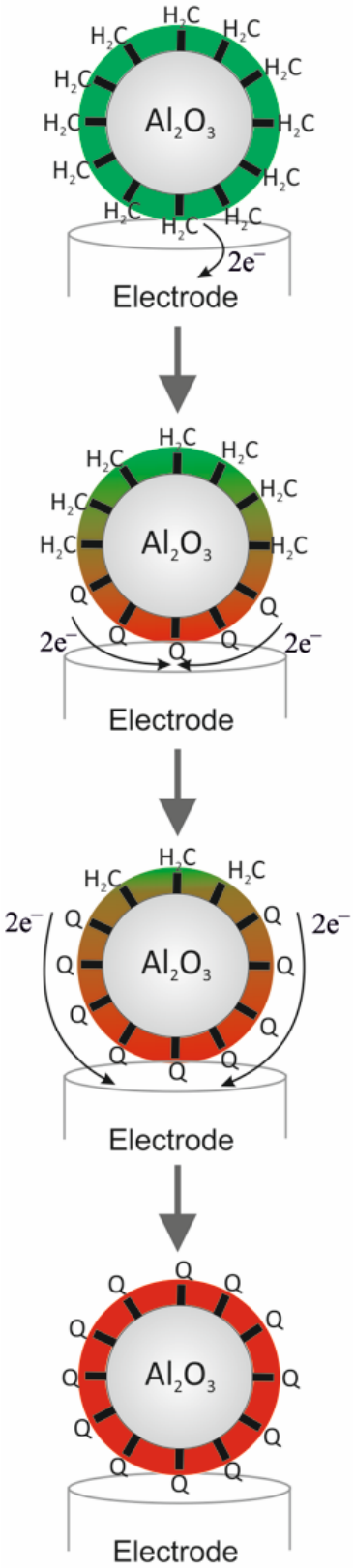

Figure 5.1: Model of charge diffusion over the surface of a sphere. H_2C is catechol and Q is 1,2-benzoquinone.

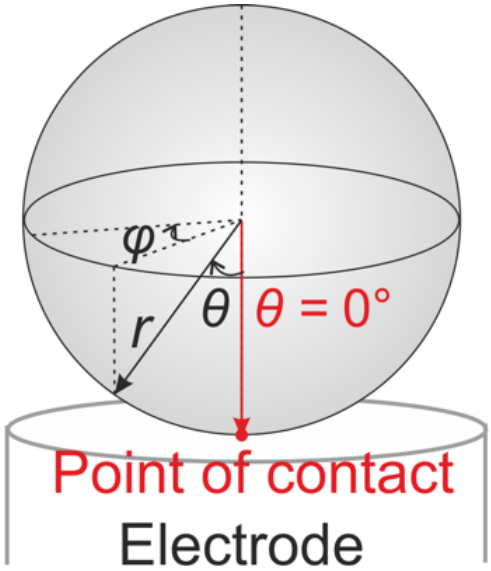

Figure 5.2: Perfect sphere model with spherical coordinates (r, θ and φ) and the point of contact between the sphere and electrode surface.

The assumption is made that the movement of charge obeys Fick's Second Law,

$$\frac{\partial \Gamma(\theta)}{\partial t} = D\nabla^2\Gamma(\theta) \tag{5.1}$$

where the Laplacian operator in spherical coordinates (r, θ, φ) is defined as

$$\nabla^2 = \frac{\partial^2}{\partial r^2} + \frac{2\partial}{r\partial r} + \frac{1}{r^2}\frac{\partial^2}{\partial\theta^2} + \frac{\cos\theta}{r^2\,\sin\theta}\frac{\partial}{\partial\theta} + \frac{1}{r^2\,\sin^2\theta}\frac{\partial^2}{\partial\varphi^2} \tag{5.2}$$

Because the charge movement is confined to the surface layer as shown in Figure 5.1, and as charge transfer only occurs at the point of contact ($r = r_s$, where r_s is the radius of the sphere), Eq. 5.2 can be simplified as

$$\nabla^2 = \frac{1}{r_s^2}\frac{\partial^2}{\partial\theta^2} + \frac{1}{r_s^2\tan\theta}\frac{\partial}{\partial\theta} \tag{5.3}$$

The equation describing diffusion over the sphere surface can be expressed in dimensionless

variables

$$\frac{\partial\Gamma(\theta)/\Gamma_i}{\partial\tau} = \frac{\partial^2\Gamma(\theta)/\Gamma_i}{\partial\theta^2} + \frac{1}{\tan\theta}\frac{\partial\Gamma(\theta)/\Gamma_i}{\partial\theta} \tag{5.4}$$

with the dimensionless time (τ) defined as

$$\tau = tD_i/r_s^2 \tag{5.5}$$

where t is time and D_i is the diffusion coefficient of charge transfer over the surface of the sphere. Eq. 5.4 can be solved numerically[4] on the basis of the boundary condition discussed above using an implicit finite difference (IFD) method to get the dimensionless coverage ($\Gamma(\theta)/\Gamma_i$). The solution can be exploited to derive the expression for charge (Q) at time t,

$$\frac{Q}{F} = \int_0^\pi 2\pi r_s^2 n\left(\Gamma_i - \Gamma(\theta)\right)\ \sin\theta\ \mathrm{d}\theta \tag{5.6}$$

where n is the number of electrons transferred per molecule, and F is the Faraday constant (96 485 C mol^{-1}). Eq. 5.6 can be used to derive the current as a function of t for chronoamperometry,

$$\frac{I}{F} = \frac{\partial Q}{\partial t} = -2\pi r_s^2 n\int_0^\pi \frac{\partial\Gamma(\theta)}{\partial t}\ \sin\theta\ \mathrm{d}\theta \tag{5.7}$$

or in dimensionless variables as

$$Nu = -\int_0^\pi \frac{\partial\Gamma(\theta)/\Gamma_i}{\partial\tau}\ \sin\theta\ \mathrm{d}\theta \tag{5.8}$$

with the dimensionless current (Nu) defined as

$$Nu = \frac{I}{2\pi nFD_i\Gamma_i} \tag{5.9}$$

The plot ("working curve") of log Nu versus log τ using the perfect sphere model[4] is shown in Figure 5.3.

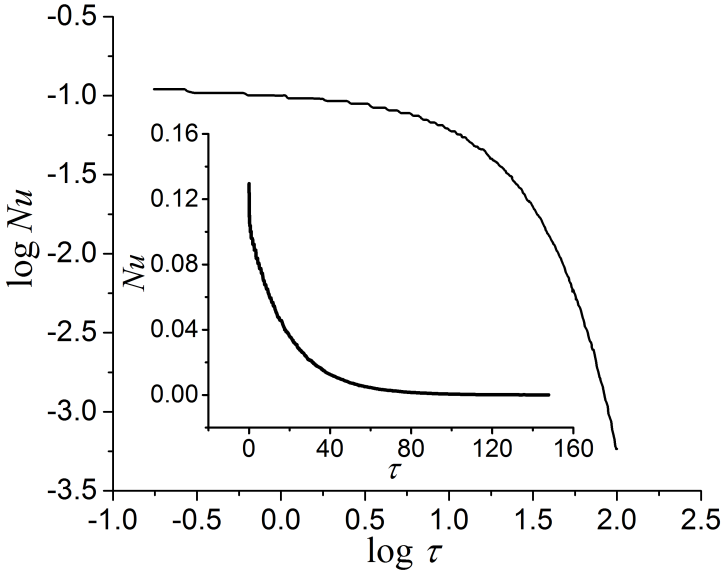

Figure 5.3: Dimensionless log-log plot for a full sphere in point contact with the electrode surface. Inlay: corresponding dimensionless current-time plot for the sphere.

Figure 5.3 shows that the logarithm of dimensionless current decreases very rapidly at longer times because of exhaustive electrolysis of adsorbate. In the experiments reported later, Figure 5.3 is used for the analysis of individual particle current/time impacts.

In the following, for the first time, adsorption of redox active species on individual insulating particles will be quantified electrochemically by using impact experiments. Modelling of individual impact spikes will be shown to be consistent with the theory for charge diffusion over the surface of a sphere.

5.2 Experimental

Details about the chemical reagents and buffer solutions here utilised can be found in Chapter 2, Section 2.1. The structures of catechol (H_2C) and its oxidation product, 1,2-benzoquinone (Q) are shown in Chapter 4, Figure 4.1. 0.1 M KCl was used as the supporting electrolyte. The catechol-modified alumina particles (H_2C-Al_2O_3) were prepared following the method described in Chapter 2, Section 2.2.1. The electrochemical measurements were carried out using a μAutolabII potentiostat. A glassy carbon elec-

trode (GCE, diameter 3.0 mm) and a carbon fibre microdisc electrode (μ-CE, diameter 10 μm) were used as working electrodes, with surface preparation as described in Chapter 2, Section 2.3.3. A platinum mesh and a saturated calomel electrode (SCE) were used as the counter and reference electrode respectively. Details about scanning electron microscope (SEM) imaging can be found in Chapter 2, Section 2.4.

5.3 Results and Discussion

This work first reports the cyclic voltammetry of ensembles of catechol-adsorbed alumina formed *via* abrasive modification of glassy carbon electrodes. Second, the chronoamperometry of individual catechol-modified alumina particle impacts at carbon fibre microdisc electrodes is analysed. Finally, the impact transients are fitted utilising the model of charge diffusion over the surface of a sphere.

5.3.1 Cyclic Voltammetry

First, a "transfer experiment" was conducted to confirm the voltammetry of catechol-adsorbed alumina at a glassy carbon electrode (GCE) so as to estimate suitable redox potentials for the subsequent impact experiments. The GCE was abrasively modified with catechol-alumina (H_2C-Al_2O_3) following the method described in Chapter 2, Sections 2.2.1 and 2.3.3. The modified electrode was immerged into a pH 3.0 buffer. The ensemble voltammetry (Figure 5.4, red line) was recorded from -0.30 to $+0.90$ V and then reversed to -0.30 V at a scan rate of 150 mV s^{-1}. Figure 5.4 shows that oxidative and reductive peaks were observed at *ca.* $+0.42$ V and $+0.35$ V, respectively. This is consistent with Chapter 3 showing that catechol strongly adsorbed on the surface of alumina undergoes redox conversion to adsorbed 1,2-benzoquinone at these potentials. For comparison, a blank voltammogram was recorded in the same solution but on an unmodified-alumina-

immobilised GCE (Figure 5.4, black line). It is apparent that there is no redox signal observable on the unmodified-alumina-immobilised GCE. The voltammetry of catechol-adsorbed alumina has been fully discussed in Chapters 3 and 4.

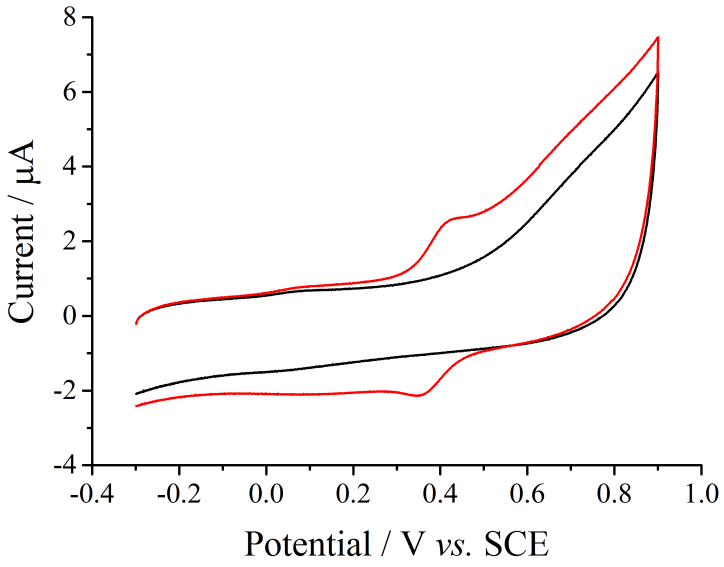

Figure 5.4: Cyclic voltammograms measured in pH 3.0 buffer. Red: at a catechol-alumina-modified glassy carbon electrode. Black: at an unmodified-alumina-immobilised glassy carbon electrode. Scan rate = 150 mV s^{-1}.

5.3.2 Particle Impact Chronoamperometry

According to the results in the preceding section, for the case of catechol-alumina particle impacts at a carbon fibre microdisc electrode (μ-CE), oxidation might be expected to take place when the potential applied to the electrode is at least *ca.* +0.40 V or higher. Chronoamperograms were recorded at the potential of +0.90 V after a known amount of catechol-alumina was added. Here, a large overpotential was applied to fully drive the exhaustive oxidation of the surface-bound catechol (as discussed more fully later). In Figure 5.5, the red line shows impact spikes corresponding to the oxidation of catechol when the particles are in contact with μ-CE. The measurements were repeated five times. For comparison, chronoamperograms were recorded at +0.90 V with addition of the same amount of unmodified alumina. No impact spikes were observed (Figure 5.5, black line).

This confirms that the oxidation of catechol on the surface of alumina is the source of the impact signal. Data for other potentials is reported later.

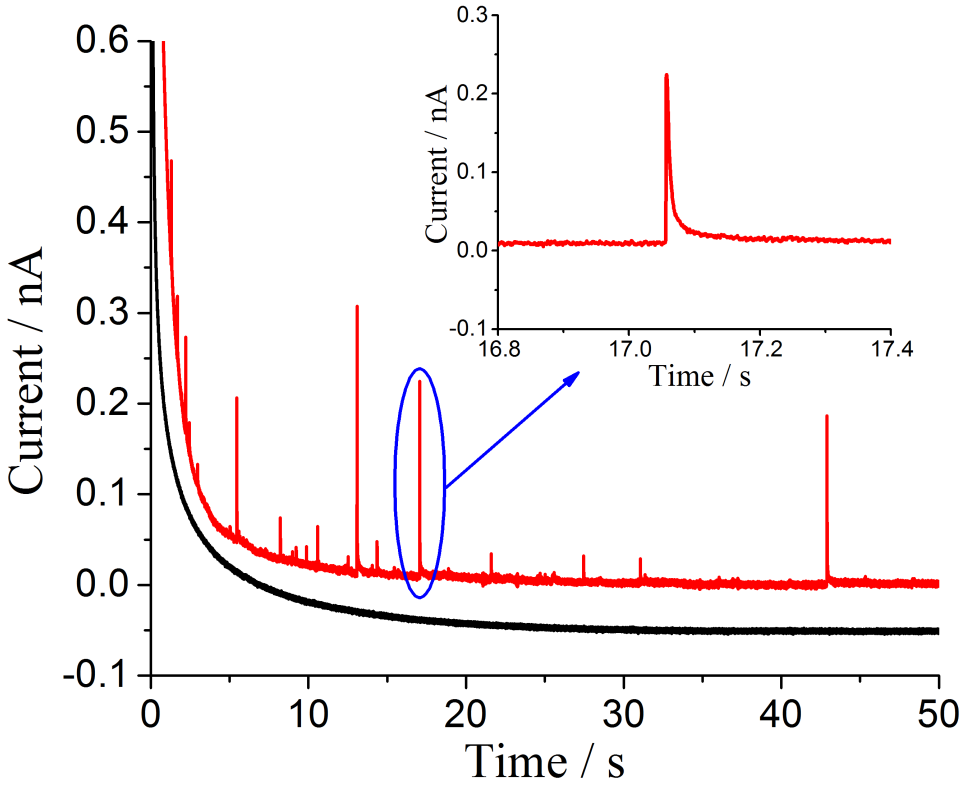

Figure 5.5: Chronoamperograms measured at +0.90 V at a carbon fibre microdisc electrode. Red: oxidation spikes for catechol-alumina particles. Inlay: zoom of circled individual spike. Black: no spikes are seen for unmodified alumina particles. The baseline has been vertically shifted downwards by 50 pA for clarity.

The charge passed during the collision between a catechol-alumina particle and μ-CE can be derived by integrating the individual current spikes. Figure 5.6 shows the distribution of charge passed per individual spike (Q) over five 50 s scans. Following the framework of a log-normal distribution, the mean charge is generated by ORIGIN as 0.60 $\pm$ 0.07 pC. Q can be related to the coverage of catechol on the alumina particles *via*

$$Q = neN \tag{5.10}$$

where n is the number of electrons transferred per catechol molecule ($n = 2$), e is the electronic charge, and N is the number of catechol molecules adsorbed per alumina particle.

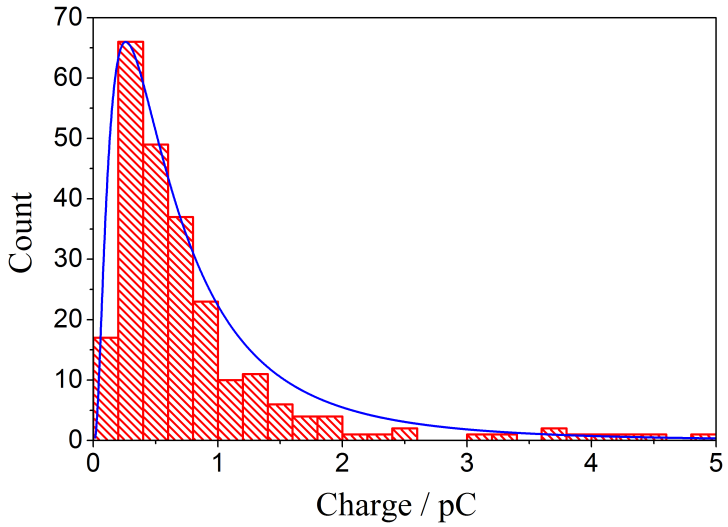

Figure 5.6: Histogram of charge passed per individual spike, relating to catechol-alumina particles. The log-normal distribution is plotted in the blue curve. The mean charge is 0.60 ± 0.07 pC.

The latter is given by the following equation

$$N = \frac{S_{alumina}}{S_{catechol}} \tag{5.11}$$

where $S_{alumina} = 4\pi r_{alumina}^2$ is the surface area of an alumina particle, with the radius of alumina denoted as $r_{alumina}$, and $S_{catechol}$ is the molecular area of a single adsorbed catechol molecule. Combining Eq. 5.10 and 5.11 gives

$$S_{catechol} = \frac{4\pi r_{alumina}^2 ne}{Q} \tag{5.12}$$

where $r_{alumina} = 0.29 \pm 0.20$ μm from SEM (Chapter 2, Section 2.4) and $Q = 0.60 \pm 0.07$ pC from impact experiments. The value of $S_{catechol}$ can, hence, be derived as 5.6 × 10^{-15} cm^2. This suggests that the coverage is close to that of a full monolayer, since by approximating $S_{catechol}$ as a rectangle (Figure 5.7) with bond lengths for C-C (aromatic), C-H, and C-O being 140, 110 and 136 pm, respectively, and assuming a close packed array a molecular area of *ca.* 5.5 × 10^{-15} cm^2 is estimated. With the measured $S_{catechol}$, the

average coverage (Γ_i) of catechol on the alumina is estimated as $(3.0 \pm 2.5) \times 10^{-10}$ mol cm^{-2}.

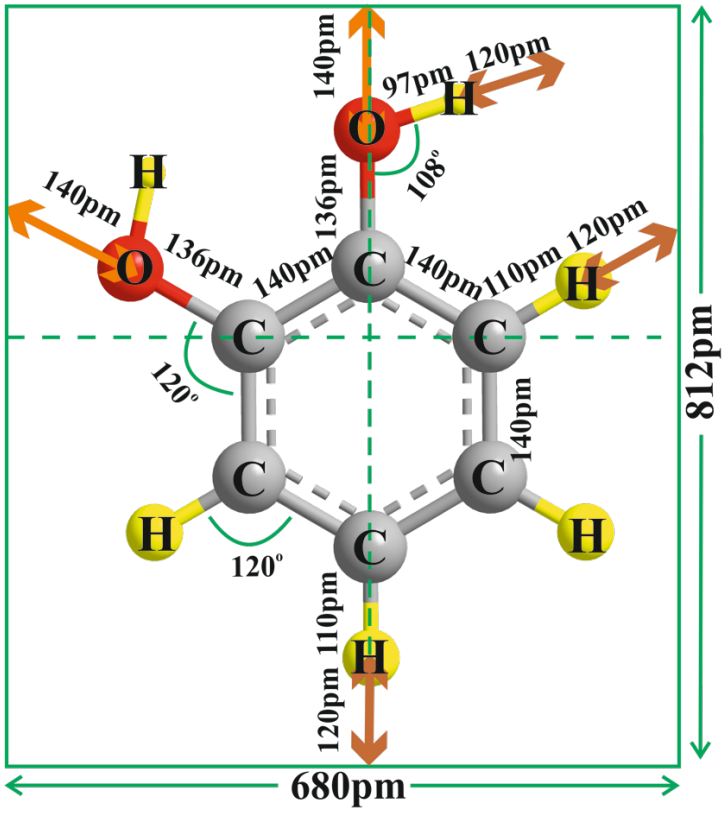

Figure 5.7: Catechol molecular area model.

It is also helpful to compare the size distribution measured *via* electrochemical impacts with that measured using SEM combined with the estimated area occupied by an adsorbed catechol molecule on the alumina particle surface. A log-normal distribution is used here, since experimental histograms show the typical pattern of a log-normal distribution. The comparison is shown in Figure 5.8, and good agreement is seen. The impact data is slightly weighted in favour of smaller, faster diffusing particles, and so there is a small discrepancy at larger radii.[6]

To find the influence of potential on the impact experiments, chronoamperograms were recorded at different potentials, from +0.30 to +1.30 V, after the same amount of catechol-alumina was added. The mean charge passed per individual spikes (Q) was plotted against

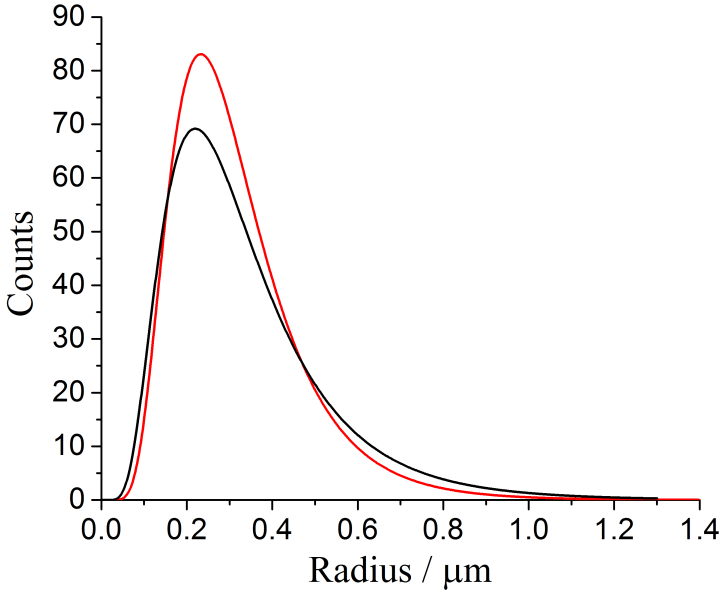

Figure 5.8: Size distribution of catechol-alumina particles by two methods. Red: obtained from impacts at a carbon fibre microdisc electrode. The mean radius is 0.29 ± 0.15 μm. Black: obtained from scanning electron microscope image. The mean radius is 0.29 ± 0.20 μm. Both mean radii are generated from log-normal distributions.

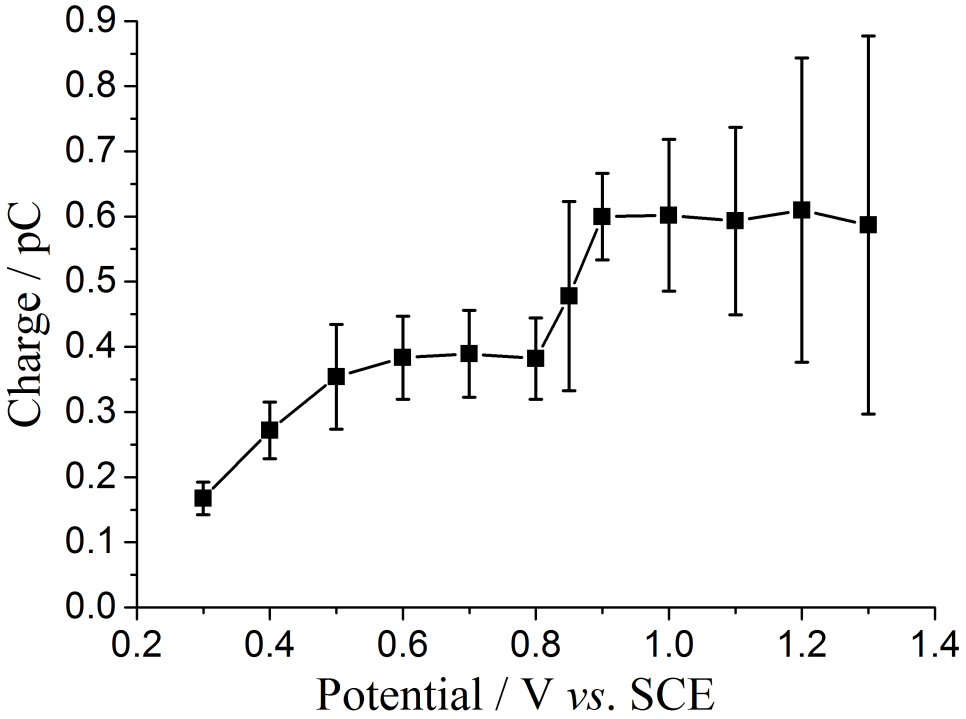

Figure 5.9: Potential variation of the mean charge passed per individual spike. The mean charge at each potential is generated from a log-normal distribution. The error of the mean charge is given by $SD/n''^{1/2}$, where SD is the standard deviation and n'' is the number of spikes.[7]

the potential, as shown in Figure 5.9. It can be seen that the amplitude of impact spikes is dependent of the potential applied. Overall, the amount of charge observed around +0.90 V and above is expected from the ensemble voltammetry discussed earlier where a two-electron oxidation of H_2C to Q is seen. However, the entire plot resembles a "voltammogram" of two separate voltammetric waves, one near +0.40 V as expected but the second at a much higher potential of *ca.* +0.85 V. This can be understood as follows.

5.3.3 Discussion

When the potential is above +0.90 V, Q remains constant at its maximum value of *ca.* 0.6 pC, consistent with the two-electron oxidation of catechol being fully driven

$$H_2C - 2e^- - 2H^+ \rightleftarrows Q \tag{5.13}$$

At lower potentials between +0.40 and +0.80 V, it appears that only the process

$$H_2C - e^- - H^+ \rightleftarrows SH \tag{5.14}$$

is observed since approximately half the charge is passed. The onset potential of this process is similar to that seen in the ensemble voltammetry. The contrast between the impact and ensemble voltammetry likely lies in the mechanism by which H_2C is converted into Q. As noted earlier, this involves the following rate-determining step (Chapters 3 and 4)

$$2SH \rightarrow Q + H_2C \tag{5.15}$$

so that a disproportionation (DISP) mechanism is followed. The measurement time scale for ensemble voltammetry is relatively slow (seconds) so that there is ample time for the disproportionation of SH to occur on the voltammetry time scale and, hence, for a full

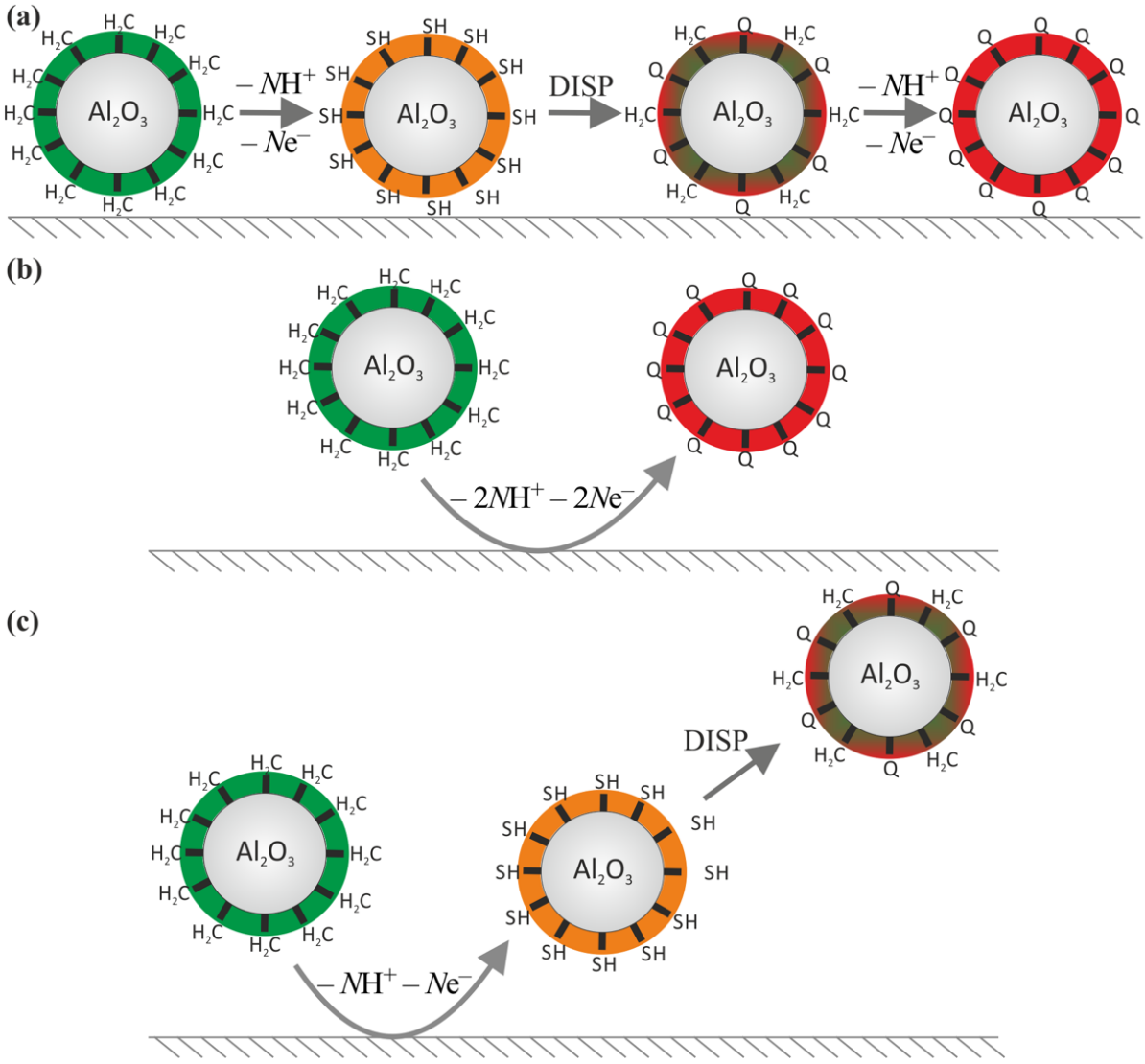

Figure 5.10: Different mechanisms corresponding to (a) ensemble voltammetry when the potential is at +0.40 V, (b) impact voltammetry when the potential is above +0.90 V, and (c) impact voltammetry when the potential is above +0.40 V. N is number of catechol molecules adsorbed per alumina particle.

two-electron reaction to be seen around +0.40 V and at more positive potentials. In contrast, during impact coulometry, the duration of the impacts is limited to around *ca.* $10 \sim 100$ ms. It seems, therefore, that the disproportionation kinetic step is outrun during impacts, and so for potentials around +0.40 V, the reaction is limited at the one-electron stage. In order for a second electron to be transferred, the reactant must be measured to *ca.* +0.85 V to drive the reaction

$$\mathrm{SH} - \mathrm{e}^- - \mathrm{H}^+ \rightleftarrows \mathrm{Q} \tag{5.16}$$

via electron transfer from SH to the electrode rather than *via* disproportionation followed by electron transfer from H_2C. Therefore, a change of mechanism is seen between the impact and ensemble voltammetry. The mechanisms and contrasts are summarised in Figure 5.10.

5.3.4 Modelling Individual Spike Transients

Following the model of charge diffusion over the surface of a sphere (Figure 5.1),[4] the individual impact spikes can be used to determine the diffusion coefficient (D_i) of charge transfer between catechol molecules over the surface of alumina particles. The coverage (Γ_i) of catechol on the surface of alumina can also be derived. Individual impact spikes from chronoamperograms at +0.90 V were picked for baseline correction and analysis. Then, the decaying part of the transient was analysed (Figure 5.11 inlay, red line). Figure 5.11 illustrates the fitting of the experimental data (in red) in order to fit the curvature of the theoretical data (in black) (note the log-log scale). This fitting was repeated for at ten individual impact spikes to obtain the mean value of D_i and Γ_i.

Given the relation between I and Nu, using Eq. 5.5 and 5.9 together with the "working curve" shown in Figure 5.3, it is found that $D_i = (2.5 \pm 0.5) \times 10^{-6}$ cm^2 s^{-1} and $\Gamma_i =$

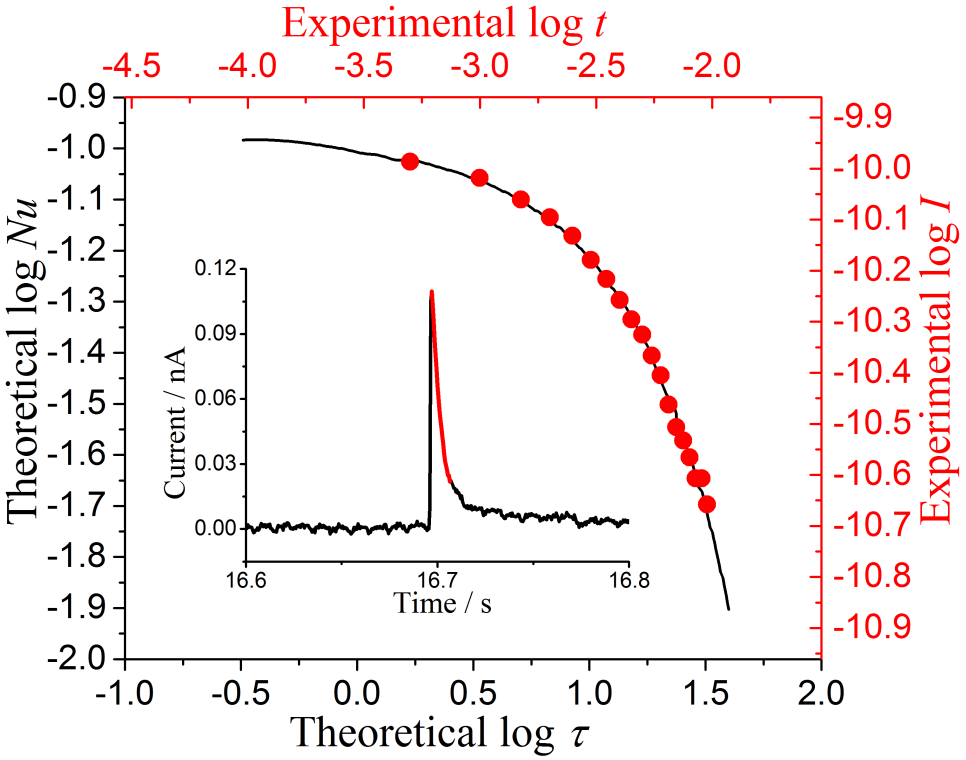

Figure 5.11: Comparison of the experimental (in red) and theoretical (in black) data. The scale of horizontal and vertical axes is 3.0 and 1.1, respectively, for both experimental and theoretical data. Inlay: chronoamperometry of the individual spike with baseline corrected. The transient in red is chosen for analysis, the logarithm of which corresponds to the red dots.

$(3.0 \pm 0.9) \times 10^{-10}$ mol cm^{-2}. The value of Γ_i is consistent with the value measured from full integration of the spike charge.

5.4 Conclusions

A new electrochemical method has been developed to use particle impacts to quantify the adsorption of redox active species on the surface of insulating particles. The amplitude of impact spikes has been found to vary with the potential applied to the electrode. At high potential, the oxidation of catechol can be fully driven to two-electron process, while at low potential, only one-electron oxidation occurs since the kinetics of the disproportionation reaction that operates in ensemble voltammetry are outrun.

Using the theory of charge diffusion over the surface of a sphere, individual impact

spikes were analysed to give the diffusion coefficient of charge transfer between catechol molecules over the surface of alumina as $(2.5 \pm 0.5) \times 10^{-6}$ cm^2 s^{-1}. The coverage of catechol on the alumina surface was found to be $(3.0 \pm 0.9) \times 10^{-10}$ mol cm^{-2}. This value is close in agreement with an estimation made assuming that catechol molecules are close-packed in a monolayer over the surface of the alumina.

References

[1] Lin, Q.; Compton, R. G. *Journal of Physical Chemistry C* **2015**, *119*, 23463–23469.

[2] Zhou, Y.-G.; Rees, N. V.; Compton, R. G. *Chemical Communications* **2012**, *48*, 2510–2512.

[3] Rees, N. V.; Zhou, Y.-G.; Compton, R. G. *Chemical Physics Letters* **2012**, *525526*, 69–71.

[4] Thompson, M.; Wildgoose, G. G.; Compton, R. G. *ChemPhysChem* **2006**, *7*, 1328–1336.

[5] Amatore, C.; Bouret, Y.; Maisonhaute, E.; Goldsmith, J. I.; Abruña, H. D. *Chemistry - A European Journal* **2001**, *7*, 2206–2226.

[6] Ellison, J.; Tschulik, K.; Stuart, E. J. E.; Jurkschat, K.; Omanović, D.; Uhlemann, M.; Crossley, A.; Compton, R. G. *ChemistryOpen* **2013**, *2*, 69–75.

[7] Stuart, E. J.; Tschulik, K.; Batchelor-McAuley, C.; Compton, R. G. *ACS Nano* **2014**, *8*, 7648–7654.

Chapter 6

Impacts Reveal and Quantify Monolayer Adsorption on Single Alumina Particles

The previous chapter introduced the use of particle impacts to quantify adsorption of redox active species on single insulating particles by simulation of individual spike transient. This chapter applies this method to various further species, including catechol, 9,10-anthraquinone, chloranil and poly(vinylferrocene). The corresponding charge diffusion coefficients and coverages over the surface of alumina particles are derived. It is demonstrated that by the use of individual particle impacts, the complexity of measurements with ensembles of particles can be circumvented.

6.1 Introduction

Proof of concept of a method has been provided in Chapter 5 to quantify adsorption and charge diffusion of electroactive species on the surface of individual insulating particles (Figure 6.1). In this method, particles are modified with electroactive species and suspended in aqueous solution for impact experiments. The impact spike transient is then simulated on the basis of the theory for Fickian charge diffusion from one molecule to another over the surface of a full sphere[1]. The electron diffusion over the surface of the particle is assumed to be faster than for example rotation of the sphere. The modelling is

achieved by introducing two parameters, the dimensionless time (τ) and the dimensionless current (Nu), defined as the following (Chapter 5)

$$\tau = tD_i/r_s^2 \tag{6.1}$$

$$Nu = \frac{I}{2\pi nFD_i\Gamma_i} \tag{6.2}$$

where t and I is time and current in particle impact chronoamperometry, n is the number of electrons transferred per modifier molecule, F is the Faraday constant (96 485 C mol^{-1}), Γ_i is surface coverage of modifier, and D_i is diffusion coefficient of charge transferred over the surface of the sphere. The theoretically generated log-log plot of Nu versus τ ("working curve") is shown in Chapter 5, Figure 5.3.

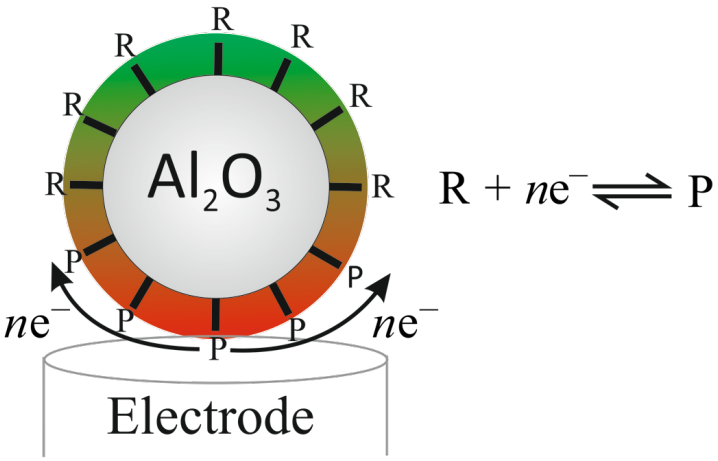

Figure 6.1: Charge diffusion model: reactant (R) reduced to product (P).

In this chapter, adsorption and charge diffusion of catechol, 9,10-anthraquinone, chloranil (tetrachloro-1,4-benzoquinone) and poly(vinylferrocene) on the surface of alumina particle are studied *via* impacts by modelling the individual spike transients. The surface coverages of redox active species on the surfaces of insulating alumina particles derived from this method will be shown to be consistent with the charge passed per impact spike, and revealed to be consistent with a *ca.* full monolayer coverage as estimated from the molecular size for the molecules lying flat on the surface.

6.2 Experimental

Details about the chemical reagents and buffer solutions here utilised can be found in Chapter 2, Section 2.1. The redox reactions of catechol (H_2C), 9,10-anthraquinone (AQ), chloranil (tetrachloro-1,4-benzoquinone, TCBQ) and poly(vinylferrocene) (PVFc) is shown in Figure 6.2. 0.1 M KCl was used as the supporting electrolyte. The alumina particles were modified following the method described in Chapter 2, Section 2.2.1. Voltammetric measurements were realised using a μAutolab III potentiostat, and impact chronoamperograms were recorded using an in-house-built low-noise potentiostat (Chapter 2, Section 2.3). A glassy carbon electrode (GCE, diameter 3.0 mm) and a carbon fibre microdisc electrode (μ-CE, diameter 33 μm) were used as working electrodes, with their surfaces prepared as described in Chapter 2, Section 2.3.3. Compared to the size of μ-CE used in Chapter 5 (diameter 10 μm), a bigger size was used here to enhance probability of particle-electrode collisions. A platinum mesh and a saturated calomel electrode (SCE) were used as the counter and reference electrode, respectively.

6.3 Results and Discussion

This work first reports the cyclic voltammetry of the four types of modified alumina particles immobilised on a glassy carbon electrode. The particles are catechol-alumina, 9,10-anthraquinone-alumina, chloranil-alumina and poly(vinylferrocene)-alumina. Second, collisions between the modified particles and a carbon fibre microdisc electrode are studied *via* particle impact chronoamperometry. Finally, the experimental spike transients are simulated using the charge diffusion theory, allowing the derivation of surface coverage and charge diffusion coefficient of modifiers over the surface of the sphere, leading to the insight that the coverage is approximately monolayer.

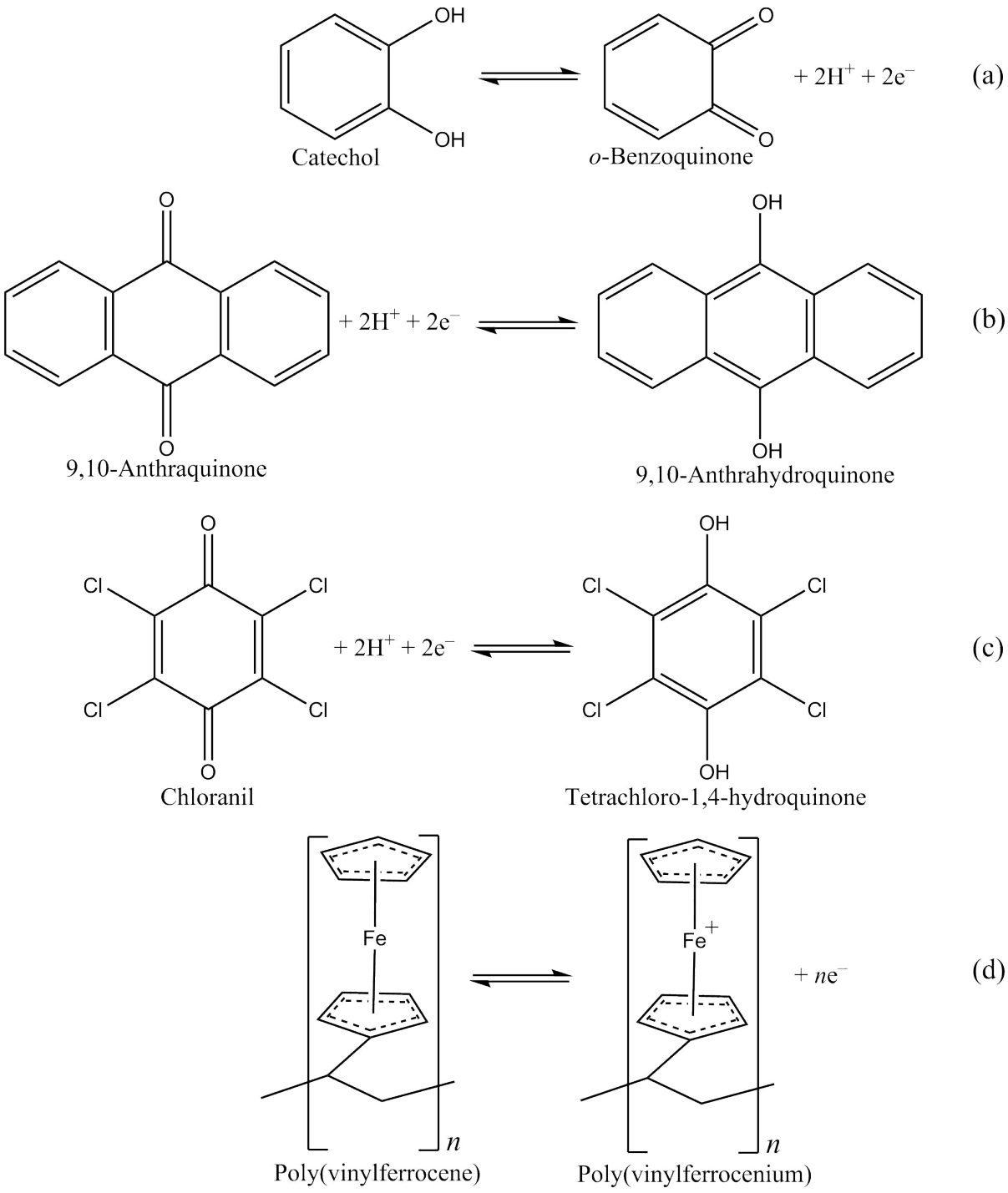

Figure 6.2: Redox reactions of catechol (H2C), 9,10-anthraquinone (AQ), chloranil (TCBQ) and poly(vinylferrocene) (PVFc).

6.3.1 Cyclic Voltammetry

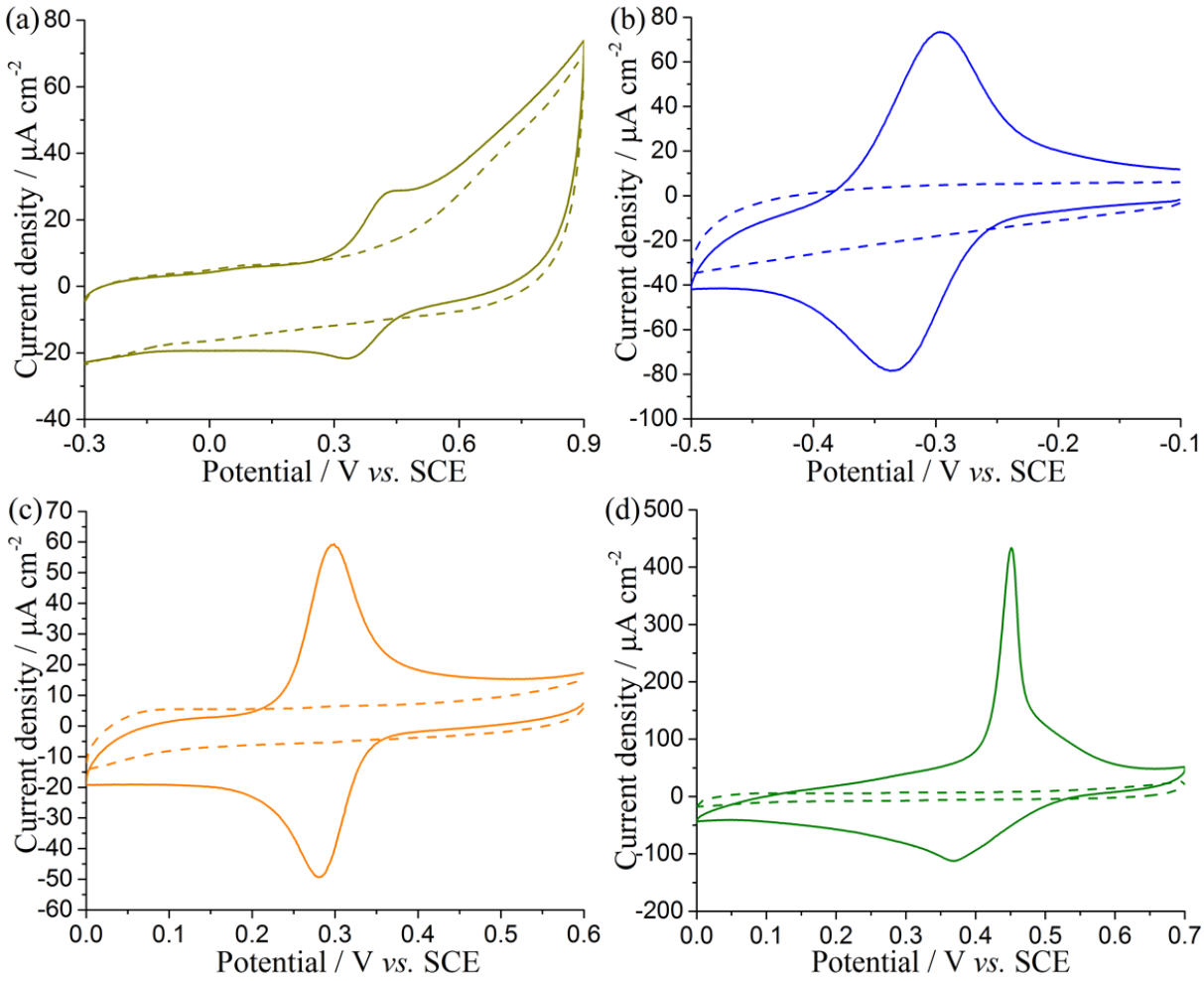

Figure 6.3: Voltammograms in pH 3.0 buffer at a glassy carbon electrode immobilised with modified (lines) and unmodified (dashed line) alumina particles. (a) Catechol-alumina, (b) 9,10-anthraquinone-alumina, (c) chloranil-alumina, and (d) poly(vinylferrocene)-alumina. Scan rate = 100 mV s^{-1}. Current density is obtained from dividing the current by the geometric area of the electrode.

The cyclic voltammetry of modified alumina particles immobilised onto a GCE surface was conducted to confirm the adsorption of modifiers on the surface of alumina. Catechol-alumina (H_2C-Al_2O_3) was first abrasively modified onto the GCE (Chapter 2, Section 2.3.3). The electrode was transferred to pH 3.0 buffer. Cyclic voltammetry was run from −0.30 to +0.90 V (*vs.* SCE) and reversed to −0.30 V at a scan rate of 100 mV s^{-1} (Fig. 6.3a, line). For comparison, a blank voltammogram was recorded in the same solution using a GCE immobilised with unmodified alumina (Fig. 6.3a, dashed line). An

oxidative response can be observed at *ca.* +0.42 V, corresponding to the oxidation of the adsorbed catechol to 1,2-benzoquinone (Figure 6.2a). The oxidative peak occurs at the same potential as reported in Chapters 3 $\sim$ 5.

Second, 9,10-anthraquinone-alumina (AQ-Al_2O_3) was abrasively modified onto the GCE. The electrode was transferred to pH 3.0 buffer to scan the voltammetry from −0.10 to +0.50 V (*vs.* SCE) and back to −0.10 V (Figure 6.3b, line). The dashed line in Figure 6.3b shows the blank voltammogram recorded in the same range using a GCE immobilised with unmodified alumina. A reductive response commencing at *ca.* −0.34 V corresponds to the reduction of the adsorbed 9,10-anthraquinone to 9,10-anthrahydroquinone (Figure 6.2b). The reduction potential is in a good agreement with the literature reported value as −0.36 V for 9,10-anthraquinone-modified carbon powder immobilised at a basal plane pyrolytic graphite electrode[3], after recalculating the literature value of the potential to pH 3.0 with the use of Nernst equation. Third, chloranil-alumina (TCBQ-Al_2O_3) was abrasively modified onto the GCE and the electrode was transferred to pH 3.0 buffer. A voltammogram was recorded in the potential window between +0.60 and 0 V (*vs.* SCE, Figure 6.3c, line), in comparison with another blank voltammogram at a GCE immobilised with unmodified alumina (Figure 6.3b, dashed line). A reductive peak at *ca.* +0.28 V can be ascribed to the reduction of chloranil to tetrachloro-1,4-hydroquinone (Figure 6.2c). The observed midpoint potential, +0.29 V, is close to the value reported for chloranil derivatised carbon paste electrode in pH 3.0 buffer, as +0.20 V after corrected the reference electrode to SCE.[4]

Fourth, poly(vinylferrocene)-alumina (PVFc-Al_2O_3) was drop-casted onto the GCE prior to its voltammetric measurement between 0 and +0.70 V (*vs.* SCE) in pH 3.0 buffer (Figure 6.3d, line). The dashed line in Figure 6.3d depicts the blank voltammogram obtained using a GCE immobilised with unmodified alumina. The oxidative signal at *ca.* +0.45 V can be described by the one-electron oxidation of the ferrocene moiety to

the ferrocenium cation (Figure 6.2d). This is close to the value, +0.52 V, reported for poly(vinylferrocene) modified graphene nanoplatelets immobilised onto the edge-plane pyrolytic graphite electrode.[5] The back peak is broader and smaller than the forward peak, which can be rationalised to the ion-pairing between the ferrocenium cation and the chloride anion from the supporting electrolyte. The ferrocenium cation is hence stabilised, and its reduction becomes thermodynamically less favourable.[6] However, for consistency, KCl was still chosen to be the supporting electrolyte so that parameters of PVFc-Al_2O_3 can be comparable to the other three types of modified particles. Note the reason of drop-casting PVFc-Al_2O_3 instead of abrasive modification is that the former gives significantly better oxidative signal. This may originate from variability of electrical contact between the modified alumina particles and glassy carbon electrode surface in terms of surface preparation.

It is inferred from the voltammetric signals that catechol, 9,10-anthraquinone, chloranil and poly(vinylferrocene) are all adsorbed on the surface of alumina particles. However, the voltammetry cannot be employed to determine the surface coverage of redox active species on the particles. The modification of ensembles of particles on a macroelectrode often leads to agglomeration and/or aggregation[7–9], complicating possible simulation or quantitative analysis. In contrast, impact chronoamperometry ensures the individual particle being measured is directly in contact with the microelectrode[9]. Therefore, in order to genuinely quantify adsorption of the molecules on the particles, the study of impacts of individual particles is probably essential.

6.3.2 Particle Impact Chronoamperometry

With the aim to quantify the adsorption of different molecules on single alumina particles, impact chronoamperometry was conducted. The cyclic voltammetry in the preceding section allows estimations of the minimum potentials required for impacts of individual

modified alumina particle at a μ-CE to be seen, although a large overpotential was typically applied to fully drive the exhaustive redox of the surface bound molecules (Chapter 5). The oxidation of H_2C-Al_2O_3 and PVFc-Al_2O_3 should take place when the applied potential is more positive than +0.42 and +0.45 V, and the reduction of AQ-Al_2O_3 and TCBQ-Al_2O_3 should occur when the applied potential is more negative than −0.34 and +0.28 V, respectively.

The modified alumina particles were suspended in pH 3.0 buffer. The electrode was potentiostatted at +0.90, −0.80, −0.50 and +1.00 V for H_2C-Al_2O_3, AQ-Al_2O_3, TCBQ-Al_2O_3 and PVFc-Al_2O_3, respectively, for 20 s to run chronoamperometry. Fig. 6.4 shows impact spikes can be observed, with the number of spikes recorded in Table 6.1a. The charge passed during the particle-electrode collision can be derived by integrating the area under the individual spikes. The histograms in Figure 6.5 shows the distribution of the charge passed per impact spike (Q), with the average value of (6.0 ± 0.7), (4.3 ± 3.4), (5.1 ± 1.0) and (2.1 ± 0.8) × 10^{-13} C for H_2C-Al_2O_3, AQ-Al_2O_3, TCBQ-Al_2O_3 and PVFc-Al_2O_3, respectively (Table 6.1b). Q can be correlated with the surface coverage (Γ_i) of the modifier on the alumina particle *via* (Chapter 4)

$$\Gamma_i = \frac{Q}{neN_A S_{alumina}} \tag{6.3}$$

where e is the electronic charge and N_A is the Avogadro constant. $S_{alumina}$ is the surface area of alumina with the value of *ca.* 1.06 × 10^{-8} cm^2, according to $S_{alumina} = 4\pi r_{alumina}^2$ where $r_{alumina}$ is the radius of alumina (*ca.* 0.29 μm, Chapter 2, Section 2.4). According to Figure 6.2, the value of n is 2 for catechol, 9,10-anthraquinone and chloranil, but 1 for poly(vinylferrocene). With the measured Q, Γ_i can be estimated as (2.9 ± 0.3), (2.1 ± 1.7), (2.5 ± 0.5), and (2.1 ± 0.8) × 10^{-10} mol cm^{-2} for H_2C-Al_2O_3, AQ-Al_2O_3, TCBQ-Al_2O_3 and PVFc-Al_2O_3, respectively (Table 6.1d). These values are consistent with monolayer coverage assuming molecules are close-packed parallel to the surface of

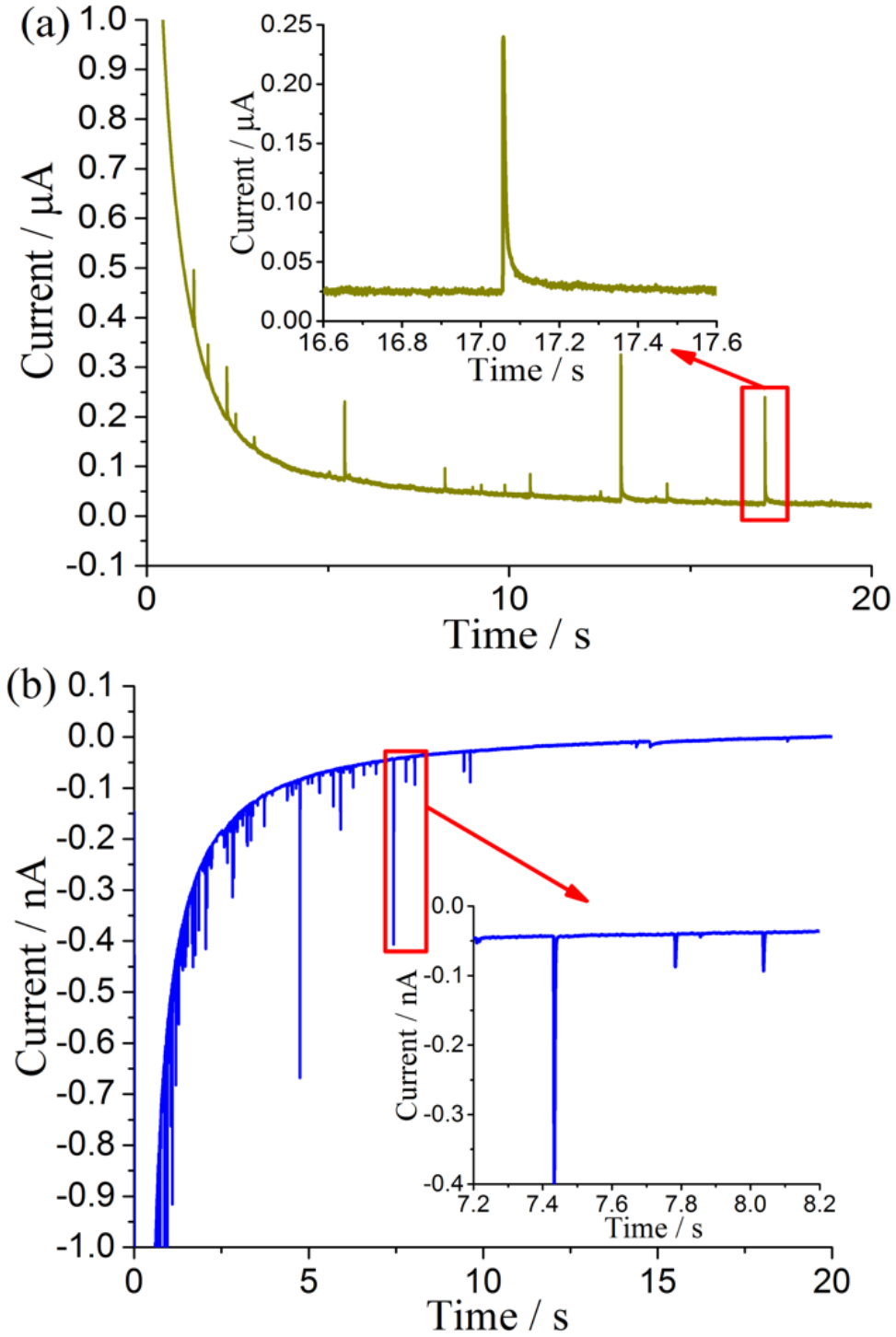

Figure 6.4: Particle impact chronoamperograms of modified alumina particles at a carbon fibre microdisc electrode, in pH 3.0 buffer. Various potentials were applied to the electrode for different particles: (a) Catechol-alumina at +0.90 V, and (b) 9,10-anthraquinone-alumina at −0.80 V. Baselines are corrected for modelling individual spike transients in the following discussion.

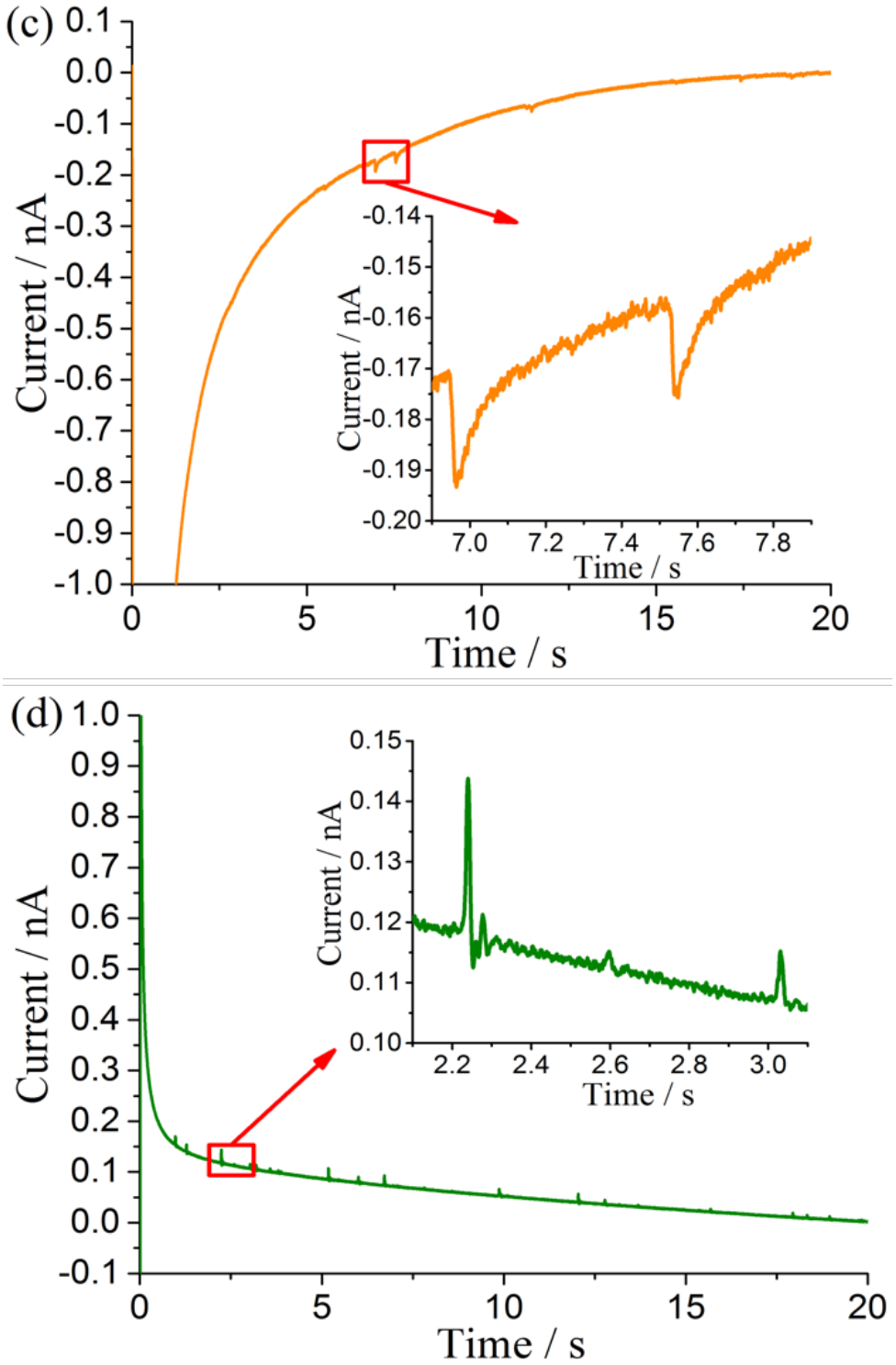

Figure 6.4: Particle impact chronoamperograms of modified alumina particles at a carbon fibre microdisc electrode, in pH 3.0 buffer. Various potentials were applied to the electrode for different particles: (c) chloranil-alumina at −0.50 V, and (d) poly(vinylferrocene)-alumina at +1.00 V. Baselines are corrected for modelling individual spike transients in the following discussion.

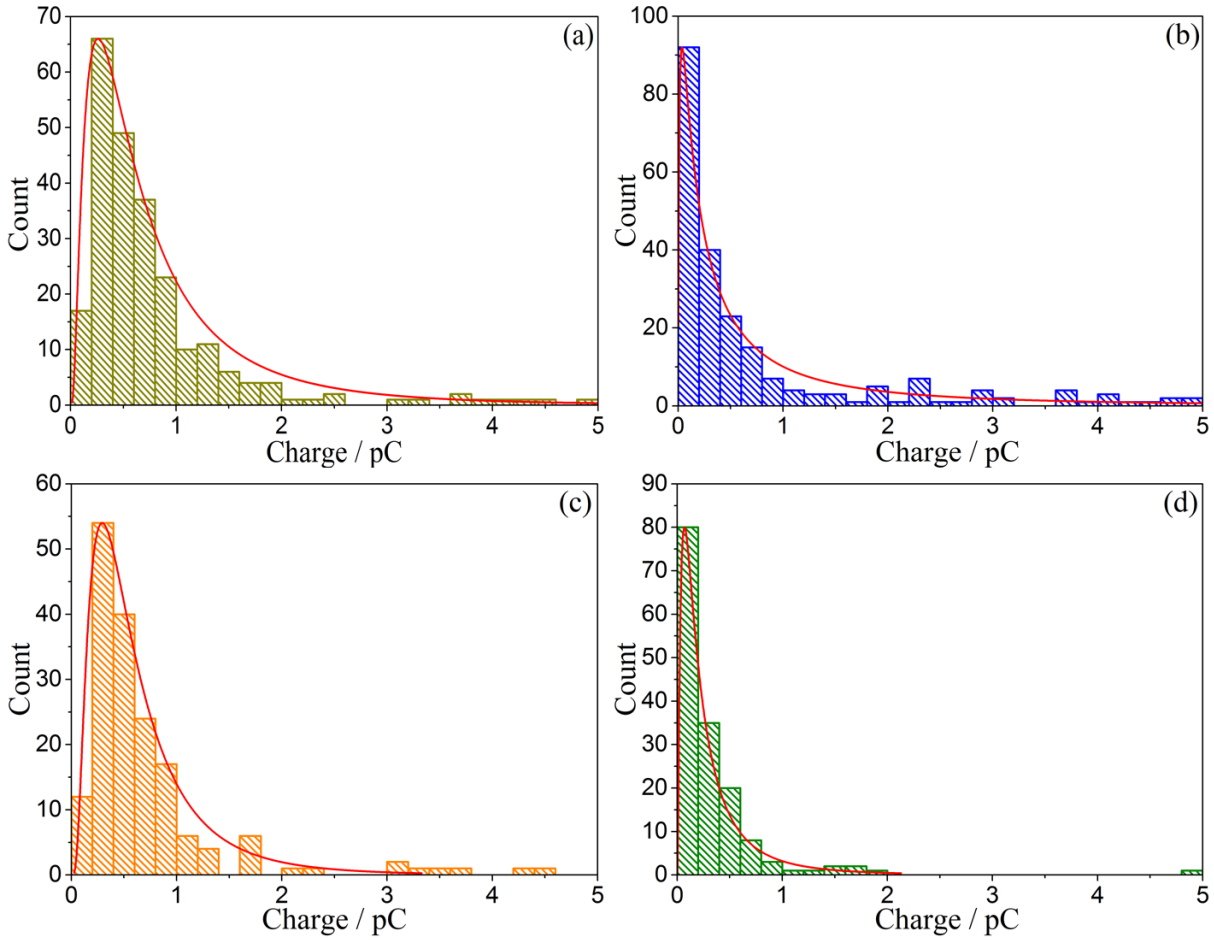

Figure 6.5: Histograms of charge passed per impact spike, with log-normal distribution plotted in the curve. (a) Catechol-alumina, (b) 9,10-anthraquinone-alumina, (c) chloranil-alumina, and (d) poly(vinylferrocene)-alumina.

the single alumina particle, according to $\Gamma_i = S_{alumina}/S_{molecule}$ where $S_{molecule}$ is the molecular area of modifiers calculated as follows, using catechol as an example (Chapter 5, Figure 5.7). By assuming each molecule is a rectangle, both side lengths can be estimated by using trigonometry for bond lengths, bond angles and Van der Waals radii of periplanar atoms. $S_{molecule}$ can hence be predicted, as listed in Table 6.1c. Note that $S_{molecule}$ for ferrocene moiety in poly(vinylferrocene) is estimated by considering the planar five-membered ring with a two-membered alkyl chain (Figure 6.2d) in a rectangle parallel to the surface of alumina. The corresponding Γ_i values are (3.0 ± 2.5), (1.6 ± 1.6), (2.0 ± 1.9) and (2.9 ± 2.8) × 10^{-10} mol cm^{-2} for H_2C-Al_2O_3, AQ-Al_2O_3, TCBQ-Al_2O_3 and PVFc-Al_2O_3, respectively (Table 6.1e).

Modifier	(a)	(b)	(c)	(d)	(e)	(f)	(g)
	Number of impact spikes	Average charge passed per impact spike / 10^{-13} C	Molecular area of modifiers / 10^{-15} cm^2	Surface coverage of modifiers on single alumina particles / 10^{-10} mol cm^{-2}			Diffusion coefficient of charge / 10^{-6} cm^2 s^{-1}
				From (b)	From (c)	From spike transient simulation	
Catechol	246	6.0 ± 0.7	5.5	2.9 ± 0.3	3.0 ± 2.5	3.0 ± 0.9	2.5 ± 0.5
Anthraquinone	375	4.3 ± 3.4	10	2.1 ± 1.7	1.6 ± 1.6	1.5 ± 1.4	7.9 ± 4.0
Chloranil	172	5.1 ± 1.0	8.4	2.5 ± 0.5	2.0 ± 1.9	2.7 ± 1.7	0.4 ± 0.2
Ferrocene moiety of poly(vinylferrocene)	156	2.1 ± 0.8	5.6	2.1 ± 0.8	2.9 ± 2.8	2.1 ± 0.7	2.4 ± 0.8

Table 6.1: Parameters for the four modified alumina particles

6.3.3 Modelling Individual Spike Transients

Following the model developed from the theory of charge diffusion from one molecule to another over the surface of a full sphere[1], the work turns to model individual impact spike transients. As shown in the inlays of Figure 6.6, individual spikes were first chosen from particle impact chronoamperometry. After baseline subtraction, the decaying part of the transients (Figure 6.6 inlays, highlight) was analysed. The logarithm of corresponding current versus time was then plotted, as shown as circles in Figure 6.6. The theoretical log Nu versus log τ was also plotted, as shown as curves in Figure 6.6. Since the scale of theoretical log τ and log Nu is 3.5 and 3.0, respectively, the experimental log t and log I should be adjusted to be the same scale. In order for experimental circles to fit theoretical curves, differences in horizontal and vertical axes will be observed. According to the relation between t and τ (Eq. 6.1) as well as I and Nu (Eq. 6.2), the differences can be used to derive the coverage (Γ_i) and charge diffusion coefficient (D_i) of the modifier on the surface of individual alumina particles. The modelling was repeated for five individual spikes to obtain the average value of Γ_i and D_i.

For H_2C-Al_2O_3, AQ-Al_2O_3, TCBQ-Al_2O_3 and PVFc-Al_2O_3, the coverages were found to be (3.0 ± 0.9), (1.5 ± 1.4), (2.7 ± 1.7), and $(2.1 \pm 0.7) \times 10^{-10}$ mol cm^{-2}, respectively (Table 6.1e), and diffusion coefficients were found to be (2.5 ± 0.5), (7.9 ± 4.0), (0.4 ± 0.2), and $(2.4 \pm 0.8) \times 10^{-6}$ cm^2 s^{-1}, respectively (Table 6.1g). Table 6.1 shows the value of coverages are reasonable, comparing well to the average charge passed per impact spike, as well as monolayer estimation from alumina surface area as demonstrated in the preceding section. Note that the values reported are of ferrocene moiety of poly(vinylferrocene), but not of the polymer. The diffusion coefficient for TCBQ-Al_2O_3 is about one magnitude smaller compared to the other three modified alumina particles. This can be noted from the inlay of Figure 6.6c that the impact spike transient of TCBQ-Al_2O_3 is much less steep than the other three. The low diffusion coefficient reflects a slow intrinsic charge diffusion

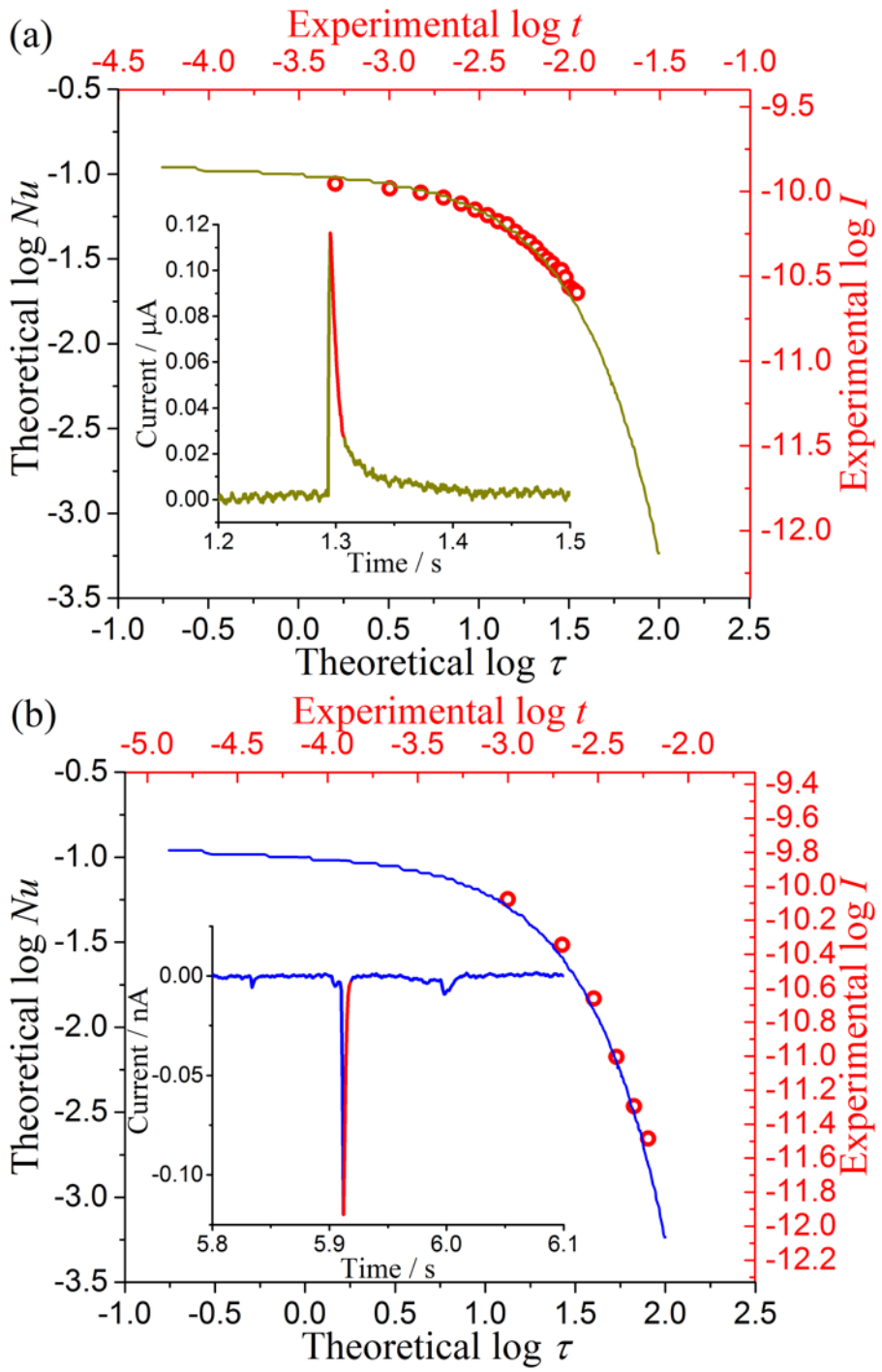

Figure 6.6: Comparison of theoretical (curves, bottom and left axes) and experimental (circles, top and right axes) log-log plot. The scale of both horizontal axes and both vertical axes is 3.5 and 3.0, respectively. Inlay: chronoamperometry of the experimental impact spike, with baseline subtracted for the modelling. The transients highlighted are used for analysis, the logarithm of which correspond to the circles. (a) Catechol-alumina, and (b) 9,10-anthraquinone-alumina.

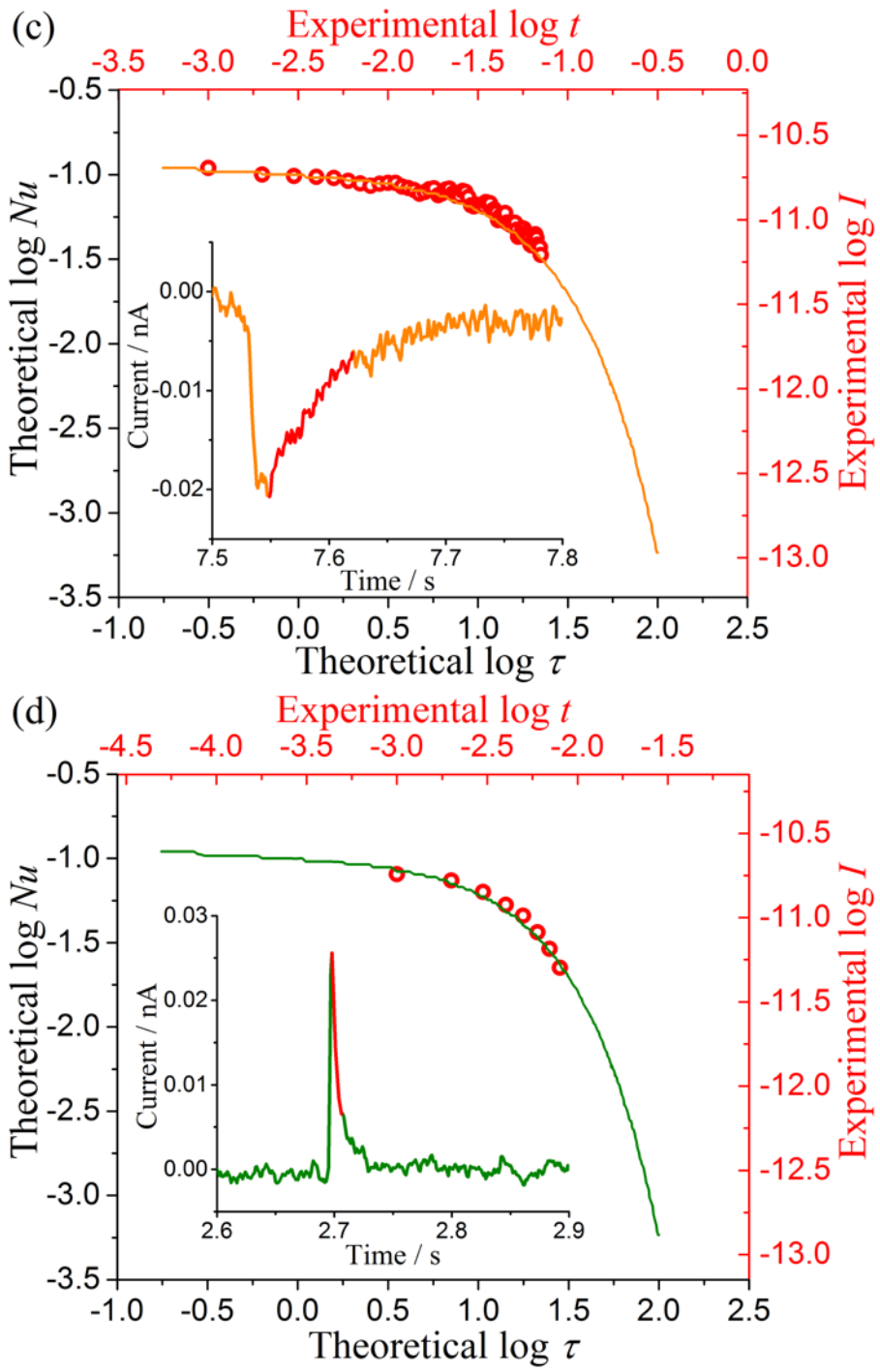

Figure 6.6: Comparison of theoretical (curves, bottom and left axes) and experimental (circles, top and right axes) log-log plot. The scale of both horizontal axes and both vertical axes is 3.5 and 3.0, respectively. Inlay: chronoamperometry of the experimental impact spike, with baseline subtracted for the modelling. The transients highlighted are used for analysis, the logarithm of which correspond to the circles. (c) chloranil-alumina, and (d) poly(vinylferrocene)-alumina.

between adsorbed chloranil molecules.

6.4 Conclusions

This chapter has successfully simulated individual impact spike transients to determine the charge diffusion coefficients among the molecules over the surface of alumina, as (2.5 $\pm$ 0.5), (7.9 $\pm$ 4.0), (0.4 $\pm$ 0.2), and (2.4 $\pm$ 0.8) $\times$ 10^{-6} cm^2 s^{-1}, respectively, for catechol, 9,10-anthraquinone and chloranil molecules, and ferrocene moiety of poly(vinylferrocene). The surface coverages were found to be (3.0 $\pm$ 0.9), (1.5 $\pm$ 1.4), (2.7 $\pm$ 1.7), and (2.1 $\pm$ 0.7) $\times$ 10^{-10} mol cm^{-2}, accordingly. The new electrochemical method of modelling impacts reveals monolayer adsorption of diverse species on single insulating particles by comparison of theoretical and experimental log-log plot for the spike current-time transient. Note however that care must be taken to ensure the transient timescale is sufficiently long to avoid distortion by the measuring electronics[10, 11].

References

[1] Thompson, M.; Wildgoose, G. G.; Compton, R. G. *ChemPhysChem* **2006**, *7*, 1328–1336.

[2] Batchelor-McAuley, C.; Ellison, J.; Tschulik, K.; Hurst, P. L.; Boldt, R.; Compton, R. G. *Analyst* **2015**, *140*, 5048–5054.

[3] Pandurangappa, M.; Lawrence, N. S.; Compton, R. G. *Analyst* **2002**, *127*, 1568–1571.

[4] Ojani, R.; Raoof, J.-B.; Zamani, S. *Electroanalysis* **2005**, *17*, 1740–1745.

[5] Lin, Q.; Lin, C.; Wu, H.; Batchelor-McAuley, C.; Compton, R. G. *The Journal of Physical Chemistry C* **2016**, *120*, 20216–20223.

[6] Yang, M.; Batchelor-McAuley, C.; Gonçalves, L. M.; Lima, C. F. R. A. C.; Vyskočil, V.; Tschulik, K.; Compton, R. G. *Electroanalysis* **2016**, *28*, 197–202.

[7] Toh, H. S.; Batchelor-McAuley, C.; Tschulik, K.; Uhlemann, M.; Crossley, A.; Compton, R. G. *Nanoscale* **2013**, *5*, 4884–4893.

[8] Toh, H. S.; Compton, R. G. *ChemistryOpen* **2015**, *4*, 261–263.

[9] Toh, H. S.; Jurkschat, K.; Compton, R. G. *Chemistry - A European Journal* **2015**, *21*, 2998–3004.

[10] Kätelhön, E.; Tanner, E. E. L.; Batchelor-McAuley, C.; Compton, R. G. *Electrochimica Acta* **2016**, *199*, 297–304.

[11] Kätelhön, E.; Feng, A.; Cheng, W.; Eloul, S.; Batchelor-McAuley, C.; Compton, R. G. *The Journal of Physical Chemistry C* **2016**, *120*, 17029–17034.

Chapter 7

Stochastic Detection and Characterisation of Individual Ferrocene Derivative Tagged Graphene Nanoplatelets

Building on the impact studies of alumina particles in the previous four chapters, the work now turns to study graphene nanoplatelets. In this chapter, the GNPs are "tagged" with a ferrocene derivative. Chronoamperometry is then utilised to observe single particle impacts when the GNPs suspended in solution collide with a carbon fibre microwire electrode held at an oxidising potential, resulting in a current "spike". The impacts are associated with two types of charge transfer: Faradaic due to oxidation of the "tag" and capacitative due to disruption of the double layer. In contrast, non-derivatised ferrocene does not exhibit any significant adsorption on the GNP material.

The work herein presented has been published in *the Analyst*[1] and was performed in collaboration with Mr. Haoyu Wu, Dr. Christopher Batchelor-McAuley, Dr. Luís M. Gonçalves and Dr. Carlos F. R. A. C. Lima (University of Porto, Porto, Portugal). Mr. Haoyu Wu should be recognised for his contribution in collecting some of the experimental results. Dr. Christopher Batchelor-McAuley helped with the interpretation of the experimental results. The ferrocene derivative was synthesised by Dr. Luís M. Gonçalves and Dr. Carlos F. R. A. C. Lima.

7.1 Introduction

Graphene nanoplatelets (GNPs) are commonly activated *via* modification of diazonium salts[2, 3] or carbon radical formation from cleaved carbon-halide bonds[4, 5]. Because of the strong reactivity of the reagent, undesirable multi-layer coverage can be formed due to polymerisation. The strong chemisorption on the graphitic plane may result in destruction of the aromaticity and distortion of the voltammetric response of GNPs.[6] On the contrary, activation *via* physisorption utilising the $\pi - \pi$ stacking with aromatic molecules is thought to maintain the aromaticity of GNPs.[7, 8] Furthermore, the resulting surface coverage is limited to monolayer coverage, hence a clear voltammetric response is expected.

In this chapter, impacts of 1-(biphen-4-yl)ferrocene tagged GNPs (Figure 7.1) are investigated. The ferrocene aryl derivative is physisorbed onto the GNPs prior to dispersion in a supporting electrolyte. By potentiostatting a carbon fibre microwire electrode at an oxidising potential, sharp current transients are observed as individual tagged GNPs collide with the electrode. Two types of physical origins of the impact spikes are observed: Faradaic and capacitative. Capacitative impacts[9–11] occur when the applied potential deviates from the potential of zero charge (PZC) of the electrode/solution interface. Upon particle-electrode collisions, the double layer is disrupted and electrons flow in or out of the electrode depending on whether the applied potential is positive or negative against the PZC. Faradaic impacts[12–14] take place when the electrode is held at a sufficiently negative or positive potential to trigger a redox reaction of the electroactive modifier adsorbed on the particle surface. When the particle collides with the electrode, electrons transfer between the electroactive modifier and the electrode.

In the following particle impacts are used for the detection of GNPs *via* redox tagging. The impact spikes evidence monolayer coverage of modifier on the particle surface, with electrochemical quantification of surface coverage.

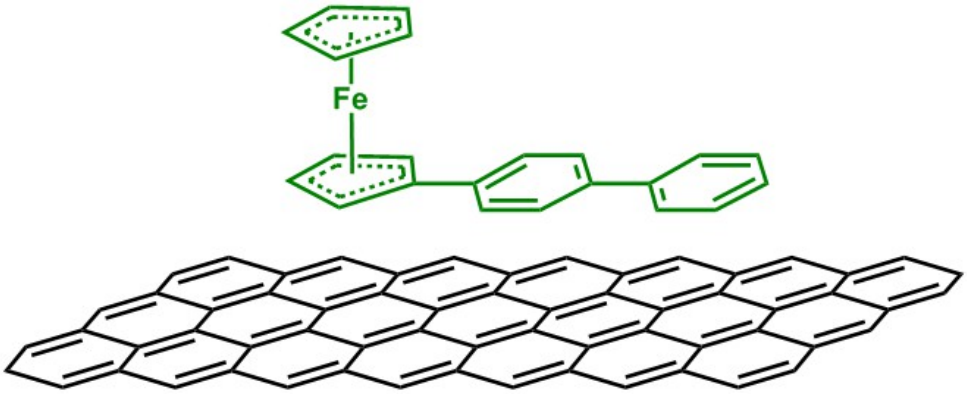

Figure 7.1: Possible structure of 1-(biphen-4-yl)ferrocene tagged graphene nanoplatelets (GNPs).

7.2 Experimental

Details about the chemical reagents and solutions here utilised can be found in Chapter 2, Section 2.1. 1-(biphen-4-yl)ferrocene was synthesised by Dr. Luís M. Gonçalves and Dr. Carlos F. R. A. C. Lima, using a Suzuki-Miyaura cross coupling reaction[15–17]. A solution of K_2CO_3 (1.4 mol per equivalent) in 12 mL of water per 1 mmol of the limiting reactant was added to a solution of 1-bromoferrocene (1 mol per equivalent), 1-(biphen-4-yl)boronic acid (1.2 mol per equivalent) and palladium (II) acetate, $Pd(OAc)_2$, (2 mol %) in the same volume of dimethylformamide. The resultant mixture was heated and stirred at 80 °C for 5 h. The final solution was allowed to cool to room temperature and extracted with dichloromethane. The organic layer was washed with water and aqueous 0.1 M KOH, dried over anhydrous sodium sulfate and evaporated, yielding the product as impure orange flakes in 53% yield. The compound was washed with methanol and diethyl ether and further purified by sublimation under reduced pressure to yield orange crystals of 1-(biphen-4-yl)ferrocene. The purity of the compound was examined by gas chromatography with a flame ionisation detector (GC-FID) to be higher than 99% (mass ratio).[17]

The structures of 1-(biphen-4-yl)ferrocene and graphene nanoplatelets (GNPs) are shown in Figure 7.1. 0.1 M $NaClO_4$ was used as the supporting electrolyte. The GNPs

were modified following the method described in Chapter 2, Section 2.2.2. Voltammetric and chronoamperometric measurements were recorded using a μAutolab II potentiostat. An edge-plane pyrolytic graphite (EPPG) electrode (diameter 4.0 mm) and a carbon fibre microwire electrode (diameter 7.0 μm) were used as working electrodes, with their surfaces prepared as described in Chapter 2, Section 2.3.3. Compared to the particle impacts experiment in Chapters 5 and 6, a carbon fibre microwire electrode with a higher surface area was used here, because GNPs (16.5 $\pm$ 5 μm in width) are bigger in size than alumina particles (0.58 $\pm$ 0.40 μm in diameter). A graphite rod and a saturated calomel electrode (SCE) were used as the counter and reference electrode, respectively.

7.3 Results and Discussion

This section first reports the cyclic voltammetry of ferrocene, 1-(biphen-4-yl)ferrocene, and corresponding modified graphene nanoplatelets (GNPs) adsorbed upon a macro EPPG electrode. Second, the chronoamperometric response of modified GNPs impacting at a carbon fibre microwire electrode is presented. For comparison, chronoamperograms of unmodified GNPs are also demonstrated. Finally, the influence of the electrode potential on the impacts experiment is discussed with respect to the magnitude of the charge passed.

7.3.1 Cyclic Voltammetry: Adsorption Transfer Experiments

Adsorption transfer experiments were undertaken to study the cyclic voltammetry of 1-(biphen-4-yl)ferrocene adsorbed on an EPPG electrode. The voltammetry is used to study the electroactivity of the ferrocene derivative and demonstrate the enhanced adsorptive ability of the modified ferrocene over ferrocene itself. An EPPG electrode was first modified with 1-(biphen-4-yl)ferrocene following the method as described in Chapter 2, Section 2.3.3. The electrode was then transferred to a 25 mL blank solution. Cyclic

voltammetry was run between −0.20 V and +0.70 V at a scan rate of 50 mV s^{-1} (Figure 7.2c). The oxidative peak potential is +0.45 V and the peak area is *ca.* 32 μC. For comparison, a ferrocene-modified EPPG electrode was studied in the same blank solution (Figure 7.2b). The oxidation of ferrocene can be observed as a broad wave, with the peak potential of +0.22 V and the peak area of *ca.* 1.6 μC. The oxidative response in both voltammograms can be described by the one-electron oxidation of the ferrocene moiety to the corresponding ferrocenium cation:

$$\text{R-Fc} \rightleftarrows \text{R-Fc}^{+} + \text{e}^{-} \tag{7.1}$$

where R is the aromatic 1-(biphen-4-yl) group (Figure 7.2c) or proton (Figure 7.2b).

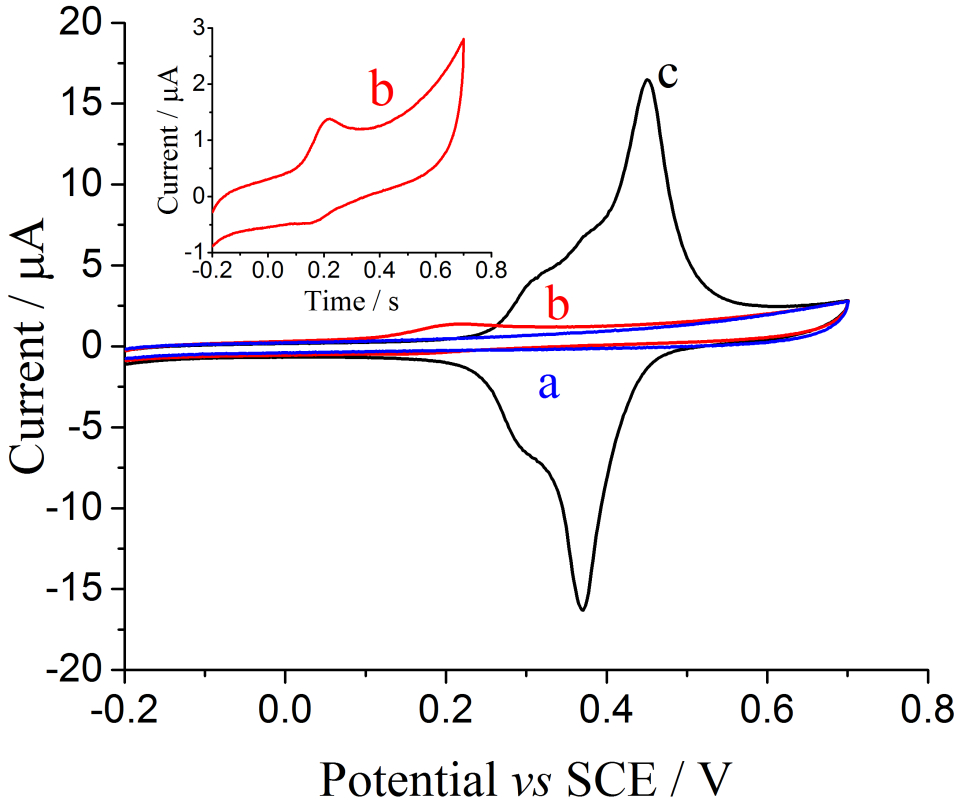

Figure 7.2: Voltammograms measured using a ferrocene- and 1-(biphen-4-yl)ferrocene-modified EPPG electrode in a blank solution. The electrode modification was achieved by immersing the electrode into a 2 mM solution in acetonitrile for 30 s. (a) Blank. (b) Ferrocene and its zoom-in (inlay). (c) 1-(biphen-4-yl)ferrocene. Scan rate = 50 mV s^{-1}.

The voltammograms of ferrocene and 1-(biphen-4-yl)ferrocene in Figure 7.2 show three differences. First, the charge in the back peak is found to change relative to the magnitude of the forward wave: for adsorbed ferrocene the change is *ca.* 44% (Figure 7.2, inlay), while for 1-(biphen-4-yl)ferrocene the change is *ca.* 3% and of a similar size to the forward peak. Second, the oxidative peak potential is shifted by 0.23 V more positive on going from ferrocene to 1-(biphen-4-yl)ferrocene. Third, and most importantly, the magnitude in terms of charge of voltammetric response is very significantly larger in 1-(biphen-4-yl)ferrocene. The former two observations likely arise due to the increased ion-pairing strength and/or solubility of the ferrocenium cation as compared to the cation of 1-(biphen-4-yl)-ferrocenium, causing a shift in the formal potential for the process.[18] The third observation of the enhanced magnitude of the redox response is associated with the much stronger adsorption of 1-(biphen-4-yl)ferrocene to the graphitic surface.

7.3.2 Cyclic Voltammetry: Abrasive Modification Experiments

Abrasive modification experiments were also conducted to confirm the adsorption of 1-(biphen-4-yl)ferrocene on the GNPs. The tagged GNPs were prepared (Chapter 2, Section 2.2.2) and abrasively modified onto an EPPG electrode (Chapter 2, Section 2.3.3). The electrode was then transferred to a 25 mL blank solution. Cyclic voltammetry was run between -0.20 V to $+0.60$ V at a scan rate of 50 mV s^{-1} (Figure 7.3c). An oxidative peak can be observed at $+0.45$ V, which is similar to that in adsorption transfer experiments. The stability of 1-(biphen-4-yl)ferrocene-modified GNPs was examined by repeating the same experiment with various time after preparation. The inlay in Figure 7.3 shows voltammograms overlay regardless of variation in time after preparation. A control experiment with unmodified GNPs was also taken in the blank solution and no oxidation was observed (Figure 7.3b). Figure 7.3a also shows the absence of any redox signals corresponding to the unmodified EPPG electrode.

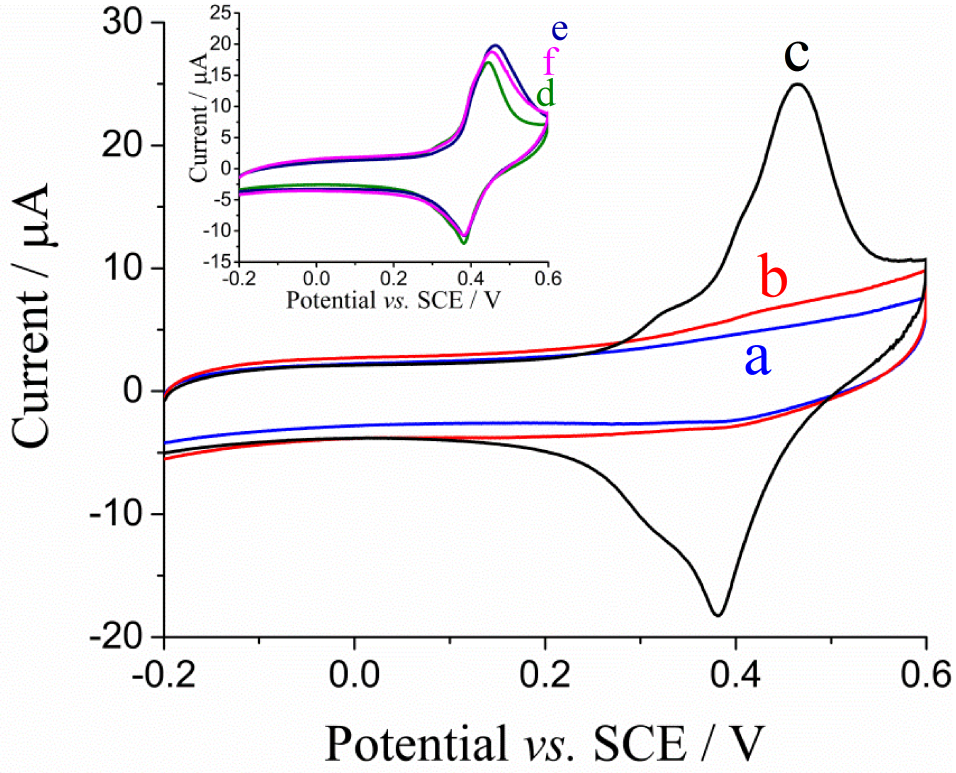

Figure 7.3: Voltammograms measured using a GNPs-modified EPPG electrode in a blank solution. The modification was achieved by abrading the electrode on a filter paper with modified/unmodified GNPs. (a) Blank. (b) Unmodified GNPs. (c) 1-(biphen-4-yl)ferrocene-modified GNPs. Inlay shows voltammograms of 1-(biphen-4-yl)ferrocene-modified GNPs with variation in time after preparation. (d) 10 min, (e) 30 min, and (f) 100 min after preparation. Scan rate = 50 mV s^{-1}.

Comparison Figure 7.3b and c confirms that 1-(biphen-4-yl)ferrocene was successfully modified onto the GNPs, further evidencing the strong adsorption between the molecules and the single GNP. The tagged GNPs were also proved to be stable, since the voltammetry (Figure 7.3, inlay) remains unchanged with different time lengths after preparation.

7.3.3 Particle Impact Chronoamperometry: Faradaic and Capacitative

With the aim to characterise individual GNPs, particle impacts experiments were conducted to investigate possible electron transfer between the single tagged GNP and a carbon fibre microwire electrode. Since ferrocene aryl derivatives have been demon-

strated to adsorb strongly on the graphitic surface[18], GNPs were modified with 1-(biphen-4-yl)ferrocene as done to amplify the electrochemical response. The results in the preceding section provide the basis for the 1-(biphen-4-yl)ferrocene-modified GNPs impacts at carbon fibre microwire electrode. Oxidation is expected to occur when the potential applied to the electrode is *ca.* +0.45 V (Figure 7.3c) or higher. 0.28 mg of 1-(biphen-4-yl)ferrocene-modified GNPs was transferred to a 5 mL blank solution. The solvent was removed by evaporation, leaving the dry modified GNPs powders to be transferred to a blank solution. The electrode was potentiostatted at +0.40 V and +0.90 V, respectively, for 20 s to run chronoamperometry. For comparison, chronoamperograms were also recorded after the same amount of unmodified GNPs was added to the blank solution.

Figure 7.4a shows at +0.40 V, impact spikes present for both unmodified (ii) and 1-(biphen-4-yl)ferrocene-modified (i) GNPs. The average charge passed per spike (Q) can be derived by taking the average of the integrated area under the individual spikes. For the spikes in 1-(biphen-4-yl)ferrocene-modified GNPs, Q is 6.6 ± 1.0 pC. These spikes are in comparable size with those seen in unmodified GNPs, with Q of 2.5 ± 0.2 pC. However, at +0.90 V (Figure 7.4b), the size of spikes in 1-(biphen-4-yl)ferrocene-modified GNPs are greatly enhanced to 39.2 ± 5.0 pC, while the size of spikes in unmodified GNPs remains at 3.3 ± 0.5 pC. The frequency of impacts are analysed in Figure 7.5, which shows the number of spikes per 20 s chronoamperometry scan when different potentials are applied to the electrode. The impact frequency exhibits a random distribution. This phenomenon is consistent with the fact that the particle diffusion is independent of the applied potential and/or the modification of the GNPs.

Having evidenced impact spikes for both 1-(biphen-4-yl)ferrocene-modified and unmodified GNPs, the work next turns to consider the physical origin of the charge transfer process. When a GNP collides with the electrode, two possible types of charge transfer

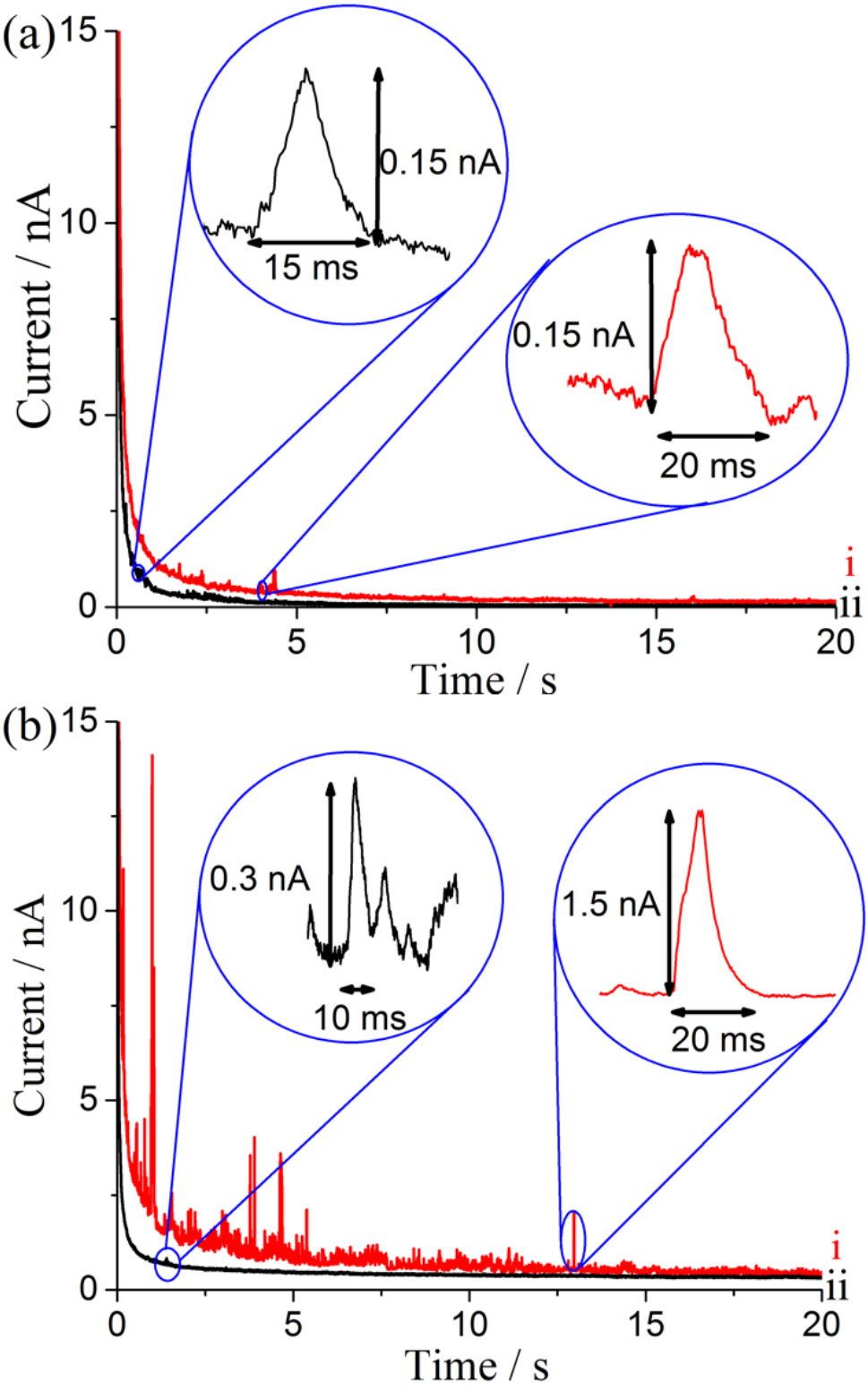

Figure 7.4: Comparison of spike size at different potentials from chronoamperograms in a 3.33×10^{-14} M suspension using a carbon fibre microwire electrode in a blank solution. (a)+0.40 V and (b)+0.90 V. (i) Suspension of 1-(biphen-4-yl)ferrocene-modified GNPs. (ii) Suspension of unmodified GNPs.

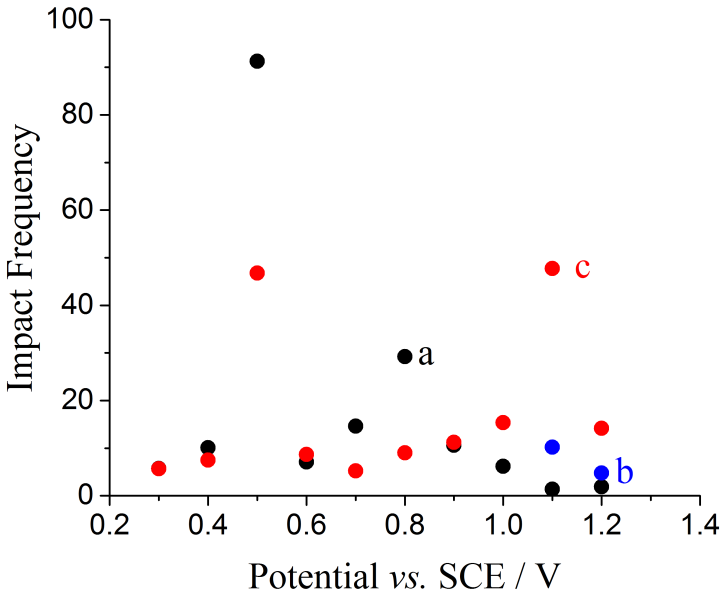

Figure 7.5: Potential variation of the impact frequency: plot of number of spikes per 20 s scan against potential. (a) 1-(biphen-4-yl)ferrocene-modified GNP. (b) ferrocene-'modified' GNP. (c) Unmodified GNP.

may occur, giving rise to spikes: Faradaic and capacitative. Faradaic impacts require a threshold potential to be applied, above which the redox reaction takes place over the time scale of impact. This causes a sharp increase in the charge transferred between the particles and electrode.[19–23] In contrast, capacitative impacts show a steady increase of the charge transferred when the applied potential is altered away from the potential of zero charge (PZC) of the electrode/solution interface.[9–11] Upon increasing the applied potential changes from +0.40 to +0.90 V, unmodified GNPs show a relatively small increase of *ca.* 0.8 pC in Q (Figure 7.4ii) confirming it follows capacitative behaviour[11]. When an unmodified GNP collides with the potentiostatted electrode, the GNP becomes charged. In order to maintain charge neutrality, electrons move into the electrode when the applied potential is positive to PZC. An oxidative impact spike can hence be observed. In contrast, upon crossing the oxidative potential of +0.45 V (Figure 7.2c), 1-(biphen-4-yl)ferrocene-modified GNPs show an increase to *ca.* 39.2 pC in Q (Figure 7.4i). This strongly suggests that Faradaic impacts occur due to the oxidation of 1-(biphen-4-yl)ferrocene adsorbed on the GNPs. When a GNP collides with the po-

tentiostatted electrode, electrons transfer from 1-(biphen-4-yl)ferrocene to the electrode. Note that the capacitative charging of the GNPs likely occurs simultaneously with the Faradaic process, but it only contributes *ca.* 3.3 pC to the overall Q of *ca.* 39.2 pC during the impacts.

7.3.4 Analysis of Impacts: Monolayer Coverage *vs.* Microcrystal Formation

The impact signals were analysed to quantify the coverage of 1-(biphen-4-yl)ferrocene on the surface of the GNPs. Chronoamperometric experiments were run at different potentials, ranging from +0.30 to +1.20 V, in both 1-(biphen-4-yl)ferrocene-modified and unmodified GNPs. Furthermore, as a control experiment, chronoamperograms were recorded at high potentials, +1.10 and +1.20 V, in ferrocene-'modified' GNPs. The scan was repeated at each potential until a large sample size (n'', the number of spikes) was obtained for statistics. The average charge passed per spike (Q) was plotted against the applied potential, as shown in Figure 7.6.

Figure 7.6c shows that upon moving to more positive potentials, the charge transferred per spike of unmodified GNPs shows a small but steady increase, corresponding to capacitative impacts as studied previously[11]. Figure 7.6b shows that the charge for ferrocene-'modified' GNP remains at similar values as seen in unmodified GNPs, even at high potentials. Hence due to the similarity between the charge passed during an impact, the underivatised ferrocene is concluded to not significantly modify the GNP surface. In contrast, the charge of 1-(biphen-4-yl)ferrocene-modified GNPs (Figure 7.6a) rises dramatically at *ca.* +0.70 V and reaches a plateau after +0.90 V. The maximum Q from the average values from +0.90 to +1.20 V is 41.5 ± 5.2 pC, denoted as Q_{total}. This sharp increase very likely indicates that Faradaic charge transfer is occurring during the course of GNP impact. Capacitative charging of the GNP will also take place with a small

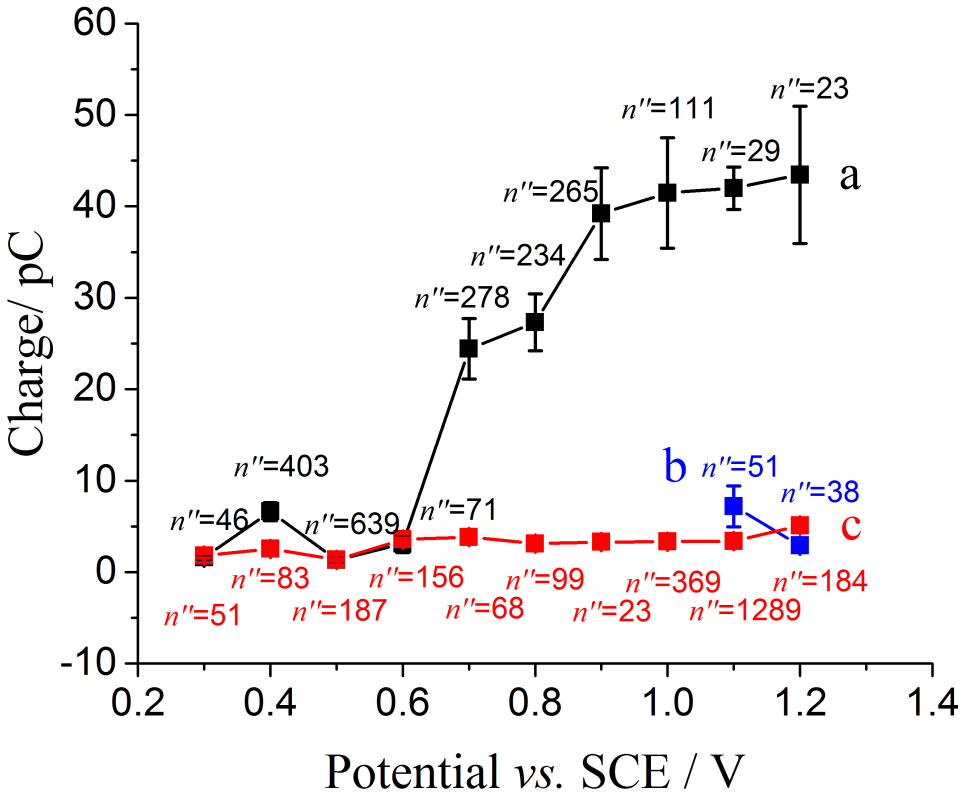

Figure 7.6: Potential variation of the average charge transferred per individual impact spike. The error of the average charge is obtained from $SD/n''^{1/2}$, where SD is the standard deviation and n'' is the number of spikes. (a) impacts of 1-(biphen-4-yl)ferrocene-modified GNPs. (b) impacts of ferrocene-'modified' GNPs. (c) impacts of unmodified GNPs.

contribution of 3.8 ± 0.9 pC to the overall Q_{total}. This is derived from the average Q of unmodified GNPs in the same potential range and denoted as $Q_{capacitative}$.

The surface coverage (Γ_i) of 1-(biphen-4-yl)ferrocene on the GNPs can be determined according to the measurements shown in Figure 7.6. The charge passed due to Faradaic impacts ($Q_{Faradaic}$) can be found *via* the equation

$$Q_{total} = Q_{Faradaic} + Q_{capacitative} \tag{7.2}$$

where $Q_{total} = 41.5 \pm 5.2$ pC and $Q_{capacitative} = 3.8 \pm 0.9$ pC as discussed earlier. During the Faradaic impacts, oxidation of 1-(biphen-4-yl)ferrocene involves one-electron transfer. The number of 1-(biphen-4-yl)ferrocene molecules (N) can be related to $Q_{Faradaic}$ *via*

$Q_{Faradaic} = Ne$, where e is the electronic charge. According to the radius of GNP ($r = 8.3$ μm), the area of GNP (S_{GNP}) can be estimated as 4.3×10^{-6} cm^2 from $S_{GNP} = 2\pi r_{GNP}^2$. The area occupied by each individual 1-(biphen-4-yl)ferrocene molecule (S_{R-Fc}) can be correlated to N and S_{GNP} *via* $S_{R-Fc} = S_{GNP}/N$. Similarly, Γ_i can be expressed *via* the equation

$$\Gamma_i = \frac{N}{N_A S_{GNP}} \tag{7.3}$$

where N_A is the Avogadro constant. Combining the equations, S_{R-Fc} and Γ_i can be calculated as $(1.8 \pm 0.3) \times 10^{-14}$ cm^2 per molecule and $(9.1 \pm 1.2) \times 10^{-11}$ mol cm^{-2}, respectively. These values are consistent with a monolayer coverage of 1-(biphen-4-yl)ferrocene on the surface of a single GNP. The correlation in charge between the expected value and observation strongly evidences the lack of aggregation or agglomeration of the tagged GNPs.

Comparing the "switch on" threshold potential between the ensemble voltammetry (Figure 7.3c) and the individual impact chronoamperometry of 1-(biphen-4-yl)ferrocene modified GNP (Figure 7.6a), the value increases from *ca.* +0.45 V to +0.70 V. The change in onset potential may originate from two possibilities. First, the measurement for ensemble voltammetry is slow and of time scale of seconds, which is sufficiently slow for the oxidation to be electrochemically reversibly. However, the duration of individual impact spike is only $10 \sim 100$ ms. Therefore, an overpotential may be required (Chapter 5) to fully drive the exhaustive oxidation of the 1-(biphen-4-yl)ferrocene adsorbed on the GNPs during single particle impact coulometry. Second, the potential shift could be interpreted as the effect of ohmic contact[24, 25] between the single GNP and the electrode. Resistance is introduced due to the electron tunnelling at the contact point. A more positive potential is thus required to overcome the resistance in impact studies as compared to ensemble voltammetry.

7.4 Conclusions

The monolayer adsorption of 1-(biphen-4-yl)ferrocene onto the graphene nanoplatelets (GNPs) has been demonstrated. The modified GNPs have been used in impacts experiments at a carbon fibre microwire electrode, where Faradaic and capacitative spikes are observed. The charge passed per individual spike by Faradaic process has been used to determine the surface coverage as $(9.1 \pm 1.2) \times 10^{-11}$ mol cm^{-2}, consistent with monolayer coverage. Analysis of the impact spikes has revealed that unsubstituted ferrocene cannot modify the GNPs. The change in onset potential between the ensemble voltammetry and the individual impact chronoamperometry has been investigated and is likely due to the shortened duration time scale and/or increased ohmic contact during particle-electrode collisions. The particle impacts method provides a powerful route to detect and characterise carbon nanomaterials facilitated by redox tagging. A quantitative analysis of the kinetics of electron transfer will be attempted in the next chapter.

References

[1] Wu, H.; Lin, Q.; Batchelor-McAuley, C.; Gonçalves, L. M.; Lima, C. F. R. A. C.; Compton, R. G. **2016**, *141*, 2696–2703.

[2] Gam Derouich, S.; Rinfray, C.; Izzet, G.; Pinson, J.; Gallet, J.-J.; Kanoufi, F.; Proust, A.; Combellas, C. *Langmuir* **2014**, *30*, 2287–2296.

[3] Allongue, P.; Delamar, M.; Desbat, B.; Fagebaume, O.; Hitmi, R.; Pinson, J.; Savéant, J.-M. *Journal of the American Chemical Society* **1997**, *119*, 201–207.

[4] Jouikov, V.; Simonet, J. *Electrochemistry Communications* **2014**, *46*, 132–136.

[5] Poizot, P.; Simonet, J. *Electrochemistry Communications* **2012**, *23*, 137–140.

[6] Li, Q.; Batchelor-McAuley, C.; Lawrence, N. S.; Hartshorne, R. S.; Compton, R. G. *New Journal of Chemistry* **2011**, *35*, 2462–2470.

[7] Katz, E. *Journal of Electroanalytical Chemistry* **1993**, *361*, 109–114.

[8] Katz, E. *Journal of Electroanalytical Chemistry* **1994**, *365*, 157–164.

[9] Banks, C. E.; Rees, N. V.; Compton, R. G. *Journal of Physical Chemistry B* **2002**, *106*, 5810–5813.

[10] Rees, N. V.; Banks, C. E.; Compton, R. G. *Journal of Physical Chemistry B* **2004**, *108*, 18391–18394.

[11] Poon, J.; Batchelor-McAuley, C.; Tschulik, K.; Compton, R. G. *Chemical Science* **2015**, *6*, 2869–2876.

[12] Zhou, Y.-G.; Rees, N. V.; Compton, R. G. *Chemical Communications* **2012**, *48*, 2510–2512.

[13] Rees, N. V.; Zhou, Y.-G.; Compton, R. G. *Chemical Physics Letters* **2012**, *525526*, 69–71.

[14] Lin, Q.; Compton, R. G. *Journal of Physical Chemistry C* **2015**, *119*, 23463–23469.

[15] Miyaura, N.; Yanagi, T.; Suzuki, A. *Synthetic Communications* **1981**, *11*, 513–519.

[16] Miyaura, N.; Suzuki, A. *Chemical Reviews* **1995**, *95*, 2457–2483.

[17] Lima, C. F. R. A. C.; Fernandes, A. M.; Melo, A.; Gonçalves, L. M.; Silva, A. M.; Santos, L. M. *Physical Chemistry Chemical Physics* **2015**, *17*, 23917–23923.

[18] Yang, M.; Batchelor-McAuley, C.; Gonçalves, L. M.; Lima, C. F. R. A. C.; Vyskočil, V.; Tschulik, K.; Compton, R. G. *Electroanalysis* **2016**, *28*, 197–202.

[19] Zhou, Y.-G.; Rees, N. V.; Compton, R. G. *Angewandte Chemie International Edition* **2011**, *50*, 4219–4221.

[20] Zhou, Y.-G.; Rees, N. V.; Pillay, J.; Tshikhudo, R.; Vilakazi, S.; Compton, R. G. *Chemical Communications* **2012**, *48*, 224–226.

[21] Stuart, E. J.; Zhou, Y.-G.; Rees, N. V.; Compton, R. G. *RSC Advances* **2012**, *2*, 6879–6884.

[22] Zhou, Y.-G.; Haddou, B.; Rees, N. V.; Compton, R. G. *Physical Chemistry Chemical Physics* **2012**, *14*, 14354–14357.

[23] Haddou, B.; Rees, N. V.; Compton, R. G. *Physical Chemistry Chemical Physics* **2012**, *14*, 13612–13617.

[24] Kätelhön, E.; Compton, R. G. *ChemElectroChem* **2015**, *2*, 64–67.

[25] Li, X.; Batchelor-McAuley, C.; Whitby, S. A. I.; Tschulik, K.; Shao, L.; Compton, R. G. *Angewandte Chemie International Edition* **2016**, *55*, 4296–4299.

Chapter 8

Impacts Reveal Electron Transfer Kinetics of the Ferrocene / Ferrocenium Couple Immobilised on Graphene Nanoplatelets

The previous chapter reported Faradaic and capacitative impacts of graphene nanoplatelets. In this chapter, the particle impacts technique is used to evaluate the kinetics of the ferrocene/ferrocenium redox couple in aqueous solution *via* immobilisation on graphene nanoplatelets. Single graphene nanoplatelets modified with poly(vinylferrocene) are allowed to impact a microelectrode. For the duration (*ca.* 10 $\sim$ 100 ms) of the impacts, the individual graphene nanoplatelet adopts the potential of the electrode and acts as a "chemically modified nanoelectrode". The study of individual impacts facilitates the resolution of fast electron transfer kinetics. The work herein presented has been published in *ChemElectroChem*[1] and was performed in collaboration with Mr. Haoyu Wu and Dr. Christopher Batchelor-McAuley. The assistance of Mr. Haoyu Wu in collecting some of the experimental data is acknowledged. Dr. Christopher Batchelor-McAuley helped to interpret of the experimental results and derive the equations in Section 8.3.3.

8.1 Introduction

The ferrocene/ferrocenium (Cp_2Fe/Cp_2Fe^+) redox couple is one of the most important electrochemical systems finding widespread usage as an outer-sphere electron transfer redox reaction

$$Cp_2Fe \rightleftarrows Cp_2Fe^+ + e^- \tag{8.1}$$

The fundamental importance of this couple is probably best highlighted by Chidsey[2] who used a surface bound ferrocene species to evidence the validity of the Marcus-Hush electron transfer model. Significant work in the literature has focused on the measurement of electron transfer kinetics of the Cp_2Fe/Cp_2Fe^+ couple using metallic electrodes.[2–4] Recently, there is an increasing demand on the production of new carbon nanomaterials and characterisation of the electron transfer properties of these solids. Measurement of the response of the Cp_2Fe/Cp_2Fe^+ couple at these materials[5–10] is one route by which the influence of the carbonaceous electronic structure upon the influence the electron transfer process can be probed. However, such studies involving large ensembles of particles are commonly complicated by the measurement of non-ideal voltammetry.[11, 12] Such non-idealities are possibly the result of multilayer formation and/or associated capacitive effects serving to alter or distort the voltammetric response.

As compared to modification of graphene nanoplatelets (GNPs) with single ferrocene molecules (Chapter 7), modification with polymers such as poly(vinylferrocene) (PVFc, Figure 8.1) introduces a higher number of electroactive centres in the nanoparticles, leading to greater impact signals and facilitating electron transfer kinetic studies. Impacts can be used to study the size[13, 14], concentration[15] and catalytic properties[16] of particles, as well as the surface coverage of redox moieties (Chapters 5 $\sim$ 7) on the particle surface. However, the quantitative measurements of electron transfer kinetics at individual particles is very limited.[17]

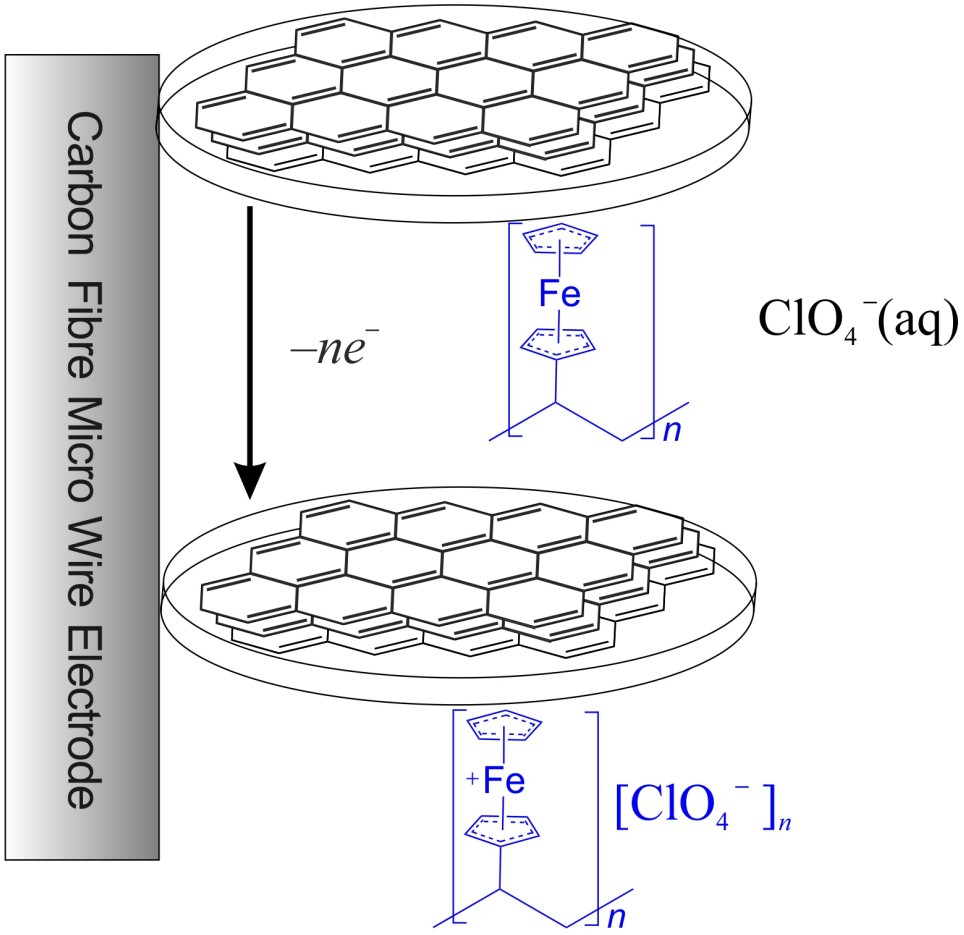

Figure 8.1: Model for the impacts between the poly(vinylferrocene)-modified graphene nanoplatelets and the carbon fibre microwire electrode. n is the number of monomer units of ferrocene immobilised on the nanoplatelet.

This chapter demonstrates the use of particle impacts to access the kinetics of the Cp_2Fe/Cp_2Fe^+ redox couple. Graphene nanoplatelets are chemically modified with PVFc and studied by using the particle impacts method. Upon impact, each individual GNP acts as a single nanoelectrode and, hence, can be used to probe the electron transfer to the modifying layer. Conventionally, macro- or microelectrodes are used to study the kinetics of a redox process, but such experiments often exhibit distorted voltammetry. The study of *individual* GNPs significantly minimises capacitive effects and ensures the particle being measured is directly contacting the electrode;[18] thus facilitating the measurement of fast electron transfer.[19–21] A strategy is thus demonstrated that allows the study of electron transfer at new nanomaterials, such as the GNPs or carbon nanotubes and

nanodots, among others.

8.2 Experimental

Details about the chemical reagents and solutions here utilised can be found in Chapter 2, Section 2.1. The structures of poly(vinylferrocene) (PVFc) and graphene nanoplatelets (GNPs) are shown in Figure 8.1. 0.1 M $NaClO_4$ was used as the supporting electrolyte. The GNPs were modified following the method described in Chapter 2, Section 2.2.2. Voltammetric and chronoamperometric measurements were recorded using a μAutolab II potentiostat. An edge-plane pyrolytic graphite (EPPG) electrode and a carbon fibre microwire electrode were used as working electrodes, with their surfaces prepared as described in Chapter 2, Section 2.3.3. A graphite rod and a saturated calomel electrode (SCE) were used as the counter and reference electrode, respectively.

8.3 Results and Discussion

First, the cyclic voltammetry of an ensemble of poly(vinylferrocene)-modified graphene nanoplatelets (PVFc-GNPs) immobilised on an edge-plane pyrolytic graphite (EPPG) electrode is established, confirming the adsorption of PVFc onto the GNPs surface. Second, impacts of individual PVFc-GNPs at a carbon fibre microwire electrode are investigated. The charge transferred per impact spike is then studied as a function of the applied potential. In particular, the overall charge transferred is conserved during an impact event,[22] using the electronics employed allowing measurement *via* the integration of individual spikes. Finally, the electron transfer rate is inferred by modelling of this response.

8.3.1 Cyclic Voltammetry

The cyclic voltammetry of poly(vinylferrocene) (PVFc) was first studied at an EPPG electrode, at which a layer of PVFc had been drop-casted (Chapter 2, Section 2.3.3). The electrode was then transferred to a 25 mL blank solution. Cyclic voltammetry was run from 0 V to +0.70 V (*vs.* SCE) and swept back to 0 V at a scan rate of 50 mV s^{-1} (Figure 8.2b). For comparison, an unmodified EPPG electrode was used to record the voltammetry in the same solution (Figure 8.2a). A well-defined oxidative response is observed at *ca.* +0.42 V. This is in a good agreement with a literature report[23], as +0.41 V for PVFc coated multiwalled carbon nanotubes modified glassy carbon electrode in pH 7.4 buffer. The redox response can be ascribed to the oxidation of the ferrocene moiety to the ferrocenium cation, as shown in Eq. 8.1.

Following the procedure described in Chapter 2, Section 2.2.2, PVFc-GNPs were prepared. In order to demonstrate the adsorption of PVFc onto the GNPs, an EPPG electrode was modified by abrading it on PVFc-GNPs powders (Chapter 2, Section 2.3.3). The electrode was transferred to a 25 mL blank solution. Cyclic voltammetry was recorded between 0 V and +0.70 V (*vs.* SCE) at a scan rate of 50 mV s^{-1} (Figure 8.2c). An oxidative peak occurs at +0.39 V, which is close to the oxidation potential in drop-casting PVFc on the electrode surface (Figure 8.2b). Therefore, PVFc was confirmed to be modified onto the GNPs.

Figure 8.2 shows the reductive back peak is less defined than the oxidative forward peak at both PVFc (b) and PVFc-GNPs (c) modified EPPG electrodes. This could be due to the co-ordination[24] of the ferrocenium and the anion from supporting electrolyte, which stabilises the former sufficiently that its reduction becomes thermodynamically unfavourable. However, this influence of ion-pairing has been minimised by the choice of $NaClO_4$ as compared say to KCl. By transferring the same PVFc-modified electrode to a blank solution supported with 0.1 M KCl, a voltammogram was recorded as shown

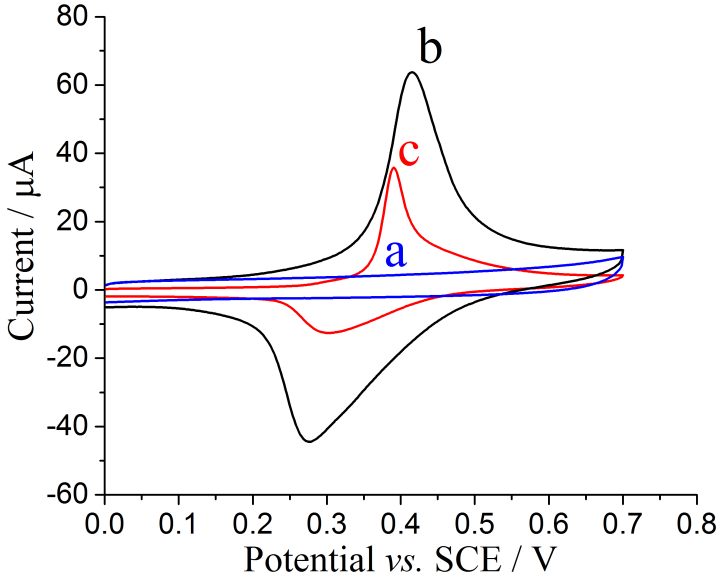

Figure 8.2: Voltammograms in a blank solution, at (a) unmodified, (b) poly(vinylferrocene) drop-casting modified, and (c) poly(vinylferrocene)-modified graphene nanoplatelets abrasively modified, edge-plane pyrolytic graphite electrodes. Scan rate = 50 mV s^{-1}.

in Figure 8.3b. The same PVFc-GNPs-modified electrode was also used in the same blank solution to run the voltammetry, as shown in Figure 8.3d. Comparison of solid and dashed lines of Figure 8.3 shows that by immobilising the same amount of PVFc or PVFc-GNPs onto the electrode, the voltammetry in 0.1 M $NaClO_4$ gives rise to a better defined redox response as compared to 0.1 M KCl. Furthermore, modification with PVFc *via* drop-casting (Figure 8.3a and b) shows a higher peak current and a larger peak-to-peak separation as compared to modification with PVFc-GNPs *via* abrading (Figure 8.3c and d). While the higher peak current originates from the greater concentration of PVFc adsorbed on the electrode surface, the resulting larger peak-to-peak separation implies the non-ideality of voltammetry. With the increasing concentration of the electroactive species, the capacitive effect enhances, leading to a more distorted voltammetric response. To bypass this issue towards the study for electrode kinetics of the Cp_2Fe/Cp_2Fe^+ couple, particle impacts method can be introduced as an effective alternative.

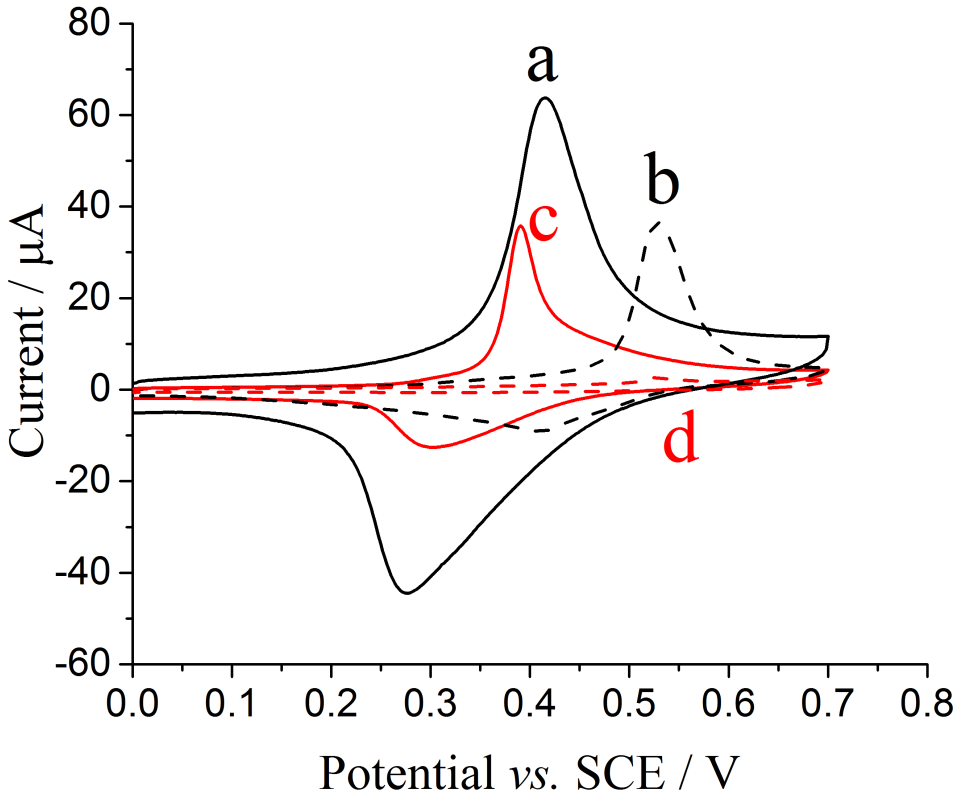

Figure 8.3: Voltammograms measured in a blank solution using an edge-plane pyrolytic graphite electrode. (a) and (b): poly(vinylferrocene)-modified electrode *via* drop-casting. (c) and (d): poly(vinylferrocene)-modified graphene nanoplatelets immobilised electrode *via* abrasive modification. Solid lines: in 0.1 M $NaClO_4$. Dashed lines: in 0.1 M KCl. Scan rate = 50 mV s^{-1}.

8.3.2 Particle Impact Chronoamperometry

Having evidenced the adsorption of PVFc on the GNPs, individual modified GNP particles was next studied *via* particle impacts. Chronoamperometry was used to detect and characterise impacts of PVFc-GNPs at a carbon fibre microwire electrode. According to the cyclic voltammetry studies in the preceding section, oxidation of PVFc might be expected to occur when the potential applied to the electrode is *ca.* +0.39 V or more (Figure 8.2b).

A carbon fibre microwire electrode was immersed into a 5 mL PVFc-GNPs suspension and potentiostatted for 20 s at +0.30 V and +1.00 V, respectively. As a control experiment, chronoamperograms were also recorded in the presence of unmodified GNPs in the

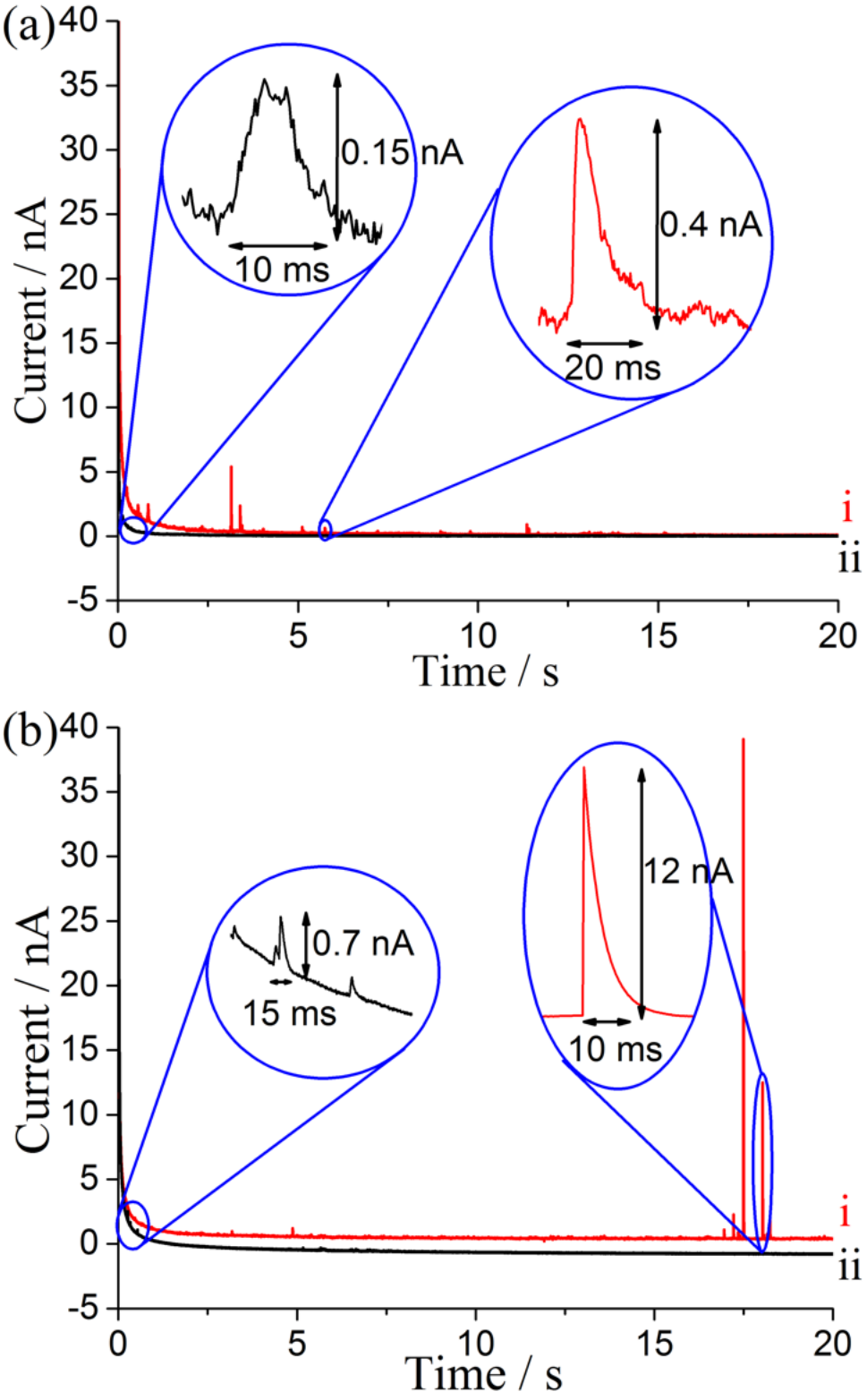

Figure 8.4: Chronoamperograms of 3×10^{-14} M graphene nanoplatelets suspension measured using a carbon fibre microwire electrode in a blank solution. (a) +0.30 V and (b) +1.00 V. (i) Suspension of poly(vinylferrocene)-modified graphene nanoplatelets. (ii) Suspension of unmodified graphene nanoplatelets. For clarity, (i) in (b) is shifted downward by 2 nA.

same solution using the same electrode. As shown in Figure 8.4a, impact spikes can be observed in the presence of both PVFc-GNPs (i) and unmodified GNPs (ii). The average charge passed per spike (Q) can be quantified by taking the average of the individual spike areas. At +0.30 V (Figure 8.4a), Q for PVFc-GNPs (i) is 3.6 ± 0.7 pC, which is comparable in size as that for unmodified GNPs (ii) being 1.8 ± 0.2 pC. When the applied potential increases to +1.00 V (Figure 8.4b), the charge passed for the PVFc-GNPs (i) becomes very much higher at 60.6 ± 8.7 pC. In contrast, Q for the unmodified GNPs (ii) remains at 3.3 ± 0.4 pC.

The surface coverage (Γ_i) of PVFc on the GNPs can be determined as the following, according to the measurements from Figure 8.4. The charge passed due to Faradaic impacts ($Q_{Faradaic}$) can be expressed as

$$Q_{total} = Q_{Faradaic} + Q_{capacitative} \tag{8.2}$$

where Q_{total} = 60.6 ± 8.7 pC from PVFc-GNPs and $Q_{capacitative}$ = 3.3 ± 0.4 pC from unmodified GNPs. During the Faradaic process, n-electron was transferred from the ferrocene moiety to the ferrocenium cation, where n is the number of Cp_2Fe monomer units in PVFc and e is the electronic charge

$$Q_{Faradaic} = ne \tag{8.3}$$

Combining Eq. 8.2 and 8.3 gives $n = (3.6 \pm 0.7) \times 10^8$. Apart from particle impacts, the value for n can also be crudely estimated from molecule modelling (Chapters 5 and 6). The area of each Cp_2Fe monomer (S_{Cp_2Fe}) can be estimated as *ca.* 4.9×10^{-15} cm^2, according to its volume[25] and the known Fe-Cp bond length[26]. As the radius of GNP (r_{GNP}) is 8.3 μm, the area of GNP (S_{GNP}) can be estimated as 4.3×10^{-6} cm^2 from $S_{GNP} = 2\pi r_{GNP}^2$. With the assumption that Cp_2Fe monomers are close-packed and

adsorbed on the surface of the GNPs *via* π-π interaction, n can be correlated to S_{Cp_2Fe} and S_{GNP} *via*

$$n = \frac{S_{GNP}}{S_{Cp_2Fe}} \tag{8.4}$$

Hence n can be calculated as 9×10^8. The value derived from impacts $(3.6 \pm 0.7) \times 10^8$ is under the limit of 9×10^8, so it is reasonable to conclude that the average charge passed per spike at +1.0 V is consistent with a monolayer coverage of PVFc on the surface of a GNP. This is achieved likely by interaction between the Cp rings in PVFc and the aromatic rings in the GNPs. Due to monolayer insertion of counter ions into PVFc, transfer of ClO_4^- from water into the PVFc layer is unlikely to be the rate-determining step.

The surface coverage (Γ_i) can be derived *via* the equation

$$\Gamma_i = \frac{n}{N_A S_{GNP}} \tag{8.5}$$

where N_A is the Avogadro constant. Hence Γ_i can be determined as *ca.* $(3.3 \pm 0.6) \times 10^{-10}$ mol cm^{-2}.

Upon collisions between a graphene nanoplatelet and the electrode, two possible types of charge transfer take place resulting in impact spikes, namely capacitative and Faradaic. The physical origin of the two types of processes has been elaborated in Chapter 7. Figure 8.4ii shows that Q for unmodified GNPs increases slightly for only *ca.* 1.5 pC upon elevation of the applied potential from +0.30 to +1.00 V, indicating it follows capacitative behaviour. In contrast, Figure 8.4i demonstrates a sharp increase of *ca.* 57 pC in Q for PVFc-GNPs between +0.30 and +1.00 V. This likely corresponds to Faradaic impacts arising from the oxidation of PVFc adsorbed on the GNPs. Note that at +0.30 V (Figure 8.4a) Q for PVFc-GNPs (i) is marginally higher ($\sim$ *ca.* 1.8 pC) than that for unmodified GNPs (ii), this discrepancy arises due to the onset of the oxidation of PVFc

which commences at +0.25 V (Figure 8.2b).

8.3.3 Analysis of Impacts: Electron Transfer Kinetics

A potential dependent study was then conducted to investigate the electrode kinetics involved in the Faradaic process. Chronoamperometry was repeated with the applied potential varied from +0.30 to +1.20 V, for 0.28 mg of PVFc-GNPs suspended in a 5 mL blank solution using a carbon fibre microwire electrode. The average charge passed per spike (Q) was plotted against the electrode potential (Figure 8.5, blue squares). For comparative purposes, the potential variation of the capacitative impact spikes for the unmodified GNPs was recorded (Figure 8.5, black squares). The blue squares in Figure 8.5 shows the onset of PVFc-GNPs oxidation at *ca.* +0.70 V. The complete oxidation of PVFc-GNPs occurs when the applied potential is above +0.90 V, reaching the maximum charge passed per spike (Q_{max}) at 66.0 ± 5.2 pC. These data, again, suggest Faradaic charge transfer from PVFc-GNPs to the electrode during the collisions.

Having established the oxidation of PVFc-GNPs at both EPPG and carbon fibre microwire electrodes, it can be revealed that the "switch on" threshold potential increases from *ca.* +0.39 V in the "ensemble" voltammetry (Figure 8.5, red line) to *ca.* +0.70 V in the individual impact chronoamperometry (Figure 8.5, blue squares). The origin of this potential shift of *ca.* 300 mV reflects, at least in part, the finite electron transfer kinetics of the PVFc/$PVFc^+$ couple revealed by the short time scale of the impacts, which has been elaborated in Chapter 7. To scrutinise the cause of onset potential shift, Tafel analysis was performed with the individual impact data to derive the transfer coefficient (β for oxidation) for the Cp_2Fe/Cp_2Fe^+ couple.[27–30] Utilising the relationship between the average charge passed per impact spike and the applied potential (Figure 8.5), Tafel analysis can be realised by taking the lower potential data (green line), where the electron transfer is hypothesised to be under pure kinetic-control. Note that in comparison

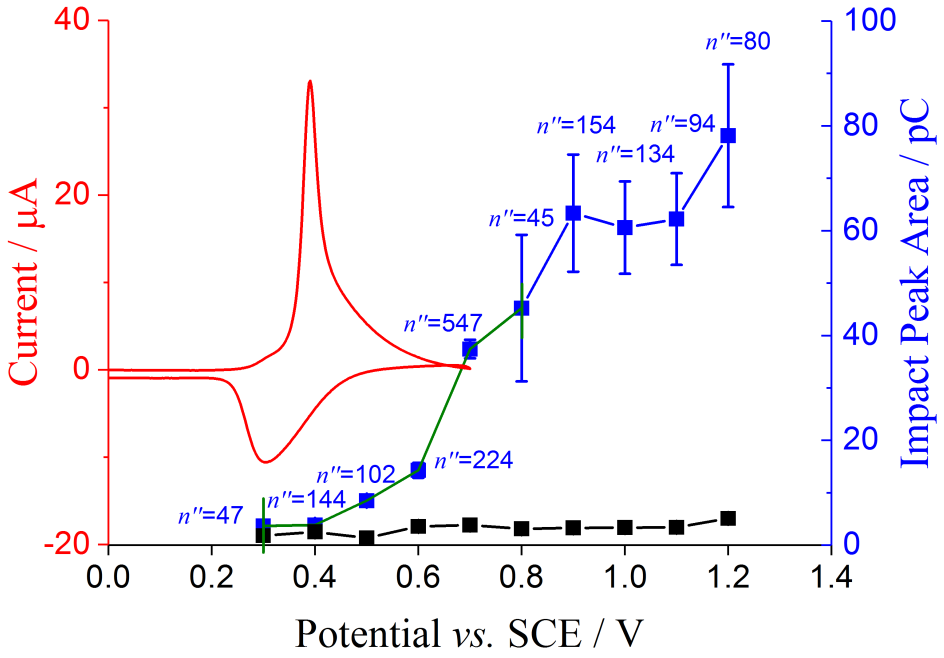

Figure 8.5: Analysis for poly(vinylferrocene)-modified graphene nanoplatelets in a blank solution. Red line: voltammogram of poly(vinylferrocene)-modified graphene nanoplatelets immobilised electrode. Scan rate = 50 mV s^{-1}. Squares: the average charge transferred per impact spike of poly(vinylferrocene)-modified (blue) and unmodified (black) graphene nanoplatelets. The error bars are derived from $SD/n''^{1/2}$, where SD is the standard deviation and n'' is the number of spikes. Green line: Tafel analysis region.

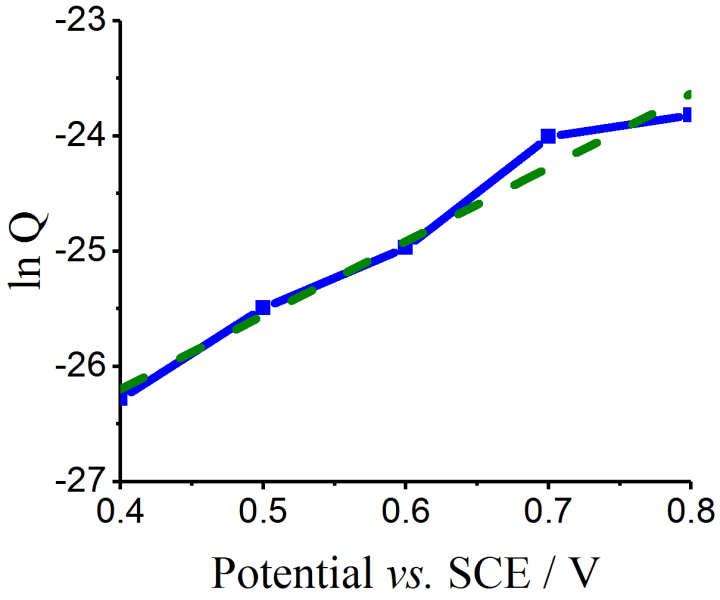

Figure 8.6: Tafel plot for potential variation of the average charge transferred per impact spike of poly(vinylferrocene)-modified graphene nanoplatelets.

with the signal from the drop-cast layer, significant overpotential is present so that any cathodic reaction can be neglected. As shown in Figure 8.6, ln $|Q|$ was plotted versus potential, giving a straight line of gradient $\beta F/RT$. The transfer coefficient, β, can hence be estimated as 0.18 ± 0.02.

A simple physical model (Figure 8.1) is next developed for the impacts between the PVFc-GNPs and carbon fibre microwire electrodes. During an impact, charge is transferred to the electrode from ferrocene units in the PVFc layer on the individual GNP. The electron transfer undergoes first order kinetics with a rate of k_{Fc} (s^{-1}), which can be related to the changing surface coverage of ferrocene units, Γ_{Fc} (mol cm^{-2}), *via*

$$\frac{d\Gamma_{Fc}}{dt} = -k_{Fc}\Gamma_{Fc} \tag{8.6}$$

where t is time. Hence, assuming Butler-Volmer kinetics accurately describe the rate of electron transfer by

$$k_{Fc} = k^0 \exp\left(\frac{\beta F \eta}{RT}\right) \tag{8.7}$$

where k^0 is the standard electrochemical rate constant (s^{-1}), F is the Faraday constant (96 485 C mol^{-1}), η is the overpotential corresponding to $E - E_f^0$ (with the formal potential E_f^0), R is the ideal gas constant (8.314 J K^{-1} mol^{-1}) and T is the absolute temperature (K). After substituting Eq. 8.7 in 8.6, the solution for Eq. 8.6 becomes

$$\ln \Gamma_{Fc}|_{initial}^{final} = -k^0 t_{impact} \exp\left(\frac{\beta F \eta}{RT}\right) \tag{8.8}$$

where t_{impact} is the duration of the impacts event. The value of t_{impact} used is 18 ms, derived from the average duration of all the Faradaic impact spikes. By setting the limit of the integral $\Gamma_{Fc,final} = 0.5\ \Gamma_{Fc,initial}$, the overpotential at which 50% of the material is

oxidised ($\eta_{1/2}$) can be defined. Eq. 8.8 can thus be simplified and rearranged to give

$$k^0 = -\frac{\ln 0.5}{t_{impact} \exp\left(\frac{\beta F \eta_{1/2}}{RT}\right)} \tag{8.9}$$

Measurement of the 'half-wave' potential ($E_{1/2}$ = +0.70 V) and formal potential (E_f^0 = +0.35 V) from Figure 8.5 yields the value for $\eta_{1/2}$ as 0.35 V. Substitution of all the known parameters gives $k^0 = 3 \pm 1$ s^{-1}, which is consistent with prior literature estimations ranging from 0.35 to 44 s^{-1}, either for direct charge transfer from ferrocene derivatives to carbon electrodes[6–9], or indirect charge transfer *via* multiwalled carbon nanotubes[5]. The value for k^0 is determined assuming the absence of contact resistance between the particles and the electrode, hence possible interference from contact resistance cannot be completely ruled out during the particle impacts so that the value of 3 ± 1 s^{-1} should be considered to be a lower limit for k^0. Although the use of current decay curves in the impact spikes is feasible for extraction of k_{Fc} by taking log (current) versus time, the kinetic information is complicated by the impulse response of the potentiostat.[22] However, the individual impact spike area remains undisturbed,[22] so the method employed in this work is effective for electron transfer kinetic studies.

8.4 Conclusions

This chapter has successfully demonstrated the measurement of electron transfer kinetics for individual poly(vinylferrocene)-modified graphene nanoplatelets *via* particle impacts. Graphene nanoplatelets, acting as temporary nanoelectrodes for the short duration of their contact with the electrode, allows the resolution of fast electron transfer kinetics which for the Cp_2Fe/Cp_2Fe^+ couple in 0.1 M $NaClO_4$ is 3 ± 1 s^{-1} or faster. This strategy provides a promising tool to obtain kinetic information relating to a wide range of applications in

energy storage, drug delivery, bioimaging, sensors and composites.

References

[1] Wu, H.; Lin, Q.; Batchelor-McAuley, C.; Compton, R. G. *ChemElectroChem* **2016**, *3*, 1478–1483.

[2] Chidsey, C. *Science* **1991**, *251*, 919.

[3] Sharp, M.; Petersson, M.; Edström, K. *Journal of Electroanalytical Chemistry and Interfacial Electrochemistry* **1979**, *95*, 123–130.

[4] Gooding, J. J.; Chou, A.; Liu, J.; Losic, D.; Shapter, J. G.; Hibbert, D. B. *Electrochemistry Communications* **2007**, *9*, 1677–1683.

[5] Zhou, H.; Yang, W.; Sun, C. *Talanta* **2008**, *77*, 366–371.

[6] Henstridge, M. C.; Batchelor-McAuley, C.; Gusmão, R.; Compton, R. G. *Chemical Physics Letters* **2011**, *517*, 108–112.

[7] Landis, E. C.; Hamers, R. J. *Chemistry of Materials* **2009**, *21*, 724–730.

[8] Gietter, A. A.; Pupillo, R. C.; Yap, G. P.; Beebe, T. P.; Rosenthal, J.; Watson, D. A. *Chemical Science* **2013**, *4*, 437–443.

[9] Fortgang, P.; Tite, T.; Barnier, V.; Zehani, N.; Maddi, C.; Lagarde, F.; Loir, A.-S.; Jaffrezic-Renault, N.; Donnet, C.; Garrelie, F.; Chaix, C. *ACS Applied Materials & Interfaces* **2016**, *8*, 1424–1433, PMID: 26710829.

[10] Liu, G.; Liu, J.; Böcking, T.; Eggers, P. K.; Gooding, J. J. *Chemical Physics* **2005**, *319*, 136–146.

[11] Stuart, E. J.; Tschulik, K.; Batchelor-McAuley, C.; Compton, R. G. *ACS Nano* **2014**, *8*, 7648–7654.

[12] Zhou, X.; Cheng, W.; Compton, R. G. *ChemElectroChem* **2015**, *2*, 691–699.

[13] Zhou, Y.-G.; Rees, N. V.; Compton, R. G. *Angewandte Chemie International Edition* **2011**, *50*, 4219–4221.

[14] Giovanni, M.; Ambrosi, A.; Sofer, Z.; Pumera, M. *Electrochemistry Communications* **2015**, *56*, 16–19.

[15] Stuart, E. J.; Zhou, Y.-G.; Rees, N. V.; Compton, R. G. *RSC Advances* **2012**, *2*, 6879–6884.

[16] Xiao, X.; Bard, A. J. *Journal of the American Chemical Society* **2007**, *129*, 9610–9612.

[17] Kahk, J. M.; Rees, N. V.; Pillay, J.; Tshikhudo, R.; Vilakazi, S.; Compton, R. G. *Nano Today* **2012**, *7*, 174–179.

[18] Toh, H. S.; Jurkschat, K.; Compton, R. G. *Chemistry - A European Journal* **2015**, *21*, 2998–3004.

[19] Amatore, C.; Maisonhaute, E. *Analytical Chemistry* **2005**, *77*, 303–A.

[20] Amatore, C. *Comptes Rendus de l'Académie des Sciences* **1996**, *323*, 757–771.

[21] Amatore, C.; Arbault, S.; Maisonhaute, E.; Szunerits, S.; Thouin, L. In *Trends in Molecular Electrochemistry*; Pombeiro, A. J. L., Amatore, C., Eds.; Marcel Dekker: New York, 2004; Chapter 12.

[22] Kätelhön, E.; Tanner, E. E. L.; Batchelor-McAuley, C.; Compton, R. G. *Electrochimica Acta* **2016**, *199*, 297–304.

[23] Šljukić, B.; Banks, C. E.; Salter, C.; Crossley, A.; Compton, R. G. *Analyst* **2006**, *131*, 670–677.

[24] Yang, M.; Batchelor-McAuley, C.; Gonçalves, L. M.; Lima, C. F. R. A. C.; Vyskočil, V.; Tschulik, K.; Compton, R. G. *Electroanalysis* **2016**, *28*, 197–202.

[25] Goehring, M.; Zirker, G. *Zeitschrift für Naturforschung, B: A Journal of Chemical Sciences* **1955**, *10*, 58–58.

[26] Dunitz, J.; Orgel, L.; Rich, A. *Acta Crystallographica* **1956**, *9*, 373–375.

[27] Batchelor-McAuley, C.; Compton, R. G. *Journal of Electroanalytical Chemistry* **2012**, *669*, 73–81.

[28] Compton, R. G.; Banks, C. E. *Understanding Voltammetry, 2nd edition*; Imperial College Press, 2011.

[29] Guidelli, R.; Compton, R. G.; Feliu, J. M.; Gileadi, E.; Lipkowski, J.; Schmickler, W.; Trasatti, S. *Pure and Applied Chemistry* **2014**, *86*, 245–258.

[30] Guidelli, R.; Compton, R. G.; Feliu, J. M.; Gileadi, E.; Lipkowski, J.; Schmickler, W.; Trasatti, S. *Pure and Applied Chemistry* **2014**, *86*, 259–262.

Chapter 9

Catalytic Single Particle Impacts: Theory and Experiment. Poly(vinylferrocene)-Modified Graphene Nanoplatelet Mediated L-Cysteine Oxidation

The previous chapter demonstrated the use of particle impacts to evaluate electron transfer kinetics. In this chapter, the method is further developed to measure a catalytic reaction rate constant, synergising both experiment and theory. The theory of catalytic particle impacts is developed specifically for the case of a single particle in contact with an electrode for a short period of time, in which it mediates electron transfer to or from a species in homogeneous solution. The theory is applied to impacts of chemically modified graphene nanoplatelets, in which the immobilised ferrocene/ferrocenium couple is used to mediate the oxidation of L-cysteine in aqueous solution.

The work herein presented has been published in *The Journal of Physical Chemistry C*[1] and was performed in collaboration with Ms. Chuhong Lin, Mr. Haoyu Wu and Dr. Christopher Batchelor-McAuley. Ms. Chuhong Lin developed the theory and simulation in Section 9.2 and 9.4.3. Mr. Haoyu Wu helped to collect some of the experimental data. Dr. Christopher Batchelor-McAuley contributed to the idea of this project and helped with experimental planning.

9.1 Introduction

Ferrocene and its derivatives are widely applied as catalysts in biochemistry and energy technology, since they show rapid electron transfer reactions and so can be used to mediate electron transfer with species, which otherwise show slow electron transfer, such as ascorbic acid[2], sulphide or thiol species[4, 5], and sodium-air batteries[3]. In order to observe mediated redox reaction *via* particle impacts, ferrocene can be adsorbed onto the graphene nanoplatelets (GNPs) (Chapters 7 and 8) and dispersed in an aqueous solution with the electroactive species. Herein, poly(vinylferrocene) (PVFc) as a polymer based form of ferrocene is used in order to introduce a high number of catalytic centres. During an impact with an electrode, each single GNP temporarily acts as an individual tiny electrode and adopts the potential applied.[6] When the potential becomes more positive than that required for ferrocene oxidation, an electrochemical reaction takes place on the GNP. The formed adsorbed ferrocenium cations can then bring about mediated electron transfer from solution phase species. Note that the use of individual GNPs circumvents the non-ideal voltammetry[7–11] of large ensembles of particles measured at macro- and microelectrodes, and so provides a more reliable route to measure electron transfer kinetics and mechanisms (Chapter 8).

In this chapter, L-cysteine, an amino acid with a thiol group (Figure 9.1), is employed as the electroactive species under observation. This chapter demonstrates the use of poly(vinylferrocene)-modified graphene nanoplatelets (PVFc-GNPs) as a mediator for the oxidation of L-cysteine in aqueous solutions (Figure 9.2), and develops the theory

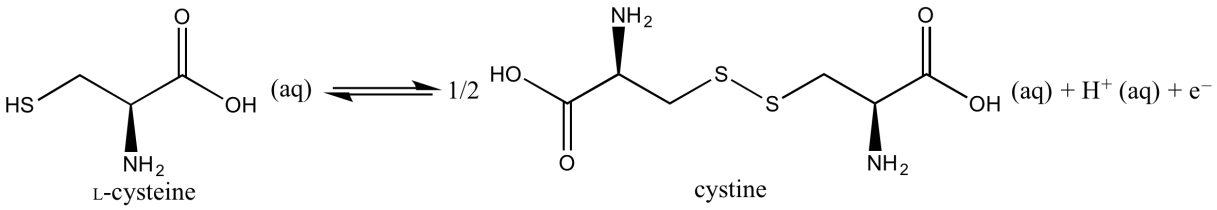

Figure 9.1: Oxidation of L-cysteine to produce cystine.

of catalytic single particle impacts. The kinetics and mechanism of the catalysis is then assessed synergising both experiment and theory.

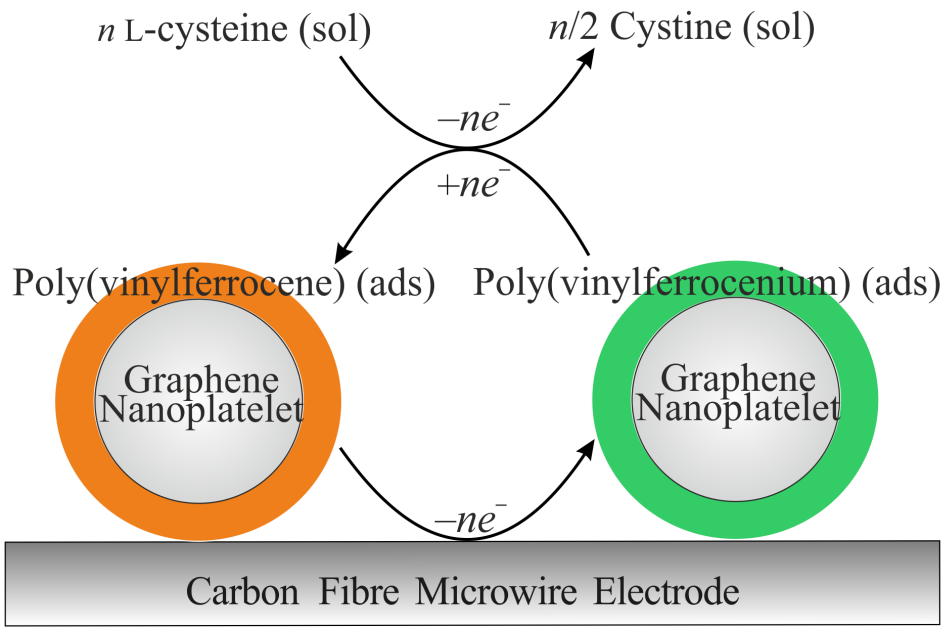

Figure 9.2: Model for catalytic single particle impacts: poly(vinylferrocene)-modified graphene nanoplatelets mediated L-cysteine oxidation in aqueous solutions.

9.2 Theory and Simulation

The simulation model for the mediated catalytic reaction on the individual graphene nanoplatelet (GNP) is developed by Ms. Chuhong Lin in this section.

9.2.1 Theoretical Model

When a modified GNP impacts on an inert electrode, the mediated reaction takes place on the individual GNP. The impacting GNP is treated as a transient microdisc electrode, and the mediated reaction on the GNP is interpreted by an EC' mechanism, where electron transfer between the adsorbed redox species (E) is followed by a heterogeneous catalytic reaction (C'):

$$\mathrm{A(ads)} \overset{k^0}{\rightleftarrows} \mathrm{B(ads)} + \mathrm{e}^- \tag{9.1}$$

$$\mathrm{B(ads) + R(sol) \xrightarrow{k_c} A(ads) + P(sol)} \tag{9.2}$$

where A and B refer to the adsorbates, and R and P are the reactant and the product in the solution. In this work, A is the poly(vinylferrocene) (PVFc) modified on the GNP, and R is the L-cysteine dissolved in the solution.

Assuming electron transfer kinetics can be described by the Butler-Volmer equation, the reaction rate equations for the adsorbate A and the reactant R can be expressed as

$$\begin{aligned}\frac{\partial \Gamma_A}{\partial t} =& - k^0 \exp\left(\frac{\beta F}{RT}(E - E^0_{f,A(ads)/B(ads)})\right)\Gamma_A \\ &+ k^0 \exp\left(-\frac{\alpha F}{RT}(E - E^0_{f,A(ads)/B(ads)})\right)(\Gamma_{max} - \Gamma_A) \\ &+ k_c(\Gamma_{max} - \Gamma_A)C_{R(surf)}\end{aligned} \tag{9.3}$$

$$D_R \frac{\partial C_R}{\partial z}\bigg|_{surf} = -k_c(\Gamma_{max} - \Gamma_A)C_{R(surf)} \tag{9.4}$$

where Γ_A is the surface coverage of the adsorbate A (mol cm^{-2}), k^0 is the standard electrochemical rate constant of reaction 9.1 (s^{-1}), α and β are the transfer coefficients in the Butler-Volmer equation[12, 13], E is the potential applied on the electrode (V), $E^0_{f,A(ads)/B(ads)}$ is the formal potential (V) for the redox couple A(ads)/B(ads) defined under the condition $\Gamma_A = \Gamma_B$, F is the Faraday constant (96 485 C mol^{-1}), R is the gas constant (8.314 J mol^{-1} K^{-1}), T is the absolute temperature (K), k_c is the catalytic rate constant of reaction 9.2 (M^{-1} s^{-1}), $C_{R(surf)}$ is the surface concentration of the reactant R (mol cm^{-3}), D_R is the diffusion coefficient of R (cm^2 s^{-1}), and z is the coordinate perpendicular to the electrode surface (cm). As the maximum adsorption of A, Γ_{max}, on the electrode surface is a constant, the surface coverage of B always equals $\Gamma_{max} - \Gamma_A$. Since the catalytic step is assumed irreversible, the concentration of P is not involved in the simulation.

For the present, it is assumed the impact occurs for enough time to undertake a voltammetric sweep. For convenience, the overpotential η (V), equals $E - E^0_{f,A(ads)/B(ads)}$, is applied in the simulation. In cyclic voltammetry, when the potential window is [$\eta_{initial}$, $\eta_{reverse}$] (for the ferrocene/ferrocenium redox reaction, $\eta_{initial} < \eta_{reverse}$), the overpotential η is a function of the time t (s) and the scan rate ν (V s^{-1}):

$$\eta = \begin{cases} \eta_{initial} + \nu t, & t \leqslant \dfrac{\eta_{reverse} - \eta_{initial}}{\nu} \\ \eta_{reverse} + \nu\left(t - \dfrac{\eta_{reverse} - \eta_{initial}}{\nu}\right), & t > \dfrac{\eta_{reverse} - \eta_{initial}}{\nu} \end{cases} \tag{9.5}$$

Note that in the experiments discussed below, a large overpotential is applied to establish a steady-state current.

The current I (A) is generated only from reaction 9.1, which can be calculated by

$$I = F \int \left[k^0 \exp\left(\frac{\beta F}{RT}\eta\right)\Gamma_A - k^0 \exp\left(-\frac{\alpha F}{RT}\eta\right)(\Gamma_{max} - \Gamma_A)\right] \mathrm{d}A \tag{9.6}$$

where A refers to the area of the electrode surface (cm^2). The theory developed is general for any disc and the specific application to particle impacts is considered below.

Migration and convection in the experiments can be neglected, as the solution is assumed to be fully supported by the electrolyte, there is no external force applied to the solution, and the experimental time is short enough to avoid natural convection.[14, 15] Thus, the concentration of R in solution is described by the diffusion equation, Fick's Second law:

$$\frac{\partial C_R}{\partial t} = D_R \nabla^2 C_R \tag{9.7}$$

By solving the partial differential Eq. 9.7 combined with the boundary conditions Eqs. 9.3 and 9.4, the current on the electrode can be derived.

9.2.2 Numerical Simulation

The reaction is considered to take place on a microdisc (GNP). The latter is illustrated in Figure 9.3a, where the cylindrical coordinates z and r represent the directions perpendicular to and radial from the microdisc, respectively. Figure 9.3b shows the calculation grids implemented in the simulation. Expanding grids[16, 17] are applied to optimise the computation, and all the simulation results presented in this work are fully converged.

The resulting problem was solved numerically by means of the Newton-Raphson method and the alternating direction implicit (ADI) method, the details of which can be found in the literature [17]. The simulation was written in C++ with OpenMP for multithreading, and simulations were performed using an Intel(R) Xeon(R) 3.60G CPU. The runtime was approximately 20 minutes per voltammogram.

9.2.3 Voltammetric Characterisation

The voltammograms of an electron transfer in the simple oxidation of adsorbate A ("E reaction", Figure 9.4a) and a heterogeneous EC' reaction (Figure 9.4b) were simulated for various standard electrochemical rate constants, k^0. In the simple E reaction, the maximum surface coverage was selected as 2×10^{-10} mol cm^{-2}, the radius of the GNP as 8.3 μm, and the scan rate as 0.05 V s^{-1}. As shown in Figure 9.4a, a peak is generated around the formal potential of the A(ads)/B(ads) redox couple and the current drops to zero at high overpotentials. This wave-shape and the decrease to zero current are a consequence of the finite amount of electroactive species on the GNP surface. A decrease in k^0 causes changes in both the adsorption peak height and the peak position. For the EC' reaction, the concentration of R was selected as 1 mM, the catalytic rate constant as 1×10^3 M^{-1} s^{-1}, and the diffusion coefficient of R as 1×10^{-5} cm^2 s^{-1}. The rest of the simulation conditions were the same as those set for the E reaction. Figure 9.4b shows when the product of the E reaction becomes the mediator of the following catalytic reac-

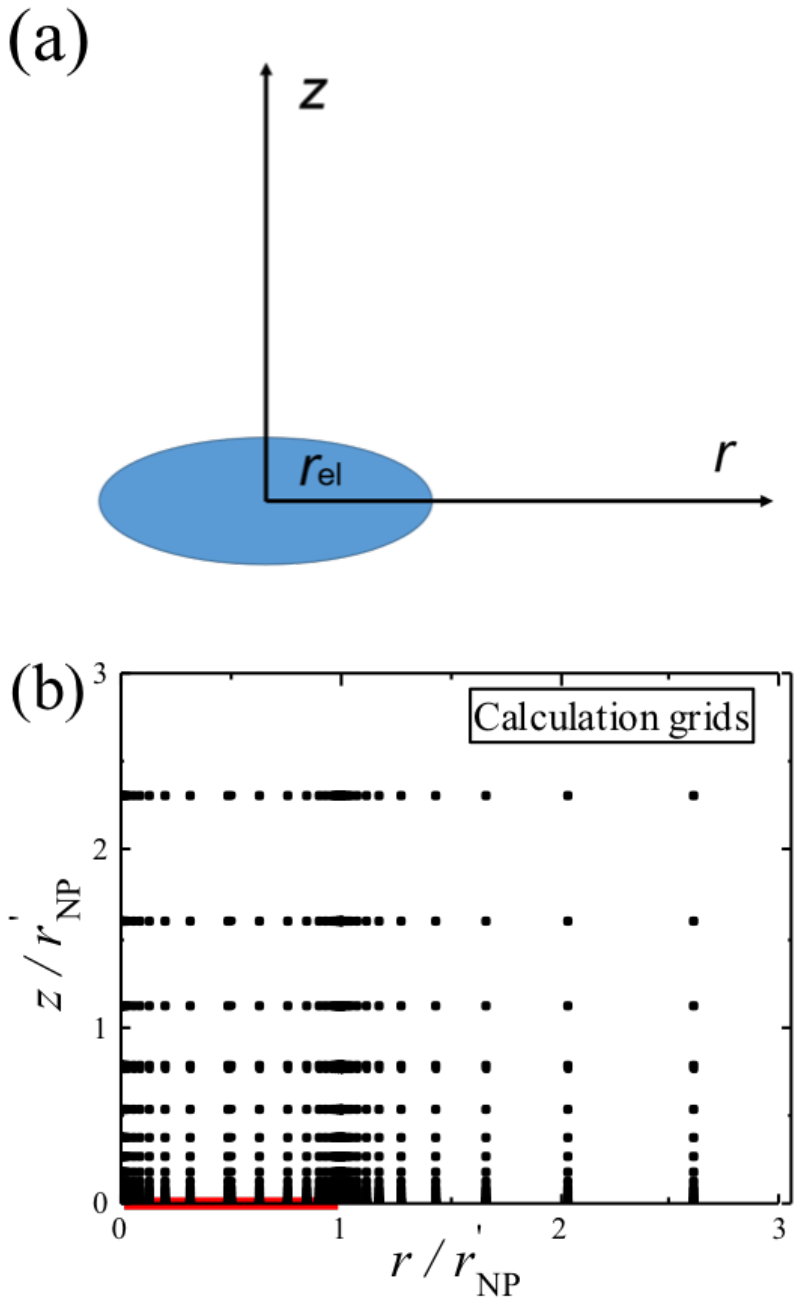

Figure 9.3: (a) Two-dimensional scheme of the microdisc which approximates the graphene nanoplatelet. (b) Calculation grids applied in the simulation. The red line shows the position of the microdisc.

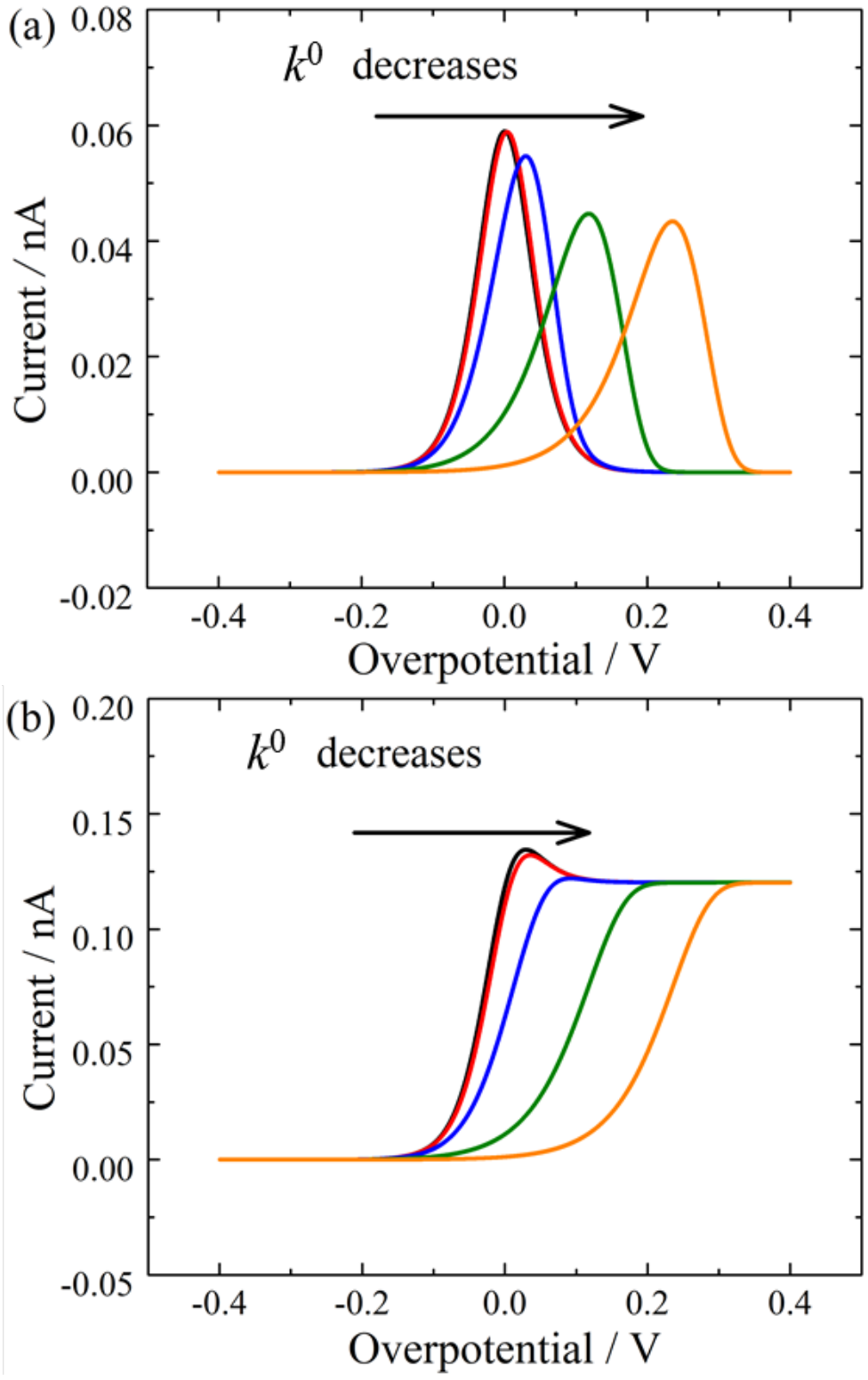

Figure 9.4: Influence of the electron transfer rate on the cyclic voltammograms: (a) E reaction. (b) EC' mechanism. The k^0 values applied in the simulation are 100, 10, 1, 0.1, 0.01 s^{-1}, respectively. The rest of the simulation conditions can be found in the text.

tion, the current signal is enhanced and the voltammogram shows distinct and different wave-shape. The peak vanishes and the current at high overpotentials is not zero but reaches a steady state. The effect of k^0 is reflected on the half-wave potential while the steady-state current is independent of k^0.

For the case of particle impacts where the entire reaction is confined to an impacting particle, such as a GNP, the tiny size of the latter ensures that the steady-state diffusion of R is rapidly established. The analytical expression of the steady-state current can be derived on the basis of the steady-state approximation. At steady state, the reaction rate of the intermediate B of reactions 9.1 and 9.2 should be zero. Given that $\Gamma_B = \Gamma_{max} - \Gamma_A$, the reaction rate of the adsorbate A is zero as well:

$$\begin{aligned} \frac{\partial \Gamma_A}{\partial t} =& - k^0 \exp\left(\frac{\beta F}{RT}\eta\right)\Gamma_A + k^0 \exp\left(-\frac{\alpha F}{RT}\eta\right)(\Gamma_{max} - \Gamma_A) \\ &+ k_c(\Gamma_{max} - \Gamma_A)C_{R(surf)} \\ &= 0 \end{aligned} \tag{9.8}$$

The current density at steady state can be then expressed as:

$$\frac{I}{FS} = k_c(\Gamma_{max} - \Gamma_A)C_{R(surf)} \tag{9.9}$$

At the steady-state, the diffusion on the GNP surface can be approximated as linear and the concentration of R, as well as the surface coverage of A, is considered uniform in the radial direction. Therefore, the concentration difference only appears on the direction perpendicular to the GNP surface and the concentration gradient of R at the GNP surface can be calculated by

$$D_R \frac{\partial c_R}{\partial z}\bigg|_{surf} = D_R \frac{C_R^* - C_{R(surf)}}{\delta} = k_c(\Gamma_{max} - \Gamma_A)C_{R(surf)} \tag{9.10}$$

where δ is the diffusion layer thickness. For a disc electrode, the diffusion layer thickness equals $\pi r_e/4$. The surface coverage of the adsorbate A is zero at steady state. Combining Eq. 9.9 with 9.10 gives the steady-state current for a heterogeneous EC' reaction on a microdisc:

$$I_{ss} = FS\frac{k_c C_R^* \Gamma_{max}}{1 + \frac{\pi k_c \Gamma_{max} r_e}{4D_R}} \tag{9.11}$$

Therefore, when the steady-state current is known, the catalytic reaction rate constant of the heterogeneous EC' reaction (k_c) can be determined.

It is interesting to note if the catalytic reaction is extremely fast compared to the diffusion process of the reactant R, so that $k_c\Gamma_{max} \geqslant D_R/\delta$, the steady-state current of the EC' reaction will reach its maximum value:

$$I_{ss,max} = FS\frac{4D_R C_R^*}{\pi r_e} \tag{9.12}$$

where the maximum steady-state current, $I_{ss,max}$, is only limited by the diffusion of the reactant R.

9.3 Experimental

Details about the chemical reagents and solutions here utilised can be found in Chapter 2, Section 2.1. The structure of L-cysteine is depicted in Figure 9.1, along with the oxidation product, cystine. 0.1 M KCl was used as the supporting electrolyte. pH 7.0 buffer was used to mimic a biological environment. The graphene nanoplatelets (GNPs) were modified with poly(vinylferrocene) following the method described in Chapter 2, Section 2.2.2. Voltammetric measurements were realised using a μAutolab III potentiostat, and impact chronoamperograms were recorded using an in-house-built low-noise potentiostat (Chapter 2, Section 2.3). An edge-plane pyrolytic graphite (EPPG) electrode and a carbon

fibre microwire electrode were used as working electrodes, with their surfaces prepared as described in Chapter 2, Section 2.3.3. A platinum mesh and a saturated calomel electrode (SCE) were used as the counter and reference electrode, respectively.

9.4 Results and Discussion

This section reports first how poly(vinylferrocene)-modified graphene nanoplatelets (PVFc-GNPs) were immobilised on an edge-plane pyrolytic graphite (EPPG) electrode. The corresponding cyclic voltammetry is then discussed, in order to determine the overpotential required to fully drive the reaction. Second, PVFc-GNPs were dispersed in the blank solution with different concentrations of L-cysteine. The impacts of individual PVFc-GNP at a carbon fibre microwire electrode were studied chronoamperometrically. Finally, the experimental results were simulated using the theoretical model, allowing inference of the mechanism and measurement of the catalytic rate constant.

9.4.1 Cyclic Voltammetry

Following the synthesis of PVFc-GNPs (Chapter 2, Section 2.2.2), the nanoplatelets were placed on a filter paper for the abrasive modification of the electrode (Chapter 2, Section 2.3.3). The modified electrode was then transferred to a 25 mL pH 7.0 buffer. Cyclic voltammetry was run from 0 to +0.70 V (*vs.* SCE) and reversed to 0 V at a scan rate of 50 mV s^{-1} (Figure 9.5c). Another unmodified electrode was immersed in the same blank solution to run the voltammogram (Figure 9.5d).

Comparison of the lines shows that an oxidative response can be observed at *ca.* +0.52 V with the peak height of *ca.* 2.6 μA (Figure 9.5, inlay), which corresponds to the oxidation of the adsorbed ferrocene moiety to the ferrocenium cation:

$$Cp_2Fe(ads) + Cl^- \rightleftarrows Cp_2Fe^+Cl^-(ads) + e^- \tag{9.13}$$

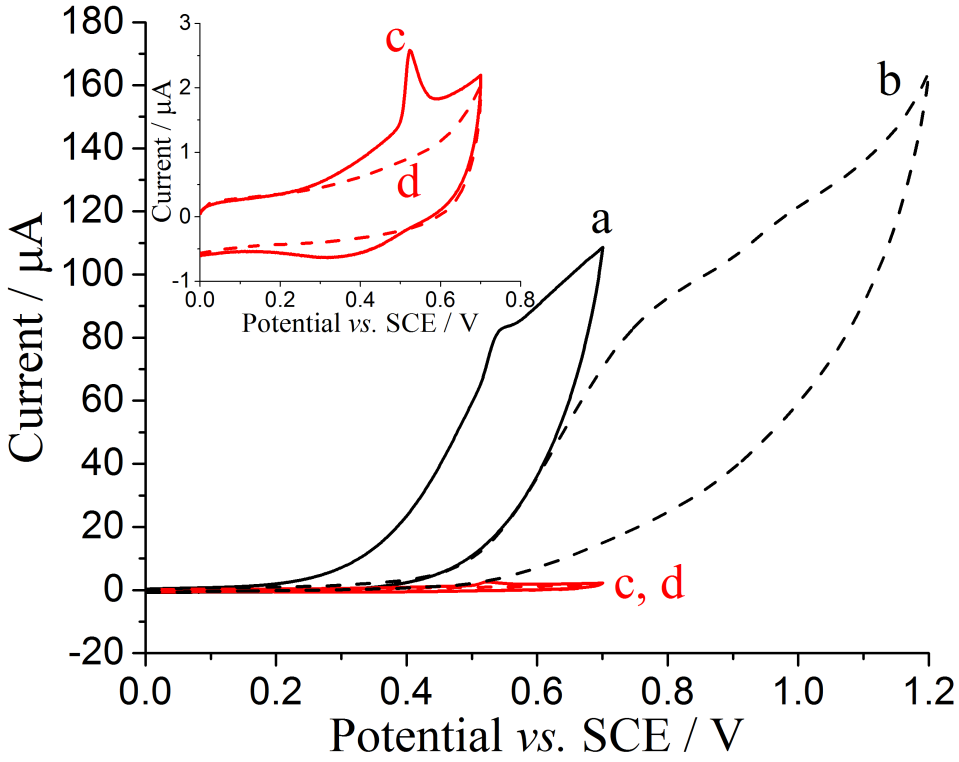

Figure 9.5: Voltammogram in a pH 7.0 buffer at poly(vinylferrocene)-modified graphene nanoplatelets immobilised edge-plane pyrolytic graphite electrodes *via* abrasive modification (a and c), and at unmodified electrodes (b and d). A concentration of 10 mM L-cysteine is present in a and b. L-Cysteine is absent in c and d. Scan rate = 50 mV s^{-1}.

The inlay of Figure 9.5 shows a reductive response as a broad peak at *ca.* +0.32 V with the height of *ca.* 0.6 μA. The back peak is less well-defined as the forward peak, as a result of the ion-pairing between the ferrocenium cation and the chloride anion from the supporting electrolyte. Such coordination stabilises the ferrocenium cation, and hence, its reduction becomes less favourable (the so-called "square scheme"[18, 19]). In contrast, PVFc-GNPs supported with $NaClO_4$ shows a higher redox signal at a lower potential (Figure 9.6). However, 10 mM L-cysteine was observed to precipitate in 25 mL of pH 7.0 buffer supported with 0.1 M $NaClO_4$, precluding its use in the mediated oxidation of L-cysteine. KCl was the optimal electrolyte due to the higher solubility of L-cysteine.

The investigation next examined the cyclic voltammetry of L-cysteine-containing solutions at EPPG electrode. An unmodified electrode was immersed in 25 mL of 10 mM

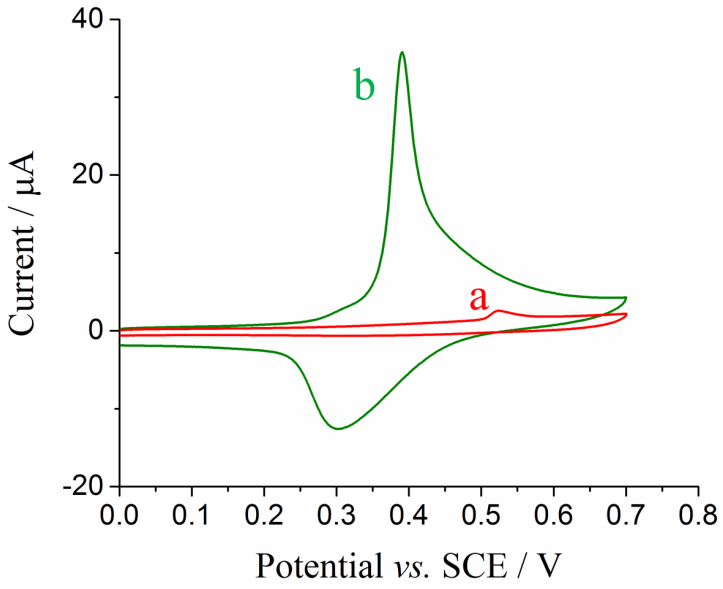

Figure 9.6: Voltammograms measured in a pH 7.0 buffer, using a poly(vinylferrocene)-modified graphene nanoplatelets immobilised edge-plane pyrolytic graphite electrodes *via* abrasive modification. Solution is supported with (a) 0.1 M KCl and (b) 0.1 M $NaClO_4$. Scan rate = 50 mV s^{-1}.

L-cysteine pH 7.0 buffer to record the voltammogram in a wide potential window between 0 and +1.20 V (*vs.* SCE). Figure 9.5b shows a poorly defined oxidative response at *ca.* +0.80 V, which is in a good agreement with the reported value, +0.81 V, for the *direct* oxidation of L-cysteine in a pH 7.0 buffer[5]. In contrast, when the modified electrode was transferred to the same 10 mM L-cysteine solution to run the voltammetry (Figure 9.5a), an oxidative response was observed at *ca.* +0.54 V, close to the oxidation potential of the ferrocene moiety. This can be ascribed to the oxidation of L-cysteine mediated by the ferrocenium cation. The following EC' catalytic mechanism is proposed:

$$Cp_2Fe(ads) \overset{k^0}{\rightleftarrows} Cp_2Fe^+(ads) + e^- \tag{9.14}$$

$$Cp_2Fe^+(ads) + \text{L-cysteine(sol)} \overset{k_c}{\rightarrow} Cp_2Fe(ads) + \text{product(sol)} \tag{9.15}$$

where the Cp_2Fe/Cp_2Fe^+ couple serves as the catalyst for the oxidation of L-cysteine, k^0 is the standard electrochemical rate constant of the Cp_2Fe/Cp_2Fe^+ couple at the GNPs

surface, and k_c is the heterogeneous rate constant of reaction 9.15. After the ferrocene moiety is oxidised at the GNPs surface, an electron is transferred from L-cysteine to the ferrocenium cation adsorbed at the GNPs. Cystine is generated at a much lower potential (Figure 9.5a) compared to the direct oxidation of L-cysteine (Figure 9.5b). The outcome of the catalysis shows an oxidative signal, as well as a relative loss of chemical reversibility due to the tiny concentration of the Cp_2Fe/Cp_2Fe^+ couple in comparison with L-cysteine.[20] After the conversion of Cp_2Fe to Cp_2Fe^+, the latter participates in the catalytic cycle. Since little Cp_2Fe^+ is left to reproduce Cp_2Fe, there is a negligible reductive back peak in Figure 9.5a.

Although the catalytic response is qualitatively observed on the PVFc-GNP-modified EPPG electrode in Figure 9.5, the voltammetric signal cannot be applied to determine the kinetic parameters in the catalytic oxidation reaction of L-cysteine. Given that the mass transport to the EPPG electrode modified with a porous GNP layer is uncertain, it is difficult to interpret the scan rate dependence of the signal. Moreover, the modification of particles on the electrode can lead to agglomeration and/or aggregation[7, 10, 11], which again militates against modelling and quantitative analysis. Therefore, in order to correctly understand the kinetics of the electrocatalytic reaction, the direct measurement of the reaction signal on the individual particles is needed.

9.4.2 Particle Impact Chronoamperometry

Having evidenced that PVFc-GNPs can mediate the oxidation of L-cysteine, we next turn to study the impacts of PVFc-GNPs in L-cysteine-containing solutions at carbon fibre microwire electrodes. According to the results in the cyclic voltammetry at the PVFc-GNPs-modified EPPG electrodes, the mediated oxidation of L-cysteine is expected to commence when the potential applied to the electrode is at least *ca.* +0.54 V (*vs.* SCE).

The electrode was potentiostatted at +1.00 V (*vs.* SCE) to allow a large overpotential (Chapter 8) to fully drive the reactions 9.14 and 9.15. As discussed in the context of Figure 9.4, at high overpotentials the oxidation of L-cysteine at an individual PVFc-GNP can reach a steady state, allowing the characterisation of the catalytic mechanism and kinetics. The prepared PVFc-GNPs were first suspended in 5 mL of pH 7 / 0.1 M KCl solution with the absence of L-cysteine. A chronoamperometry was run using a carbon fibre microwire electrode. When there is no L-cysteine in the solution (Figure 9.7a), impact spikes of PVFc-GNPs were observed. The charge passed per spike can be estimated by taking the integrated area under the individual spike, with the average value denoted as $\bar{Q}$. For the absence of L-cysteine, $\bar{Q}$ is 6^{+8}_{-6} pC. The PVFc-GNPs was then suspended in 5 mL of 20 mM L-cysteine / 0.1M KCl solution. Figure 9.7e shows the impact signals are significantly enhanced, with the value for $\bar{Q}$ as 180 ± 172 pC. Further, the experiment was repeated for various concentrations of L-cysteine, 5 mM (Figure 9.7b), 10 mM (Figure 9.7c), and 15 mM (Figure 9.7d). The corresponding $\bar{Q}$ for the three concentrations is 13^{+45}_{-13}, 62 ± 31 and 131 ± 105 pC, respectively. The variation is shown in Figure 9.8 (squares), where $\bar{Q}$ is plotted against the concentration of L-cysteine ($C^*_{L-cysteine}$).

In order to demonstrate the switch on/off of the reactions 9.14 and 9.15 corresponding to the oxidation of the ferrocene moieties, a potential +0.20 V was applied to the electrode to run the chronoamperometry of PVFc-GNPs in the same series of solutions varying the concentration of L-cysteine. The corresponding $\bar{Q}$ is plotted against $C^*_{L-cysteine}$, as shown as dots in Figure 9.8. Despite of the change in $C^*_{L-cysteine}$, $\bar{Q}$ remains constant at 2 ± 1 pC.

There are two possible physical origins of the charge transfer involved in the impacts: a catalytic response following the Faradaic process as demonstrated above, or a capacitative response (Chapter 7). In the former case, Faradaic charge transfer first takes place between PVFc and the electrode (Eq. 9.14), the resulting ferrocenium cation then un-

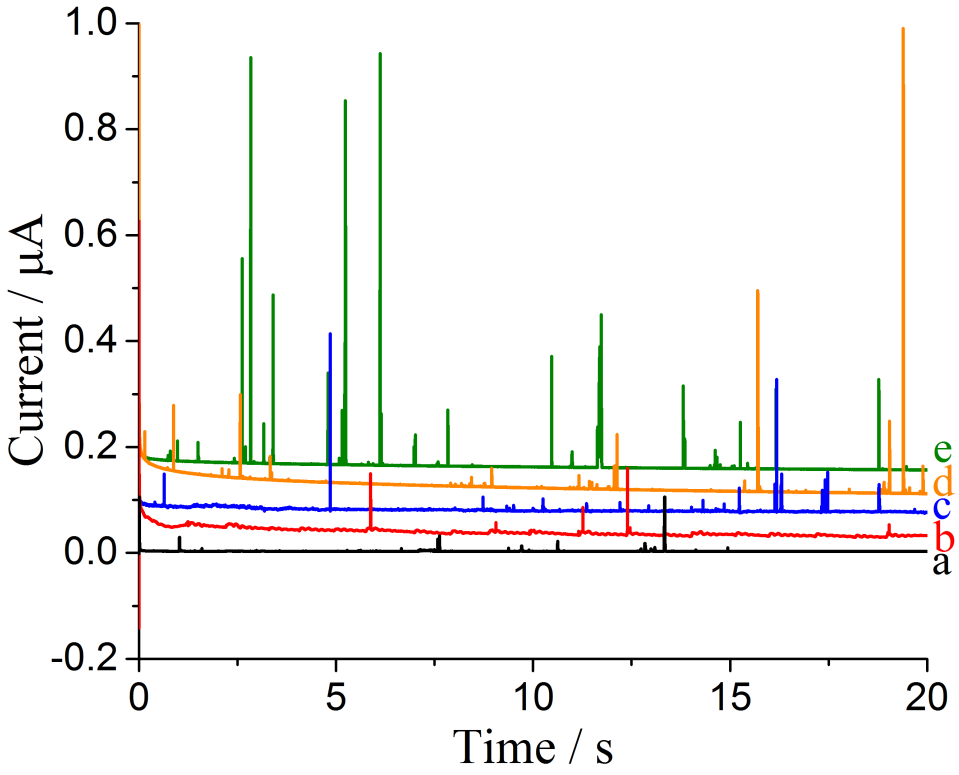

Figure 9.7: Impact chronoamperograms of 3×10^{-14} M graphene nanoplatelets suspension at carbon fibre microwire electrodes potentiostatted at +1.00 V (*vs.* SCE), in a pH 7 buffer. Various concentration of L-cysteine is used: (a) 0 mM, (b) 5 mM, (c) 10 mM, (d) 15 mM, and (e) 20 mM. Baselines are shifted vertically for clarity.

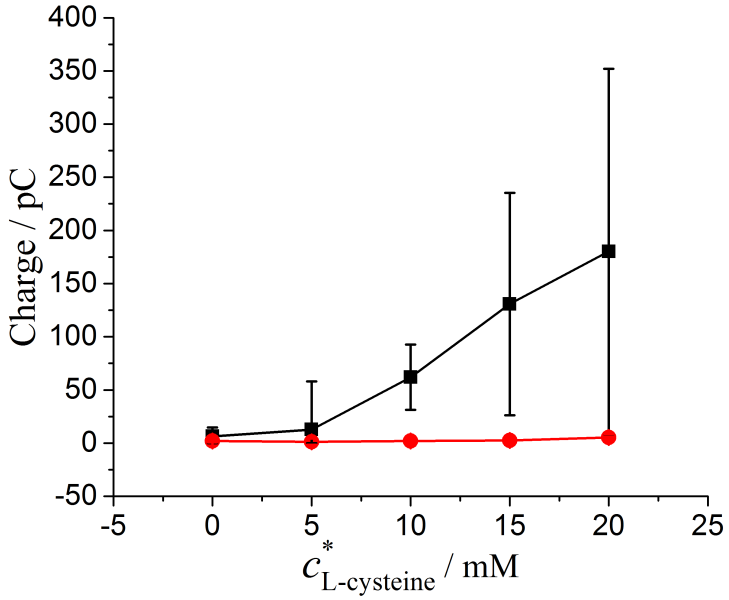

Figure 9.8: The average charge passed per impacts spike dependence of L-cysteine concentration ($C^*_{L-cysteine}$), at +1.00 V (squares) and +0.20 V (dots) *vs.* SCE. The error bars are obtained from $SD/n''^{1/2}$, where SD is the standard deviation and n" is the number of spikes.

dergoes further electron transfer with L-cysteine in the solution to produce cystine (Eq. 9.15). The overall charge transfer should relate to the concentration of L-cysteine. Herein a threshold potential is required to drive the redox reaction (Eq. 9.14) and the subsequent catalytic reaction (Eq. 9.15). In the latter case, a particle becomes charged upon collision with the potentiostatted electrode. To maintain the charge neutrality, electrons move in or out of the electrode when the applied potential deviates from the potential of zero charge (PZC). The charge transfer should be independent of the reactions. Figure 9.8 shows at +0.20 V (*vs.* SCE), $\bar{Q}$ remains unchanged at different $C^*_{L-cysteine}$; hence, only capacitative impacts likely occur. At +1.00 V (*vs.* SCE), $\bar{Q}$ increases with $C^*_{L-cysteine}$, implying impacts arise due to the catalysis of L-cysteine following the Faradaic electron transfer between PVFc and the GNPs (reactions 9.14 and 9.15).

9.4.3 Simulation of Impact Spikes: Derivation of Catalytic Rate Constant

As discussed in the context of Eq. 9.11, a steady-state current can be used to infer kinetic information for the catalytic reaction of L-cysteine on PVFc-GNPs. However, due to the short residence time of the colloid, direct measurement of the steady-state current (I_{ss}) on an individual GNP is not easy.[21] Instead, an average I_{ss} is obtained implicitly from the reaction charge (Q) and duration (t_{impact}) per impact spike, *via* $I_{ss} = Q/t_{impact}$. Q and t_{impact} are collected at high overpotentials where the steady-state current is reached. After analysis of the impact spikes, the experimental I_{ss} is plotted as a function of $C^*_{L-cysteine}$ varying from 5 mM to 20 mM (Figure 9.9, black squares with error bars). The experimental I_{ss} is shown to be proportional with $C^*_{L-cysteine}$, which is consistent with Eq. 9.11. This supports the choice of mechanism used in analysing the experimental data.

In Figure 9.9, the red and blue lines are the theoretical prediction for the largest and

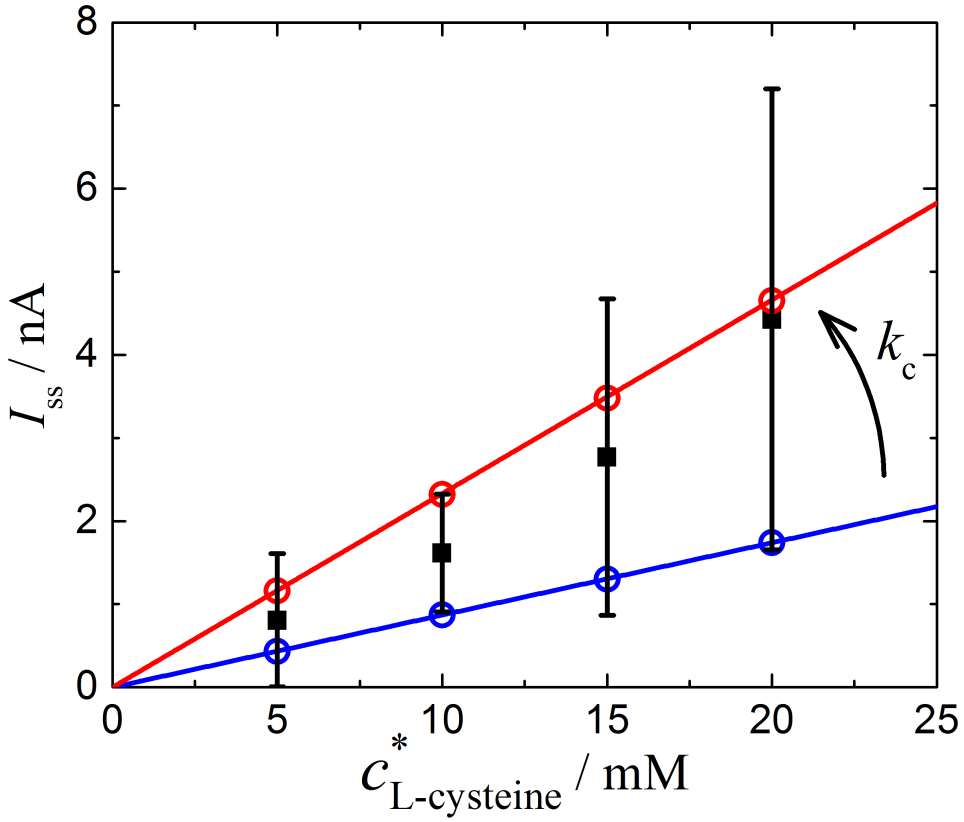

Figure 9.9: L-Cysteine concentration ($C^*_{L-cysteine}$) variation of the steady-state current (I_{ss}) per impact spike. Black squares: experimental I_{ss}. The error bars are obtained from $SD/n''^{1/2}$. Circles: simulated I_{ss}, with catalytic reaction rate (k_c) of 1.3 $\times$ 10^3 M^{-1} s^{-1} (red) and 3.6 $\times$ 10^3 M^{-1} s^{-1} (blue). Lines: calculated I_{ss} from Eq. 9.11 to fit experimental I_{ss} within its error bars. The gradient change between the red and blue lines corresponds to a range of k_c. In the simulation, parameters used are Γ_{max} = 2 $\times$ 10^{-10} mol cm^{-2}, k^0 = 3 s^{-1}, r_e = 8.3 μm and $D_{L-cysteine}$ = 7.9 $\times$ 10^{-5} cm^2 s^{-1}.

the lowest steady-state currents, according to the distribution of the experimental values of I_{ss}. The gradient of the two lines is used to derive the boundary of the catalytic rate constant (k_c). A range of k_c can hence be determined by considering the distribution of the experimental I_{ss}. According to Eq. 9.11, after plotting I_{ss} against $C^*_{L-cysteine}$, the gradient can be expressed as

$$\frac{\mathrm{d}I_{ss}}{\mathrm{d}C^*_{L-cysteine}} = FS\frac{k_c\Gamma_{max}}{1+\dfrac{\pi k_c\Gamma_{max}r_e}{4D_{L-cysteine}}} \tag{9.16}$$

where the maximum surface coverage (Γ_{max}) and the standard electrochemical rate con-

stant (k^0) were measured from the redox reaction of PVFc/PVFc$^+$ in Chapter 8, as *ca.* 2×10^{-10} mol cm^{-2} and *ca.* 3 s^{-1}, respectively. The diffusion coefficient of L-cysteine ($D_{L-cysteine}$) was reported as 7.9×10^{-5} cm^2 s^{-1}.[22] The radius of GNP (r_e) is 8.3 μm. The catalytic rate constant (k_c) can thus be derived from the blue and red line, as 1.3 and 3.6×10^3 M^{-1} s^{-1}, respectively. Moreover, the values for k_c are used to simulate the I_{ss} (Figure 9.9, circles). The simulated results match with the analytical lines, demonstrating the validity of Eq. 9.11 in derivation of k_c. Note the error bar becomes larger at higher concentration of L-cysteine (Figures 9.8 and 9.9), reflecting the increasing variation of experimental results.

9.5 Conclusions

The theory for catalytic particle impacts has been developed for the case where the impacting particle mediates electron transfer to a solution phase species bringing about chemical reactions. For tiny particles, the fast diffusion of the reactant to the surface can establish a steady-state current which reflects the concentration of the target. The theory has been applied to the oxidation of cysteine mediated with ferrocene modified graphene nanoplatelets and a rate constant estimated.

References

[1] Lin, Q.; Lin, C.; Wu, H.; Batchelor-McAuley, C.; Compton, R. G. *The Journal of Physical Chemistry C* **2016**, *120*, 20216–20223.

[2] Casado, C. M.; Cuadrado, I.; Morán, M.; Alonso, B.; Barranco, M.; Losada, J. *Applied Organometallic Chemistry* **1999**, *13*, 245–259.

[3] Yin, W.-W.; Yue, J.-L.; Cao, M.-H.; Liu, W.; Ding, J.-J.; Ding, F.; Sang, L.; Fu, Z.-W. *Journal of Materials Chemistry A* **2015**, *3*, 19027–19032.

[4] Lawrence, N. S.; Tustin, G. J.; Faulkner, M.; Jones, T. G. J. *Electrochimica Acta* **2006**, *52*, 499–503.

[5] Raoof, J. B.; Ojani, R.; Kolbadinezhad, M. *Bulletin of the Chemical Society of Japan* **2005**, *78*, 818–826.

[6] Thearle, R. A.; Sofer, Z.; Bouša, D.; Pumera, M. *ChemPhysChem* **2016**, *17*, 2096–2099.

[7] Toh, H. S.; Batchelor-McAuley, C.; Tschulik, K.; Uhlemann, M.; Crossley, A.; Compton, R. G. *Nanoscale* **2013**, *5*, 4884–4893.

[8] Stuart, E. J.; Tschulik, K.; Batchelor-McAuley, C.; Compton, R. G. *ACS Nano* **2014**, *8*, 7648–7654.

[9] Zhou, X.; Cheng, W.; Compton, R. G. *ChemElectroChem* **2015**, *2*, 691–699.

[10] Toh, H. S.; Compton, R. G. *ChemistryOpen* **2015**, *4*, 261–263.

[11] Toh, H. S.; Jurkschat, K.; Compton, R. G. *Chemistry - A European Journal* **2015**, *21*, 2998–3004.

[12] Guidelli, R.; Compton, R. G.; Feliu, J. M.; Gileadi, E.; Lipkowski, J.; Schmickler, W.; Trasatti, S. *Pure and Applied Chemistry* **2014**, *86*, 245–258.

[13] Guidelli, R.; Compton, R. G.; Feliu, J. M.; Gileadi, E.; Lipkowski, J.; Schmickler, W.; Trasatti, S. *Pure and Applied Chemistry* **2014**, *86*, 259–262.

[14] Dickinson, E. J. F.; Limon-Petersen, J. G.; Rees, N. V.; Compton, R. G. *The Journal of Physical Chemistry C* **2009**, *113*, 11157–11171.

[15] Ngamchuea, K.; Eloul, S.; Tschulik, K.; Compton, R. G. *Analytical Chemistry* **2015**, *87*, 7226–7234.

[16] Gavaghan, D. J. *Journal of Electroanalytical Chemistry* **1997**, *420*, 147–158.

[17] Compton, R. G.; Laborda, E.; Ward, K. R. *Understanding Voltammetry: Simulation of Electrode Processes*; Imperial College Press, 2014.

[18] Laborda, E.; Olmos, J. M.; Martínez-Ortiz, F.; Molina, A. *Journal of Solid State Electrochemistry* **2015**, *19*, 549–561.

[19] Laborda, E.; Olmos, J.-M.; Torralba, E.; Molina, A. *Analytical Chemistry* **2015**, *87*, 1676–1684.

[20] Lin, Q.; Li, Q.; Batchelor-McAuley, C.; Compton, R. G. *Physical Chemistry Chemical Physics* **2013**, *15*, 7760–7767.

[21] Kätelhön, E.; Feng, A.; Cheng, W.; Eloul, S.; Batchelor-McAuley, C.; Compton, R. G. *The Journal of Physical Chemistry C* **2016**, *120*, 17029–17034.

[22] Raoof, J. B.; Ojani, R.; Beitollahi, H.; Hosseinzadeh, R. *Analytical Sciences* **2006**, *22*, 1213–1220.

Chapter 10

Conclusions

This thesis has investigated the use of electrochemistry in the detection and characterisation of solid particles at micron-scale. A new electrochemical method has been developed to use particle impacts to quantify the adsorption of redox active molecules on the surface of insulating particles. From simulations of the spike transients, the surface coverages of catechol (1,2-hydroxybenzene), 9,10-anthraquinone, tetrachloro-1,4-benzoquinone, and poly(vinylferrocene) on alumina were found to be (3.0 ± 0.9), (1.5 ± 1.4), (2.7 ± 1.7), and (2.1 ± 0.7) × 10^{-10} mol cm^{-2}, respectively. These values are in close agreement with the estimation made assuming that molecules are close-packed in a monolayer over the surface of alumina.

Having gained insights into the insulating particles, the investigation was developed onto the conductive particles. Measurement of fast electron transfer for the ferrocene/ferrocenium redox couple immobilised on graphene nanoplatelets has been proven feasible *via* the use of particle impacts. In 0.1 M $NaClO_4$ aqueous solution, the electrochemical rate constant was found to be 3 ± 1 s^{-1} or faster. This strategy provides a promising tool with which for obtaining kinetic information relating to a wide range of redox couple by the use of graphene nanoplatelets. Moreover, a theory for catalytic particle impacts has been established for the case where impacting particle mediates electron transfer to a solution phase electroactive species, bringing about chemical reactions. Successful modelling was demonstrated for the spike charge in ferrocene-modified graphene nanoplatelets

mediated L-cysteine oxidation, with the determination of the catalytic rate constant as $(2.4 \pm 1.2) \times 10^3$ M^{-1} s^{-1}.

Impacts of particles modified with redox active molecules thus provides a powerful electrochemical approach enabling sensitive detection and quantitative analysis of solid particles at micron-scale. The electroanalysis of alumina and graphene nanoplatelets in this thesis will be valuable in future work, particularly in the application of modified graphene nanoplatelets as nanocomposites in solar cells, transparent conductors, and supercapacitors; as well as the application of modified alumina as supports for metal catalysts in the exhaust of automobiles, and preparation of analgesic and antipyretic drugs. The extension to other particle types is evident.